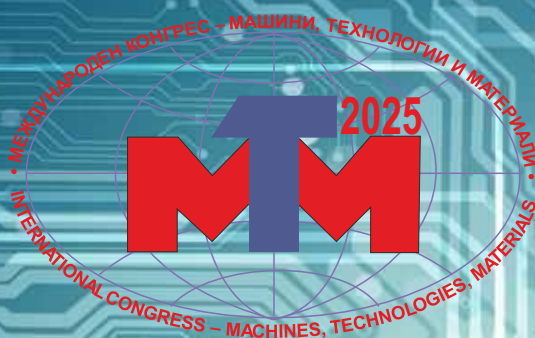# XXII INTERNATIONAL SCIENTIFIC CONGRESS

SUMMER SESSION

03 - 06.09.2025, VARNA, BULGARIA

MACHINES
TECHNOLOGIES
MATERIALS 2025

PROCEEDINGS

VOLUME III
MATERIALS
MANAGEMENT
MACHINES

PROCEEDINGS

ALL ARTICLES ARE PUBLISHED AFTER PEER REVIEW BY TWO INDEPENDENT REVIEWERS.

C O N T E N T S

The Influence of Heat Treatment on Mechanical and Corrosion Properties of High-Chromium White Cast Irons Modified by Titanium and Boron

Kemal Delijić[1,*], Mirjana Filipović[2]

University of Montenegro, Faculty of Metallurgy and Technology, (MNE)[1]

University of Belgrade, Faculty of Technology and Metallurgy, (SRB)[2]

[1]kemal@ac.me; [2]mirjanaf@tmf.bg.ac.rs

Abstract: The effect of individual additions of Ti and B into high chromium white cast irons (HCWCIs) on the structure, corrosion and selected mechanical properties was investigated. Two different heat treatments were applied, high-temperature treatment at 960 ^oC/1h, and subcritical treatment at 550 ^oC/4 h. The microstructure was investigated by OM and SEM; compositions of matrix and carbides were analyzed by EDS. Mechanical behavior of HCWCIs was analyzed by measuring hardness, toughness, abrasive/wear resistance and resistance to repeated impacts. Corrosion behavior was evaluated electrochemically, by linear and Tafel polarization methods in 0,1M NaCl solution. The properties of the modified HCWCIs were compared with the properties of the base unmodified HCWCI alloy (ASTM A532-IIE).

Keywords: HCWCI, GRINDING BALLS, TITANIUM, BORON, CORROSION, IMPACT, WEAR RESISTANCE

1. Introduction

High Chromium White Cast Irons (HCWCIs) are iron-based alloys containing 11-30 wt% Cr and 1.8-3.6 wt% C, often additionally alloyed with Mo, Mg, Cu and Ni [1]. HCWCI has been proven to be an effective material for applications in aggressive environments where abrasion and erosion resistances are required. The high wear resistance of HCCI is attributed to the combination of hard primary and/or eutectic carbides of M_7C_3 (M: Fe, Cr and other strong carbide formers) and relatively ductile ferrous matrix [2]. The properties of these irons are influenced by the type, hardness, morphology, distribution, volume fraction and orientation of eutectic carbides, as well as the matrix microstructure, which supports the carbide phase [3, 4]. Different structures of the matrix can be achieved by alloying element and applying specific heat treatments. Pearlite, martensite and austenite are among the typical microconstituents in the matrix [2]. Most researchers have focused on either strengthening the matrix by destabilizing it or improving wear resistance with alloy additions [1, 5]. The addition of small amounts of carbide-forming elements (Ti, B, V, W,..) that bind carbon in the form of carbides, different from cementite, with higher hardness and a much more favorable morphology and reduce the carbon content in the matrix, enable the improvement of both impact toughness and resistance to abrasion wear [4]. Different critical and subcritical heat treatments also alter the initial casting microstructure of HCCIs and lead to varying degrees of secondary carbide precipitation [1, 6, 7]. HCWI alloys with B addition have been investigated and found to increase the wear resistance [8-15]. Boron influences the microstructure of HCWI alloys in three ways: B is a C substitute element and effectively increases the C equivalent of the alloy, resulting in a higher volume fraction of carbides, most of the B is distributed in the carbides, forming complex carboborides such as $M_3(C,B)$ and $M_7(C,B)_3$, instead of M_3C and M_7C_3; higher B content promotes the formation of M_2B and M_3B boride phases which have a much higher hardness and fracture toughness compared to carbide phases of M_7C_3; B addition decreases the solubility of carbon in γ-Fe which increases carbide nucleation sites during solidification resulting in carbide refinement [8]. The addition of Ti gives the strongest driving force for carbide formation, indicating that TiC carbide is expected to precipitate preferentially from the melt, even in rapid cooling conditions [16]. Titanium addition influences the microstructure of HCWI in these ways: Ti addition alters the solidification sequence by forming TiC; by TiC forming Ti addition depletes the carbon concentration in the melt which leads to a decrease in the volume fraction of M_7C_3 carbide [16];

For this study, four sets of HCWCI grinding balls with dimensions of ø60 mm were cast, with the addition of 0.36% and 2.37% by weight Ti and the addition of 0.021% and 0.071% by weight B. Additionally, one set of "base alloy" grinding balls (chemical composition defined by ASTM A532-IIE) was cast and tested under the same conditions, with the aim of comparing the properties of novel cast balls with the properties of standard alloys.

2. Experimental procedure

The chemical composition of tested alloys is listed in Table 1. The melting process of HCWC irons, individually alloyed with titanium (0,36 wt%, and 2,37 wt%) and boron (0,021 wt%, and 0,071 wt%), was carried out in an induction furnace. Grinding balls with 60mm of diameter were cast into gray cast iron water cooled permanent molds with alloyed-steel inserts (a cluster of eight balls). The casting temperature was 1470 ^oC - 1490 ^oC and the mold temperature was 130 ^oC - 140 ^oC. After casting, the grinding balls were kept 3 minutes in the mold and further cooled in ambient air. Two different heat treatments were applied: heating to the destabilization temperature of 960 ^oC, holding at this temperature for 1 h, then cooling in air; subcritical thermal treatment - heating to a temperature of 550 ^oC, holding at this temperature for 4 h, then cooling in air. The samples were tested in the as-cast and both heat treated tempers. The microstructure was investigated by optical microscopy and SEM, and compositions of matrix and carbides were analyzed by EDS.

Table 1. Chemical composition of tested HCWCI alloys, wt%

Element,	Base alloy[1] wt%	Alloy 1 (add. Ti)	Alloy 2 (add. Ti)	Alloy 3 (add. B)	Alloy 4 (add. B)
C	2,91	2,93	2,72	2,64	3,28
Si	0,83	0,97	1,81	1,28	0,96
Mn	0,79	0,79	0,93	0,80	0,71
P	0,029	0,024	0,018	0,047	0,031
S	0,016	0,015	0,014	0,013	0,012
Cr	17,83	17,96	14,53	14,28	17,92
Mo	1,15	1,15	1,16	1,08	1,02
Cu	0,84	0,89	1,51	0,92	0,97
Ni	0,11	0,11	0,12	0,10	0,13
Al	0,051				
B	<0,002	<0,002	<0,002	**0,021**	**0,071**
Ti	0,021	**0,360**	**2,370**	0,109	0,038
V	0,041	0,060	0,130	0,072	0,060
Nb		0,008	0,022	0,056	0,180
W	<0,001	<0,001	0,102	<0,001	<0,001
Cr/C	6,13	6,13	5,34	5,41	5,46
[1] high chromium cast white iron, chemical composition ASTM A532-IIE					

Mechanical behavior of HCWCIs was analyzed by measuring Rockwell hardness, toughness (Charpy V notch pendulum impact test), wear resistance and resistance to repeated impacts. The dry sand/rubber wheel method, defined by the ASTM G65 standard, was used to test abrasion resistance. The resistance to repeated impacts is tested by simulating ball impacts during rotary milling (repeated or cyclic impacts). In this test, grinding balls are dropped from a height of 3.5 m and hit another grinding balls located in the bent section of the tube of the device. There are usually 18 grinding balls in the bent section of the tube, while another four are located in the transport system, so the test is carried out with a total of 22 grinding balls. Corrosion behavior was evaluated by linear and

Tafel polarization electrochemical methods in 0,1 M NaCl solution. Electrochemical measurements were carried out in a conventional three-electrode glass cell, composed of a specimen as a working electrode (HCWCIs samples), graphite counter electrode and Ag/AgCl,KCl electrode as a reference electrode. The working surfaces of these electrodes were 1 cm^2. Before each measurement, a sample was ground with a series of SiC abrasive papers and then polished. The properties of the novel modified HCWCIs in the as-cast and heat-treated tempers were compared with the properties of the base unmodified HCWCI (ASTM A532-IIE).

3. Results

Microstructures of investigated as-cast grinding balls, at the surface and in central zones of the cross-sections, are presented in Fig. 1. Titanium influences the formation of a fine-grained and more homogeneous structure in the cross-section of the tested as-cast grinding balls, Fig. 1.b.c. The difference in the size of the surface-center phases exists, but much less pronounced in Ti-modified HCWCIs than in the base ASTM A532-IIE alloy. Also, the volume fraction of primary austenite dendrites is higher, and the amount of eutectic and M_7C_3 carbides is lower if compared to the base alloy, noting that with increasing Ti content this difference is greater, Figure 1.b-c. The presence of TiC carbide particles is observed, with the volume fraction of TiC being significantly higher in HCWCI alloys containing higher amount of titanium, Figure 2. The influence of boron on the microstructure is also very obvious - boron-modified HCWCI alloys have a significantly finer structure compared to the base and titanium-modified alloys, Figure 1.d-e. Boron also affects the transformation of austenite during cooling after crystallization, and the degree of transformation of austenite into martensite is higher than in Ti-modified HCWCs. With increasing of boron content in the HCWCIs, the volume fraction of martensite increases, Figure 3. Subcritical heat treatment of HCWCIs is generally used to eliminate retained austenite. Subcritical heat treatment of Ti-modified HCWCIs resulted in almost complete transformation of the eutectic austenite into martensite. In addition, martensite is present in a wider surface zone of primary austenite dendrites along the boundary with the eutectic M_7C_3 carbide. Subcritical heat treatment causes significant changes in the microstructure of HCWCI alloy containing 0.021%B. The degree of martensitic transformation of eutectic and primary austenite is high, with the note that a certain level of austenite to pearlite transformation can also be observed. The microstructure of the metal-matrix of the HCWCI alloys after high-temperature treatment at 960 ^{o}C/1h is typical for this type of material and this heat treatment regime. It consists mainly of precipitated secondary carbides and martensite, with a very small volume fraction of retained austenite. In this type of alloy, fine and almost globular particles of secondary carbide of the $M_{23}C_6$ type (zone axis [100]), with a size of less than 1 μm, precipitate at the destabilization temperature.

Mechanical properties

The measured Rockwell hardness values, as the average measured values for the cross-section of the balls are reported in Table 2. The results obtained from the hardness measurements of the samples are relatively close among the different alloys in the same tempers. The differences in hardness of the grinding balls are a consequence of the different volume fraction of the carbide phases as well as the volume fraction of austenite, or martensite in the structure. Subcritical heat treatment increases the hardness of all tested alloys. The highest increase in hardness (about 7%) is indicated for the alloy modified with 0.021 wt% boron. The tested grinding balls have the highest hardness after high-temperature heat treatment. The highest hardness increase after this heat treatment, (≈ 26%), in relation to the as-cast temper, is indicated for the Ti-modified HCWCI alloy modified with 2.37 wt% Ti. The highest hardness (63.3 HRC) is measured on grinding balls made of the HCWCI alloy modified with the addition of 0.071 wt% boron.

surface   center

(a) Base alloy, ASTM A532-IIE

(b) Alloy 1, (addition of 0,36 wt% Ti)

(c) Alloy 2, (addition of 2,37wt% Ti)

(d) Alloy 3 (addition of 0,021 wt% B
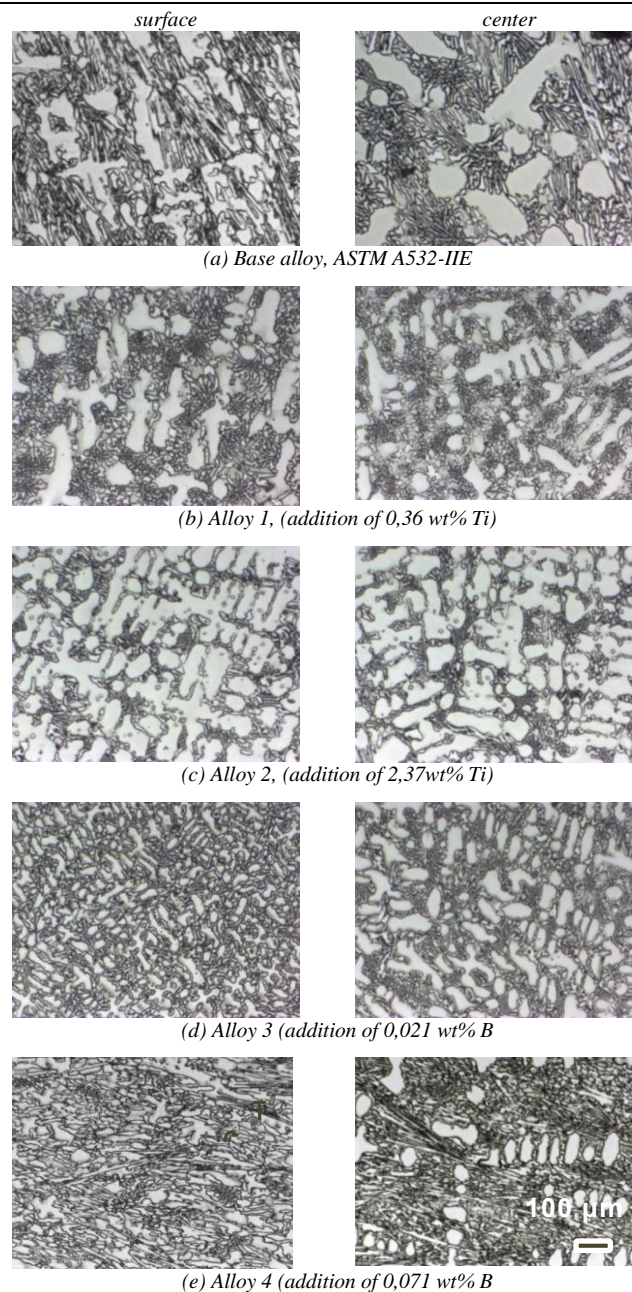
(e) Alloy 4 (addition of 0,071 wt% B
Fig. 1. Optical micrographs of as-cast grinding balls structure (surface and center of grinding ball
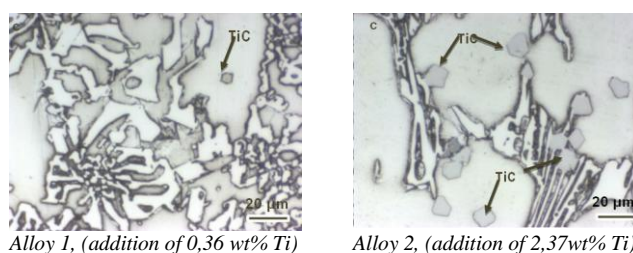
Alloy 1, (addition of 0,36 wt% Ti)   Alloy 2, (addition of 2,37wt% Ti)
Fig. 2. Optical micrographs of as-cast grinding balls structure (center)modified by Ti adition
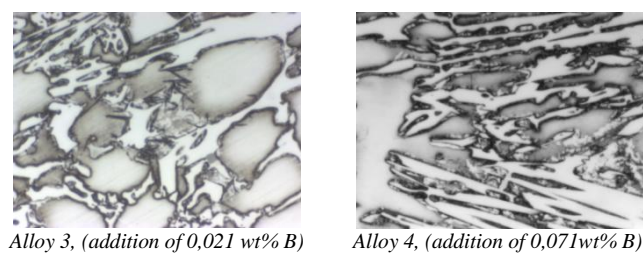
Alloy 3, (addition of 0,021 wt% B)   Alloy 4, (addition of 0,071wt% B)
Fig. 3. Optical micrographs of as-cast grinding balls structure (center)modified by B addition

Table 2. The influence of heat treatments (subcritical and high-temperature) on hardness of HCWCIs, modified with Ti (0,36 and 2,37 wt%) and B (0,021 and 0,071wt%).

Type of alloy	Rockwell hardness, HRC		
	As-cast	Subcritical heat treatment	High-temp. treatment
Base alloy*	52,5	54,4	60,2
Alloy 1 (0,36 wt% Ti)	53,8	55,1	62,1
Alloy 2 (2,37 wt% Ti)	46,8	48,4	59,2
Alloy 3 (0,021 wt% B)	51,8	55,5	61,4
Alloy 4 (0,071 wt% B)	53,4	55,1	63,3

Impact toughness tests were performed on an instrumented Charpy pendulum 150/300 J (V notch pendulum impact test), according to Standard EN ISO 14556. The influence of modification of tested HCWCIs by addition of Ti and B on the impact toughness in the as-cast temper is presented in Figure 4.
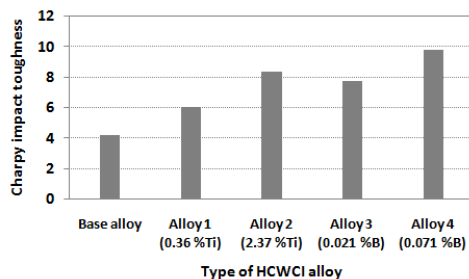
Figure 4. The influence of the individual addition of Ti and B on the Charpy V notch impact toughness of tested as-cast HCWCIs

The Charpy impact toughness of all modified HCWCI alloys is 45–133% higher than the impact energy of the reference base alloy. The highest total impact energy was measured for the alloy containing 0.071 wt% B. Impact toughness increases with increasing titanium content. The HCWCI alloy with 2.37 wt% Ti has approximately 40% higher total impact energy compared to the alloy with 0.36 wt% Ti, and 100% higher than the reference alloy. This is mainly due to the lower volume fraction of carbide in the structure, taking into account the fact that cracks propagate easily through the eutectic carbide phase. These alloys have an austenitic metal matrix microstructure. Similarly, impact toughness increases with increasing boron content. The HCWCI alloy modified with 0.071 wt% B has 25% higher total impact energy than the alloy with 0.021 wt% B, and 133% higher than the reference alloy.

The results of the abrasion resistance tests are presented in Figure 5. The dry sand/rubber wheel method ("Asian" device), defined by the ASTM G65 standard, was used. All tested HCWCIs modified with Ti or B additions show better resistance to abrasion wear, noting that higher Ti or B content also results in lower mass/volume losses. Furthermore, both applied heat treatments improve the abrasion wear resistance of all tested alloys. Subcritical heat treatment can reduce the mass/volume loss by 1.6 – 10%, and high-temperature treatment can reduce it by 15 – 27% compared to the as-cast temper.

Figure 5. The influence of heat treatments and Ti or B addition on abrasion wear resistance of tested HCWCIs

The best resistance to abrasion wear is indicated for the HCWCI alloy modified with the addition of 0.071 wt% B. It is interesting to note that, for example, HCWCI alloy with 2.37 wt% Ti has a lower

volume fraction of carbide phase in the structure and lower hardness, but has almost 26% higher wear resistance than the reference alloy in all tested tempers.

The results of testing the resistance to repeated impacts of grinding balls of three as-cast alloys (base alloy and alloys modified individually with 0.36 wt% Ti and 0.071 wt% B) are presented in Figure 6.
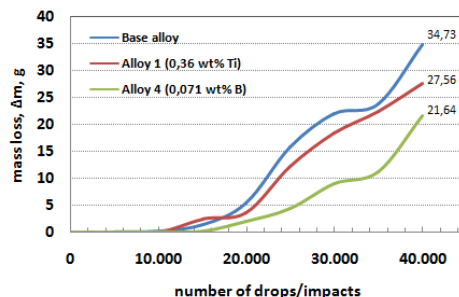
Figure 6. Resistance to repeated impacts of as-cast grinding balls

The weight loss of the tested grinding balls was insignificant up to 20,000 drops - it is less than 4 grams. After 20,000 drops, the beginning of flaking on the surface of some samples was noticed. With a further increase in the number of falls/impacts, the mass loss of the tested balls increases significantly, with a smaller weight loss measured for the modified alloys compared to the base alloy. The lowest mass loss after 40,000 drops was measured for the alloy with the addition of 0.071 wt% B, and compared to the base alloy it is 37% lower mass loss levels.

Corrosion properties

Two techniques have been used for testing of corrosion properties of grinding balls: linear polarization and Tafel extrapolation. The influence of subcritical and high temperature heat treatments on corrosion rates of tested HCWCI alloys in 0,1 M NaCl under linear polarization is presented in Table 3.

Table 3. The influence of subcritical and high temperature heat treatments on corrosion rates of tested HCWCI alloys in 0,1 M NaCl (linear polarization)

Type of alloy	Corrosion rate mmpy		
	As-cast	Subcritical heat treatment	High-temp. treatment
Base alloy	0,319	0,471	0,401
Alloy 1 (0,36 wt% Ti)	0,131	0,172	0,166
Alloy 2 (2,37 wt% Ti)	0,303	0,343	0,359
Alloy 3 (0,021 wt% B)	0,089	0,391	0,319
Alloy 4 (0,071 wt% B)	0,164	0,537	0,132

Modification of HCWCI alloys by individual additions of titanium or boron reduces corrosion rates, if compared to the corrosion rates of the base alloy, for all of three tempers: as-cast, subcritical and high temperature heat treatments. Both types of applied heat treatments cause a certain increase in the corrosion rates, when compared to their as-cast state, for all tested HCWCI alloys, under linear polarization.

Tafel curves of the as-cast and heat treated HCWCI alloys are shown in Figure 7. The single addition of titanium or boron shifts the Tafel curves of modified HCWCIs towards less negative values, compared to the curves that characterize the behavior of the basic HCWCI alloy in 0.1 M NaCl. Modifying the composition/structure of HCWCIs by individual additions of titanium or boron reduces the corrosion rates of as-cast and heat treated grinding balls. The lowest corrosion rate in the as-cast state and after high-temperature heat treatment was measured for HCWCI alloy modified with the addition of 0.071 wt% B. Subcritical heat treatment reduces the corrosion rate, indicating that the alloy with the addition of 0.36 wt% Ti shows the lowest corrosion rates at this temper. The results of both electrochemical techniques indicate the less active corrosion of titanium or boron modified HCWCIs grinding balls in 0,1M NaCl solution if compared to base HCWCI alloy behavior.
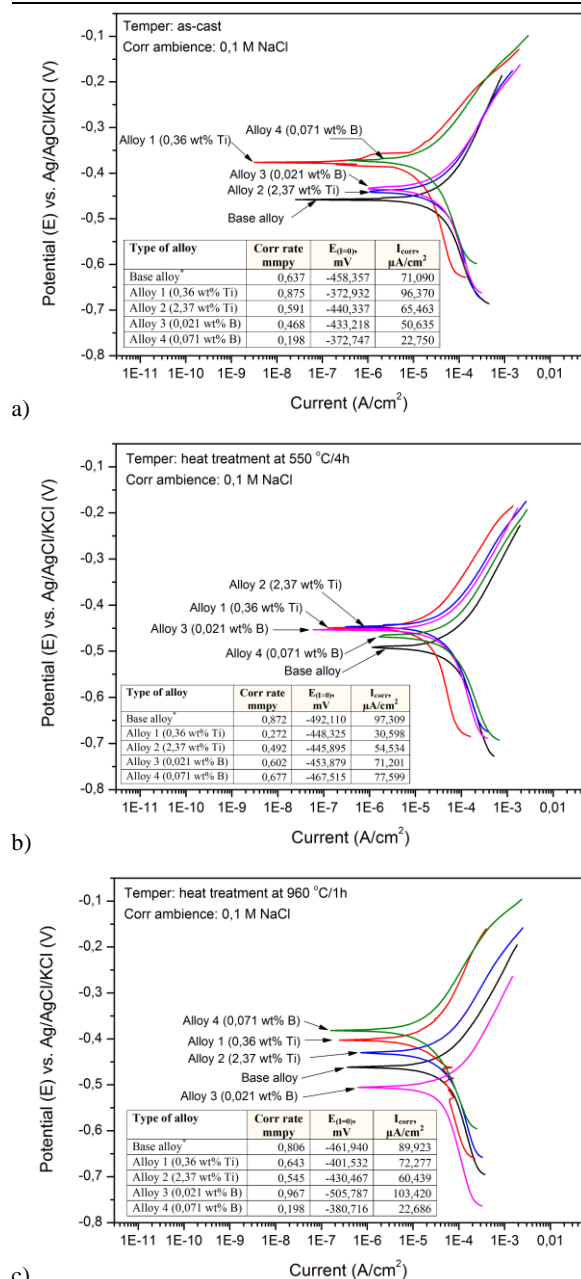
Figure 7. Tafel curves for tested HCWCI alloys modified by individual addition of Ti an B: (a) as-cast, (b) heat treated at 550 °C/4h and (c) heat treated at 960°C/1h.

4. Conclusion

HCWCI alloys modified with the addition of Ti or B have a significantly finer structure if compared to the base unmodified alloy. Boron especially affects the transformation of austenite during cooling after crystallization, and the degree of transformation of austenite into martensite is higher than in titanium-modified HCWCs. Subcritical and high-temperature heat treatment increases the hardness of all tested alloys. The highest increase in hardness ($\approx$ 7%) after subcritical treatment is indicated for the alloy modified with 0.021 wt% B. The highest increase in hardness after high-temperature treatment, ($\approx$ 26%) compared to the as-cast temper, is indicated for the HCWCI modified with 2.37 wt% titanium. The Charpy impact toughness of all modified HCWCI alloys is 45–133% higher than the impact energy of the reference base alloy. The highest total impact energy was measured for the alloy containing 0.071 wt% B. HCWCIs modified with Ti or B show better resistance to abrasion wear, noting that higher Ti or B content also results in lower mass/volume losses. Both applied heat treatments improve the abrasion wear resistance of all tested alloys. Subcritical heat treatment can reduce the mass/volume loss by 1.6 –

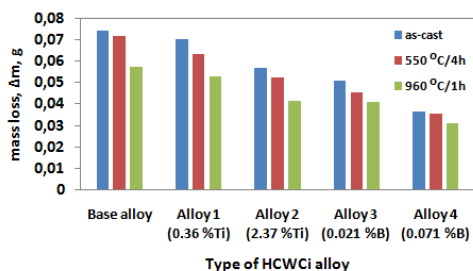10%, and high-temperature treatment can reduce it by 15 – 27% compared to the as-cast temper. The best resistance to abrasion wear is indicated for the HCWCI alloy modified with the addition of 0.071 wt% B. Modification of HCWCI alloys by individual additions of titanium or boron reduces corrosion rates, if compared to the corrosion rates of the base alloy, for all of three tempers: as-cast, subcritical and high temperature heat treatments. Both types of applied heat treatments cause a certain increase in the corrosion rates, when compared to their as-cast state.

5. References

1. Kaya, S., et. all, *Influences of Cr on the microstructural, wear and mechanical performance of high-chromium white cast iron grinding balls*, Journal of Materials and Manufacturing Vol. 1 No. 1 (1:23-30), DOI:10.5281/zenodo.7107351 (2022)
2. R.J. Chung, et al, *Effects of titanium addition on microstructure and wear resistance of hypereutectic high chromium cast iron Fe–25wt.%Cr–4wt.%C,* Elsevier, Wear 267 (2009) 356-361, DOI: 10.1016/j.wear.2008.12.061 (2009)
3. High Alloy White Irons, *Total Materia*, ref.13 December 20, 2002
4. Delijić K., Filipović M., *The Effect of Vanadium, Niobium and Boron on Microstructure, Mechanical and Corrosion Properties of High-Chromium White Cast Irons*, International Journal for Science, Technics and Innovations for the Industry, Issue 8/2022 pp. 286-289, ISSN 1314-507x (2022)
5. Jain, A.-S., et all, *Refinement of primary carbides in hypereutectic high-chromium cast irons: a review,* Journal of Materials Science 56(2), 999-1038, (2021)
6. Zhang, M.X., Kelly, P.M., & Gates, J.D., *The effect of heat treatment on the toughness hardness and microstructure of low carbon white cast irons,* J. Mater. Sci., 36, 3865–3875. (2001)
7. Powell G.L.F., & Bee, J.V., *Secondary carbide precipitation in an 18 wt% Cr–1 wt% Mo white iron*, J. Mater. Sci., 31, 707–711. (1996)
8. Zhu, C., et all, *Effect of boron addition on the microstructure and wear resistance of laser beam directed energy deposited high chromium white irons*, Wear Volumes 546-547 1 June 2024, 205320, https://doi.org/10.1016/j.wear.2024.205320 (2024)
9. Kaleicheva J., et all, *Effect of boron on the wear behavior of high chromium white cast irons*, Proc. of the 14th International Scientific and Practical Conference. Volume 3, 119-123 Print ISSN 1691-5402 Online ISSN 2256-070X https://doi.org/10.17770/etr2023vol3.7294 (2023)
10. Naiheng M.A., Qichang R., Qingde Z. *Corrosion-abrasion wear resistance of 28%Cr white cast iron containing boron* Wear, 132 (1989), pp. 347-359, 10.1016/0043-1648(89)90083-5
11. Z. Liu, Y. Li, X. Chen, K. Hu *Microstructure and mechanical properties of high boron white cast iron* Mater. Sci. Eng., A, 486, pp. 112-116, 10.1016/j.msea.2007.10.017 (2008)
12. Y. Peng, H. Jin, J. Liu, G. Li *Effect of boron on the microstructure and mechanical properties of carbidic austempered ductile iron* Mater. Sci. Eng., A, 529, pp. 321-325, 10.1016/j.msea.2011.09.034 (2011)
13. J. Hufenbach, K. et. all. *The effect of boron on microstructure and mechanical properties of high-strength cast FeCrVC* Mater. Sci. Eng., A, 586, pp. 267-275, 10.1016/j.msea.2013.07.085 (2013)
14. M. Çöl, F.G. Koç, H. Öktem, D. Kır *The role of boron content in high alloy white cast iron (Ni-Hard 4) on microstructure, mechanical properties and wear resistance* Wear, 348–349, pp. 158-165, 10.1016/j.wear.2015.12.007 (2016)
15. H. Lu, T. Li, J. Cui, Q. Li, D.Y. Li *Improvement in erosion-corrosion resistance of high-chromium cast irons by trace boron* Wear, 376–377, pp. 578-586, (2017)10.1016/j.wear.2017.02.014
16. Chengbo Zhu et all, *Effect of Ti and TiC additions on the microstructure and wear resistance of high chromium white irons produced by laser directed energy deposition*, Wear Volumes 510–511, 15 December 2022, 204519, https://doi.org/10.1016/j.wear.2022.204519 (2022)

Effect of increased iron content on the porosity of AlSi7Mg alloy die castings

Jaroslaw Piatkowski[1], Leszek Chowaniec[2], Tomasz Matula[1,*], Marco Reyna[3], German Sanchez[3]
Silesian University of Technology, Poland[1]
Superior Industries Production Poland Sp. z o.o., Poland[2]
Superior Industries Production, Mexico[3]
tomasz.matula@polsl.pl

Abstract: *Defects in die castings can include underfilling, blistering, sticking to the mold, and cracking. However, the factor that most affects the quality of castings is porosity. The primary causes of porosity are gaseous impurities and improper mold venting, which lead to gaseous porosity. Additionally, a poorly selected gating system, low casting speed, excessively short piston paths, low post-pressure, and low casting temperatures all contribute to shrinkage porosity. An additional factor contributing to the occurrence of pores is the increasing proportion of scrap (from production and post-production), which contains a wide variety of impurities. Gaseous inclusions (e.g., hydrides) can be removed from the liquid alloy by refining it, but metallic impurities are worse. In Al-Si alloys, one of the most detrimental elements is iron, which enters solution due to its low solubility in the solid state, at levels exceeding 0.6 wt%. At high percentages, it crystallizes in morphologically unfavorable phases, which deteriorate service properties, increase brittleness and porosity of castings, and limit their use. This paper presents the results of a study of the effect of increased iron content (from 0.8wt.% to 1.5wt.%, in 0.2wt.% increments) on the porosity of AlSi7Mg alloy die castings. Porosity evaluation, conducted using microscopic metallography methods, was performed both qualitatively and quantitatively. It was found that the unfavorable morphology and dimensions of the Al$_5$FeSi phase hinder the free flow of liquid alloy at the crystallization front. The lamellar-ligneous separations "close" the space between the dendrites of the α(Al) solid solution, causing the formation of shrinkage porosity. Increasing the iron content of die-cast Al-Si alloys forces the use of higher doping pressures, but not enough to cause "ejaculations" of the alloy in the dividing plane of the casting mold.*

***Keywords:** ALUMINUM ALLOYS, DIE CASTING, IRON PHASES, SHRINKAGE POROSITY*

1. Introduction

The relatively good strength combined with low density, high conductivity, and corrosion resistance makes cast aluminum alloys widely used in many industries, such as automotive and aerospace. These properties are primarily dependent on the various types of microstructures that result from the production process. Depending on the technology, the structure of Al-Si alloys can be significantly altered, primarily in terms of the morphology and size of the components, i.e., solid solution dendrites α(Al), silicon crystals in the eutectic α(Al) + β(Si), and intermetallic phases. The production method also affects casting defects, such as shrinkage and gas porosity [1-3]. However, despite the presence of these defects, casting manufacturers must ensure that the required level of product quality is maintained. In the case of porosity, foundries establish control procedures using, for example, microstructure testing to identify defects and reject products that contain pores as a criterion for assessing their quality and marketability.

This is because porosity negatively affects several properties, primarily the strength and fatigue resistance of Al-Si alloys. Studies [4, 5] indicate that an increase in porosity of approximately 1% causes a reduction in Rm strength of roughly 40% and a significant decrease in castability.

2. Purpose and scope of the research

The research aimed to determine the effect of increasing iron content on the porosity of AlSi7Mg alloy castings obtained by pressure casting. It was characteristic that all studies on the impact of increased iron content on the microstructure of the AlSi7Mg alloy were conducted at the Superior Industries Production of Poland foundry under industrial production conditions.

The scope of the research included:

- melting AlSi7Mg alloy with different iron content and casting samples,
- microstructure testing in terms of shrinkage porosity in castings,
- analysis of results, summary, and conclusions.

3. Research material and methodology

The feedstock for producing AlSi7Mg alloy was metallurgical ingots, which were inspected for type and element content by the supplier's certificate. At specified intervals, samples were taken for chemical composition analysis to verify the accuracy of the supplier's certificate. If the chemical composition of the alloy met the customer's requirements, the metal was remelted in gas furnaces. After reaching a temperature of approx. 740°C, the alloy was poured from the melting furnaces into a transport ladle (2000 kg), where it was modified with AlTi5B master alloy and refined with nitrogen and a nitrogen-hydrogen mixture (90%N+10%H$_2$) using the bubbling method. After the liquid alloy had settled and all impurities (dross) had been removed from its surface, the ladle was transported to a casting machine connected to an electric furnace, from which a sample was taken to measure the density and check the chemical composition. Metallographic sections were prepared from the chemical composition samples, following the recommendations of the Büehler expert system. The sections were polished, not etched. The experimental plan and test procedure are shown in Figure 1.

Sample No.	Iron content, wt.%
1	0.8
2	0.9
3	1.0
4	1.1
5	1.2
6	1.3
7	1.4
8	1.5
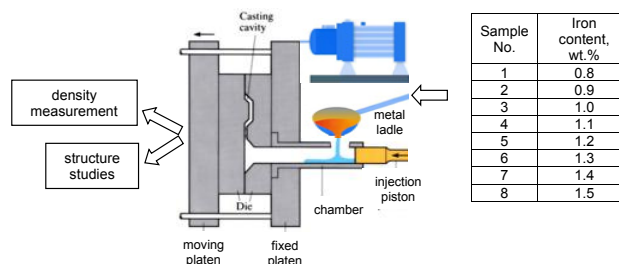
Fig. 1 Experimental plan and research scheme for the AlSi7Mg alloy.

Microstructure (LM) studies were performed using an Olympus GX-51 light microscope in bright-field mode at a total magnification of 50x. For the quantitative assessment of porosity, 15 images were taken in random fields of view, resulting in a total analysis area of approximately 70.5mm^2. Porosity was measured using quantitative metallography methods with the ImageJ image analyzer [6]. The program developed a macro instruction covering the following steps: obtaining a set of images, normalization, noise removal using a median filter, pore detection via the Otsu binarization method, and measurement of the volume fraction of pores, the volume fraction of pores in the area with the highest porosity, and the pore surface area. Microstructure observations (SEM) were performed on a Hitachi S-3400N scanning microscope equipped with a Thermo Noran energy dispersive X-ray spectrometer (EDS), Thermo Noran and wavelength dispersion (WDS) Thermo MagnaRay, and a detector for electron backscatter diffraction (EBSD) INCAHKL Nordys (Hitachi High-Technologies Tokyo, Japan).

4. Research results and their analysis

The results of the chemical composition of the AlSi7Mg alloy are presented in Table 1. This is a standard alloy used, among other applications, in pressure casting, such as for the production of car rims.

Table 1: *Results of the chemical composition of the AlSi7Mg* alloy, in wt.% (average values from 8 measurements).*

Sam. No.	Si	Fe	Cu	Mn	Mg	Zn	Ti	Ca	Sr
1.	6.82	0.78			0.36	0.00	0.10		
2.	7.09	0.89			0.39	0.03	0.15		
3.	6.98	0.98			0.42	0.02	0.13		
4.	7.12	1.12	<0.01	<0.02	0.44	0.03	0.14	<0.01	<0.02
5.	7.20	1.21			0.39	0.03	0.12		
6.	6.91	1.31			0.40	0.03	0.15		
7.	6.87	1.42			0.44	0.02	0.15		
8.	7.12	1.51			0.42	0.03	0.14		

4.1. Density measurement results

The density (density index) of cast aluminum alloys is determined by measuring the mass of a sample of pure aluminum and its volume using the liquid displacement method (known as Archimedes' method). The difference between the dry and wet weights of the sample enables the calculation of the volume of empty spaces (pores). For AlSi7Mg alloy, the density should be between 2.46 g· cm^{-3} and 2.54 g· cm^{-3}. A density outside this range indicates poor quality. A density that is too high may indicate a failure to maintain process parameters (e.g., an excessively low temperature in the heating furnace or an overly high pressure), while a density that is too low may indicate an excessive presence of pores in the microstructure.

The results of density (ρ) measurements of AlSi7Mg alloy with different iron contents are shown in Figure 2.
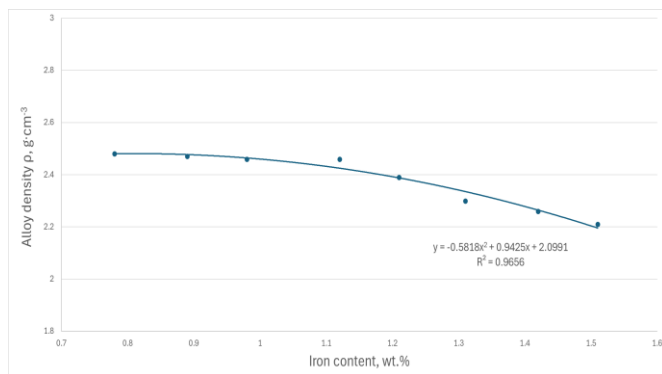
Fig. 2 *Change in the density index of the AlSi7Mg alloy depending on the iron content.*

4.2. Density measurement results

Representative microstructures (LM) of the AlSi7Mg alloy with increasing iron content are shown in Figure 3. This figure displays shrinkage pores, for which selected quantitative parameters are presented in Figure 4. The dispersion of results, measured by standard deviation, is shown in Table 2.
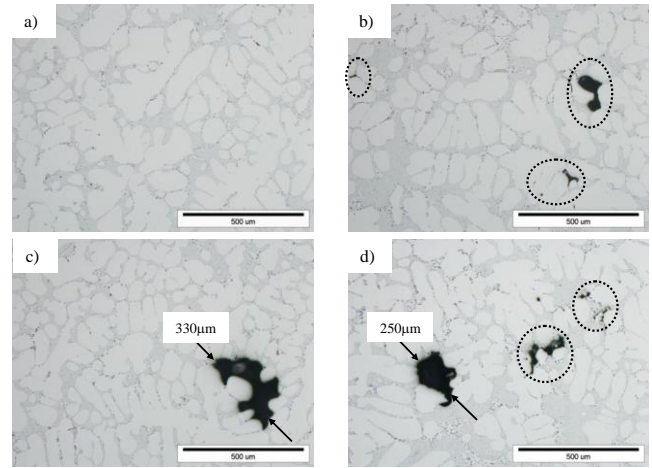
Fig. 3 *Microstructure (LM) of AlSi7Mg alloy with shrinkage porosity: a) sample no. 1 (0.78%Fe); b) sample no. 3 (0.98%Fe); c) sample no. 5 (1.21%Fe); d) sample no. 7 (1.42%Fe).*

Table 2: *Quantitative analysis of porosity in AlSi7Mg alloy*

Sample No.	Iron content, wt.%	Pore volume fraction[1] – mean value, %	Pore volume fraction[2] – the most porous area, %	SD of volume fraction, %
1	0.8	0.16 ± 0.01	0.53 ± 0.01	0.05
2	0.9	0.22 ± 0.01	0.61 ± 0.01	0.06
3	1.0	1.49 ± 0.02	3.43 ± 0.02	0.07
4	1.1	2.24 ± 0.02	4.98 ± 0.02	0.08
5	1.2	3.02 ± 0.03	5.78 ± 0.03	0.14
6	1.3	3.94 ± 0.04	6.38 ± 0.04	0.17
7	1.4	4.24 ± 0.02	7.99 ± 0.02	0.09
8	1.5	5.07 ± 0.02	9.89 ± 0.02	0.10
Sample No.	Pore surface area[3], μm^2	SD of pore surface area, μm^2	Pore diameter – mean value[4], μm	SD of pore diameter, μm
1	3.0 ± 0.1	0.7	100-160	1.7
2	4.1 ± 0.1	0.9	160-220	2.2
3	11.1 ± 0.4	1.8	180-220	2.9
4	19.9 ± 0.4	2.2	280-320	4.4
5	28.5 ± 0.5	2.9	320-360	5.9
6	32.4 ± 0.5	3.3	320-360	8.5
7	49.2 ± 1.2	5.1	250-360	11.8
8	58.2 ± 1.2	7.3	250-390	14.5

Where:
SD – Standard Deviation
[1] – fraction of volume occupied by pores in the image area;
[2] – fraction of volume occupied by pores in the most porous area of the image;
[3] – average area of the flat cross-section of pores,
[4] – average value of the longest diameter of the flat cross-section of pores.

a)

b)

c)

d)
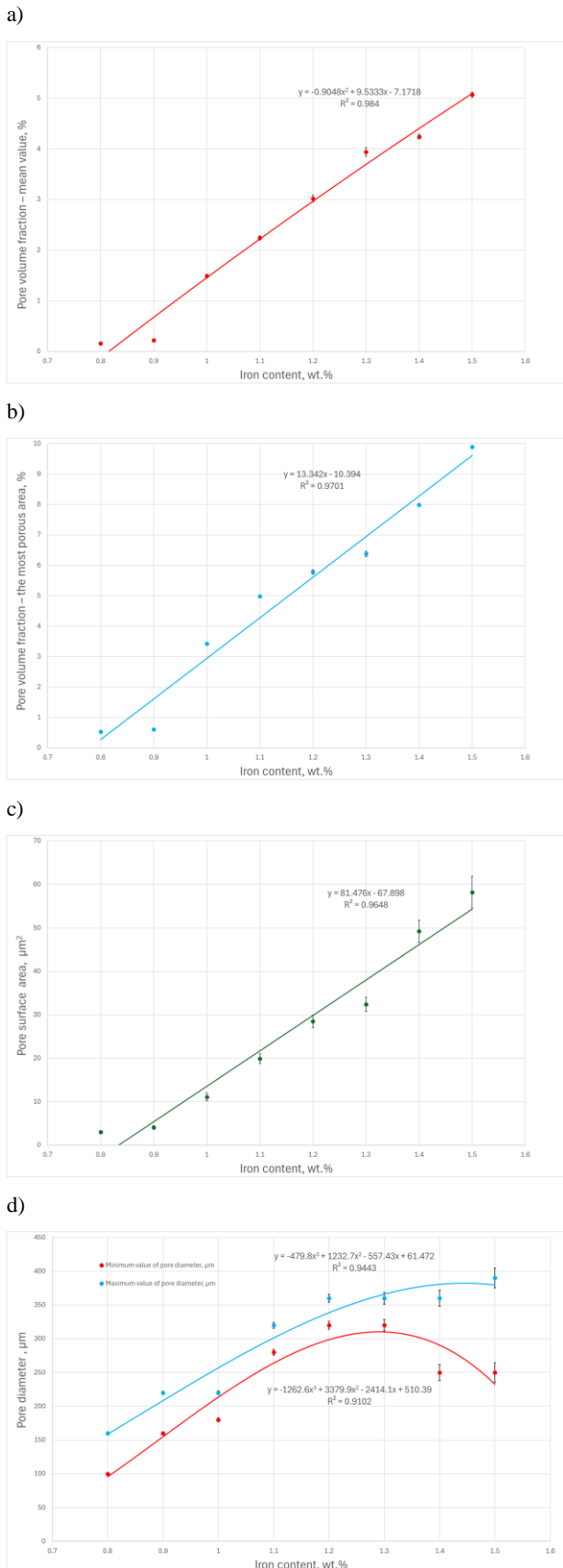
Fig. 4 *Effect of increasing iron content on selected shrinkage porosity parameters in AlSi7Mg alloy: a) pore volume fraction – mean value; b) pore volume fraction – the most porous area; c) pore surface area; d) pore diameter.*

The analysis of the quantitative metallography measurements for the AlSi7Mg alloy, as shown in Figure 4, indicates that as the iron content increases, the proportion of shrinkage porosity also increases, and the pores become larger. This is likely due to the

increasing proportion of hydrogen in the alloy (10% H$_2$), added during bubbling, which causes a decrease in its density [7]. These results are consistent with studies [8-10], but their confirmation requires additional research.

The acceptable proportion and size of pores in a casting (sometimes in specific locations, known as critical locations) depend on the individual customer's requirements. However, it is often assumed that for die castings made of AlSi7Mg alloy, the acceptable diameter of individual pores (in the foundry where the X-ray tests were performed) is up to 0.2 mm (200μm). Exceeding this value means that the casting does not meet the quality criteria specified by the customer and is therefore considered defective.

To determine the causes of shrinkage porosity, the microstructure of the AlSi7Mg alloy was re-observed at higher magnifications. Selected results are presented in Figure 5.
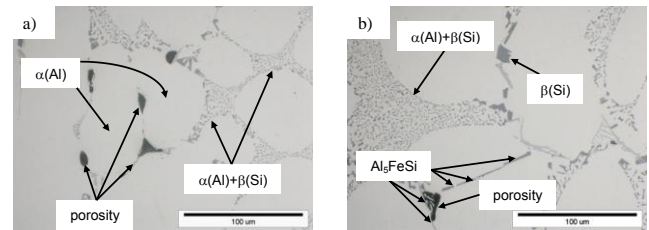
Fig. 5 *Microstructure (LM) of AlSi7Mg alloy showing the causes of shrinkage porosity: a) at the grain boundaries of the α(Al) solution; b) as a result of Al$_5$FeSi phase crystallization.*

An analysis of the microstructure of the AlSi7Mg alloy and die casting parameters [6, 11] shows that there are two types of causes for shrinkage pores, namely:

- too low pressure in the third phase of casting, resulting in porosity at the grain boundaries of the α(Al) solution – Figure 5a,
- excessive iron content in the alloy, which hinders the flow of liquid metal due to the crystallization of Al$_5$FeSi (β-Fe) phases, around which porosity forms – Figure 5b.

5. Summary

Although numerous studies have been conducted on the influence of iron content on the microstructure and performance properties of aluminum alloys, this topic remains a relevant area of research. This mainly concerns die casting, in which, due to technological advances, individual stages of the melting and casting process of aluminum alloys are changing, especially the requirements for the metallurgical purity of castings, measured, for example, by the permissible porosity. For this reason, research in this area is still relevant and necessary.

The data presented show that an increase in iron content (from 0.8 wt.% to 1.5 wt.%) causes an increase in the porosity of AlSi7Mg alloy die castings. Up to a content of approx. 1.0 wt.% Fe, the metallographic indicators of shrinkage pores are within the acceptable diameter range, i.e.:

- pore quantity parameters (field volume friction – mean value and most porous area),
- pore size parameters (pore surface area and pore diameter – mean value).

When the content exceeds approximately 1.0 wt.% Fe, the calculated quantitative metallography indices of shrinkage pores (Fig. 4) exceed the acceptable diameter value of 200 μm for the AlSi7Mg alloy.

These results align with the density index measurement, which indicates that up to approximately 1.0 wt.% Fe, the density of the alloy is ρ=2.46 g· cm^{-3} (acceptable value). Above this value, the

density of the AlSi7Mg alloy decreases, which indicates an above-normal shrinkage porosity.

Studies of the microstructure of the AlSi7Mg alloy and analysis of die casting parameters [6, 11] have also shown that there are two types of causes for the formation of shrinkage pores, i.e.:

- too low pressure in the third phase of casting, resulting in the formation of pores at the grain boundaries of the α(Al) solution – Figure 5a, and

- too high a proportion of iron in the alloy, which hinders the flow of liquid metal due to the crystallization of Al_5FeSi phases, around which porosity forms – Figure 5b.

To prevent the crystallization of morphologically unfavorable β-Al_5FeSi phases, various additives are introduced into Al-Si alloys, e.g., manganese, chromium, cobalt [12, 13] or strontium [14, 15]. Their purpose is to change the morphology of β-Fe phases from plate-needle to less harmful, e.g., dendritic. An example microstructure of the AlSi7Mg alloy, before and after the addition of manganese, is shown in Figure 6.
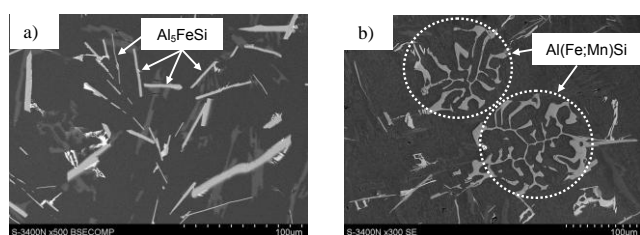
Fig. 6 Microstructure (SEM) of the AlSi7Mg alloy: a) without manganese; b) with manganese addition.

However, it should be remembered that the proportion of alloying additives, which limits the negative impact of the β-Fe phase, is strictly dependent on the proportion of iron, whose critical content ($Fe_{crit.}$) in Al-Si alloys is determined by the equation [16, 17]:

$$Fe_{crit.} \approx 0.075 \times (wt.\%Si) - 0.05 \ \% \qquad (1)$$

Exceeding the Fecrit in Al-Si alloys (especially die-cast alloys) results not only in the crystallization of β-Fe phases with unfavorable morphology, but also in the formation of sludge. Its share is determined by the so-called "sludge factor" (SF) and the Mn/Fe ratio, whose values are defined differently depending on the chemical composition of the alloy, the manufacturing technology, and the metallurgical purity of the feedstock components [18-20]:

$$SF = (wt.\%Fe) + (2 \times wt.\%Mn) + (3 \times wt.\%Cr) \ \% \qquad (2)$$

However, these issues are not the focus of this study and will be continued in the future.

6. Reference

1. L. Kucharčík, M. Brůna, A. Sládek, Arch. of Foundry Eng., **14**, 4 (2014)
2. A. Samuel, Y. Zedan, H. Doty, V. Songmene, F. Samuel, Materials Science and Engineering, **1**, 16 (2021)
3. N. S. Tiedj, J. A. Taylor, M. A. Easton, Metallurgical and Materials Transactions, **43**, 13 (2012)
4. J. Cais, V. Weiss, J. Svobodova, Arch. of Foundry Eng., **14**, 6 (2014)
5. T. H. Ludwig, M. Di Sabatino, L. Arnberg, D. Dispina, Int. J. of Metalcasting, **6**, 10 (2012)
6. J. Piątkowski, S. Roskosz, S. Stach, Adv. in Sci. and Tech. Research J., **18**, 11 (2024)
7. T. Magnusson, L. Arnberg, Metallurgical and Materials Transactions, **32**, 9 (2001)
8. S. Samavedam, S. B. Sakri, D. R. Hanumantha, S. Sundarrajan, Canadian Metallurgical Quarterly, **53**, 10 (2014)
9. S. Samavedam, S. Sundarrajan, Arch. of Foundry Eng., **16**, 8 (2016)
10. G. K. Sigworth, W. Chengming, Metallurgical Transactions B, **24**, 6 (1993)
11. J. Piątkowski, L. Chowaniec, Journal of Physics, **3035**, 10 (2025)
12. B. Wang, J. Wang, X. Liu, Q. Li, X. Liu, Materials Science & Engineering, **A858**, 11 (2022)
13. M. Mahta, M. Emamy, A. Daman, A. Keyvani, J. Campbell, International Journal of Cast Metals Research, **18**, 7 (2005)
14. S. G. Shabestari, M. Mahmudi, M. Emamy, J. Campbell, International Journal Cast Metals Research, **15/1**, 8 (2002)
15. J .A. Garcia-Hinojosa, C. R. González, G. M. González, Y. Houbaert, Materials Processing Technology, **143-144**, 5 (2003)
16. H. R. Kotadia, N. Bareker, M. H. Khan, J .I. Ahuir-Torres, A. Das, Materials Today Sustainability, **30**, 33 (2025)
17. J. A. Taylor, Procedia Materials Science, **1**, 15 (2012)
18. S. Ferraro, A. Fabrizi, G. Timelli, Materials Chemistry and Physics, **153**, 12 (2015)
19. D. Bösch, S. Pogatscher, M. Hummel, W. Fragner, P. J. Uggowitzer, M. Göken, H. W. Höppel, Metallurgical and Materials Transactions, **46A**, 11 (2015)
20. Y. Fu, G. G. Wang, A. Hu, T. Li, K. B. Thacker, J. P. Weiler, H. Hu, Journal of Magnesium and Alloys, **10**, 15 (2022)

Effect of Combined Heat and Mechanical Processing on the Hardness and Wear Resistance of X160CrMoV12 Tool Steel

Regita Bendikiene[*], Lina Kavaliauskiene
Kaunas University of Technology, Faculty of Mechanical Engineering and Design, Lithuania
regita.bendikiene@ktu.lt

Abstract: This study investigated the effect of cold plastic deformation at Bridgman anvil chamber temperature on the hardness and wear resistance of X160CrMoV12 steel using hardness testing, X-ray diffraction (XRD), abrasive grinding wear (AEMW) testing, optical examination, and scanning electron microscopy (SEM). Three batches of samples were prepared for the experiment: I – hardened, II – hardened and then tempered at 600°C for 1.5 hours, III – hardened and then plastically deformed. The samples were hardened at three temperatures: 1100, 1150, and 1200 °C. The highest amount of retained austenite, reaching 69.02%, was observed when hardening at 1200°C, while at lower temperatures, 17.36% and 38.14% were formed, respectively. After hardening (batch II), the amount of retained austenite decreased proportionally by approximately 7 times for each hardening temperature. The effect of plastic deformation (batch III) is observed by analysing the hardness of samples from the surface to the depth, reaching an average hardening depth of 0.08 mm. To check how well it holds up to wear, the surfaces of three test batches were tested using an abrasive grinding test with a load of 5N. Hardened and plastically deformed specimens showed greater resistance to abrasion than hardened and tempered specimens. The results confirmed that the optimal hardening temperature for achieving maximum wear resistance of this steel is 1100°C.

Keywords: COLD WORK TOOL STEEL, RETAINED AUSTENITE, TEMPERING, SECONDARY HARDENING, BRIDGMAN ANVIL DEFORMATION, WEAR RESISTANCE.

1. Introduction

High carbon and chromium tool steels are an important engineering material for the manufacture of cutting tools and cold forming dies. Due to the dense chromium carbides that form, which distinguish them from other alloys, they are highly resistant to wear and even corrosion. This positive effect on the mechanical properties of tool steel is explained by the formation of two types of carbides, namely primary and secondary carbides [1]. Primary carbides increase resistance to abrasive wear, while secondary carbides affect resistance to plastic deformation [2]. Therefore, these steels can withstand high wear stress during service, especially when used for castings and tools [3].

In general, harder materials are more resistant to wear, but this is mainly true for purely annealed metals and similar alloys [4]. Therefore, most research focuses on improving wear resistance, mainly by modifying the microstructure through specific heat treatment methods [5,6]. The desired mechanical and operational properties are achieved by selecting the appropriate heat treatment, which creates a specific microstructure. High hardness is usually achieved by transforming austenite into martensite, and tempering controls the toughness. The grain size or phase distribution of tool steels can also be controlled by additional heat treatment or other processes [7,8]. During conventional tempering, the martensitic matrix is reinforced with dispersed carbides, which increases strength and hardness.

The transformation of retained austenite in high carbon and chromium steels has been extensively studied but is still not fully understood [9,10]. Studies have shown that retained austenite can transform into ferrite and cementite, martensite or bainite. Ferrite and cementite are formed during isothermal tempering, while martensite and bainite are formed during post-tempering cooling. The isothermal transformation to ferrite and carbides occurs in two stages [11]. The transformation mode of retained austenite depends on the steel composition and heat treatment, and this greatly affects the final mechanical properties [12]. Although the mechanism is known, there is little information in the literature on how retained austenite transforms during the hardening of cold-worked tool steel.

Studies show that under high abrasive wear, samples with a bainite structure exhibit better wear resistance than tempered martensite, even with similar mechanical properties [13]. Other researchers have studied industrial wear during cold rolling of cold-worked tool steels, examining how wear and lubrication affect the coefficient of friction over time, with the aim of extending the service life of high-carbon and high-chromium tool steels [14]. However, when parts are subjected to severe wear, conventional heat treatment is not sufficient, so surface properties are improved using severe plastic deformation (SPD) methods such as channel angular pressing, high-pressure spinning, cumulative rolling, scouring, surface mechanical abrasive treatment, and friction stir treatment [3,15-19].

Cold plastic deformation, such as cold rolling, can significantly improve the mechanical properties of alloy steels such as X160CrMoV12 by producing a fine-grained microstructure with a high content of alpha'-martensite, which can increase the yield strength to about 1000MPa [20]. Twinning and transformation-induced plasticity (TWIP and TRIP) are crucial to understanding how cold plastic deformation improves the strength and microstructure of alloy steels such as X160CrMoV12, helping critical industrial parts last longer and perform better [21].

This article examines how X160CrMoV12 steel behaves during heat treatment, comparing conventional methods such as hardening and subsequent tempering with the effect of less frequent plastic deformation on wear resistance. To explore the potential of the steel, higher than normal tempering temperatures were used to create more retained austenite, which then transforms and improves wear resistance. These results are valuable both scientifically and practically, as they provide important insights into how to improve the processability of cold-worked tool steel X160CrMoV12 in industry.

2. Materials and Methods

X160CrMoV12 steel contains 11-12.5% chromium, which improves hardenability, increases secondary hardness and heat resistance, and also increases wear resistance due to the formation of more chromium carbides [22-24]. For this study, forged and soft-annealed steel bars (13 mm) from the same batch were cut into 10 × 10×50mm specimens for heat treatment, plastic deformation, microstructure analysis, and wear resistance testing. Heat treatment was performed in a Nabertherm N 7/H furnace with precise time and temperature control. The samples were hardened at 1100, 1150 and 1200°C and then oil quenched. Batch I was tested as-hardened, Batch II was tempered at 600°C for 1.5 hours and air-cooled, and Batch III was cold-formed using a Bridgman anvil at room temperature. This method applied a torsional strain of up to 30% at high pressure (6GPa) to avoid sample fracture during high deformations. The samples (10 mm thick) were rotated at approximately 1 rpm between two 50 mm carbide anvils, reducing the thickness to approximately 7 mm. The volume change measured the extent of deformation. This high-pressure process ensured uniform deformation without cracks, making it ideal for improving the microstructure of X160CrMoV12 steel and studying its mechanical behavior under extreme conditions.

The Rockwell hardness (HRC) of all samples was measured before and after heat treatment, plastic deformation and abrasion tests using a Mitutoyo HM-200 machine with a diamond indenter and a holding time of 10s. The Vickers hardness (HV) was also measured on the plastically deformed samples perpendicular to the surface using the same machine at a load of 0.98N and a holding time of 10s to assess the depth of hardness relative to the base metal.

Metallographic samples were prepared and etched with 5% nital solution. The hardened samples were scanned under an optical microscope using an MLA 10 and a Zeiss Axio Scope A1. The samples after tempering or deformation were analyzed by SEM with EDS (Zeiss EVO MA-15). The retained austenite and carbides were identified by X-ray diffraction (Bruker AXS D5005).

Abrasion resistance was measured by mass loss in an abrasive wheel abrasion test. Samples (10×10×50 mm) were tested at a speed of 0.4 m/s for 60 minutes, with the abrasive changed every 10 min. Mass loss was recorded every 10 minutes using a balance with an accuracy of 0.001 g. The total abrasion path length was 2400 m.

3. Results

The annealed steel X160CrMoV12 contains 6-12% chromium, which can cause carbides to be distributed unevenly, forming "raws" or "net" that weaken the steel. This problem is common in cold-worked steels with high chromium content, but can be reduced by plastic deformation [15]. Steels containing more than 1% carbon are expected to achieve high hardness and good wear resistance after heat treatment. Due to the high content of carbide-forming elements, this tool steel easily forms carbides. Standard practice recommends tempering at 1020-1050°C (61-65HRC) to increase retained austenite and wear resistance [7,8,26]. In this study, higher tempering temperatures were used to investigate their effects. At these temperatures, more chromium carbides dissolve, the chromium and carbon content in austenite increases, the martensite onset temperature decreases, and retained austenite is promoted. This results in less fine carbides and grain growth, but secondary hardening occurs after tempering. A total of 45 samples were quenched and oil-cooled. Higher-than-standard temperatures help enhance wear resistance, toughness, and performance in demanding applications. Five samples per batch were tested, and average results are shown in Table 1 for comparison.

Table 1: Hardness test results after conventional hardening and post-treatment.

Batch	Hardening temperature, °C	Hardness, HRC	Post-treatment	HRC after post-treatment
I	1100	61	None	61
I	1150	55	None	55
I	1200	35	None	35
II	1100	61	Tempered at 600°C for 1.5 h	47
II	1150	55	Tempered at 600°C for 1.5 h	49
II	1200	35	Tempered at 600°C for 1.5 h	51
III	1100	61	Plastic deformation, 30%	64
III	1150	55	Plastic deformation, 30%	59
III	1200	35	Plastic deformation, 30%	53

The hardness decreases from 61 to 35HRC as the tempering temperature increases from 1100 to 1200°C. Although the hardness initially increases between 1000 and 1025°C due to the higher content of dissolved alloying elements, it decreases at higher temperatures due to the higher content of retained austenite [27]. This is confirmed by optical analysis. The microstructure consists mainly of martensite (grey, fine needles), retained austenite (light areas) and undissolved M_7C_3 chromium carbides (Fig. 1). The sample hardened at 1200°C shows a significantly higher content of retained austenite.
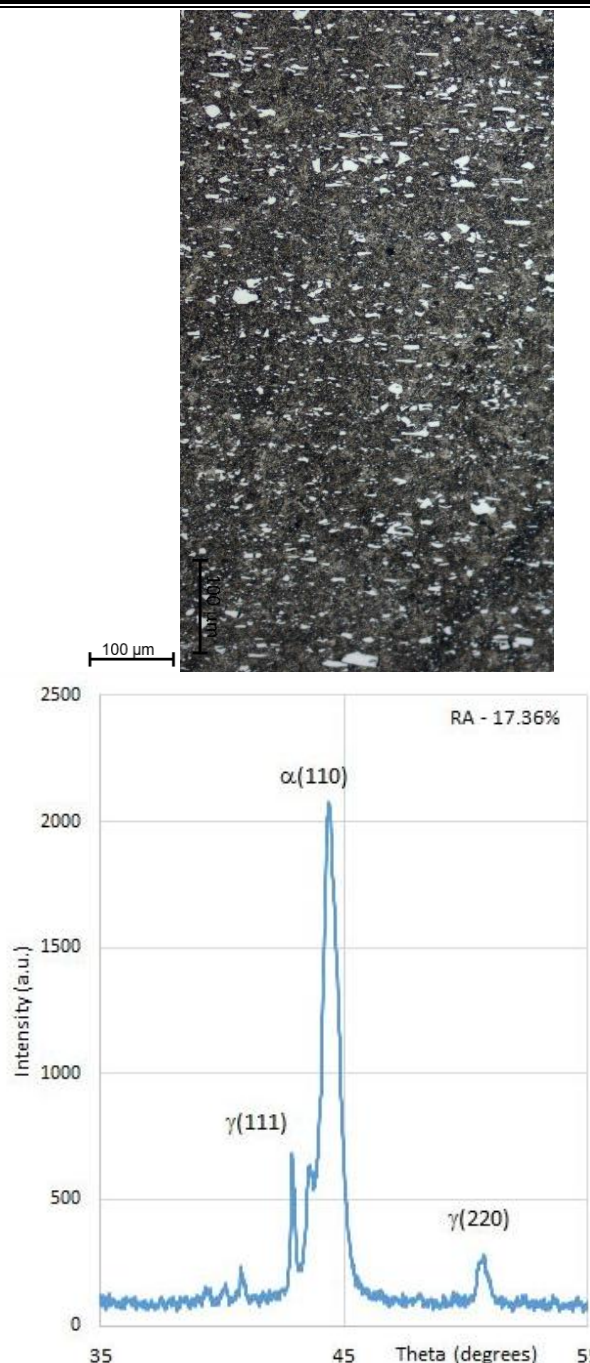
Fig. 1 Microstructure and X-ray diffraction pattern of samples hardened at 1100 °C.

In high-chromium steels with a Cr/C ratio greater than 3, carbide transformations occur in the following sequence: $M \rightarrow Fe_3 C \rightarrow (Fe,Cr)_3 C \rightarrow (Cr,Fe)_7 C_3$ [7,28]. At 1100°C, primary Fe-rich M_7C_3 chromium carbides form linear patterns in the microstructure (Fig. 1). These coarse carbides, which remain undissolved, limit the growth of austenite grains and increase wear resistance. At higher tempering temperatures (1150 and 1200°C), this linear arrangement disappears and the carbides are distributed more evenly.

After hardening, the samples of batch II were tempered at 600°C for 1.5 h and air cooled. The microstructure of the sample tempered at 1100°C shows many fine secondary spheroidal carbides, typical of high tempering temperatures [9], as well as fewer primary irregular chromium carbides in a fine martensitic matrix (Fig. 2). To completely remove the remaining austenite and achieve the highest hardness (62-64 HRC) along with maximum toughness, double or even triple tempering is generally recommended [9,30]. However, in this study, only a single

tempering was used to evaluate how samples from all three batches performed under abrasive wear conditions.
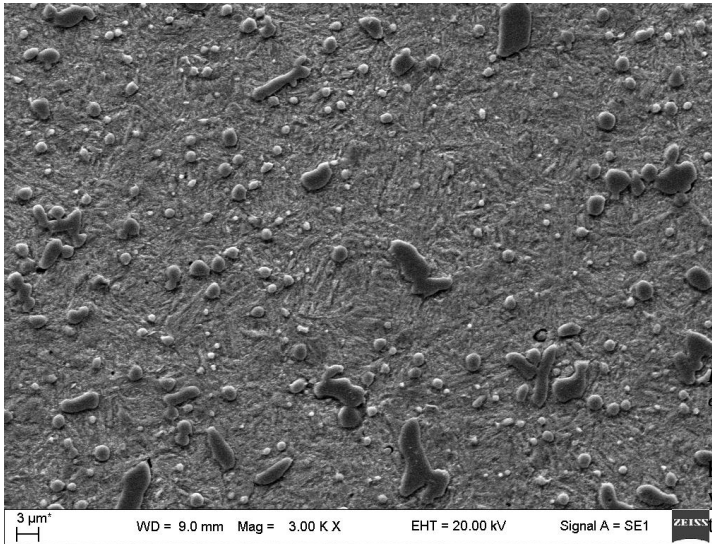
Fig. 2: SEM images of batch II samples annealed at 600°C for 1.5 h prior hardened at 1100°C.

The amount of retained austenite (RA) in the quenched and tempered samples (Fig. 3) clearly decreased: from 17.36 to 1.93% at 1100°C, from 38.14 to 7.26% at 1150°C and from 69.02 to 11.43% at 1200°C. However, after a single tempering at 600°C, the secondary hardening effect is not fully achieved – the maximum hardness remains below 60HRC, even for the sample tempered at 1200°C. This indicates that the remaining 11.43% RA can transform into martensite after the second tempering, potentially increasing the hardness [31]. Hardness results show that the alloyed carbides begin to dissolve, allowing the alloying elements to enter the austenite, which transforms into hard martensite upon cooling. These elements also stabilize the superheated austenite and slow down the precipitation of carbides, resulting in a structure composed of retained austenite, undissolved carbides and martensite, while preserving the austenite grain structure [28].
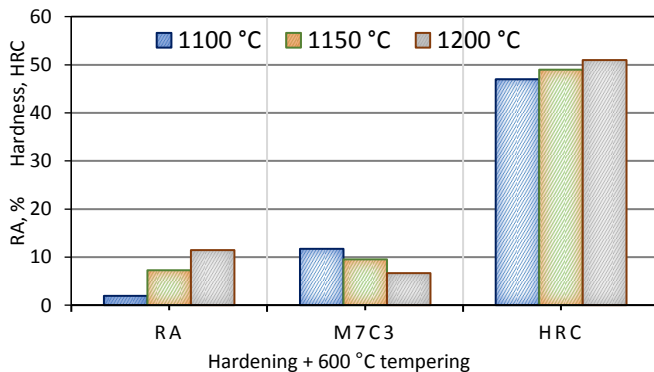
Fig. 3: Austenite and carbide phase content after hardening at the indicated temperatures and tempering at 600°C in batch II.

Batch III samples were subjected to 30% plastic deformation using the Bridgman torsional anvil test after hardening at various temperatures. Since it is known that high plastic deformation significantly reduces grain size [16,18], it was sought to determine how this would affect the wear resistance of the samples. To test this, the samples were subjected to high pressure and rotated between two anvils under tension. The average thickness of the plastically deformed layer in all samples was about 0.08 mm. Compared to the structure after hardening, the microstructure after deformation was much finer and more uniform. The Rockwell hardness after deformation increased, and the highest value of 64HRC was achieved in samples hardened at 1100°C. A slight increase was also observed at 1150°C (from 55 to 59HRC), and the largest jump occurred at 1200°C (from 35 to 53HRC) (Fig. 4).
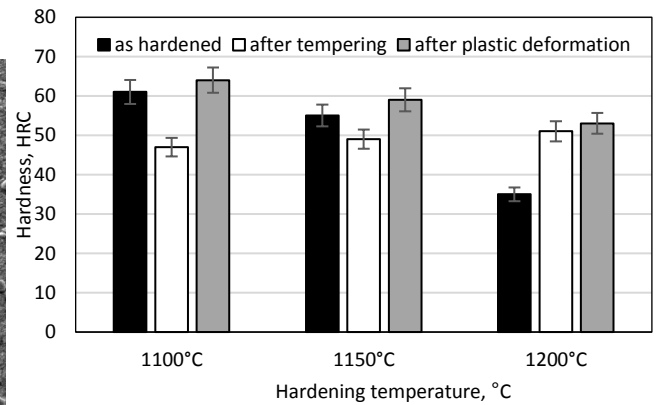
*Fig. 4: Total hardness values of samples treated according to the experimental procedure.*

The positive effect of plastic deformation on increasing hardness is obvious. Since high hardness is very important for the wear resistance of cold-worked tool steels, it is especially important to achieve it after hardening [33]. Previous studies have shown that wear is highly dependent on conditions, especially sliding speed, and that lubricants should be avoided because they can cause uneven wear and increase friction [14]. During plastic deformation, tool steel hardens by dislocation formation and rearrangement. The formed martensite helps to block the growth of austenite grains and improves wear resistance [34], as confirmed by hardness measurements (Table 1), which vary with the tempering temperature.

The last and most important part of this study was the abrasion evaluation. All samples were subjected to abrasion tests, and the results showed that abrasion resistance directly correlates with hardness (Fig. 5). The hardened and tempered samples showed 3-4 times less mass loss than the others, mainly due to the high retained austenite content, which improves wear resistance. The deformed layers showed similar wear properties, with small differences between tempering temperatures. Their finer, more uniform structure generally leads to better properties than coarse-grained, hardened samples [18]. Although cold working increases hardness and can improve wear resistance, its effect is less significant than hardening alone [35]. Future studies could investigate the variation in the degree of plastic deformation or the application of surface treatments such as nitriding [36], which depend on the ability of nitrogen to diffuse into the steel.
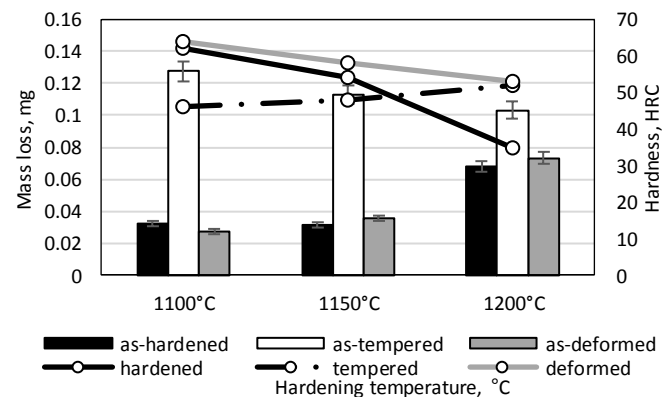
Fig. 5: Wear and hardness results of three test batches.

It is noteworthy that samples hardened at 1150°C, in which ~38% austenite remained [4], exhibited the highest wear resistance in batch I.

4. Conclusions

1. Increasing the tempering temperature from 1100 to 1200°C increases the retained austenite content from 17.36 to 69.02%, more

than four times. This is evident in the microstructure, where the 1200°C sample retains much more austenite than the samples treated at lower temperatures.

2. Higher tempering temperatures result in a more even distribution of carbides, but require more intensive tempering to achieve optimal hardness and strength.

3. During wear tests, the hardened specimens lost about 3.5 times less mass than the quenched specimens, therefore exhibiting significantly better wear resistance. Retained austenite plays a key role in increasing wear resistance and reducing crack formation.

4. Applying plastic deformation after hardening increases the hardness and improves the microstructure, resulting in a slight increase in wear resistance compared to the as-hardened samples. This highlights the benefits of combining thermal and mechanical treatments for better results.

5. Although this treatment process can be more expensive and time-consuming, it can be justified in cases where higher wear resistance and longer component life are important, which helps save money in the long run.

For future studies, alternative deformation methods such as parallel channel angular pressing (ECAP) or high pressure twisting (HPT) could provide deeper insights into the improvement of microstructure and wear resistance. Testing of similar steel grades such as AISI D2, AISI 440C and AISI 52100 would help determine whether the findings are more broadly applicable. These steels are commonly used in tools, bearings and cutting applications that require high hardness and wear resistance. To expand the study, wear tests under different conditions, such as impact (ASTM G99), fatigue (ASTM G77), or abrasion (ASTM G65), would provide a better understanding of how these materials perform in real-world conditions. Each test simulates a specific wear environment, helping to evaluate the durability of steel in various industries.

5. References

1. M.A.S. Abdul Rahim, M. Minhat, N.I.S. Binti Hussein, M.S. Salleh, Metall. Res. Technol. 115, 1 (2018). https://doi.org/10.1051/metal/2017048
2. Q. Shasha, T. Huan, Z. Hongshan, H. Pengfei, T. Tinghui, D. Han, J. Mater. Res. Technol. 28, 3207 (2024). https://doi.org/10.1016/j.jmrt.2023.12.264
3. L. Quan, C. Xiaomi, L. Kun, C. Valentino, A.M. Lo Kin Ho, X. Zhengchao, K. Chi Tat, Surf. Coat. Tech. 481, 130609 (2024). https://doi.org/10.1016/j.surfcoat.2024.130609
4. S. Kritika, R.K. Khatirkar, G. Sapate Sanjay, Wear 328-329, 206 (2015). https://doi.org/10.1016/j.wear.2015.02.019
5. M.D. Conci, D.M.A. Centeno, H. Goldenstein, P.F.S. Farina, Mater. Res. 26, 7 (2023). https://doi.org/10.1590/1980-5373-MR-2023-0059
6. C. Trevisiol, A. Jourani, S. Bouvier, Trib. Intern. 113, 411 (2017). https://doi.org/10.1016/j.triboint.2016.11.001
7. T. Nykiel, T. Hryniewicz, J. Mater. Eng. Perform. 23(6), 5 (2014). https://doi.org/10.1007/s11665-014-0979-5
8. M.A. Mochtar, W.N. Putra, M. Abram, Mater. Res. Express. 10(5), 13 (2023). https://doi.org/10.1088/2053-1591/acd61b
9. M.A. Rehan, A. Medvedeva, L.E. Svensson, L. Karlsson, Metall. Mater. Transact. A 48A, 5233 (2017). https://doi.org/10.1007/s11661-017-4232-5
10. A. Wong, Modelling and Alloy Design [Apollo - University of Cambridge Repository], (2023). https://doi.org/10.17863/CAM.96614
11. F. Elhigazi, A. Artemev, Comp. Mater. Science 186, 109961 (2021). https://doi.org/10.1016/j.commatsci.2020.109961
12. B. Adamczyk-Cieslak, M. Koralnik, R. Kuziak, K. Majchrowicz, T. Zygmunt, J. Mizera, J. Mater. Eng. Perform. 31, 4419 (2022). https://doi.org/10.1007/s11665-021-06547-w
13. W. Zhirui, W. Wei, L. Man, T. Junyu, X. Guang, Wear 512-513, 204512 (2023). https://doi.org/10.1016/j.wear.2022.204512
14. H. Boungomba, P. Moreau, T. Sadat, L. Lilensten, M. Dubar, L. Dubar, Wear 542-543, 205272 (2024). https://doi.org/10.1016/j.wear.2024.205272
15. R. Bendikiene, L. Kavaliauskiene, Weld. World 61(5), 893 (2017). https://doi.org/10.1007/s40194-017-0476-3
16. T.C. Lowe, R.Z. Valiev, J. Miner. Met. Mater. Soc. 56, 64 (2004). https://doi.org/10.1007/s11837-004-0295-z
17. M. Merah, M.A. Azeem, H.M. Abubaker, F. Al-Badour, J. Albinmousa, A.A. Sorour, Mater. 14(17), 16 (2021). https://doi.org/10.3390/ma14175023
18. K. Harish, D. Kiran, P.S. Durgeshwar, M.G. Jitendra, K. Manish, A. Vanya, Mater. Today: Proc. 6 (2023). https://doi.org/10.1016/j.matpr.2023.02.194
19. E. Kaveh, A.Q. Anwar, A. Saeid, K. Kei, V. Aptukov, R. Asfandiyarov, A. Maki, V. Astanin, A. Bachmaier, V. Beloshenko, et al., J. Alloy. Compd. 1002, 174667 (2024). https://doi.org/10.1016/j.jallcom.2024.174667
20. A. Weidner, A. Muller, A. Weiss, H. Biermann, Mater. Sci. Eng. A 571, 68 (2013). https://doi.org/10.1016/j.msea.2013.02.008
21. M. Seleznev, J. Mantel, M. Schmidtchen, U. Prahl, H. Biermann, A. Weidner, Steel Res. Intern. 18, 2400472 (2024). https://doi.org/10.1002/srin.202400472
22. M.A. Essam, A.Y. Shash, M.K. El-Fawakhry, E. El-Kashif, H. Megahed, Metals 13(2), 382 (2023). https://doi.org/10.3390/met13020382
23. S. Farahany, M. Ziaie, N.A. Nordin, J. Mater. Eng. Perform. 32, 9000 (2023). https://doi.org/10.1007/s11665-022-07791-4
24. H-x. Chi, D-s. Ma, H-x. Xu, W-l. Zhu, J-q. Jiang, J. Iron Steel Res. Intern. 23(5), 484 (2016). https://doi.org/10.1016/S1006-706X(16)30076-0
25. R. Bendikiene, A. Ciuplys, R. Sertvytis, A. Surzhenkov, D. Tkachivskyi, M. Viljus, R. Traksmaa, M. Antonov, P. Kulu, J. Mater. Res. Technol. 9(4), 7068 (2020). https://doi.org/10.1016/j.jmrt.2020.05.042
26. ASM Handbook Committee, Heat Treaters Guide: Standard Practice and Procedures for Steel, 2nd edn, ASM International, Metals Park, OH (1982) 423–6.
27. S. Kahrobaee, M. Kashefi, Int. J. Eng. 28(2), 234 (2015). https://doi.org/10.5829/idosi.ije.2015.28.02b.09
28. Z. Zheng, M. Lei, C. Huang, M. Wan, Mater. Res. Express. 11, 12 (2024). https://doi.org/10.1088/2053-1591/ad2576
29. E. Günerli, M. Bayramoğlu, N. Geren, Eur. Mech. Sci. 6(4), 263 (2022). https://doi.org/10.26701/ems.1186751
30. B. Liu, T. Qin, W. Xu, C. Ji, Q. Wu, M. Chen, Z. Liu, Materials 12(22), 3714 (2019). https://doi.org/10.3390/ma12223714
31. F.L. Sucupira, M.J.R. Sandim, H.R.Z. Sandim, B. Santos Dagoberto, R.A. Renzetti, Mater. Charact. 115, 90 (2016). https://doi.org/10.1016/j.matchar.2016.03.023
32. F. Xingguo, X. Xiaofeng, Z. Yang, C. Dihui, W. Zhicheng, Y. Xudong, Y. Yachong, Y. Yongqiang, J. Mater. Res. Technol. 29, 1665 (2024). https://doi.org/10.1016/j.jmrt.2024.01.177
33. C. Hongxiao, D. Yingnan, Z. Nan, G. Jinbo, Z. Jian, M. Dangshen, Mater. Res. Express. 10, 12 (2023). https://doi.org/10.1088/2053-1591/ad1545
34. S. Kumar, S.R. Maity, L. Patnaik, Mater. Today: Proc. 44(1), 949 (2021). https://doi.org/10.1016/j.matpr.2020.11.004
35. Y. Tang, H. Pan, D.Y. Li, Wear 476, 203642 (2021). https://doi.org/10.1016/j.wear.2021.203642
36. D. Tobola, W. Brostow, K. Czechowski, P. Rusek, Wear 382–383, 29 (2017). https://doi.org/10.1016/j.wear.2017.03.023

Effect of chromium on the microstructure of AlSi7Mg alloy with increased iron content

Jaroslaw Piatkowski[1], Leszek Chowaniec[2], Tomasz Matula[1,*], Marco Reyna[3], German Sanchez[3]

Silesian University of Technology, Poland[1]

Superior Industries Production Poland Sp. z o.o., Poland[2]

Superior Industries Production, Mexico[3]

tomasz.matula@polsl.pl

Abstract: *The need to protect the environment by reducing the energy intensity of production, the amount of waste, and reducing greenhouse gas emissions, as well as shrinking bauxite resources, means that secondary raw materials are playing an increasingly important role in aluminum alloy smelting. However, the increase in the proportion of scrap results in a higher content of various impurities, the worst of which is iron in the group of metallic ones. It is well known that manganese is one of the most commonly used additives to neutralize morphologically unfavorable β-Al$_5$FeSi phases. However, there is little information about the effects of other transition elements, such as chromium. Accordingly, the study's results concern the effect of chromium on the microstructure of AlSi7Mg alloy with increased iron content (from 0.4wt.% to 1.4wt.%, in 0.2% increments). Based on SEM/EDX and XRD studies, it was found that the addition of chromium causes the transformation of the lamellar-needle phase β-Al$_5$FeSi into the α-Al$_{13}$(Fe,Cr)$_4$Si$_4$ phase with a dendritic morphology (so-called "Chinese script"). However, care should be taken not to exceed the permissible value of the chromium/iron quotient (Cr/Fe ~ about 1/3). Otherwise, the morphology of the α-Al$_{13}$(Fe,Cr)$_4$Si$_4$ phase changes from more "fluffy" to massive polygons. This is accompanied by an unfavorable increase in the slime ratio from about 1.6 to more than 3.0%.*

Keywords: AlSi7Mg ALLOY; MICROSTRUCTURE, ALUMINUM SCRAP, IRON-RICH AND CHROMIUM-RICH PHASES

1. Introduction

One of the most common and harmful impurities found in cast aluminum alloys is iron. Its impact on mechanical properties, especially plasticity, is particularly detrimental when it exceeds approximately 0.4% by weight (for gravity casting) [1-4] and approx. 1.8% by weight (for die casting) [5-9]. This is because iron has low solubility in the solid solution α(Al), i.e. from 0.052% at 655°C to 0.0052% at 450°C [10]. For this reason, it has a strong tendency to combine with other elements to form intermetallic phases of varying stoichiometry, morphology, and size [11, 12]. In Al-Si-Mg alloys, in addition to the Mg$_2$Si phase, there is a high probability of crystallization of Al$_9$Fe$_2$Si phases with a monoclinic structure and Al$_8$FeMg$_3$Si$_2$ (ρ phase) with a hexagonal structure. In addition, metastable ternary phases β-Al$_4$FeSi (25.4% Fe and 25.5% Si) and β-Al$_3$FeSi (33.9% Fe and 16.9% Si) crystallize under conditions of thermodynamic imbalance [2]. However, the most undesirable phases are mainly α_H-Al$_8$Fe$_2$Si and especially β-Al$_5$FeSi (so-called β-Fe). Due to its low coherence with the matrix and large size, the β-Fe phase increases the brittleness of the alloy, hinders the mechanical processing of castings, and reduces tensile strength [13-16]. In addition, its plate-needle morphology impairs the castability, ductility, and corrosion resistance of aluminum alloys [1-3]. The morphology and size of these phases, which depend mainly on the chemical composition and cooling rate [17, 18], can be changed by introducing various elements, such as Mn; Co, Mo, and Cr. Due to the similarity of the crystallographic lattice and lattice parameters to those of iron, these elements can alter the morphology of the β-Fe phases from plate-like to so-called "Chinese characters" or polyhedral solids, thereby increasing their precipitation and making them smaller [19, 20]. The best described and most popular alloying additive is manganese [6, 11, 17]. However, some studies indicate that chromium may be equally effective [18, 21, 22]. Still, its effect on the change in the morphology of β-Fe phases in Al-Si alloys with increased iron content has not been thoroughly investigated.

2. Purpose and scope of the research

The study aimed to determine the effect of increasing iron and chromium content on the microstructure of AlSi7Mg alloy cast by gravity into a sand mold. To achieve this goal, the scope of the research included, among other things:

- preparing AlSi7Mg alloy melts with increasing iron and Cr content according to the experimental plan (Fig. 1),
- testing the chemical composition of AlSi7Mg alloy with varying iron and chromium content,
- testing the microstructure of the alloy.

This work aimed to check how the increasing content of iron and chromium, as a so-called "morphological corrector" of the β-Fe phases, affects the change in the microstructure of the AlSi7Mg alloy.

3. Research material and methodology

The AlSi7Mg alloy was smelted from an AlSi20 alloy diluted with pure aluminum (99.95% by mass) to achieve an approximate content of 7% by mass of Si and alloying additives: AlMg10 (10% by mass of Mg) and AlCr50 (50% by mass of Cr). According to the literature review [22], the chromium content was selected to be one-third of the iron content. The feedstock components were melted in a Balzers VSG 02/631 electric furnace in a 0.8-liter SiC crucible. After aging in the furnace, the alloys were modified with AlSr10 (10 wt.% Sr) master alloy and refined with Rafglin-3 in an amount of approx. 0.05 wt.%. After reaching a temperature of approx. 740°C, the alloys were cast into a sand mold (93% quartz sand; 7% bentonite; 3.5-4.5% water) in the shape of a cylinder with a diameter of ϕ=50mm and a height of h=100mm. The experimental plan is shown in Figure 1.

The chemical composition of the castings was analyzed on the surface using a Foundry Master CCD 01L00113 WAS-AG emission spectrometer (SpectroLab, Kleve, Germany). Ten samples were taken, the two extreme ones were discarded, and the arithmetic mean was calculated from the remaining eight, rounded to two or three decimal places.

Samples for metallographic testing were cut from the center of the sand casting (at a height of approx. 80 mm). The surfaces of the samples were ground and polished with polishing pastes according to the standard procedure for preparing metallographic specimens.

Microstructure observations were performed using a MeF2 light microscope (LM) and a Hitachi S-3400N scanning electron microscope (SEM) equipped with an energy dispersive X-ray spectrometer (EDS) Thermo Noran and wavelength dispersion (WDS) Thermo MagnaRay, as well as an INCA HKL Nordys II (Hitachi High-Technologies Tokyo, Japan) detector for backscattered electron diffraction (EBSD) testing. For a better indication of structural components, some of the specimens were subjected to deep etching in 5% HF acid. X-ray testing was performed using a Philips X`Pert diffractometer with a copper anode tube (λCuKα -1.54178 Å), powered by a current of 30 mA at a voltage of 40 kV. The recording was performed using the step-scanning method with a step of 0.04° and a counting time of 10 seconds, in the 2θ angle range from 20° to 140°. The slit on the incident beam was 1°, and on the diffracted beam, 2°. Sollera slits of 0.04 mm were used. Qualitative phase analysis was performed

using the ICDD database. The analysis was performed using the DBWS 9807A program, and Pearson's VII degree function was used to describe the diffraction line profile. Ten images were taken, of which the ones presented here are representative images of the microstructure of the tested alloy.
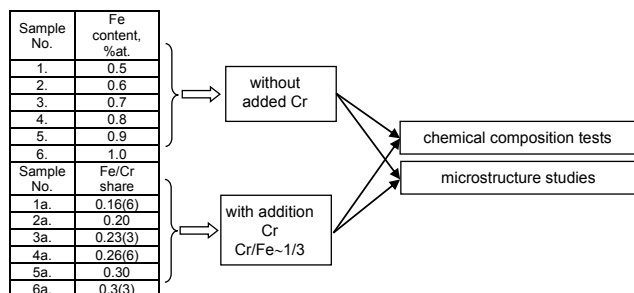
Sample No.	Fe content, %at.			
1.	0.5			
2.	0.6			
3.	0.7	without added Cr		
4.	0.8			chemical composition tests
5.	0.9			
6.	1.0			microstructure studies
Sample No.	Fe/Cr share			
1a.	0.16(6)			
2a.	0.20	with addition Cr Cr/Fe~1/3		
3a.	0.23(3)			
4a.	0.26(6)			
5a.	0.30			
6a.	0.3(3)			

Fig. 1 *Research plan for the AlSi7Mg alloy with increasing iron and chromium content.*

4. Research results and their analysis

4.1. Chemical Composition Test Results

The results of chemical composition tests of AlSi7Mg alloy with increasing iron content before and after the addition of chromium are presented in Table 1.

Table 1: *Chemical composition[2] results for AlSi7Mg[1] alloy (arithmetic mean of eight samples).*

Sample No.	Element content, wt.%							
	Si	Fe	Cr	Mg	Cu	Zn	Ti	Sr
	Without added Cr							
1.	6.79	0.47		0.41	0.03	0.014	0.059	0.015
2.	6.88	0.58		0.42	0.03	0.012	0.062	0.014
3.	6.97	0.70	<0.01	0.48	0.02	0.014	0.058	0.014
4.	6.91	0.81		0.42	0.04	0.013	0.061	0.013
5.	6.79	0.90		0.44	0.04	0.014	0.064	0.014
6.	6.89	1.01		0.46	0.03	0.013	0.060	0.013
	After the addition of Cr (AlCr)							
1a.	6.84	0.48	0.156	0.41	0.02	0.013	0.053	0.014
2a.	6.94	0.58	0.193	0.42	0.02	0.013	0.060	0.014
3a.	6.87	0.70	0.239	0.44	0.02	0.012	0.060	0.013
4a.	6.94	0.80	0.270	0.42	0.03	0.014	0.058	0.014
5a.	6.86	0.89	0.290	0.44	0.03	0.011	0.061	0.013
6a.	6.87	1.00	0.336	0.45	0.02	0.011	0.061	0.015

[1] – the rest is aluminum,

[2] – other < 0.02.

4.2. Microstructure test results

Representative microstructures (LM) and (SEM) of the AlSi7Mg alloy without chromium and after its introduction are shown in Figure 2.

To identify the components of the AlSi7Mg alloy structure, microanalysis of the chemical composition and X-ray diffraction tests were conducted, with the results presented in Figures 3 and 4.
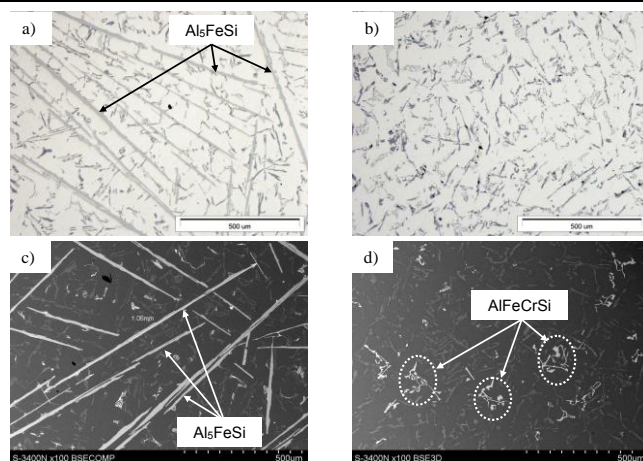
Fig. 2 *Microstructure of the AlSi7Mg alloy: a, c) without chromium; b, d) after the introduction of chromium; a, b) LM; c, d) SEM (magnification ×100).*

wt.%	Al-K	Si-K	Cr-K	Fe-K
Point 1	98.2	1.8	--	--
Point 2	2.6	97.4	--	--
Point 3	45.2	11.1	26.7	17.1
at.%	Al-K	Si-K	Cr-K	Fe-K
Point 1	98.3	1.7	--	--
Point 2	2.7	97.3	--	--
Point 3	58.0	13.6	17.7	10.6

Fig. 3 *Microstructure and microanalysis results of the chemical composition of the AlSi7Mg alloy after the addition of chromium.*

The results of microanalysis of the chemical composition of the AlSi7Mg alloy after the addition of chromium indicate that an $Al_X(Fe;Cr)_YSi_Z$ phase crystallizes. To identify it, XRD (X-ray diffraction) tests were performed, with the results shown in Figure 4.
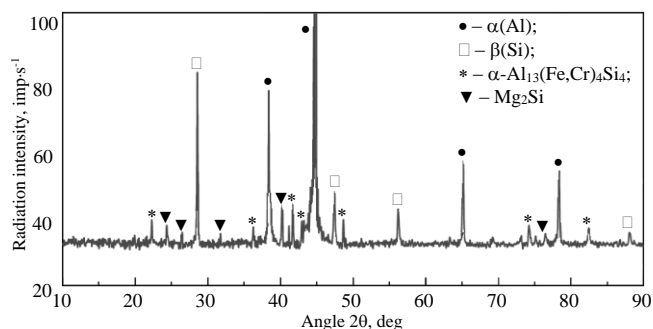
Fig. 4 *XRD pattern of AlSi7Mg alloy with chromium addition.*

Previous studies of the microstructure of AlSi7Mg alloy without chromium additive [23] show that, in addition to traditional components, i.e. solid solution dendrites α(Al), silicon β(Si) crystals, which are part of the eutectic α(Al)+ β(Si) and the Mg_2Si

phase, which is a component of the eutectic α(Al)+Mg$_2$Si+β(Si), a β-Al$_5$FeSi phase was identified. Due to their plate-needle morphology and length of up to 1000 μm – Fig. 2c (during gravity casting), the β-Fe phase precipitates are brittle and constitute privileged sites for stress propagation. After the addition of chromium, the Al$_{13}$(Fe,Cr)$_4$Si$_4$ phase, known as the α-FeCr phase (Fig. 4), with a dendritic morphology (Fig. 2d), was identified in the microstructure of the AlSi7Mg alloy, replacing the β-Al$_5$FeSi phase. The remaining components of the AlSi7Mg alloy structure, with the addition of chromium, are unchanged, regardless of the iron and chromium content.

Studies of the microstructure of the AlSi7Mg alloy also showed that with an increase in the iron (β-Fe phases) and chromium (α-FeCr phases) content, the morphology of the chromium-containing phases changes. The microstructure of the AlSi7Mg alloy with increasing iron and chromium content is shown in Fig. 5.
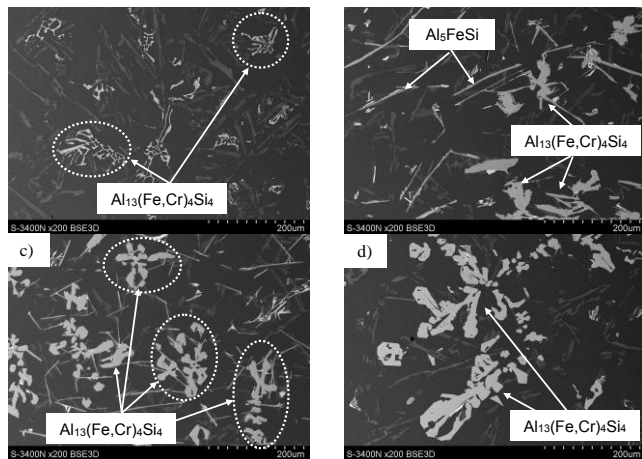
Fig. 5 SEM microstructure of AlSi7Mg alloy for different iron and chromium contents: a) 0.48 wt.% Fe and 0.156 wt.% Cr (sample 1a); b) 0.7 wt.% Fe and 0.239 wt.% Cr (sample 3a); c) 0.8 wt.% Fe and 0.27 wt.% Cr (sample 4a); d) 1.0 wt.% Fe and 0.336 wt.% Cr (sample 6a) (magnification ×200).

The microstructures shown in Figure 5 indicate that the increasing chromium content in the AlSi7Mg alloy causes a change in the morphology of the Al$_{13}$(Fe,Cr)$_4$Si$_4$ phase from dendritic to massive, interconnected solids. This phenomenon intensifies mainly when the content of Fe exceeds approx. 0.8 wt.% and Cr exceeds approx. 0.3 wt.%. These are probably particles of so-called "sludge," which, as shown by research [9, 18], is unfavorable, especially during die casting. To determine the chemical composition of the "sludge" particles, XRD tests were performed again, with the results presented in Figure 6.

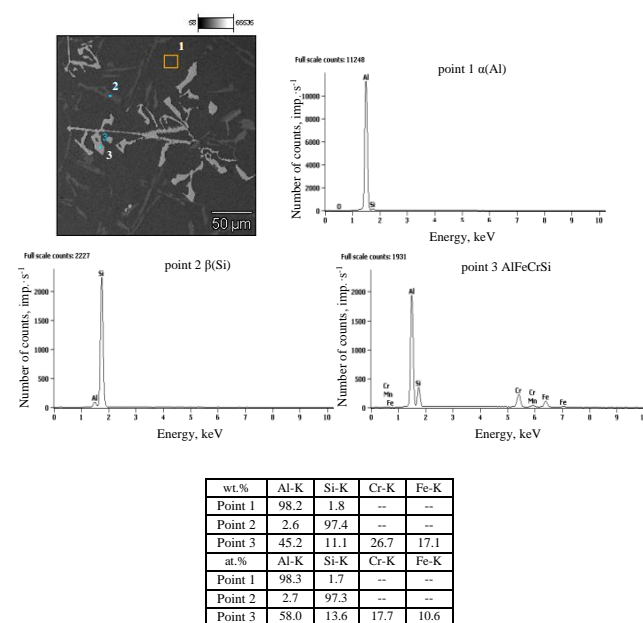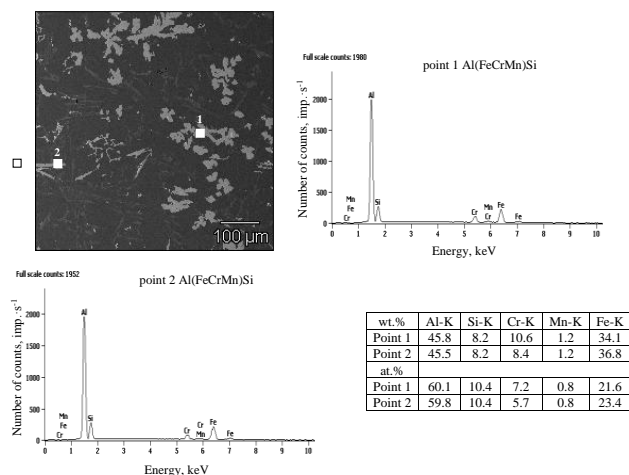*Fig. 6 Microstructure and microanalysis results of the chemical composition of the AlSi7Mg alloy after the addition of chromium.*

wt.%	Al-K	Si-K	Cr-K	Mn-K	Fe-K
Point 1	45.8	8.2	10.6	1.2	34.1
Point 2	45.5	8.2	8.4	1.2	36.8
at.%					
Point 1	60.1	10.4	7.2	0.8	21.6
Point 2	59.8	10.4	5.7	0.8	23.4

Figure 6 shows that, in addition to Al, Si, Cr, and Fe, the "sludge" particles also contain a small amount of manganese. However, the exact identification of these particles requires further XRD testing, which is beyond the scope of this article.

5. Summary

Even though manganese is a popular alloying additive causing the transformation of the unfavorable β-Al$_5$FeSi phase into the α-Al$_X$(Fe;Mn)$_Y$Si$_Z$ phase (where: x=12; 15; 19; 20; Y=3; 5, Z=1; 2; 3) is manganese [11,17], the present study has shown that chromium can be equally effective. In technical gravity-cast aluminum alloys, its permissible content is up to 0.15% by mass, and in die-castings – up to 0.25% by mass. [22, 24]. At higher chromium contents, different cooling rates, and different purity of feedstock components (including the presence of iron), intermetallic phases of the Al$_X$(Fe;Cr)$_Y$Si$_Z$ phases crystallize, having a star-shaped, dendritic (so-called "Chinese writing") or polygonal morphology [22-24]. The present study has demonstrated that the addition of chromium promotes the crystallization of the Al$_{13}$(Fe;Cr)$_4$Si$_4$ phase, as confirmed in previous studies [25]. Furthermore, this phase replaces the morphologically unfavorable β-Al$_5$FeSi phase.

Particular attention was paid to the iron and chromium content in the AlSi7Mg alloy. It was found that the content was approximately up to 0.8 wt.% Fe and approx. 0.3 wt.% Cr (Fe/Cr ratio = 1/3), the Al$_{13}$(Fe; Cr)$_4$Si$_4$ phase has a dendritic morphology and effectively "eliminates" the β-Al$_5$FeSi phase from the alloy. However, when these values are exceeded, the Al$_{13}$(Fe;Cr)$_4$Si$_4$ phase changes its structure from dendritic to massive, interconnected solids that form so-called "sludge" particles. This is an undesirable phenomenon, as research [9, 18] shows that this sludge reduces the mechanical properties, especially the ductility of the alloy, and its removal from the alloy is difficult.

To more fully investigate the effect of chromium addition on the change in the morphologically unfavorable β-Al$_5$FeSi phase, further research is required, mainly in terms of evaluating the crystallization process of chromium-rich phases and the performance properties of Al-Si alloys, which will be the subject of future publications.

6. Reference

1. C. Kammer, *Aluminium Handbook. Vol. 1: Fundamentals and Materials* (Beuth Verlag GmbH, 2011)
2. T. O. Mbuya, B. O. Odera, P. S. Ng'ang'a, International J. of Cast Metals Research, **16**, 15 (2003)
3. J. R. Davis, *Aluminum and Aluminum Alloys* (ASM Specialty Handbook, ASM International, Materials Park, OH, 1993)
4. J. A. Taylor, Procedia Materials Science, **1**, 15 (2012)
5. S. Ferraro, A. Fabrizi, G. Timelli, Materials Chemistry and Physics, **153**, 12 (2015)
6. S. Seifedine, I. L. Svensson, Metallurgical Science and Technology, **27**, 10 (2009)
7. H. Guo, X. Yang, J. Wang, J. of Alloys and Compounds, **485**, 5 (2009)
8. A. M. Samuel, F. H. Samuel, J. of Materials Science, **30**, 11 (1995)
9. D. Bösch, S. Pogatscher, M. Hummel, W. Fragner, P. J. Uggowitzer, M. Göken, H. W. Höppel, Metallurgical and Materials Transactions A, **46A**, 11 (2015)
10. N. A. Belov, A. A. Aksenov, D. G. Eskin, *Iron in Aluminum Alloys. Impurity and Alloying Element* (Taylor & Francis Inc, New York 2002)
11. S. G. Shabestari, Materials Science and Engineering, **383A**, 10 (2004)
12. W. S. Ebhota, J. Tien-Chien, *Intermetallics formation and their effect on mechanical properties of Al-Si-X alloys* (IntechOpen 2014)
13. X. Cao, J. Campbell, Materials Transaction, **47**, 10 (2006)

14. M. Mahta, M. Emamy, X. Cao, J. Campbell, Materials Science Research Trends, 21 (2008)

15. A. Pennors, A. M. Samuel, F. H. Samuel, H. W. DotyAFS Transactions, **106**, 14 (1998)

16. P. Mikołajczyk, L. Ratke, Arch. of Foundry Eng., **15**, 14 (2015)

17. S. Seifeddine, S. Johansson, I. L. Svensson, Mat. Sci. and Eng., **490A**, 6 (2008)

18. G. Gustafsson, T. Thorvaldsson, G. L. Dunlop, Metallurgical Transactions, **A17**, 8 (1986)

19. Z. Ma, A. M. Samuel, F. H. Samuel, H. W. Doty, S. Valtierra, Mat. Sci. and Eng., **490**, 6 (2008)

20. S. G. Shabestari, M. Keshavarz, M. M. Hejazi, J. of Alloys and Compounds, **477**, 8 (2009)

21. W. Eidhed, J. of Mat. Sci. and Tech., **24**, 3 (2008)

22. G. Timelli, F. Bonollo, Mat. Sci. and Eng., **A528**, 10 (2010)

23. J. Piątkowski, L. Chowaniec, T. Matuła, Machines. Technologies. Materials, **19**, 4 (2025)

24. M. Mahta, M. Ememy, A. Daman, A. Keyvani, J. Campbell, Int. J. of Cast Metals Research, **18**, 7 (2005)

25. R. Kakitani, A. V. Rodrigues, C. Silva, A. Garcia, N. Cheung, J. of Alloys and Metallurgical System, 1, 12 (2023)

Comparative study of hardness evolution in 5754 aluminum welds under AC and DC welding currents

Antanas Ciuplys[*], Regita Bendikiene, Audrius Jutas
Kaunas University of Technology, Lithuania
Antanas.Ciuplys@ktu.lt

Abstract: This study examines how thermal and mechanical effects influence hardness distribution in 4, 6, and 8 mm AA5754 aluminum plates welded using TIG with AC and DC currents. Vickers hardness (HV0.01) was measured alongside tensile tests to evaluate weld performance. Results show that AC welding produces higher but more variable hardness, while DC welding yields more stable profiles. Notably, thinner plates (4 mm) showed minimal hardness differences between current types due to faster cooling. Strain hardening increased hardness up to 125 HV and reduced variation. The extent of hardness stabilization and heat-affected zone size depended on plate thickness. Although current type influenced hardness distribution, it had little effect on fracture toughness.

Keywords: TIG WELDING, AC VS DC, ALUMINIUM, STRAIN HARDENING, THERMAL EFFECT

1. Introduction

Low density, high strength-to-weight ratio, good plasticity, and high corrosion resistance all are Al-alloys advantages over other structural materials making these alloys very suitable for use in aircraft, automotive, marine and offshore applications and other transportation industries where reduction of the structural weight of components and fuel economy plays a major role [1]. To produce different structures in these areas welding remains a very popular and important technological process [2]. Therefore, aluminium welding solutions are widely studied and discussed by scientists all over the world because welding is mainly chosen for the installation of large metal structures such as ships, bridges, construction machinery and aircraft. The gas metal arc welding (GMAW) process, gas tungsten arc welding (GTAW/TIG), friction stir welding (FSW), and electron-beam welding (EBW) are the most widely used for aluminium welding because they are suitable for various applications. Of all the possible processes, arc welding, i.e. GMAW and TIG welding are more cost-effective due to lower energy consumption and greater flexibility [3]. There are a lot of published works on the influence of controlling the quality of the welds by monitoring welding speed, welding current and its polarity, heat input, and shielding gas [4-6].

Although standard welding processes exist, attempts are made to combine the processes to achieve good penetration, reduce porosity and obtain all the mechanical characteristics required for use. It has been shown that full penetration and low macro-porosity can be achieved in a 3 mm thick AA5754-aluminum alloy using a fibre laser arc hybrid welding process with filler wire [7]. Laser-arc and MIG with the CO_2 heat source combined welding of 5754 magnesium aluminium alloy lead to increased hardness of fusion zone possibly coursed by strain and magnesium hardening and no cracks formed on bending over 120° [8].

Based on the results of tensile tests of joints welded by the TIG method, the influence of welding imperfections on the values of strength parameters of the seams has been confirmed by calculating *r* Pearson coefficient [9]. It was demonstrated that the biggest negative impact of the welding non-conformities such as lack of penetration and solid inclusions their type and shape in the weld leads to lower hardness values, which can result in further low tensile performance [10].

The 5754 series alloys are aluminium-magnesium (Al-Mg) widely used in marine vehicles, pressure vessels, fuel tanks, and the manufacturing of welded chemical and nuclear buildings due to their lightweight and excellent corrosion resistance in the atmosphere [2]. 5754-H111 is a non-heat-treatable high-strength aluminium alloy usually supplied in an annealed condition [11]. Different amounts of Fe as an alloying element in the alloy of this grade affect failure modes: when a high Fe amount alloy fails by void sheeting, low Fe shows a ductile type of failure. Different levels of Fe are caused by the formation of relatively course Fe-Mn-Al intermetallic compounds during casting [12].

It is clear from the literature that other authors analyse the influence of GMAW, FSW, EBW or hybrid laser arc, robotic, fibre laser assisted or double pulsed GMAW welding on the mechanical behaviour of the AA5754 weld, but there is a lack of published works using pure TIG welding for this grade of alloy. Therefore, the focus of this research is to assess the role of the plate thickness of AA5754-H111 on the mechanical performance of pure TIG welded joints. AC current flow is traditionally used for aluminium alloys welding and all the studies mentioned above used AC, there are no scientific results on the use of DC, only welding manuals give some advantages of DC. In order to determine the influence of both current flows on the welding process, this study is accomplished through the tensile and bending behaviour of different thickness joints. The ductility of plates is demonstrated and compared.

2. Materials and Methods

The study was concentrated on a commercial 5754 (EN 573-3:2009) aluminium alloy of 4 mm, 6 mm, and 8 mm thick plates. Samples for welding were prepared using 150 mm long and 50 mm wide plates of the aforementioned thickness. Five samples were prepared for each thickness and current flow and all measurements and tests values were averaged. A single V-groove at 60° was selected for the AC current flow welds, while no groove is required for the DC flow [13], so butt welding was performed on the DC-welded samples.

Weld pool geometry plays an important role in the performance and mechanical properties of AC welded joints [14]. It is reported that groove angle should be as small as possible to minimize the loss of alloying elements in the base metal (BM) [15]. Therefore, for AC samples, each plate with 2.4 mm root opening and 1.5 mm root face thickness was formed with one bevelled groove with an angle of 30° to ensure reasonable use of the filler rod and increase the strength of the weld.

A 2.4 mm diameter Al 5356 magnesium-based filler rod (according to ISO 18273:2015) was used in the welding process. The nominal chemical composition of the test base alloy and filler rod are shown in Table 1.

Table 1: Chemical composition

	Si	Fe	Cu	Mn	Mg	Cr	Zn	Ti	Al
Al 5754-H111	0.40	0.40	0.10	0.50	2.6-3.6	0.30	0.20	< 0.15	The rest
Al 5356	0.25	0.40	0.10	0.05-0.20	4.5-5.5	0.05-0.2	0.10	0.06-0.20	The rest

Pre-weld surface cleaning of AC welds was performed to remove grease, oxidation and moisture within 20-30 mm of the weld groove on both sides. V-milling debris was removed with a hand file from the edges of the weld groove, and the base metal oxide layer was cleaned with a stainless-steel hand brush. Equal attention was paid to the aluminium plates and filler rod, and they were cleaned with isopropyl alcohol and dried. After joining the plates for AC welding, the V-groove was cleaned again with a

stainless-steel hand brush and degreased with isopropyl alcohol. Re-degreasing was also performed on the filler rod to avoid contamination of the weld. Meanwhile, only the aluminium oxide layer was removed from the joint edges of the prepared DC-welded samples [13, 14].

The TIG technique using Sherman DIGITIG 200 AC/DC Multipro (Poland) TIG inverter type of power source was chosen for the comparative analysis of AC and DC welds, as it allows obtaining a high-quality weld joint. A large gas lens and a number 11 cup (manufactured by TBI, Germany) ensured optimal gas shielding of the weld pool. To maintain a stable arc and protect the pool from contamination, a 2.4 mm diameter non-consumable tungsten electrode WL20 (TBI, Germany) with 30° tapered conical tip and flat end diameter of 0.1 mm and an electrode protrusion of 20 mm was chosen. As the electrode tip slowly loses the required arc, it is necessary to maintain the contour of the hemispherical tip from time to time. It should be noted that in all practical cases the tungsten electrode does not transfer metal to the weld pool under normal operating conditions. The same torch travel angle (80-85°) for both current flows, and an operating angle of 80-100° was used for AC, since DC does not require an operating angle [13]. The welding parameters were confirmed based on the experimental testing of the samples and are presented in Table 2. Plates of all thicknesses were welded using both AC and DC current flows using ~100% argon or helium as shield gas, respectively, supplied from a coaxial TIG torch tip.

Table 2: TIG welding parameters

Current	Plate thickness, mm	Welding current, A	Voltage, V	Travel speed, mm/s	Shielding gas	Gas flow rate[2], l/min
AC	4	100	17 – 20	1.6	Argon[1] 99.99%	14
	6	120		1.5		
	8	160		1.4		
DC	4	75	20 – 25	1.7	Helium[1] 99.99%	14
	6	120		1.6		
	8	180		1.4		

[1] Gaschema (Lithuania), 200 bar, supplied in 50 l cylinders
[2] The flow rate is monitored by a Hercules (Germany) pressure regulator suitable for Ar or CO_2 (200 bar max. pressure and 30.32 l/min max. flow rate)

Vickers hardness measurements were performed to determine the mechanical properties of base metal, the AC and DC weld joints, and hardness of samples after the failure. A Mitutoyo HM-200 (Mitutoyo Corporation, Japan) universal tester was used to perform the hardness test with a standard load of 0.098 N and a dwell time of 10 s. Schemes for measuring the hardness of the samples after the tensile test are shown in Fig. 1. All samples were measured at room temperature five times − average values were considered for evaluation.
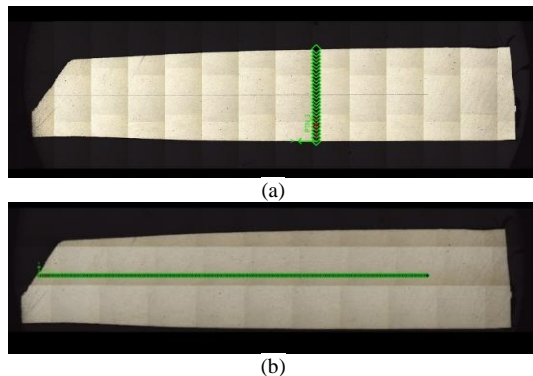

Fig. 1 Schemes of Vickers hardness measurement of transverse (a) and longitudinal (b) 6 mm thick sample

Flat tensile specimens from base metal and AC and DC welded plates of different thickness were taken according to EN ISO 4136:2012. For welded plates, it was taken transversally the welded joint so that after machining the welding axis remained in the

middle of the parallel length of the specimen. The geometric parameters of the tensile specimen with gauge length of 70 mm are presented in Fig. 2.
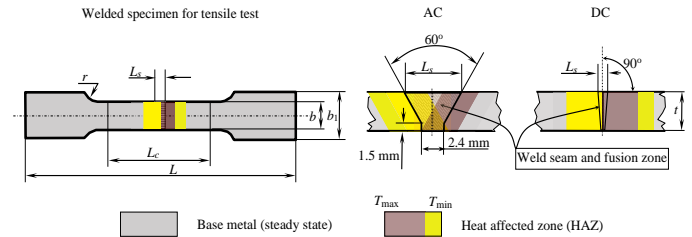

Fig. 2 Specimen geometry for tensile tests: t_s = 4/6/8 mm; b = 25 mm; b_1 = 37 mm; L_c = 70 mm; L = 300 mm; r = 25 mm; AC: L_s = 5.3/7.6/9.9 mm; DC: L_s = 4-6 mm

Destructive tensile testing at ambient temperature was performed to determine the behaviour of various thickness samples under tensile loading. The experiment was carried out using a universal testing machine 50 kN "Amsler" equipped with HBM testing device at a crosshead speed of 2 mm/min (force measurement sensor U5-100 kN (HBM); displacement sensor WA-50mm±0,1 mm; catman Express V4.5: catModule for data collection) [16]. Here, the specimens of the thickness to be tested are placed between two plates that hold the test object firmly, and then a tensile force is applied through the upper jaw, while the lower part firmly holds the tensile specimen. As a result, the sample deforms and possess fracture at some point due to various behaviour parameters such as elastic stress $\sigma_{0.05}$, ultimate stress σ_u, stress at fracture σ_{fr}, relative reduction of cross section at ultimate point Z_u, relative reduction of cross section after fracture Z_{fr}, maximum elongation A_5 (see Table 3). This determines the force required to break the welded sample and the extent to which the weld stretches or elongates to the breaking point. Three sets of samples: base metal, AC and DC welded samples underwent tensile testing according to EN ISO 4136:2012.

Table 3: Mechanical properties of the studied samples

No	Sample	$\sigma_{0.05}$	σ_u	σ_{fr}	Z_u	Z_{fr}	A_5
		MPa			%		
1	4BM	115	229	199	19	27	31.3
2	4AC	60	198	185	13	25	20.1
3	4DC	60	197	183	6	16	17.0
4	6BM	81	196	171	24	46	32.8
5	6AC	76	170	165	8	11	13.4
6	6DC	67	203	193	15	23	26
7	8BM	80	217	197	16	37	35.6
8	8AC	53	203	202	13	13	30.8
9	8DC	45	189	182	10	16	20.0

3. Experimental results

Generally, during deformation of the specimen, the microstructural non-homogeneity of weld seam which appears in sample material is also accompanied by different rate of deformation processes, which affect the tensile properties. In addition, the mechanical effect during stretching changes the hardness and its distribution in the weld and in the base metal, depending on what stage of deformation is reached, including normal elasticity (range $0 - \sigma_{0.05}$), strain hardening (range $\sigma_{0.05} - \sigma_u$) and neck formation (range $\sigma_u - \sigma_{fr}$) that is discussed as the object of the next topic.

Residual stresses σ_{res} are generated during welding. Technological parameters and welding methods influence on the characterization of their distribution and definitely influence the elastic stresses of the base material $\sigma_{BM/0.05}$. The residual stress σ_{res} is obtained by accepting that the value of the reference elastic stresses $\sigma_{BM/0.05}$ is the value of the unwelded specimen, and the elastic stresses of the welded specimen is $\sigma_{w/0.05}$. Therefore, the residual stresses σ_{res} can be written as the difference of the stresses determined for samples of different quality:

$$\sigma_{res} = \Delta\sigma_{0.05} = \sigma_{w/0.05} - \sigma_{BM/0.05} \qquad (1)$$

Numerical values of residual stresses along with mechanical properties are presented in Fig. 3(d).
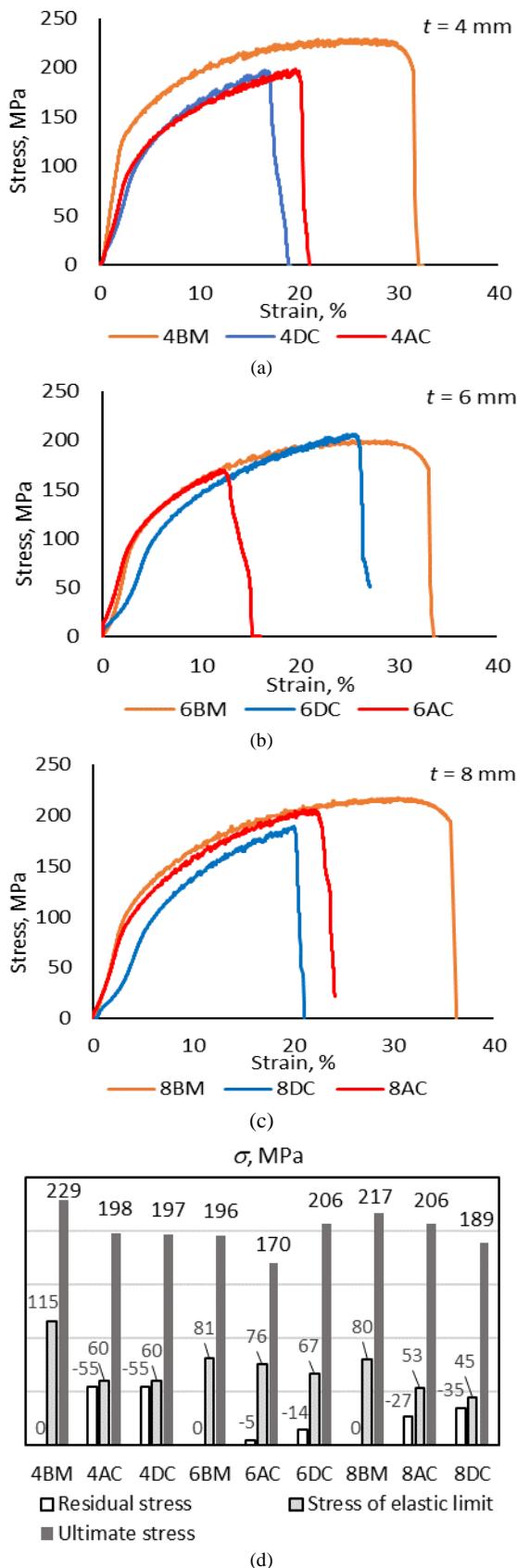

(a)

(b)

(c)

(d)

Fig. 3 *Graphical comparison of tensile curves and mechanical properties of 4/6/8BM, 4/6/8AC and 4/6/8DC samples of various thicknesses t: (a) 4 mm, (b) 6 mm, (c) 8 mm, (d) determined mechanical properties and residual stresses with their numerical values*

A negative sign indicates that the stresses are compressive, which would mean that the part of the residual stress resources is more likely to deform plastically and does not accumulate an increase in elasticity. Therefore, unlike the case of the Bauschinger effect, the elastic stresses of all welded specimens are lower than those of unwelded ones (see Fig. 3(a), (b), (c)).

The hardness of the AC and DC current flow welded samples was measured by evaluating two factors: 1) the thermal effect experienced after welding and 2) the influence of deformation after tensile test (straining). To ensure the reliability of the hardness measurement, it was measured along the z-axis (length) and perpendicularly along the x-axis (thickness). The hardness measurement diagram is presented in Fig. 4.
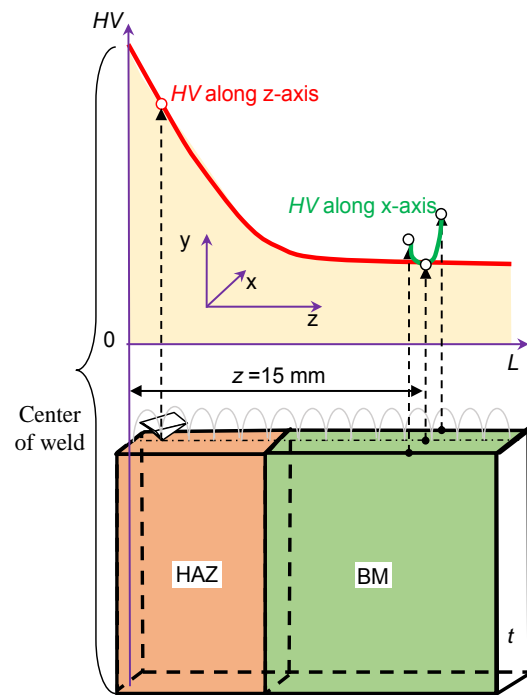

Fig 4 *Hardness measurement diagram of sample areas. HAZ is the heat affected zone and BM is the base metal*

The hardness $HV_{0.01}$ of the unwelded sample (blank) or so-called base metal (BM-0) at the plate surface is about 80 $HV_{0.01}$ in all samples, and in the centre, it drops to 70 $HV_{0.01}$ in samples 4BM-0 and 6BM-0 and even to 60 $HV_{0.01}$ in sample 8BM-0. This is influenced by the rolling of the aluminium blanks from which the samples are cut. As a result, the surface layer is hardened during rolling, while the central part of the sample remains at its original hardness. The hardness values of the unwelded samples are presented by the green curves in Fig. 5.

In the AC flow welded samples, the hardness of 90-95 $HV_{0.01}$ dominates in the centre of the weld. With DC current, some regularity is seen: as the thickness of the sample increases, the hardness in the centre of the weld decreases accordingly: 4DC-T to 90 $HV_{0.01}$, 6DC-T to 80 $HV_{0.01}$ and 8DC-T to 75 $HV_{0.01}$. This is determined by the intensity of endothermic processes and the greater inertia of thermal phenomena occurring in larger volume samples, which most likely explains the reason for the lower cooling. The measurement results are presented in Fig. 5 and Fig. 6.

In addition, the hardness measurement results are approximated by polynomial expressions: along the x-axis by using a second-order polynomial, and along the z-axis by using a third-order polynomial. All polynomials corresponding to the initial (0), thermal (T) and strain (S) states of the specimen are presented in Table 4.
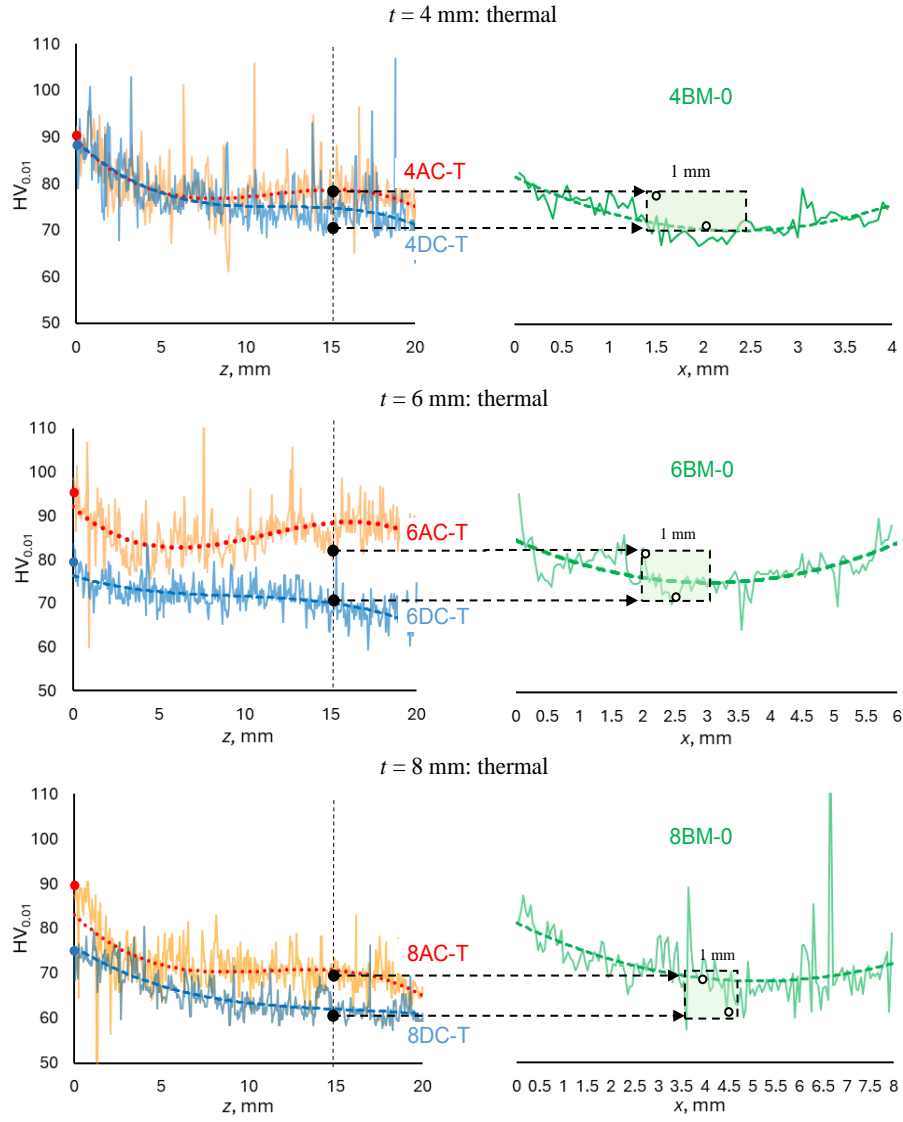
Fig. 5 *Distribution of hardness values HV$_{0.01}$ due to thermal effects in 4/6/8AC-T and 4/6/8DC-T samples of various thicknesses t what shows a diminution of hardness in z-axis (figures on the left) while reaching a steady state; on the right, a light green 1 mm area (approximately in the middle of the t thickness) is used to determine the hardness correspondence of initial state 4/6/8BM-0 samples in the x direction with 4/6/8AC-T and 4/6/8DC-T samples in the z direction taken at 15 mm from the weld centre*

Table 4: *Empirical equations for the distribution of hardening due to thermal and straining effects*

| Sample	State	Sample number	$t = 4$ mm: HV$_{x/z}$ x	z
BM	Initial	4BM-0	$2.0802x^2 - 9.818x + 81.607$	70-75
	Strained	4BM-S	$1.2195x^2 - 4.4062x + 100.41$	$-0.0024z^3 + 0.1166z^2 - 2.094x + 105.61$
AC	Thermal	4AC-T	$2.0802x^2 - 9.818x + 81.607*$	$-0.0077z^3 + 0.282z^2 - 3.4557z + 89.223$
	Strained	4AC-S	$0.534x^2 - 1.5495x + 89.1$	$-0.0124z^3 + 0.4952z^2 - 6.4263z + 120.3$
DC	Thermal	4DC-T	$2.0802x^2 - 9.818x + 81.607*$	$-0.0103z^3 + 0.3591z^2 - 3.7917z + 89.416$
	Strained	4DC-S	$0.6221x^2 - 2.5538x + 89.56$	$-0.0017z^3 + 0.135z^2 - 3.2685z + 112.23$
$t = 6$ mm: HV$_{x/z}$				
BM	Initial	6BM-0	$1.0237x^2 - 6.2368x + 84.17$	70-75
	Strained	6BM-S	$0.4701x^2 - 2.1515x + 103.21$	$-0.004z^3 + 0.1535z^2 - 2.023z + 108.13$
AC	Thermal	6AC-T	$1.0237x^2 - 6.2368x + 84.17*$	$-0.0117z^3 + 0.3908z^2 - 3.4768z + 92.084$
	Strained	6AC-S	$0.4965x^2 - 2.3734x + 93.312$	$-0.0144z^3 + 0.6012z^2 - 8.3245z + 125.16$
DC	Thermal	6DC-T	$1.0237x^2 - 6.2368x + 84.17*$	$-0.0041z^3 + 0.1138z^2 - 1.2011z + 76.327$
	Strained	6DC-S	$0.8002x^2 - 5.1576x + 104.71$	$8E{-}05z^3 + 0.0622z^2 - 2.0961z + 109.43$
$t = 8$ mm: HV$_{x/z}$				
BM	Initial	8BM-0	$0.4929x^2 - 5.0642x + 81.157$	65-70
	Strained	8BM-S	$0.3604x^2 - 2.3964x + 104.9$	$0.0003z^3 - 0.0168z^2 - 0.0796z + 102.39$
AC	Thermal	8AC-T	$0.4929x^2 - 5.0642x + 81.157*$	$-0.0105z^3 + 0.3497z^2 - 3.7185z + 83.055$
	Strained	8AC-S	$0.3267x^2 - 2.5892x + 93.715$	$-0.0109z^3 + 0.4724z^2 - 6.3009z + 113.25$
DC	Thermal	8DC-T	$0.4929x^2 - 5.0642x + 81.157*$	$-0.0031z^3 + 0.143z^2 - 2.3752z + 75.877$
	Strained	8DC-S	$0.3537x^2 - 2.487x + 89.403$	$-0.0027z^3 + 0.1832z^2 - 3.617z + 105.58$
* indicates a similarity of hardness distribution between base metal and DC-/AC-welded specimens when the hardness was measured on the line of x axis moved by 15 mm from the centre of unwelded specimens				
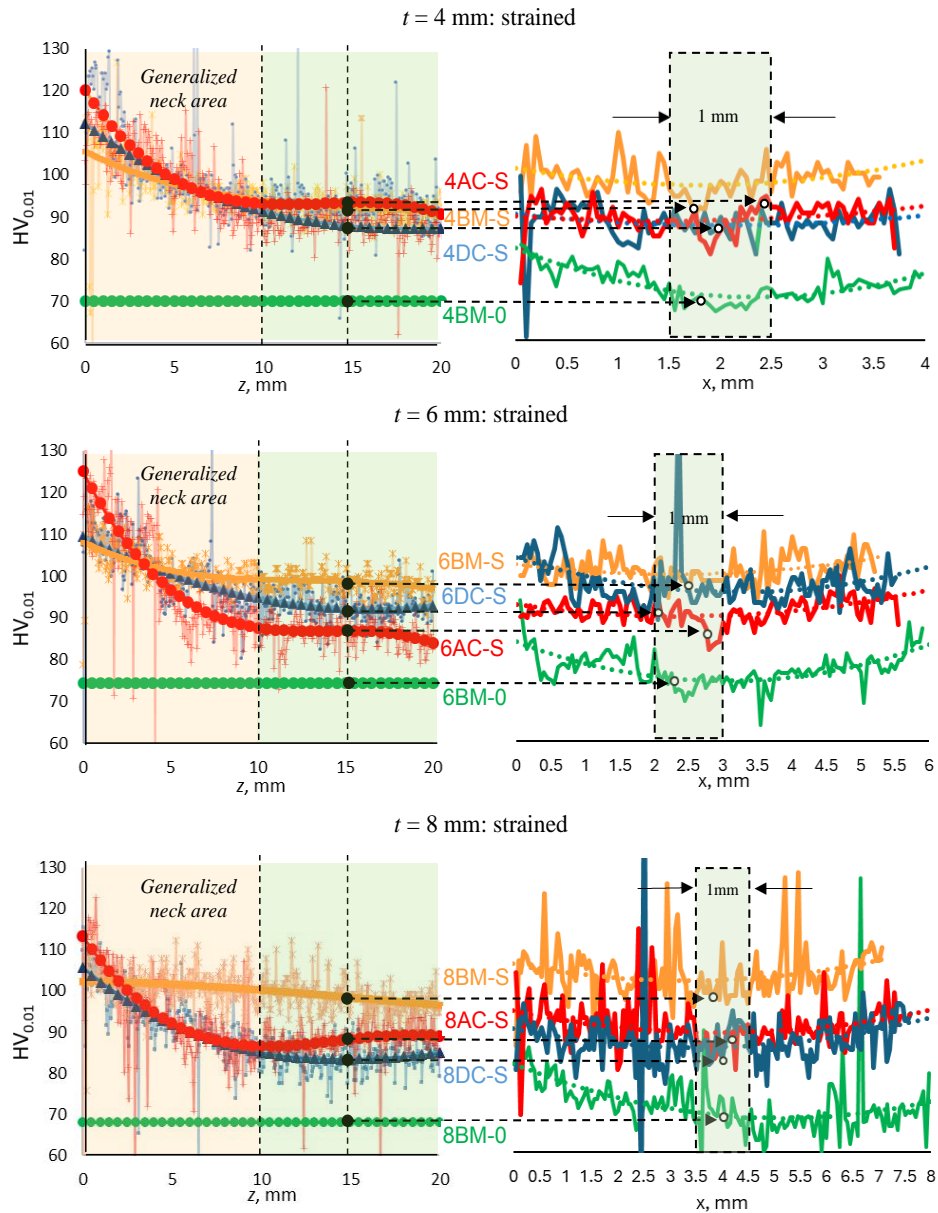
Fig. 6 *Distribution of hardness values HV$_{0.01}$ due to straining effects in 4/6/8AC-S and 4/6/8DC-S samples of various thicknesses t what shows an increase of hardness HV in x and z axes; figures on the left show hardness HV on the z-axis and graphs on the right on the x-axis; on the right, a light green 1 mm area (approximately in the middle of the t thickness) is used to determine the hardness correspondence in the x and z directions at 15 mm taken from the fracture edge along the z axis*

In Fig. 5 and Fig. 6, a distance of 15 mm from the edge of failure of the sample in the transverse direction with respect to the *x*-axis was chosen in such a way that the strain hardening is obtained outside the neck formation area, because, when it is reached, the ultimate stresses increase, hardening processes are accompanied by large plastic deformations in the neck formation zone. In addition, when measuring the hardness before and after straining, it was observed that the hardness variation of the DC-specimen is more uniform than that of the AC-specimen.

4. Discussion

The mechanical properties of the unwelded samples show that the maximum ultimate stress is in 4 mm specimen, followed by the 6- and 8 mm samples in the direction of decreasing stress (see Fig. 3). Their values are affected by the hardened layer on the surface obtained during production, where the hardness is higher than in the middle of the thickness of the sample. This can be seen in Fig. 5 of the measured hardness along the *x*-axis on the right. The percentage of deformed part in thick AC and DC welded samples has almost no effect on the mechanical properties. The elastic stresses are

influenced by residual stresses, and the stresses of ultimate strength are similar. Both AC and DC samples were observed to shift the deformation process from the BM to a weaker location, i.e., the HAZ. Based on the experimental results and what has been said above, two hypothetical statements are made to evaluate the hardness variation patterns.

Summarizing the achieved results, it can be stated that as the distance *z* increases from the AC and DC weld centre, it is simply thermally affected, the change in hardness is more stable in DC samples and wavier in AC samples until base metal HV values are reached. The hardness of the AC samples is higher than that of the samples prepared by the DC method. The strain hardening process affects both the increase of HV and the decrease of the so-called waviness. The hardness invariance distance *z* depends on the thickness of the specimen, which influences the distance L_s and the HAZ associated with the latter. If the welded sample breaks a little earlier than the statistical average, it means that the strain hardening process also stops earlier. In this work, the case was also chosen when the material of the base metal does not have time to deform and the strain hardening process moves to the fracture area at the

weld seam much more intensively compared to the base metal. This is related to 6 mm AC welded sample. The consequences of this case we observe when comparing 6 mm AC and DC welded strained samples at $z = 3...20$ mm what allows us to conclude that for the given z range, the 6AC-S sample hardness is less than 6DC-S sample. The evolution of the hardness HV is on average more reflective of its increase due to possible microscopic changes occurring in the material due to deformation, starting with elasticity (Range I), then strain hardening (Range II) and finally necking (Range III), when the hardness is the highest. Another interesting fact is that the micro-hardness $HV_{0.01}$ of the samples that were cut from samples 4AC-S, 6AC-S and 8AC-S after their fracture showed the highest values compared to the other samples of the same thickness. The current flow showed no appreciable difference in hardness $HV_{0.01}$ values for samples of the same thickness after fracture.

5. Conclusions

1. DC-welded samples have a more stable hardness distribution with increasing distance from the weld centre, while AC-welded samples have a wavier hardness profile until base metal hardness values are reached.

2. The AC-welded samples consistently show higher hardness compared to the DC-welded samples, indicating that the AC welding method increases the hardness of the material.

3. The strain hardening process not only increases the hardness, but also reduces the waviness in the hardness distribution, resulting in a more uniform hardness profile of the welded specimens.

4. The distance at which hardness stabilizes (the invariance distance, z) depends on the thickness of the specimen, which in turn affects the size of the heat affected zone (HAZ).

5. Hardness (HV) evolution is influenced by microstructural changes during deformation, AC welded specimens show faster microstructural processes leading to an increase in hardness, especially with increasing distance from the weld centre. However, no significant difference in hardness between AC and DC welding methods was observed for samples of uniform thickness after fracture.

6. References

1. Cheng J, Song G, Zhang Z, et al (2022) Improving heat-affected zone softening of aluminum alloys by in-situ cooling and post-weld rolling. J Mater Process Technol 306:117639. https://doi.org/10.1016/J.JMATPROTEC.2022.117639

2. Yürük A, Çevik B, Kahraman N (2021) Analysis of mechanical and microstructural properties of gas metal arc welded dissimilar aluminum alloys (AA5754/AA6013). Mater Chem Phys 273:125117. https://doi.org/10.1016/J.MATCHEMPHYS.2021.125117

3. Samiuddin M, Li J long, Taimoor M, et al (2021) Investigation on the process parameters of TIG-welded aluminum alloy through mechanical and microstructural characterization. Defence Technology 17:1234–1248. https://doi.org/10.1016/J.DT.2020.06.012

4. Troise M, Krichel T, Olschok S, Reisgen U (2024) Investigation of the influence of pulse parameters on the resulting weld seam quality in pulsed electron beam welding of AW 6061. Journal of Advanced Joining Processes 9:100183. https://doi.org/10.1016/J.JAJP.2023.100183

5. Abolusoro OP, Khoathane MC, Mhike W, et al (2024) Influence of welding parameters and post weld heat treatment on mechanical, microstructures and corrosion behaviour of friction stir welded aluminium alloys. Journal of Materials Research and Technology 32:634–648. https://doi.org/10.1016/J.JMRT.2024.07.175

6. Sabry I, Hewidy AM, Naseri M, Mourad AHI (2024) Optimization of process parameters of metal inert gas welding process on aluminum alloy 6063 pipes using Taguchi-TOPSIS approach. Journal of Alloys and Metallurgical Systems 7:100085. https://doi.org/10.1016/J.JALMES.2024.100085

7. Casalino G, Mortello M, Leo P, et al (2014) Study on arc and laser powers in the hybrid welding of AA5754 Al-alloy. Mater Des 61:191–198. https://doi.org/10.1016/J.MATDES.2014.04.060

8. Casalino G, Mortello M (2021) Laser-arc combined welding of aa5754 alloy. Mater Lett 284:128946. https://doi.org/10.1016/J.MATLET.2020.128946

9. Woźny P, Błachnio J, Dragan K (2019) Correlation between Strength, Hardness and the Share of Welding Imperfections in an AW 5754 Aluminium Alloy Weld Executed with the TIG Method. Journal of KONBiN 49:383–400. https://doi.org/10.2478/jok-2019-0092

10. Woźny P, Błachnio J (2018) The impact of microstructural non-conformities on microhardness of EN AW 5754 aluminium alloy welded joints made with the use of the TIG method. Journal of KONBiN 48:253–262. https://doi.org/10.2478/jok-2018-0055

11. Casalino G, Campanelli SL, Maso UD, Ludovico AD (2013) Arc Leading Versus Laser Leading in the Hybrid Welding of Aluminium Alloy Using a Fiber Laser. Procedia CIRP 12:151–156. https://doi.org/10.1016/J.PROCIR.2013.09.027

12. Sarkar J, Kutty TRG, Conlon KT, et al (2001) Tensile and bending properties of AA5754 aluminum alloys. Materials Science and Engineering: A 316:52–59. https://doi.org/10.1016/S0921-5093(01)01226-6

13. Bendikiene R, Sertvytis R, Ciuplys A (2023) Comparative evaluation of AC and DC TIG-welded 5083 aluminium plates of different thickness. The International Journal of Advanced Manufacturing Technology 127:3789–3800. https://doi.org/10.1007/s00170-023-11779-2

14. Syed Thasthagir M, Sajitha Banu A, Muthu kumaran A, et al (2024) Comparison of V groove design on mechanical performance and fracture behaviour in TIG welding of 5754-H111 aluminium alloy. Mater Today Proc. https://doi.org/10.1016/J.MATPR.2024.03.031

15. Baskutis S, Baskutiene J, Bendikiene R, Ciuplys A (2019) Effect of weld parameters on mechanical properties and tensile behavior of tungsten inert gas welded AW6082-T6 aluminium alloy. Journal of Mechanical Science and Technology 33:765–772. https://doi.org/10.1007/s12206-019-0131-6

16. Baskutis S, Baskutiene J, Bendikiene R, et al (2021) Comparative Research of Microstructure and Mechanical Properties of Stainless and Structural Steel Dissimilar Welds. Materials 14:6180. https://doi.org/10.3390/ma14206180

Study of the influence of combined thermomechanical processing modes on the mechanical properties of economically alloyed steel 5KHV2S

Igor Stepankin[1], Dmitry Kuis[2], Sergey Lezhnev[3], Evgeniy Panin[4], Valery Chigirinsky[3], Timur Useev[3]

[1] Belorusneft, 9 Rogachevskaya Street, Gomel, 246003, Belarus
[2] Belarusian State Technological University, Sverdlova str. 13a, Minsk, 220006, Belarus
[3] Rudny industrial University, 50 let Oktyabrya str. 38, Rudny, 115000, Kazakhstan
[4] Karaganda Industrial University, Republic av. 30, Temirtau, 101400, Kazakhstan

Abstract. *Despite the rapid development of metallurgical processes for the production of semi-finished products aimed at improving the modes of smelting, casting and crystallization, a significant improvement in the properties of any cast metal, ensuring its wide application in modern mechanical engineering, is achieved by combined thermomechanical processing of workpieces, combining hot metal forming and heat treatment. The technologies and equipment currently used in Kazakhstan by machine-building manufacturers have long been obsolete and ineffective. A common problem for everyone is the high energy intensity of production, its low productivity and the quality of forgings and blanks produced, which leaves much to be desired. Namely forgings and blanks are the starting materials for the manufacture of high-quality tools and technological equipment at mining and metallurgical engineering enterprises. Therefore, the purpose of this work is to develop rational modes of thermal and thermochemical processing of 5KHV2S steel, previously forged in a tool that implements alternating strain in metal, as well as to study the influence of combined thermomechanical processing modes on the mechanical properties of this steel. The studies carried out in this work on the hardness of 5KHV2S steel samples subjected to combined thermomechanical processing showed that the developed technologies contributed to an increase in both total and surface hardness compared with samples not subjected to pre-forging in a new forging tool that implements alternating strain in the metal.*
Keywords: HEAT TREATMENT, THERMOCHEMICAL PROCESSING, ECONOMICALLY ALLOYED STEEL, HARDNESS.

1. Introduction

Thermomechanical processing of alloy steels is a mandatory technological operation for processing various workpieces when forming a structure in metal products [1]. Grinding and texturing of solid solution grains in combination with directional shaping can significantly improve the mechanical and operational performance of various machine parts. As a rule, forging provides preparation of the microstructure for subsequent heat treatment of chromium and other steels containing carbide-forming elements. The intensity of the study of the structure during forging, as well as the processing of forgings and workpieces in the state of austenitic structure, provides an opportunity for the combined use of the actual hot pressure treatment in combination with heat treatment to obtain a metal structure with improved characteristics. Therefore, the development of new technologies for combined thermomechanical processing, including hot pressure treatment and subsequent heat treatment of workpieces made of economically alloyed steels for various purposes for mining and metallurgical engineering, is an urgent scientific and technical task.

As part of the implementation of the first stage of the grant theme AP09259236, a new technology for forging workpieces in a tool that implements alternating deformations in metal was developed and the influence of this technology on the evolution of microstructure and changes in the mechanical properties of steel grades 7HG2VM and 5KHV2S was investigated. In the course of experimental studies, the expediency of using the proposed forging technology and strikers for its implementation, instead of the currently used forging technology in flat strikers, has been proved, since the proposed forging technology with a similar forging as when forging in flat strikers, allows to obtain forgings and blanks of higher quality qualities with a uniformly distributed equiaxial fine-grained structure [2-3].

The purpose of this work is to develop rational modes of thermal and thermochemical processing of 5KHV2S steel, previously forged in a tool that implements alternating deformations in metal, as well as to study the influence of combined thermomechanical processing modes on the mechanical properties of this steel grade.

2. Materials and methods

To achieve this goal, the following modes of thermal and thermochemical treatment were proposed:

1) Heat treatment: quenching from a temperature of 880°C in oil, followed by tempering at a temperature of 200°C (mode 1) and 500 ° C (mode 2).

2) Thermochemical treatment:

2.1) cementation in a solid carburetor (920°C, 8 and 12 hours) + quenching from a temperature of 880°C in oil followed by tempering at a temperature of 200°C;

2.2) nitrocementation in a solid carburetor modified with carbamide (880°C, 6 and 8 hours) + quenching from a temperature of 880°C in oil, followed by tempering at a temperature of 200°C.

It should be noted that in order to conduct a comparative analysis, in parallel with the thermal and thermochemical processing of 5KHV2S steel, previously forged in a tool that implements alternating deformations in the metal, thermal and thermochemical processing of 5KHV2S steel, annealed at a temperature of 700°C with an exposure of 40 minutes, was carried out according to similar modes [3].

The designation and processing modes of the samples are given in Table 1.

Experimental studies were carried out at the laboratory base of Rudny Industrial Institute (Kazakhstan) and the Belarusian State Technological University (Belarus). Muffle furnaces SNOL 30/1300 LSF01 were used to heat the samples. The samples that were not subjected to hardening were heated in containers with cast iron shavings and a sealed gate between the lid and the body. The castle was covered with fine-grained quartz sand. During quenching, the container was removed from the furnace and immediately after opening, the samples on the suspension were removed from the chips and placed in quenching oil. During the hardening treatment carried out before quenching, two options were implemented. According to the first, carburization was carried out in containers with modified barium carbonate charcoal. After its completion, the containers were cooled together with the furnace, and then heated for quenching in a container with cast iron shavings. According to the second variant, high-temperature nitrocementation was carried out in a container with charcoal modified with urea. Since the saturation temperature coincided with the temperature of heating for quenching, it was carried out by directly removing the suspension with samples from the container with coal and immersion in quenching oil. In all cases, the polymer composition "THERMOVIT-M" was used as a quenching medium.

To determine the values of hardness indicators, as the main property characterizing the behavior of steels, a series of 5KHV2S steel samples subjected to thermal and thermochemical treatment in various modes was obtained.

Table 1 – Modes of thermomechanical processing of steel 5KHV2S

Table 1 – *Modes of thermomechanical processing of steel 5KHV2S*

Sample designation	Initial state	Thermochemical treatment modes			Heat treatment modes	
		Type of treatment	Time, hour	T, ºC	T quenching, ºC	T tempering, ºC
1	forging	-	-	-	-	-
2	annealing	-	-	-	-	-
1q200	forging	-	-	-		200
1q500	forging	-	-	-		500
2q200	annealing	-	-	-		200
2q500	annealing	-	-	-	880	500
1c8200	forging	Cementation	8			
1c12200	forging		12	920		
2c8200	annealing		8			
2c12200	annealing		12			200
1nc6200	forging	Nitrocementation	6			
1nc8200	forging		8	880		
2nc6200	annealing		6			
2nc8200	annealing		8			

The determination of the values of hardness indicators was carried out on DuraJet-10 hardness tester (EMCO-TEST, Austria) by the Rockwell method according to the standard methodology and a Duramin microhardometer (Struers, Denmark) by the Vickers method with a load on the indenter of 10-2000 g, the exposure time is 10 s. Automatic loading of the indenter, exposure and unloading, automatic load testing exclude deviations during the measurement.

The hardness testers used represent modern technologies and comply with current norms and standards.

3. Results

The results of the microhardness study are presented in Table 2.

Table 2 – *Microhardness of 5KHV2S steel samples after thermal and thermochemical treatment in various modes*

Sample number	Microhardness of the surface, MPa	Microhardness of the base, MPa
Initial state		
1	-	4250, 4180, 4320
2	-	3590, 3890, 3750
After heat treatment		
1q200	-	6490, 6550, 6630
1q500	-	5090, 5110, 5220
2q200	-	6120, 5850, 6050
2q500	-	4420, 4000, 4180
After cementation		
1c8200	7930, 7510, 7190	6870, 7020, 6810
1c12200	8040, 7730, 6970	6790, 6850, 6870
2c8200	7840, 6970, 6560	6260, 6380, 6420
2c12200	7720, 7230, 6890	6490, 6530, 6550
After nitrocementation		
1nc6200	8190, 7680, 7300	6520, 6330, 6370
1nc8200	8250, 7600, 7200	6630, 6560, 6580
2nc6200	7950, 7250, 6870	6220, 6170, 6330
2nc8200	8020, 7340, 6880	6410, 6480, 6440

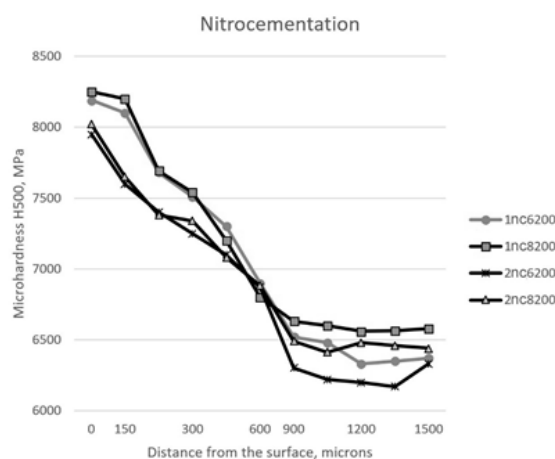Figures 1-2 show graphs of microhardness distribution over the cross section of the studied samples of 5KHV2S steel.

Fig. 1. *Microhardness distribution over the cross-section of nitrocemented layers of steel 5KHV2S after heat treatment*
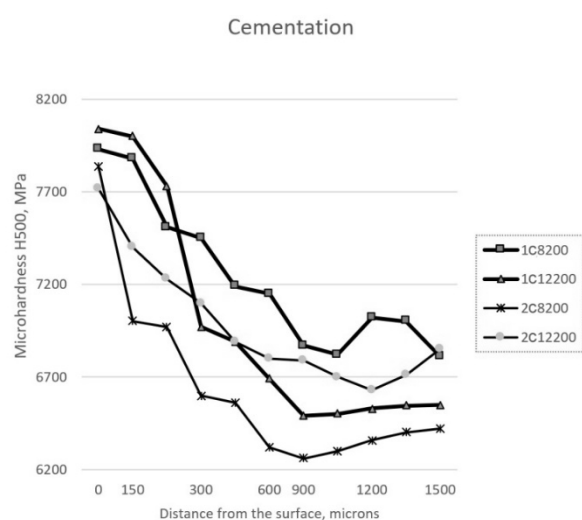

Fig. 2. *Distribution of microhardness over the cross section of carbonized layers of steel 5KHV2S after heat treatment*

4. Discussion

The results of the studies shown in Table 2 indicate a higher hardness of 5KHV2S steel samples after forging in a tool that implements alternating deformations in the metal, compared with samples after annealing. Such a difference is observed both on the initial samples and on the samples subjected to hardening heat treatment. At the same time, the hardness of the samples after forging, quenched with subsequent tempering at a temperature of 200°C and 500°C was 6.5 GPa and 5.1 GPa, respectively, and for the samples after annealing, subjected to heat treatment under the same conditions – 6.0 GPa and 4.2 GPa. As can be seen from Table 2 and the microhardness distribution graphs (Figure 1-2), such a difference in the hardness of samples after forging and annealing is observed after thermochemical treatment.

Analysis of microhardness distribution graphs over the cross-section of 5KHV2S nitrocemented steel layers (Figure 1) showed that changing the duration of nitrocementation from 6 to 8 hours does not significantly change the hardness of the surface and core. On the surface, this indicator reaches 8.2 GPa, in the core it reaches 6.5 GPa. It should be noted that an increase in the duration of nitrocementation to 8 hours was reflected in an increase in the overall thickness of the layer.

A study of the microhardness distribution of cemented layers of steel 5KHV2S after the final maintenance (Figure 2) showed that the surface microhardness tends to decrease, the maximum value of which is registered at the level of 8.0 GPa. The decrease in this parameter is due to the high content of the carbide phase in the hardened layer, reaching 50%. In addition, there is a phase based on γ-Fe. This ratio leads to a violation of the integrity of the martensitic matrix of layers, reducing their ability to resist the introduction of the indenter. As in the case of nitrocementation, the thickness of the carbonized layers increases with an increase in the saturation duration from 8 to 12 hours. The hardness of the core reaches 6.8 GPa.

5. Conclusion

A comparative analysis of the conducted studies of the hardness indicators of 5KHV2S steel samples subjected to combined thermomechanical processing in various modes showed that the developed technologies contributed to an increase in both total and surface hardness compared to samples not subjected to pre-forging in a new forging tool that implements alternating deformations in the metal, which in turn should have a positive effect on their operational properties. Studies have established that after nitrocementation with final heat treatment, the hardness on the surface reaches 8.2 GPa, in the core reaches 6.5 GPa. Cementation with final heat treatment provides a hardness of 8.0 GPa on the surface, and reaches 6.8 GPa in the core.

6. References

1 Арзамасов Б.Н. Конструкционные материалы: Справочник / Б.Н. Арзамасов. - Москва: Машиностроение, 1990. - 688 с.

2 Лежнев С.Н., Найзабеков А.Б., Панин Е.А., Куис Д.В. Эволюция микроструктуры стали 5ХВ2С при ковке поковок в бойках, реализующих знакопеременные деформации / IV Байкальский материаловедческий форум: материалы (1–7 июля 2022 года). - Улан-Удэ: Изд-во БНЦ СО РАН, 2022. – С. 528-529.

3 Lezhnev S., Naizabekov A., Kuis D., Stepankin I., Panin E., Tolkushkin A. Исследование влияния режимов комбинированной термомеханической обработки на микроструктуру экономнолегированной стали 5ХВ2С / Innovations: proceedings of IX International scientific congress (29 June 2023). – Varna: TU Sofia, 2023. – P. 68-71.

The highly dense titanium based metal matrix composites reinforced TiC densified by hot pressing

Stasiuk Oleksandr[1], Sienkiewicz Judyta[2], Serhii Taran[3], Vedel Dmytro[1], Oryshych Denys[1], Reshetnyk Oleg[1].
[1]G. V. Kurdyumov Institute for Metal Physics of the N.A.S. of Ukraine
[2]Institute of Armament Technology, Military University of Technology, Warsaw, Poland
[3]Interregional academy of personal management, Kyiv, Ukraine
E-mail: olek.stasiuk@gmail.com

Abstract: *Titanium–titanium boride (Ti/TiC) metal matrix composites have been widely identified as promising materials for various applications. The traditional ingot metallurgy processing strategies used to fabricate these materials are energy intensive and have fallen short of their perceived mass production potentials. Powder metallurgy processing of Ti/TiC composites from titanium and TiC powder blends, is currently widely used for the cost-efficient production of such composites. Additional processing by the method of hot pressing improves the structure and mechanical properties of this class of materials. The composites have the heterogenous microstructure with areas high hardness area over 1173 HV. While matrix and inclusions had the value of 700 HV.*
Keywords: TITANIUM HYDRIDE, MICROSTRUCTURE, POWDERS, MMC, HOT PRESSING

.

Introduction. Titanium alloys play a crucial role in modern aerospace, automotive, shipbuilding, and military technologies due to their high specific strength, fracture toughness, fatigue strength, corrosion resistance, non-magnetic properties, and other specialized physical-mechanical characteristics [1-3]. However, traditional titanium alloys, which are alloyed with various elements typically categorized as α- or β-phase stabilizers, often fall short in meeting the desired combination of physical and mechanical properties. For example, these alloys tend to have low wear resistance, susceptibility to fretting corrosion, and relatively low hardness [4,5]. These limitations can be addressed by developing titanium based Metal Matrix Composites (MMC) that incorporate fine hard particles such as carbides or borides [6, 7].

To eliminate the drawback mentioned above, it is necessary significantly (2 or more times) to increase the hardness of the titanium material. Among others, this will improve other properties, such as wear resistance.

Previously, in works [5-7] it was shown that employing synthesis the of mixtures of elemental powders allows to obtain a metal-matrix composite based on a Ti64 matrix reinforced with high-modulus TiC or TiB particles. Depending on the amount of the introduced hardening phase, such a material can have a hardness in a wide range from 600 to 1000 HV and even more.

However, residual pores, which number and size increases with increase of introduced into the initial powder mixture amount of TiC particles, significantly reduces standard mechanical properties, both strength and ductility. As it was shown in [8] application to sintered MMC's of hot isostatic pressure (HIP) allows reduce residual porosity to almost zero. Moreover, because of long-term high-temperature exposure under the loading of external forces inside the MMC strengthened by TiC diffusional processes between these particles and metallic matrix took place essentially changing initial phase composition and microstructure.

The hot-pressing (HP) method is widely used for densification of ceramic and metal-ceramic composite. The main advantage of HP is the obtaining the fully dense materials by applying pressure and temperature during sintering. Technology of hot pressing in air using graphite layers led to significantly decrease the price of the proses in comparison with other technologies (HP in vacuum or spark plasma sintering). Another advantage is the speed of densification, which allows the save fine microstructure. Preservation of the fine microstructure leads to an increase mechanical properties of metal matrix composites.

Materials and experimental procedure.

The basic component of the powders charge to prepare the test samples was titanium hydride with a fraction of −100 μm (Fig. 1a), whose hydrogen content and phase composition corresponded to single-phase titanium hydride (TiH_2) and titanium diboride powders (Fig. 1b). In choosing high-modulus compounds as reinforcement components for the composite, we were guided by our previous efforts that showed that TiC was an effective reinforcing addition that actively interacted with the titanium matrix at sintering temperatures to release monoboride particles.

The particle size of the starting powders was determined with a Malvern Mastersizer 2000 laser diffraction analyzer. Considering that the powder particles could coagulate, we measured their grain-size composition both in starting state and under ultrasonic vibrations. The starting titanium hydride powder mixtures that contained TiC were prepared in a drum mixer. The resultant mixture were subjected to double-action compaction at 650 MPa to make sampels. In selecting the sintering conditions, we considered our findings [7] on the sintering kinetics and structurization of the $TiH2 + TiB2$ powder mixtures. The compacts were sintered in vacuum at 1250ºC with an isothermal holding time of 4 h. The compacts were heated to the sintering temperature at a rate of 10ºC/min. The samples were cooled down in the furnace after isothermal holding. The density and porosity of the compacts and sinters were determined by hydrostatic weighing.
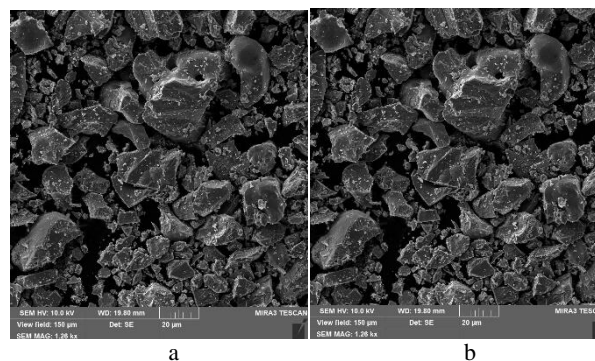

Fig.1 *Morphology of the starting titanium hydride (a) and titanium carbides (b) powders*

Samples were obtained by hot pressing without protective atmosphere at a pressure of 32 MPa in a temperature range of 1300−1500 °C under CO/CO2. The gas medium created by burning of the graphite fixture. In this apparatus, due to the CO → CO2+C reaction, efficient delivery of carbon throughout the porous volume and the reduction of oxides impurities on the surface of the sintering samples. The pre sintered composite were heated up to different temperatures using induction heating with a heat rate of 100 ◦C/min. An initial load of 7 MPa was applied until the peak temperature was achieved, and then the load was increased to 32 MPa. The dwell at the maximum temperature was 30 min, then the furnace was slowly cooled down (50 ◦C/min) to 1200 ◦C and further free cooling to room temperature to avoid crack formation.

Three-point flexural test were performed in compliance with ISO 12135 and ISO 12737 at room temperature employing an H5K-T produced by Hounsfield machine. The fracture patterns of the

samples after mechanical tests were examined by fractography and the fracture surfaces and microstructure were analyzed with a TESCAN VEGA 3 scanning electron microscope. The Vickers hardness was measured with a Wolpert hardness tester.

Results and discussion.

In our earlier studies [9], [10], we examined in detail the sintering behavior of MMCs, as well as the development of their final microstructure and properties.

As shown in Fig. 2a, pure titanium hydride exhibited a shrinkage of about 10% at 1200 °C. Under the same conditions, the Ti-6Al-4V alloy (Ti64) displayed nearly identical shrinkage of 9.5%. These shrinkage values indicate a high density of titanium-based materials produced via the hydride route.

The addition of TiC reinforcing particles to either titanium hydride or Ti64 significantly reduced shrinkage, limiting it to about 4–4.5% (Fig. 2a). This effect occurs because TiC particles—owing to their high melting point (3160 °C), thermal stability, and minimal interaction with the matrix—act as barriers to shrinkage. Consequently, composites containing 40 wt% TiC showed lower shrinkage (4.5–4%) compared to unreinforced materials (Fig. 2a).

Figure 2b presents the shrinkage behavior of composites with 40 wt% TiC during hot pressing at different temperatures. At 1300 °C, the shrinkage remained low ($\approx$ 5%) due to the high content of the reinforcing phase, which restricts full densification. In contrast, hot pressing at 1500 °C increased shrinkage to about 7.5%, resulting in very low residual porosity (~ 1%).

Titanium exhibits a nearly linear decrease in yield strength with increasing temperature, reaching about 50 MPa at 600–800 °C. Ti-6Al-4V, however, has a yield strength of only 12 MPa at 1050 °C. Titanium matrix composites, benefiting from reinforcing phases, demonstrate higher yield strength and improved mechanical performance. As a result, higher hot-pressing temperatures are required. At 1500 °C, the material attains high plasticity, enabling complete pore closure under relatively low pressures (up to 32 MPa).
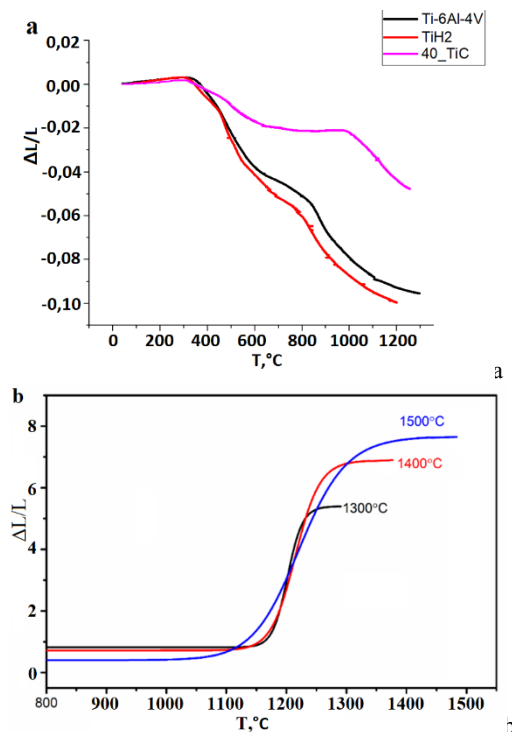

Fig. 2. Shrinkage of composite materials: a) during vacuum synthesis, b) during hot pressing

The microstructure of the titanium matrix composite Ti–40 wt.% TiC after sintering followed by hot pressing is shown in Fig. 3. For comparison, Fig. 4 presents the microstructure of a composite based on the Ti-6Al-4V (Ti64) alloy matrix containing the same amount of reinforcing phase (40 wt.% TiC).

As reported in our earlier work [10], both titanium and Ti64 alloy composites with 40 wt.% TiC exhibit porosity levels of about 14–16%. During hot deformation, the high ductility of the metallic matrix enables complete closure of pores within the rigid framework formed by the reinforcing particles.

Figure 3a illustrates the fine microstructure of a titanium-matrix composite with embedded titanium carbide inclusions. Figures 3b and 3c reveal titanium inclusions located within titanium carbide regions. This is attributed to the presence of titanium at the boundaries of carbide particles after sintering. However, hot pressing results in a fully dense composite.

Small tungsten-enriched particles were also detected in the titanium matrix (Fig. 3c,d). This occurs because industrial titanium carbide contains trace amounts of WC, introduced during the grinding stage after carbide synthesis. The content of such inclusions is below 1%, and they are primarily distributed in the titanium matrix near large clusters of titanium carbide particles.
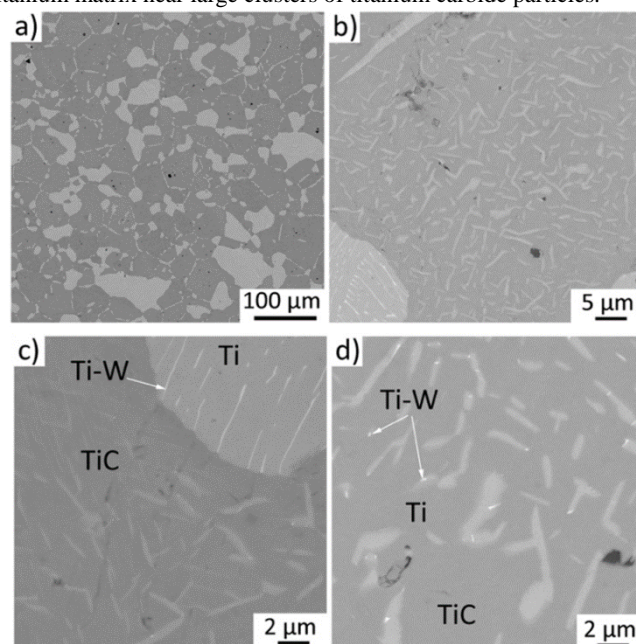

Fig.3. *Microstructure of Ti-TiC: a) general view, b) region with needle like thin inclusion of Ti, c) grain boundaries between Ti-TiC, d) region with perception of the Ti-W.*

Three distinct microstructural zones were identified in the Ti64–40 wt.% TiC composite after hot pressing. The first zone consists mainly of rounded carbide grains approximately 15 μm in size, with a 1–5 μm-thick Ti-based matrix phase present along their boundaries (Fig. 4b). The second zone is characterized by a Ti64 alloy matrix with a typical uniform lamellar α+β structure, containing TiC particles of about 10 μm (Fig. 4c). The third zone is composed predominantly of titanium carbide (Fig. 4d) and exhibits residual porosity of 3–4%, as the hot-pressing temperature of 1500 °C is insufficient to achieve full densification of pure titanium carbide. This carbide-rich region forms during hot pressing. The addition of 60Al–40V ligature powder to the Ti–TiC mixture promotes coagulation of carbide particles during powder mixing prior to sintering.

For Ti–TiC composites, segregation of pure titanium carbide was not detected. Nevertheless, chemical analysis of the carbide particles is presented in Fig. 5. This figure illustrates a gradual concentration transition at the phase boundaries.

Elemental diffusion after hot pressing was investigated for Ti64–TiC composites, as three distinct zones were identified. Under the combined effects of high temperature and applied pressure, titanium carbide partially transforms into Ti_2C—an equilibrium phase at elevated temperatures. In BSE micrographs, subtle tonal variations can be observed within the carbide zones from the center toward the

periphery, indicating chemical heterogeneity. Localized chemical analysis confirmed variations in carbon and titanium concentrations: the central porous zone consists of stoichiometric TiC, while the boundary regions adjacent to TiC contain a phase with reduced carbon content but enriched in titanium. This occurs because carbon diffuses from the carbide particles into the titanium matrix, leading to the formation of a new phase. As a result, the volume fraction of carbide inclusions in the composite increases.
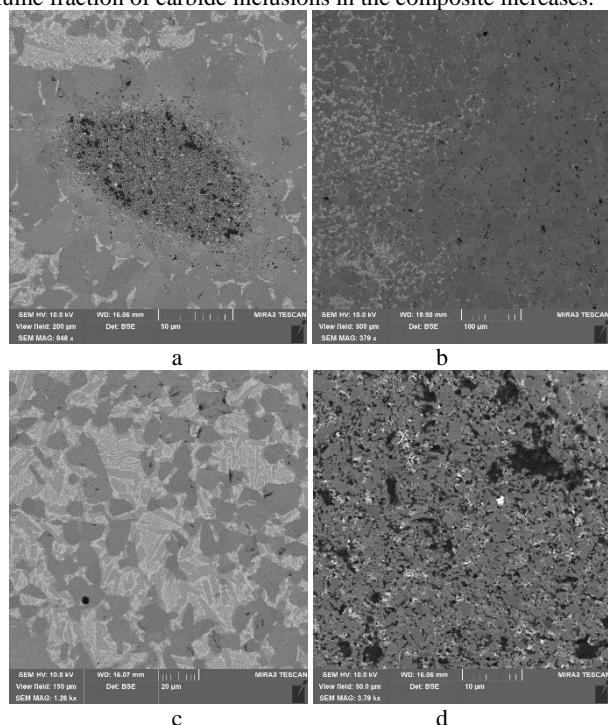

Fig.4. Microstructure of Ti64- 40 wt% TiC: a) general view, b) region with high amount of TiC, c) region with high amount of Ti64, d) region of carbide phase.
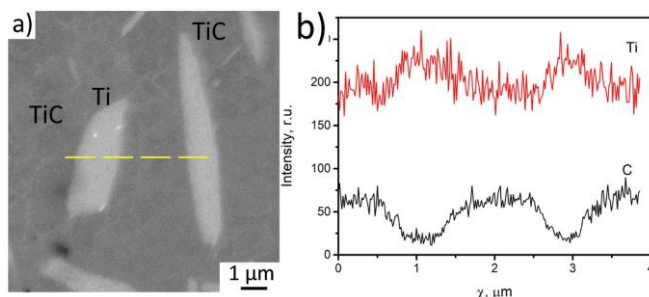

Fig.5. The microstructure of Ti-TiC after hot-presssing at 1500 °C (a) and distribution of chemical elements (b) though TiC-Ti-TiC-Ti particles yellow line in (a).

Results Figs. 4–5 show that the microstructure of the composite material is heterogeneous, resulting in variations in hardness across different zones. For the Ti–40 wt.% TiC composite, the hardness is approximately 715 HV in zones containing the matrix phase, 774 HV in carbide-rich areas where the matrix phase is present between grains, and 895 HV in regions composed entirely of carbide phases (Fig. 6).

In the Ti64–40 wt.% TiC composite, the hardness of the matrix phase containing a small fraction of carbide particles is comparable to that of the titanium-matrix composite. Zones with carbide particles separated by thin matrix layers at the boundaries exhibit hardness values around 860 HV (Fig. 6). Carbide-rich regions, which retain ~5 vol.% residual porosity and have partially depleted carbon content due to diffusion into the matrix, display hardness values of 1170 HV. Surrounding these porous clusters, carbon diffusion promotes the formation of in-situ carbide phases, resulting in the highest measured hardness of 1335 HV.
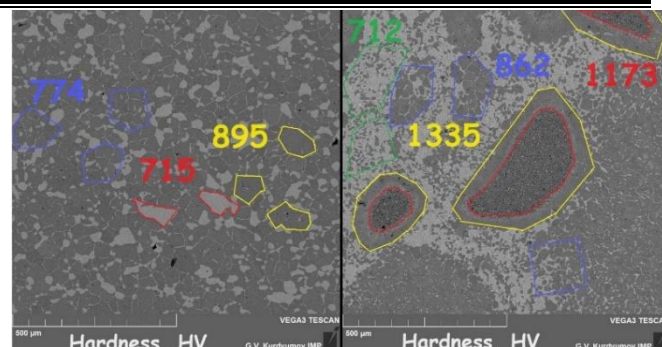

Fig.6. Hardness of Ti-40wt%TiC (a) and Ti64-40wt%TiC

Conclusions.

1. Ti and Ti64 composites reinforced with TiC, produced by sintering followed by hot pressing, develop a heterogeneous, multi-zone microstructure consisting of a matrix phase with fine TiC inclusions.

2. Hot pressing at 1500 °C significantly reduces porosity and provides high material hardness, which varies by zone: for Ti–TiC, hardness ranges from 715 to 895 HV; for Ti64–TiC, hardness reaches up to 1335 HV in zones with in situ formed carbides. The combination of high-temperature processing and TiC reinforcement ensures increased density and strengthening of the composites.

References.

1. J.S. Montgomery, M.G.H. Wells. Titanium armor applications in combat vehicles. JOM, 4 (2001), pp. 29-32

2. J. Fanning. Military application for β titanium alloys. J Mater Eng Perform, 14 (2005), pp. 686-690

3. Chao Cai et al. In-situ TiB/Ti-6Al-4V composites with a tailored architecture produced by hot isostatic pressing: microstructure evolution, enhanced tensile properties and strengthening mechanisms. Compos. B Eng. (2019)

4. Baglyuk, G.A. et al. The Effect of Charge Component Composition on the Structure and Properties of Titanium Matrix Sintered Composites with High-Modulus Compounds. Powder Metall Met Ceram 56, 45–52 (2017). https://doi.org/10.1007/s11106-017-9870-z

5. O.M. Ivasishin, et. al. Microstructure and properties of titanium-based materials promising for antiballistic protection. Progress in Physics of Metals. — 2019. — Vol. 20, No 2. — P. 285-309. DOI: https://doi.org/10.15407/ufm.20.02.285

6. Prikhodko, S.V., et. al.. Titanium Armor with Gradient Structure: Advanced Technology for Fabrication. In: Palestini, C. (eds) Advanced Technologies for Security Applications. NATO Science for Peace and Security Series B: Physics and Biophysics. Springer, Dordrecht. https://doi.org/10.1007/978-94-024-2021-0_13

7. P. E. Markovsky et al., "Mechanical Behavior of Titanium Based Metal Matrix Composites Reinforced with TiC or TiB Particles under Quasi-Static and High Strain-Rate Compression," Materials, vol. 14, no. 22, p. 6837, Nov. 2021, doi: 10.3390/ma14226837.

8. P. Markovsky et al., "Ballistic performance of titanium-based layered composites made using blended elemental powder metallurgy and hot isostatic pressing," Defence Technology, vol. 39, pp. 1–14, 2024, doi: https://doi.org/10.1016/j.dt.2024.04.002

9. Song, Y.; Dong, et al., Synthesis of Ti/TiB Composites via Hydrogen-Assisted Blended Elemental Powder Metallurgy. Front. Mater. 2020. https://doi.org/10.3389/fmats.2020.572005

10. Prikhodko, S.V., et al. Friction welding of conventional Ti-6Al-4V alloy with a Ti-6Al-4V based metal matrix composite reinforced by TiC. Weld World 65, 415–428 (2021). https://doi.org/10.1007/s40194-020-01025-8

Solid State Contact Interaction Between Metal Matrix Composite Based on Ti64 with the Composite Based on B_4C

Vedel Dmytro[1], Stasiuk Oleksandr[1], Sienkiewicz Judyta[2], Taran Serhii[3], Oryshych Denys[1], Osipov Anton[1], Reshetnyk Oleg[1]

[1] G. V. Kurdyumov Institute for Metal Physics of the N.A.S. of Ukraine
[2] Institute of Armament Technology, Military University of Technology, Warsaw, Poland
[3] Interregional academy of personal management, Kyiv, Ukraine
E-mail: vedelDV@gmail.com

Abstract: *The contact interaction between the metal matrix composite based on Ti64 and the B_4C-based composite was investigated. It is shown that the interaction process is influenced by the annealing temperature and holding time. The phase that formed independently of the contact pair is TiB. However, the thickness of the products formed at the boundary depends on the contact pair. In case of the Ti64-B_4C pair the thickness is 70 µm, while for (Ti64-40 wt% TiC)-B_4C it becomes 10 µm. This significant difference in the thickness is due to the presence of refractory particles (TiC) in (Ti64-40 wt% TiC)-B_4C couple, because the TiC phse reduce the diffusion of Ti into the contact zone.*
Keywords: CONTACT INTERACTION, METAL-MATRIX COMPOSITES, TITANIUM CARBIDE, TITANIUM BORIDE, MICROSTRUCTURE, BORON CARBIDE.

Introduction.

Titanium alloys are widely used in automotive, aerospace and advanced military applications because of their unique set of properties such as high specific weight, great strength and ductility, good corrosion resistance [1-2]. However, as technology evolves, homogeneous titanium materials may not always satisfy operating requirements. First of all, it is not possible to achieve a combination of high strength values without decreasing toughness and ductility of the material.

Boron carbide has a unique combination of high hardness (~32 GPa) and low density (2.5 g/cm^3) and attracts more and more attention every year. However, this material has one main disadvantages. It is the covalent type of chemical bond, resulting in a high melting point (2350°C, [3]) and a hot pressing (HP) temperature above 2100°C [4].The addition of the metal disiliside like $TiSi_2$, significantly decreases the temperature of densification to 1900°C [5]. On the other hand, the B_4C-$TiSi_2$ composite had the the highest mechanical properties than pure B_4C.

Our previous research [6] on the ***liquid phase*** interaction between Ti and B_4C showed multi-step mechanism of these reactions, which include solid state interaction with formation of TiB and TiC as well as further contact melting at the temperature close to the melting point of Ti. Because in the liquid phase interaction boron and carbon diffuse into titanium, and titanium does not diffuse into boron carbide, a weak and porous layer of TiB/TiC is formed.

The ***aim of this work*** was to investigate the contact interaction between MMC based on Ti and composite based on B_4C to find out the optimal regime for obtaining a dense and uniform connection between them

Materials and experimental procedure.

Hydrogenated titanium (TiH_2) powder (3.5 % H, wt.) and TiC was used as raw powder for obtaining MMC. The B_4C and $TiSi_2$ were used for fabrication ceramic composite.

Powder of hydrogenated titanium was blended with 60%Al-40%V master alloy powder (particles size < 63 µm) to form blend of total Ti-6Al-4V composition. Whenever inclusions of the second phase, such as TiC were needed to form MMC their powders were added at required amounts to the blends and mixed before the pressing. TiC powder with the size 1-30 µm was used to make MMC 40 % (vol.) of reinforcement particles. A smaller size samples, disk with dimension 40 mm and thickness 5 mm , at 150 and 640 MPa. Sintering of Ti-6Al-4V and Ti-6Al-4V-40% TiC was conducted in vacuum furnace (1250℃, 4h) followed by the slow furnace cooling. That provided dehydrogenation of titanium and formation of the bulk samples.

Powders of boron carbide were mixed with 30 vol. % $TiSi_2$ in a planetary mill in an acetone medium, using grinding beds with B_4C–20 vol % TiB_2. Disks with a diameter of 40 mm and a thickness of 6 mm were hot-pressed in a graphite mold, which was previously coated with boron nitride. Hot pressing was carried out

at temperature 1900℃, pressure 32 MPa with holding time 30 min. After hot pressing, the materials were ground, polished, and finally treated with a diamond suspension with a grain size of ~1 µm.

The well-polished disk of MMC composite on the one side and B_4C composite with the other side, placed in the graphite die and heat to the temperature of 1500℃, under a pressure 32 MPa with holding time 15 min. The addition pressure was applied to create a strong contact between MMC and B_4C composite.

Microstructure of the samples was studies by scanning electron microscopy (SEM). Scanning electron microscopy was performed on VEGA 3 (Tescan). Local chemical compositions were determined by Energy-dispersive X-ray (EDX) spectroscopy with Oxford Instruments (UK) or Bruker (Germany) analyzers. Phase content was determined by areal analysis using image analysis software ImageJ. The grain size was estimated by the line intercept method, the data reported for each phase are the average of at least 100–150 grains using ImageJ software.

Results and discussion.

The microstructure of the as sintered materials are shown on the Fig.1. The Ti-6Al-4V had a homogeneous microstructure, Fig. 1 a. The addition of TiC into Ti-6Al-4V led to the formation of large particles TiC while the size of α-Ti and β-Ti remained unchanged, Fig. 1 b.
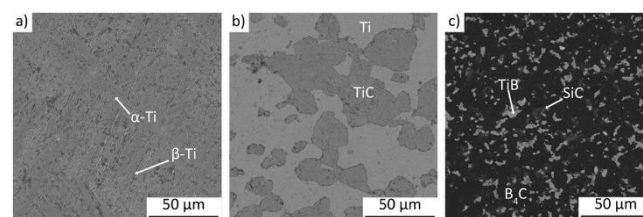

Fig.1. The microstructure of the initial materials: Ti-6Al-4V (a) and Ti-6Al-4V-40 vol% TiC (b) and B_4C-30 vol% $TiSi_2$ (c)

The microstructure of the hot pressed B_4C-30 vol% $TiSi_2$ are shown on the Fig. 1 c. As a result of the *in-situ* reaction between B_4C and $TiSi_2$, a final composite is formed with following phase composition: TiB, SiC and B_4C, Fig. 1 c. The introduction of an activating additive in B_4C is necessary, because the pure B_4C has a density of no more than 80% even at a temperature of hot pressing is 2100℃.

The cross section of the B_4C-30 vol% $TiSi_2$/ Ti-6Al-4V couple after annealing at 1500℃ shown on the Fig.2.
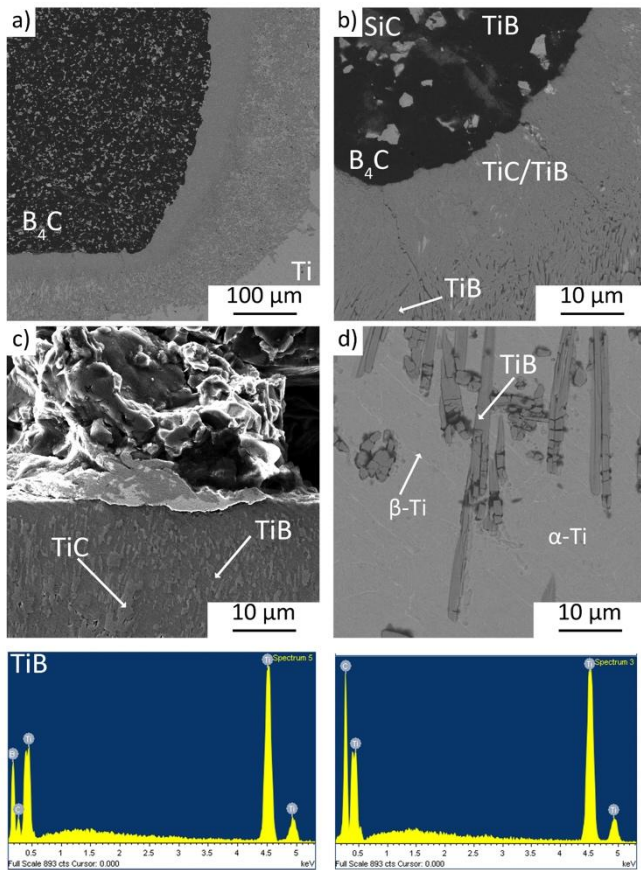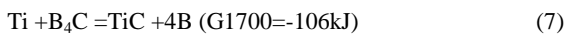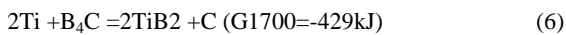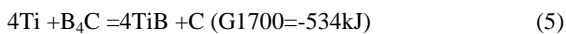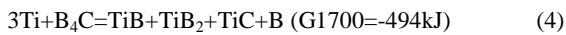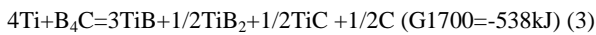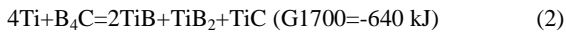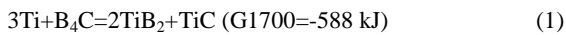
Fig.2. The cross section of the B_4C-30 vol% $TiSi_2$/ Ti-6Al-4V couple after annealing at 1500^oC for 15 min: general view (a), general view at high magnification (b), microstructure at the grain boundary between B_4C-30 vol% $TiSi_2$/ Ti-6Al-4V (c), microstructure at the boundary between formed products and Ti-6Al-4V

The contact zone can be divided into several sections: first section is B_4C composite (Fig. 2 a), second section is the dense layer consisted from TiC and TiB phase (Fig. 2 b ,c), the third section of the TiB needle and α-Ti and β-Ti phase (Fig. 2 d), the last section is pure α-Ti and β-Ti. The thickness of the second section is 20-30 μm and has cracks. The crack was formed due to the mismatch between the ceramics and newly formed brittle region. The third section had the thickness of 100 μm and consisted from needle like crystal without trace of TiC.

These phases in section 2 and 3 were formed as a result of solid-phase interaction:

$$3Ti+B_4C=2TiB_2+TiC \text{ (G1700=-588 kJ)} \quad (1)$$

$$4Ti+B_4C=2TiB+TiB_2+TiC \text{ (G1700=-640 kJ)} \quad (2)$$

$$4Ti+B_4C=3TiB+1/2TiB_2+1/2TiC +1/2C \text{ (G1700=-538kJ)} \quad (3)$$

$$3Ti+B_4C=TiB+TiB_2+TiC+B \text{ (G1700=-494kJ)} \quad (4)$$

$$4Ti +B_4C =4TiB +C \text{ (G1700=-534kJ)} \quad (5)$$

$$2Ti +B_4C =2TiB2 +C \text{ (G1700=-429kJ)} \quad (6)$$

$$Ti +B_4C =TiC +4B \text{ (G1700=-106kJ)} \quad (7)$$

According to calculations, the most probable formation of titanium boride among all possible phases is, then titanium diboride and finally titanium carbide. Thus, at the initial stages, titanium boride is formed first as the most stable phase

The C has a lower diffusion coefficient than B and firstly formed TiC at the interaction region, Fig. 2 c. It should be noted that Yang [7] and Liang [8] using the differential thermal analysis in Ti-B_4C system observed exothermic effect with maximum at ~1093∘C. Therefore, the temperature of formation of TiC and TiB by contact interaction between B_4C and Ti are very close. Appreciably at the same time B react and formed TiB needle crystal. Since the amount of boron in boron carbide is 4 times higher than carbon, the number of needle like crystals is also significantly higher.

The cross section of the B_4C-30 vol% $TiSi_2$/ Ti-6Al-4V-40 vol%TiC couple after annealing at 1500^oC shown on the Fig.3.Only a few zones can be observed. The first zone is adjacent to the boron carbide and consists of dense TiB layer. The thickness of this zone is 5 μm. Below this zone there is a thick layer of TiC. The thickness of this layer is 20 μm. It should be noted that TiC will play a role of a barrier.
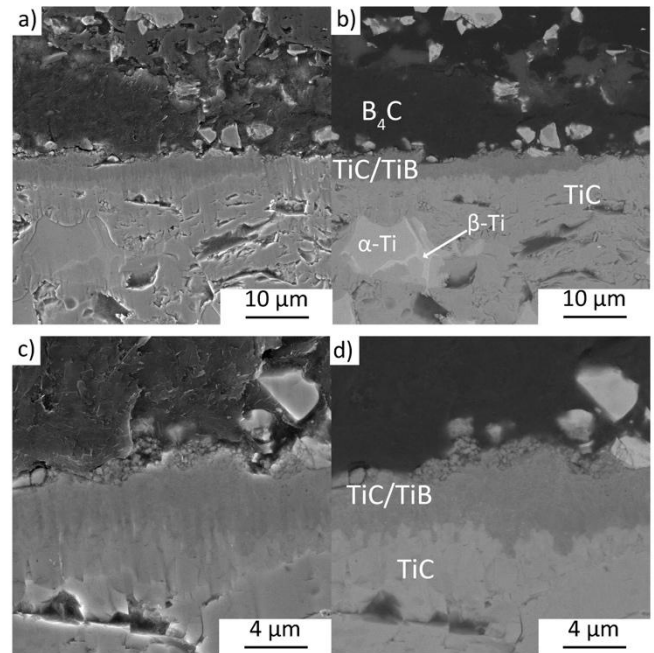

Fig.3. The cross section of the B_4C-30 vol% $TiSi_2$/ Ti-6Al-4V-40 vol%TiC couple after annealing at 1500^oC for 15 min: general view (a,b), microstructure at the grain boundary between B_4C-30 vol% $TiSi_2$/ Ti-6Al-4V-40 vol%TiC (b,c); a,c-SE;b,d-BSE mode

Because the diffusion of B to TiC is significantly low as well as self-diffusion of C intro TiC. On the other hand, the reaction between B4C and TiC is not favorable, because the Gibbs free energy is +100 kJ/mol:

$$B_4C + 4TiC = 4TiB + 5C \quad (8)$$

The formation of a layer at the grain boundary between two materials by formation the new and danse phases increases the adhesion between them. Good adhesion between B_4C and TiC brings several critical advantages, especially when they are used together in composite materials or multilayer structures. These advantages impact the mechanical, thermal, and chemical behavior of the material.

Conclusions

• During the interaction of B_4C-30 vol% $TiSi_2$/ Ti-6Al-4V, a two-stage interaction zone is formed. The total thickness of the interaction products becomes more than 150 μm. The first layer is two-phase and consists of TiB and TiC. The other layer consists of needle-like crystals of TiB that permeate the Ti matrix.

• Addition of TiC to Ti-6Al-4V significantly reduces the thickness of the interaction region to 20 μm by reducing the diffusion of B and C into the interaction region.

• The formation of layers at the boundaries between composites by co-annealing can be used to obtain layered materials.

References.

1. A.P. Mouritz. Metal matrix, fibre–metal and ceramic matrix composites for aerospace applications, in: Introduction to Aerospace Materials, Woodhead Publishing, 2012: pp. 394–410. https://doi.org/https://doi.org/10.1533/9780857095152.394..

2. M.D. Hayat, H. Singh, Z. He, P. Cao, Titanium metal matrix composites: an overview, Compos. Part A Appl. Sci. Manuf. 121 (2019) 418–438, https://doi.org/10.1016/j.compositesa.2019.04.005.

3. Domnich, V., Reynaud, S., Haber, R.A., and Chhowalla, M., Boron carbide: structure, properties, and stability under stress, J. Am. Cer. Soc., 2011, vol. 94, pp. 3605–3628.

4. Zhang, W., Yamashita, S., and Kita, H., Progress in pressureless sintering of boron carbide ceramics—A review, Adv. Appl. Ceram., 2019, vol. 118, pp. 222–239.

5. Mazur, P.V., Grigoriev, O.M., Melakh, L.M. et al. Effect of B3Si on the Structure and Properties of B4C Ceramics. J. Superhard Mater. 45, 175–185 (2023). https://doi.org/10.3103/S1063457623030176

6. Dmytro Vedel, Oleksandr Stasiuk, Dmytro Kovalchuk, Dmytro Savvakin, Vasyl Tkachuk, Serhii Akhonin, Serhiy Schwab, Pavlo Markovsky Formation of the gradient metal matrix Ti-TiB-TiC composite by 3D-printing with coaxial electron-beam technology and cored wire Journal of Alloys and Compounds 2025/4/24 https://doi.org/10.1016/j.jallcom.2025.180617

7. Y.F. Yang, H.Y. Wang, Y.H. Liang, R.Y. Zhao, Q.C. Jiang, Effect of nickel addition on the exothermic reaction of titanium and boron carbide, J. Mater. Res. 22 (2007) 169–174, https://doi.org/10.1557/jmr.2007.0010.

8. Y.H. Liang, H.Y. Wang, Y.F. Yang, Y.L. Du, Q.C. Jiang, Reaction path of the synthesis of TiC–TiB2 in Cu–Ti–B4C system, Int. J. Refract Met. Hard Mater. 26 (2008) 383–388, https://doi.org/10.1016/j.ijrmhm.2007.09.002.

Effect of titanium addition on the microstructure of precipitation-hardened martensitic stainless steel

Onici Adrian-Emanuel[1]., Geantă Victor[1]., Ştefănoiu Radu[1]., Voiculescu Ionelia[2].
[1]National University of Science and Technology Politehnica Bucharest, Faculty of Materials Science and Technology, Bucharest, Romania
[2]National University of Science and Technology Politehnica Bucharest, Faculty of Industrial Technology and Robotics, Bucharest, Romania
E-mail: onici.adrian@yahoo.ro, victorgeanta@yahoo.com, radustefanoiu@yahoo.com, ioneliav@yahoo.co.uk

Abstract: *The work aimed to evaluate the effect of microalloying titanium in proportions of 1 to 5 wt.% on the microstructure and microhardness of a precipitation-hardenable martensitic stainless steel. The standard chemical composition of martensitic steel 17-4PH was used, to which 1; 2; 3; 4 and 5 wt.% Ti was added, respectively. Microstructural analyses revealed changes in the crystal grains and precipitation effects from the solid solution of the alloy. Microhardness measurements were also performed, which demonstrated that with increasing Ti content in the alloy the metallic matrix becomes harder. The study confirms that microalloying with Ti is beneficial for the development of martensitic stainless steels to increase mechanical properties, even without the application of subsequent heat treatments. The results obtained in this work represent a starting point for the development of new customized alloy recipes, adapted to specific applications, where a high value of hardness, as well as microstructural stability or wear resistance are required.*
KEYWORDS: MARTENSITIC STEEL, MICROALLOYING, TITANIUM, MICROSTRUCTURE, MICROHARDNESS

1. Introduction

Martensitic stainless steels are mainly used for applications requiring high mechanical strength (hardness, wear) at high temperatures, such as machine parts, cutting edges, hot working tools, etc [1]. The chromium content in these steels is lower than in other grades of stainless steel, its value being at the lower acceptable limit [2-4]. Martensitic PH (Precipitation Hardening) steels are currently the most commonly used in this class. To obtain the mechanical properties, it starts with a solution treatment at a high temperature, followed by rapid cooling to ambient temperature, after which a consolidation is achieved by aging the martensite through successive reheatings [5-7]. At ambient temperature, the microstructure of these steels may contain a few percent of residual δ ferrite (up to 5%), in equilibrium with martensite, as well as small amounts of residual austenite, depending on the thermal regime applied [8]. Hardening is achieved by the precipitation of intermetallic compounds of the Ni_3Cu type [9], obtaining a tensile strength of over 1400 MPa. At the same time, the increase in mechanical characteristics by 500 MPa can occur through the appearance of Ni(Al), Ni(Ti,Al) type phases during annealing in the temperature range 400÷620°C. The tensile strength can reach values between 1200 and 1400 MPa [10] and the tensile energy KV at -30°C is over 30J.

Aging treatment at 460–490 °C allows for simultaneous increases in strength and ductility [10]. However, sensitization of PH steels can occur during aging due to the formation of $M_{23}C_6$ carbides or ε and Z phases, even for very short aging periods (15 minutes for 600 °C) [8]. As a carbide former, Ti can play an important role in increasing the hardness characteristics of steel. Titanium is used as a microalloying element in high-alloy steels, and in precipitation-hardened steels its content is usually limited to 1% by weight [11]. Alloying with Ti generates a complex microstructure, which contains a wide variety of intermetallic compounds. Chao Zhang et al. [12] demonstrated that Ni favors the formation of Ni_3Ti precipitates in the martensitic matrix. Following aging treatments performed at temperatures between 300 and 500 °C, it was observed that these precipitates prevent the transformation of residual austenite and thus contribute to the reduction of toughness. Micro-alloying with titanium can reduce the proportion of residual austenite, because it favors the martensitic transformation upon cooling, which contributes to increasing the dimensional stability in service. Research has shown that titanium can have an indirect positive effect in high-alloy martensitic steels, by fixing carbon and nitrogen in intermetallic compounds with high melting temperatures and stabilizing the passive layer [13,14].
The paper presents the effects of alloying with 1wt.% to 5wt.%Ti on the microstructure and microhardness of martensitic stainless steel 17-4PH. It was found that by increasing the Ti content, a significant increase in hardness is obtained from 333HV for 1wt.%Ti to about 485HV in the case of alloying with 5wt.%Ti. At the same time, it was observed that microalloying with titanium allowed the average grain size to be reduced by about 50%.

2. Materials and methods
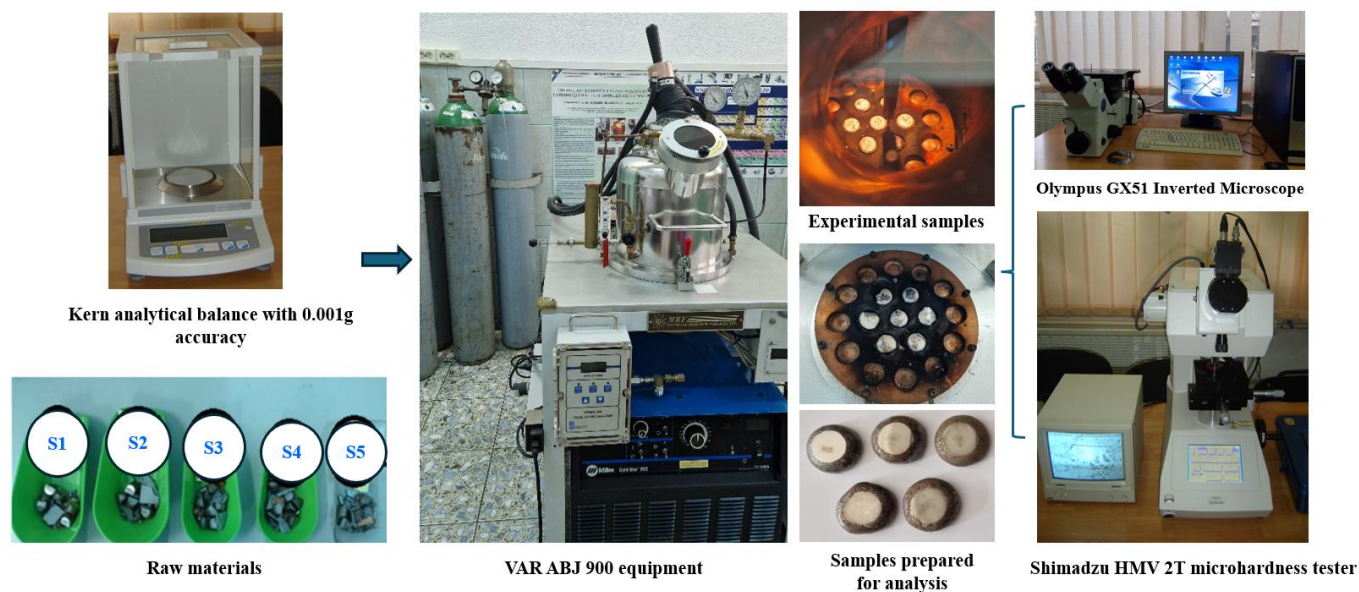
2.1. Materials

To obtain the experimental samples, the standard chemical composition of martensitic steel 17-4PH was used, to which 1; 2; 3; 4 and 5 wt.% Ti was added, respectively. The chemical composition of each experimental steel sample was measured using a SpectroMaxx optical emission spectrometer in the ERAMET laboratory, as well as a BRUKER X-ray fluorescence (XRF) spectrometer. The melting efficiency and the degree of alloy homogenization were evaluated. The chemical compositions of designed martensitic steels are presented in table 1 Even though exact concentrations for Ti were not obtained, their values are progressively increasing.

2.2. Methods

The experimental configuration, comprising the main equipment used, is presented in Figure 1. Experimental alloys were obtained in VAR ABJ 900 equipment, by electric arc melting under argon flow, using a high-purity granular raw material (over 98 wt.%). The alloy ingots were homogenized by melting 5 times on each side, on the copper plate of the equipment forcedly cooled with water. After melting, samples were taken and subjected to the metallographic preparation procedure, using IsoMet 4000 precision cutting machine. Samples were wet ground with SiC abrasive paper with increasing grit sizes (400/600/800/1200/2400 grit size), then were polished with 3 μm and 0.8 μm abrasive alumina powders in suspension. The polished surfaces were etched using Kalling's solution, according to Standard Practice for micro etching metals and alloys [15]. Microstructural analyses have been performed by optical microscopy using an Olympus GX51 inverted microscope, equipped with software for processing images AnalySIS. Microhardness measurements were performed using a Shimadzu HMV 2T microhardness tester, according to ISO 6507-1:2018 [16]. Five successive measurements were performed for each sample, with a force value of 1.96N and an indentation time of 10 sec, according to ISO 6507-1:2018.

Table 1. Chemical composition (XRF method) of experimental Ti-alloyed martensitic steel.

Sample code	C	Cr	Ni	Cu	Mn	Si	Nb	Ta	Ti	Al	V	S	P	Fe
S1		16.65	3.796	3.80	0.91	0.26	0.06	0.12	1.07	0.20	0.16	0.03	0.04	
S2		15.35	4.33	4.35	1.07	0.4	0.11	0.15	1.77	0.24	0.22	0.05	0.05	
S3	0.07	14.72	4.10	4.32	0.97	0.43	0.13	0.23	3.16	0.25	0.24	0.05	0.05	Balance
S4		14.66	4.25	4.40	1.02	0.51	0.20	0.22	3.52	0.30	0.24	0.06	0.05	
S5		14.32	4.07	4.33	1.06	0.41	0.22	0.27	4.15	0.33	0.27	0.05	0.06	

Kern analytical balance with 0.001g accuracy

Raw materials

VAR ABJ 900 equipment

Experimental samples

Samples prepared for analysis

Olympus GX51 Inverted Microscope

Shimadzu HMV 2T microhardness tester

Fig. 1. Experimental setup for obtaining and characterizing the new martensitic steel 17-4PH micro-alloyed with Ti.

3. Results and disscusion

3.1. Microstructure

The microstructure of experimental martensitic steels was analysed by optical microscopy. The morphology of the martensitic phase was analyzed at different magnifications, to identify the inclusions and intermetallic phases, and the grain refining effects were evaluated by measuring the average grain diameter. The Kalling's reagent used for etching enabled the contrast enhancement between intermetallic phases and the clear delineation of grain boundaries (figure 2).

The microstructure of sample S1 (1% Ti) shows a dendritic appearance typical of cast alloys, containing mostly martensite and ferrite. Small amounts of acicular austenite are also present on the boundaries of the martensite grains. At higher magnifications (1000x) minor intergranular segregations and larger polyhedral precipitates (approximately 10 microns) of the Ni_3Cu type are visible. The titanium is mostly dissolved in the matrix, and small amounts are found in the form of intermetallic compounds located unevenly, either intergranularly or in the body of the grains.

The microstructure of sample S2 contains predominantly martensite and small amounts of ferrite. The increase in Ti concentration caused the disappearance of residual austenite from the metallic matrix of sample S2 (1.77% Ti). This is due to the stabilizing effect of titanium for ferrite in high-alloyed Cr steels. As in sample S1, small intermetallic precipitates (below 1

micron) are present, dispersed intra-granularly or arranged along the grain boundaries. Polyhedral Ni_3Cu precipitates are also observed, placed in the dendritic-looking grains.

Sample S3 (3% Ti) contains martensite and ferrite, in which the average grain diameter is clearly refined (average 140 microns) compared to the previous samples. The dendritic aspect is much better evident in this case. The effects of internal nucleation of intermetallic compounds, with various shapes (small rounded or elongated formations), located either on the grain boundaries or intra-granularly, are observed. Ti_3Cu-type compounds with polyhedral shapes are also visible.

Sample S4 (3.5% Ti) also contains a mixture of martensite and ferrite, with a distinct intergranular network of intermetallic phases. The structure is dendritic, with the dendrites clearly oriented in the cooling directions. In this case, conglomerates of intermetallic compounds with a well-defined polyhedral appearance are observed, with dimensions of about 30 microns. At the same time, Ni_3Cu-type compounds are visible, with dimensions of about 5 microns, placed either in the grain body or on their boundaries.

The microstructure of sample S5 (4% Ti) has a similar appearance to sample 4, containing a homogeneous mixture of martensite and ferrite. The granular structure is finer and more distinctly defined.

A high density of fine precipitates placed inside the grains, and intermetallic compounds (Ni_3Cu) with a tendency to coalescence, located predominantly on the grain boundaries, are observed.
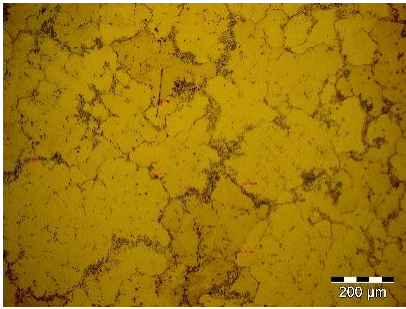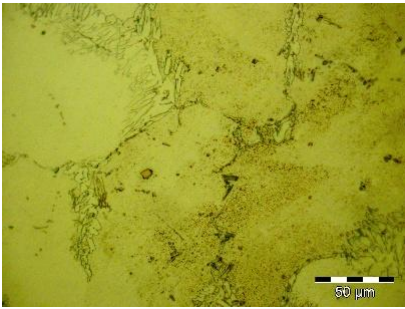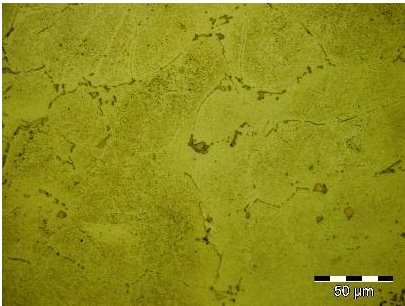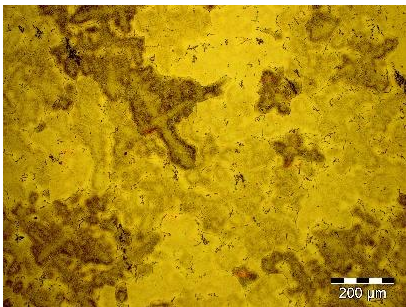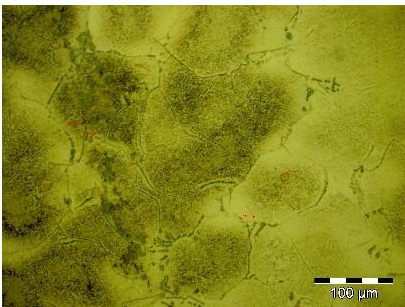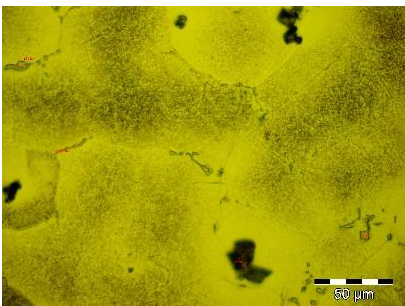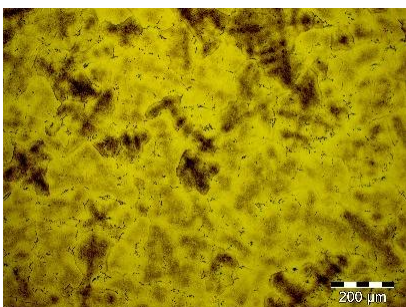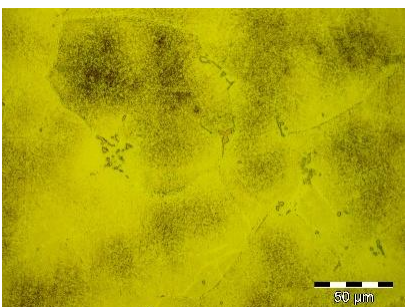
Sample code	Optical microstructure, 200x	Optical microstructure, 1000x	Grain boundary average diameter, µm
Sample S1			300
Sample S2			195
Sample S3			140
Sample S4			110
Sample S5			120

Fig. 2. *Optical microstructure of experimental martensitic steels alloyed with Ti at different magnifications.*

3.4. Microhardness

To assess the microhardness of the samples, Vickers microhardness measurements ($HV_{0.2}$) were performed. Each sample was tested in five distinct areas, and the results are presented in figure 3. The measured hardness ranged from 333.4 $HV_{0.2}$ (S1) to 485.4 $HV_{0.2}$ (S5), indicates a significant increase in hardness with increasing in titanium content (figure 3).
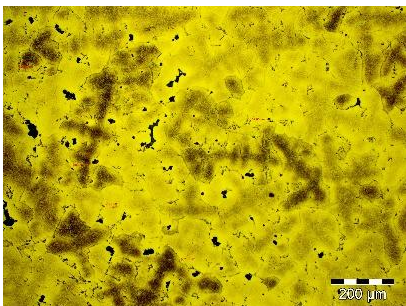
The results indicate that samples with higher Ti content (S3, S4 and S5) exhibit both an increased average hardness and a slight increase in the dispersion of the hardness value. This suggests a combined influence of titanium and microalloying elements present in the metal matrix of the high-alloy martensitic steel (Nb, Ta, V) on the material strengthening and structural homogeneity.
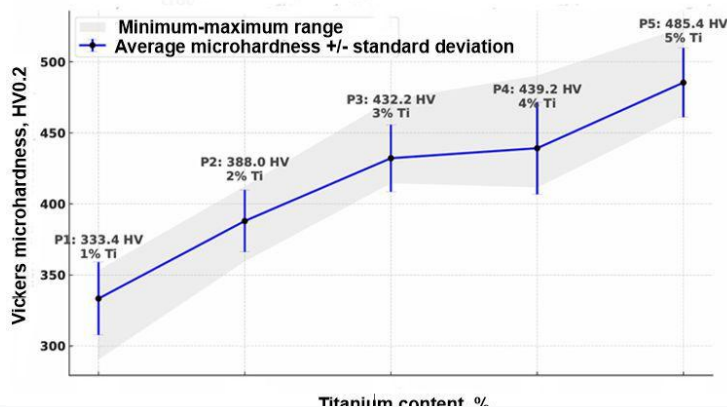

Fig. 3. *Evolution of Vickers microhardness HV0.2 of 17-4PH steel depending on the added titanium content.*

4. Conclusions

Titanium microalloying significantly influenced the microstructural characteristics and hardness properties of 17-4PH steel. The presence of titanium determined the grain refinement and precipitation of some intermetallic compounds, Ni3Cu type, which contributed to the quenching effect upon cooling of the cast samples. Vickers microhardness measurements (HV0.2) revealed an increasing trend with increasing titanium content. Thus, the average hardness values increased from approximately 333 HV0.2 for the sample with 1% Ti (S1) to approximately 485 HV0.2 for the sample with 5% Ti (S5). This result demonstrates the efficiency of the dispersed precipitation strengthening mechanism associated with the formation of hard phases of Ti3Cu, TiC and TiN. Due to its high affinity for carbon and nitrogen, titanium contributes to the formation of stable interstitial compounds, which act as nucleation centers for precipitates and inhibit the movement of dislocations, thus increasing the rigidity and resistance to plastic deformation of the alloy.

5. References

[1] Geanta V., T. Chereches, P. Lixandru, Voiculescu, I., R. Stefanoiu, D. Dragnea, T. Zecheru, L. Matache, Virtual Testing of Composite Structures Made of High Entropy Alloys and Steel, *Metals* 2017, Vol.7, Issue 11, art. Nr. 496.

[2] Davis, J.R. Stainless Steels, ASM International, 1994.

[3] Geantă, V., Ștefănoiu, R., Voiculescu, I., Daisa, D.D., The influence of the technological parameters on the efficiency of the metal melts alloying process by pulverulent material injection, Journal of Optoelectronics and Advanced Materials, vol. 13, No. 7-8, July 2011, p. 921 – 925.

[4] Ghosh, R.N. Microalloying of Steels, Springer, 2012.

[5] Lippold, J.C., Kotecki, D.J. Welding Metallurgy of Stainless Steels, Wiley, 2005.

[6] Vander Voort, G.F. Metallography: Principles and Practice, ASM, 1999.

[7] Totten, G.E. Steel Heat Treatment Handbook, CRC Press, 2006.

[8] Kauss, N., Halle, T. and Rosemann, P., Age-hardening behavior, microstructure and corrosion resistance of the copper alloyed stainless steel 1.4542, WTK 2018, IOP Conf. Series: Materials Science and Engineering 373 (2018) 012020 doi:10.1088/1757-899X/373/1/012020.

[9] Hsiao, C. N., Chiou, C. S. and Yang, J. R. Aging reactions in a 17-4 PH stainless steel, Materials Chemistry and Physics 2002, 74, p.134-142

[10] Chae, H.; Lim, S.; Lee, T.; Shin, E.; Suh, J.; Kang, S.H.; Lee, S.Y. Optimization of Aging Temperature and Heat-Treatment Pathways in Additively Manufactured 17-4PH Stainless Steel. *Materials* **2023**, *16*, 7557. https://doi.org/10.3390/ma16247557

[11] Cui, P., Xing, G., Nong, Z., Chen, L., Lai, Z, Liu, Y., Zhu, J., Recent Advances on Composition-Microstructure-Properties Relationships of Precipitation Hardening Stainless Steel, Materials (Basel) 2022 Nov 27;15(23):8443. doi: 10.3390/ma15238443

[12] Zhang, C.; Wang, C.; Wang, A.; Zheng, C.B.; Liu, Z.B.; Liang, J.X.; Su, J.; Ge, Q.L. Effect of Aging on Transformation Behavior of Reverted Austenite and Toughness in Co-Free Maraging Stainless Steel. J. Mater. Eng. Perform. 2022, 31 (9) p.1–14. doi: 10.1007/s11665-022-07018-6

[13] Park, J.H., Kang, Y., Inclusions in Stainless Steels − A Review, Steel Research International, 2017, **https://doi.org/10.1002/srin.201700130**

[14] ASTM A564/A564M-13a. Standard Specification for Age-Hardening Stainless-Steel Bars and Shapes.

[15] ASTM E407-07. Standard Practice for Micro etching Metals and Alloys.

[16] ISO 6507-1:2018. Metallic Materials – Vickers Hardness Test – Part

Relationship between mechanical parameters of shear and tensile strength of polymer materials obtained by FDM extrusion of objects

Miglena Paneva
Bulgarian Academy of Science, IICT, Sofia, Bulgaria
m.paneva7@gmail.com

Abstract: *This work examines the relationship between two of the most important mechanical parameters: shear and tensile strength in 3D printed polymer test specimens using Fused Deposition Modeling. Different types of materials were used, including those that are mechanically strong, easy to print, flexible, and heat-resistant, to determine their behavior. The study was conducted by testing test specimens printed with the same characteristics of percentage filling and pattern, layer height, and printing direction. The ratio between the shear strength and tensile strength of seven polymer materials with 30 % infill in percent was calculated. The values were compared with those of metals and polymers with 100 % density, and an estimate of the coefficient between the two parameters was made.*

Keywords: 3D PRINTING, POLYMER, SHEAR STRENGH, TENSILE STRENGH, RELATIONSHIP, DENSITY

1. Introduction

A widely used technology for manufacturing objects is Fused Deposition Modeling (FDM) in 3D printing. FDM extrusion, also known as Fused Filament Fabrication (FFF), is a material extrusion additive manufacturing process where a thermoplastic filament is heated and extruded through a nozzle to build a 3D object layer by layer [1, 2]. It is applicable in various industries such as product development, mechanical engineering, biomedical innovation, construction, etc. The most usable materials are polymers. Polymeric materials vary widely depending on their composition, ranging from extra soft to extra hard, and accordingly, their properties vary from tough and elastic to brittle, as seen in Polylactic acid, Polyethylene, Polypropylene, FilaFlex, and Polycarbonate, among others [3, 4]. In addition to the composition of the polymer materials, the characteristics and environment of printing are also of particular importance [5, 6]. Unlike steel, aluminum, and other metals, whose structure is 100 % dense, 3D printing allows for a variety of filling options. The filling percentage can be from 0 to 100% and the filling can have a different structure, which affects the strength of the object [7]. Materials testing is of particular importance for its knowledge and application. Ultimate Tensile Strength (UST) is the maximum amount of tensile (pulling) stress that a material can withstand before failure. It is typically measured in units like megapascals (MPa) [8, 9].

Tensile properties of a material indicate how it will react to forces applied to it in tension. Some materials break when a great deal of force is applied to them, while others get elongated or physically deformed in some other way. Materials that break very sharply are said to undergo a 'brittle failure'. Tensile strength is the load-bearing capacity of any object before permanent damage (brittle material) or permanent deformation (plastic material). Ultimate Shear Strength (USS) is the maximum shear stress that a material can withstand before failure. Shear stress occurs when forces are applied parallel to the surface of a material. The main difference between shear force and tensile force is that tensile force refers to cases where a deforming force is applied at right angles to a surface, whereas shear force refers to cases where a deforming force is applied parallel to a surface. The relationship between shear strength and tensile strength in metal and polymer materials is an important aspect of their mechanical properties [10]. The relations can vary significantly depending on the composition of the polymer and the presence of additives. Due to their wide range of properties, both synthetic and natural polymers play a crucial role in everyday life and the production of various parts. For plastic materials such as metals, numerous studies have been conducted in this direction, and a ratio of 60 % between shear strength and tensile strength has been established [11].

The aim of this work is to analyze the relationship between shear strength and tensile strength in metals and polymers with a dense structure and to analyze the coefficient between them. Additionally, an analysis of shear strength and tensile strength will be conducted for polymer test bodies produced by FDM printing with a 30% infill. The obtained coefficient of the studied materials will be compared with that at 100% density.

2. Analysis of the relationship between shear strength and tensile strength in metals and polymers

An analysis of literature sources has been made on the relationship between shear strength and tensile strength for various metals and polymers.

Data for aluminum alloys are taken from a basic survey, and the results show a numerical ratio USS/UST of approximately 0.60 ± 5.5 % [12]. It has been shown that in blanking or punching operations, the ultimate shear strength of an aluminum sheet can be calculated from equation (1) with an accuracy of up to 5.5% on average, using 60% of its ultimate tensile strength:

$$USS = 0.60 \times UTS \qquad (1)$$

This relationship is valid for all grades and conditions of pure aluminum and its alloys, while for annealed grades of aluminum it may not be tolerably accurate. For metals for the production of elemental parts, the numerical ratio is 0.6, obtained theoretically and empirically [13, 14]. Through experimental studies, a coefficient of 0.6 was also obtained for steels. In a wide review of metal alloys, prediction models were created without an established universal % ratio [15]. Depending on the chemical composition of steels, the coefficient varies from 0.6-0.75, and for cast iron 1.3. For polymers and polymer composites, there is no specified clear numerical coefficient, it changes depending on the structure and manufacturing process. The indicated values were obtained as a result of experimental studies [16]. For viscoelastic polymers such as rubber, it is often observed that the shear strength of rubber is approximately 50-70% of its tensile strength [17, 18]. This ratio can vary based on specific formulations and testing conditions. To accurately characterize these strengths, different testing methods are used (e.g., ASTM D412 for tensile strength and ASTM D732 for shear strength), and results can vary based on the sample preparation and testing conditions. In the article [19], laser-assisted joining of metal-polymer composites is applied, as the polymers used are PA 6, PP, and AISI 304 metal. The behavior of the mechanical characteristics is necessarily analyzed, which shows that the strong connection does not have a significant impact on the achievable tensile strength of the hybrid bond, and the form of assembly is the decisive mechanism of connection in terms of tensile strength.

In addition to polymers and metals, studies have also been conducted on tropical wood. The article presents studies on wood classes D40 and D60, used for structural purposes in accordance with the requirements of Code NBR 7190-3 (ABNT 2022). The results show an average numerical ratio for both wood classes of 0.2 [20].

Table 1 describes the mechanical characteristics of different metals and polymers - the values of tensile and shear strength, and the ratio between them.

Table 1: Relationship between shear strength and tensile strength in various metals and polymers with dense structure

Material	Group	Tensile Strength [MPa]	Shear Strength [MPa]	Ratio (Shear/ Tensile)
Non-alloy quality steel (S235JRC)	Metal	608	408	0,67
Structural carbon steel (C45)	Metal	836	528	0,63
Alloy special steel (41Cr4)	Metal	719	495	0,69
Structural steel (A36)	Metal	400	250	0,62
Stainless steel (304)	Metal	520	300	0,58
Alluminium (6061-T6)	Metal	310	207	0,67
Titan (Grade 5)	Metal	900	550	0,61
Magnesium (AZ31B)	Metal	275	170	0,62
Brass	Metal	500	300	0,6
PLA	Polymer	60	40	0,67
ABS	Polymer	40	25	0,62
PETG	Polymer	50	30	0,6
PA6 (Naylon 6)	Polymer	70	42,5	0,61
PC (Polycarbonate)	Polymer	65	40	0,62
PMMA (acryl)	Polymer	70	38	0,54
PEEK	Polymer	100	57,5	0,57

To more clearly visualize the obtained numerical ratios, an infographic of the analyzed materials was created, as shown in Fig. 1. For the Average value, a linear segment corresponding to the ratio USS/UST of 0.6 was drawn. From the visualization, it can be seen that all values are around the baseline. The highest value is 0.69, and the lowest 0.54.
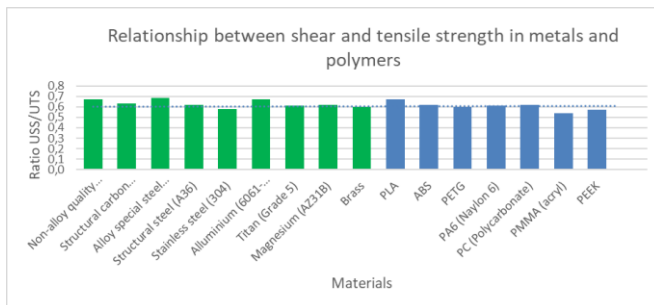
Fig. 1 *Infographic of the Relationship between Shear and Tensile Strength in Metals and Polymers.*

## 3. Relationship between shear and tensile strength in FDM printed materials

3.1. Equipment and materials used

As described above, the production of parts and objects using 3D printing can be done by choosing the density and build parameters. In a previous article, the authors selected printing parameters that resulted in a relatively light-weight, fast-printing part that was suitable for standard and functional parts with an average object size [21]. The selected parameters were 0.1 mm layer height, 30% object infill, and a Geroid structure. The test specimens were printed along the x-y axis with a nozzle size of 0.4 mm.

Using 3D printers Tevo Tornado and Ultimaker S5, shear strength and tensile strength test specimens were printed from FDM filaments: PLA, PLA Wood, PETG, ASA, CPE HG 100, PC, FilaFlex SEBS. These materials were chosen because they cover a wide range of applications with different chemical and physical properties. They are characterized as several types of groups: easy to print, high temperature resistant, wear resistant, mechanically strong, and elastic. Three test specimens were printed from each material for both types of test specimens, a total of 42 test specimens.

The shear tests were carried out using a ZD20 hydraulic testing machine. Fig. 2 shows the schematic diagram of the experiment. A shear test fixture 3 with a cylindrical specimen with a diameter of 8 mm and a length of 70 mm, subjected to tension, was mounted in grips 1 and 2 of the testing machine. The ASTM D732 standard was used to measure the shear strength of a plastic to determine whether it would withstand the required stress without buckling or cracking [22].

a)   *b)*
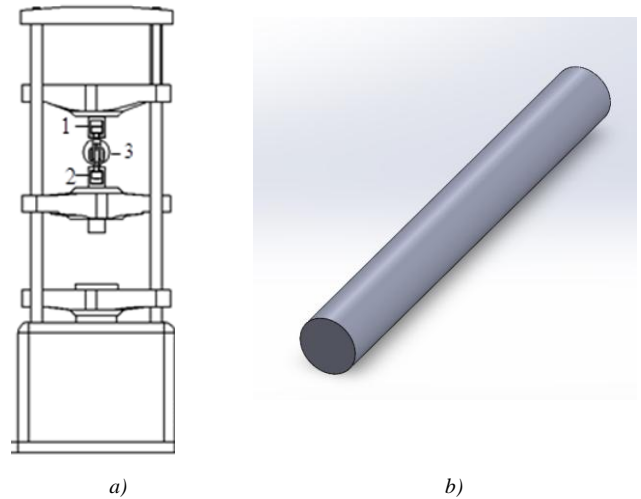
Fig. 2 *Shear testing: a) schematic diagram; b) test specimen*

The tensile strength tests were performed with a modernized Zwick 1474 testing machine restored by the team of the Department of Mechanics of the Technical University, Sofia, shown in Fig. 3. During the experiments, a 25 mm extensometer was attached, recording the displacement. The test specimens were designed according to the BDS EN ISO 527-2:2012 standard [23].

Fig. 3 *Tensile testing machine*

3.2. Experimental results

Table 2 summarizes the results of shear and tensile strength tests of the polymer specimens printed with 30% infill. The results show a correlation coefficient of 48 % for PC and 107 % for FilaFlex SEBS. The high percentage for FilaFlex can be attributed to its high elastic properties and low strength. All other results fall within the range of 50% to 64%.

Table 2: *Results of shear and tensile strength tests on test specimens with 30% filling.*

Material	$Rp_{0,2}$, MPa	USS, MPa	UST, MPa	Ratio USS / UST, %
PLA	2,3	20	38	53
PLA Wood	2,64	19	33	58
PETG	1,61	18	36	50
ASA	1,14	14	22	64
CPE HG 100	1,18	16	29	55
PC	1,87	23	48	48
FilaFlex SEBS	0,13	4	3,75	107

4. Comparative analysis of the mechanical characteristics of polymer objects with different densities

From the analysis of metals and polymers with a sample density of 100%, the materials PLA, PETG, and PC were selected, the results of which were compared with the experimentally obtained results for the same materials printed with a density of 30%. The results are summarized in Table 3. The percentage ratio of the three materials for the two densities of the samples was also calculated. The properties of the analyzed materials are similar, but PC is characterized by higher resistance to high temperatures and has higher hardness.

If we exclude the obtained ratio of USS/UST for the material Filaflex, which is from the group of rubbers, and make an average value of the remaining six types of materials, we get ratio of 54 %. The ratio for all studied materials with a density of 30 % is close, and could be defined by the following linear relation:

$$USS = 0.54*UST \qquad (2)$$

This value is significantly closer to the determined regularity for metals of 60 %.

Table 3: *Mechanical characteristics of PLA, PETG, and PC materials on test specimens with 100 % and 30 % density*

Material	PLA, %	PETG, %	PC, %
UST (MPa), 100%	60	50	65
UST (MPa), 30%	38	36	48
USS (MPa), 100%	40	30	40
USS (MPa), 30%	20	18	23
Ratio USS/UST, 30 %	53	50	48
Ratio USS/UST, 100 %	67	60	62

The obtained values of the ratio between shear strength and tensile strength are presented in a column chart for a clearer display of the results, Fig. 4. The data of the test bodies printed at 30 % filling are depicted in blue, designated as Series 1. The bars of the results of the test bodies with 100% density are depicted in red, recorded as Series 2. The diagram shows that the ratio between shear strength and tensile strength has different values. At 100 % density, the ratio is different for the three materials - 67 % for PLA, 60 % for PETG, and 62 % for PC, an average value of 63 %. At 30 % filling, there is also a difference for the three materials- for PLA is 53%, for PETG is 50%, and for PC is 48 %, but all with an average of about 50 %. These averaged values show that the ratio USS/UST is not the same for different object densities, which is 12 % lower for 30% filled bodies compared to 100% filled ones. Bodies with 100 % density have a 2 % higher percentage ratio than the general USS/UST – 60 % pattern, and at 30% filled bodies have a 10 % lower percentage ratio.
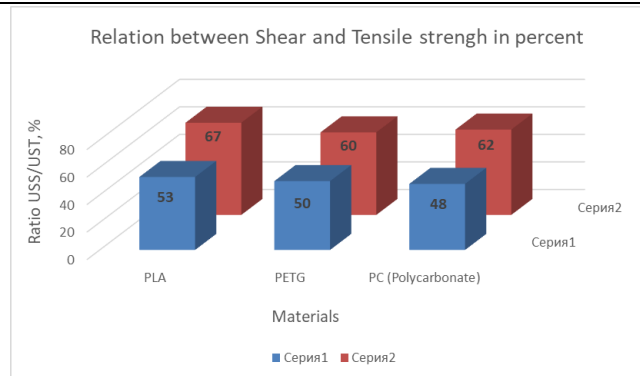

Fig. 4 *Infographic of the Ratio USS/UST of the compared polymers*

5. Conclusion

Knowledge of the relationship between shear strength and tensile strength is important in applications where polymeric materials are subjected to both types of stresses. Designers must consider both properties to ensure reliability and performance in their applications for various parts and consumer products.

It should be noted that, depending on the manufacturing method and the specific properties of polymeric and composite products, the relationship between shear strength and tensile strength can vary significantly, and no single numerical coefficient can be assumed to be universal for all densities of the object.

For 3D printed parts with 30 % infill, obtained by Fused Deposition Modeling could be used the proposed ratio (2), where USS is 54 % of UST. It is available for all FDM materials except the rubber-like. An experimental test should be made for the other densities.

6. Acknowledgment

7. References

1. F. Calignano, D. Manfredi, E. P. Ambrosio, S. Biamino, M. Lombardi, E. Atzeni, A. P. SalmiMinetola, L. F. Iuliano, Overview on additive manufacturing technologies, Proc. IEEE, **105**, 593–612, (2017). DOI: 10.1109/JPROC.2016.2625098

2. S. Wickramasinghe, T. Do, P. Tran, FDM-Based 3D Printing of Polymer and Associated Composite: A Review on Mechanical Properties, Defects and Treatments, Polymers, **12**, 1529, (2020), https://doi.org/10.3390/polym12071529.

3. P. K. Penumakala, J. Santo, A. Thomas, A critical review on the fused deposition modeling of thermoplastic polymer composites, Composites Part B: Engineering, Volume **201**, 108336, 2020, ISSN 1359-8368, https://doi.org/10.1016/j.compositesb.2020.108336

4. J. Zaburko, A. Urzędowski, J. Szulżyk-Cieplak, A. Trnik, Z. Suchorab, and G. Lagod, Analysis of thermal operating conditions of 3D printers with printing chamber, AIP Conference Proceedings, Volume **2429**: 020020, 2021, https://doi.org/10.1063/5.0070165.

5. J. M. Reverte, M. Caminero, J. Chacon, E. García-Plaza, P. López, J.-P. Bécar, Mechanical and Geometric Performance of PLA-Based Polymer Composites Processed by the Fused Filament Fabrication Additive Manufacturing Technique, Materials, **13**, 10.3390/ma13081924, (2020).

6. E. García-Plaza, P. López, M. Caminero, J. Chacon, Analysis of PLA Geometric Properties Processed by FFF Additive Manufacturing: Effects of Process Parameters and Plate-Extruder Precision Motion, Polymers, **11**, 10.3390/polym11101581, (2019).

7. C. Majewski, N. Hopkinson, "Effect of section thickness and build orientation on tensile properties and material characteristics of laser sintered nylon-12 parts", Rapid Prototyping Journal, **17**(3), 176-180, (2011).

8. T. Kalpakoglou and S. Yiatros, Metal foams: A review for mechanical properties under tensile and shear stress, Front. Mater., **9**:998673, (2022), doi: 10.3389/fmats.2022.998673.

9. L. Jiang, Y. Zhou, F. Jin, Z. Hou, Influence of Polymer Matrices on the Tensile and Impact Properties of Long Fiber-Reinforced Thermoplastic Composites, Polymers, **15**, 408, (2023), https://doi.org/10.3390/polym15020408

10. F. Gregory, Steel strength comparison: tensile, compression, torsion, bending, shear, Thermal processing, pp. 35-37, (2025), https://thermalprocessing.com/?s=STEEL+STRENGTH+CO MPARISON

11. K. Miyoshi, D. H. Buckley, Friction and metal transfer for single-crystal silicon carbide in contact with various metals in vacuum, Work of the US Gov. Public Use Permitted./ NTRS - NASA Technical Reports Server, Document ID: 19780013351, PROJECT: RTOP 506-16, Last Modified: July 15, 2025, https://ntrs.nasa.gov/citations/19780013351.

12. R. Tatara, Estimating Ultimate Shear Strength from Ultimate Tensile Strength of Aluminum and its Alloys for Blanking or Piercing, Online Journal of Mechanical Engineering, **1**(1), 37–41, (2022). https://www.scipublications.com/journal/index.php/ojme/arti cle/view/501, DOI: 10.31586/ojme.2022.501

13. R. K. Guduru, K. A. Darling, R. Kishore, R. O. Scattergood, C. C. Koch, K. L. Murty, Evaluation of mechanical properties using shear–punch testing. Materials Science and Engineering: A, **395**. pp. 307-314. (2005). 10.1016/j.msea.2004.12.048.

14. V. Conev, Mechanical properties of cold drawn steels, J. of the Bal. Trib. Assoc., Book 4, Vol.**31**, (2025). (to be published)

15. G. Genov, Revisiting the rule-of-thumb dependencies of the shear strength and the hardness on the yield and the ultimate strengths, (2020). 10.13140/RG.2.2.24105.72807,

https://www.researchgate.net/publication/355208819_REVIS ITING_THE_RULE-OF-THUMB_DEPENDENCIES_OF_THE_SHEAR_STRENGT H_AND_THE_HARDNESS_ON_THE_YIELD_AND_THE _ULTIMATE_STRENGTHS.

16. D. K. Matlocka, S. Kanga, E. De Moora, J. G. Speera, Applications of rapid thermal processing to advanced high-strength sheet steel developments, Materials Characterization, **166**, 110397, (2020), https://doi.org/10.1016/j.matchar.2020.110397

17. F. Xie, W. Tian, Sh. Li, P. Diez, S. Zlotnik, Al. G. Gonzalez, Experimental Study on the Structural Performance of Glass-Fiber-Reinforced Concrete Slabs Reinforced with Glass-Fiber-Reinforced Polymer (GFRP) Bars: A Sustainable Alternative to Steel in Challenging Environments, Polymers (Basel), **17**(8):1068, (2025), doi: 10.3390/polym17081068.

18. M. A. Muflikhun, B. Fiedler, Failure Prediction and Surface Characterization of GFRP Laminates: A Study of Stepwise Loading, Polymers (Basel). **14**(20):4322, (2022), doi: 10.3390/polym14204322.

19. K. Schricker, L. Samfaßa, M. Grätzel, G. Ecke, J. P. Bergmann, Bonding mechanisms in laser-assisted joining of metal-polymer composites, Journal of Advanced Joining Processes, **1**, 100008, (2020).

20. I. S. Menezes, T. R. Ferreira, C. G. F. deSouza, R. Prataviera, F. A. R. Lahr, L. de Freitas, H. F. dos Santos, and A. L. Christoforo, "Relationship between characteristic values of shear strength parallel to grain and tensile strength perpendicular to grain for tropical woods," BioResources **19**(4), 7408–7417, (2024).

21. M. Paneva and P. Panev, "Features of FDM printing of test specimens,", International Conference Automatics and Informatics (ICAI), Varna, Bulgaria, Published by IEEE, pp. 266-270, 2024, doi: 10.1109/ICAI63388.2024.10851504.

22. International Standard ASTM D732 – 17, Standard Test Method for Shear Strength of Plastics by Punch Tool, United States (2017), Last visited August 2025, https://storethinghiem.vn/uploads/files/D%20732%20-%2017.pdf

23. BDS EN ISO 527-2:2012; Plastics—Determination of tensile Properties—Part 2: Test Conditions for Molding and Extrusion Plastics, *Bulgarian Institute of Standardization*: Sofia, Bulgaria, (2012).

Effect of electromagnetic radiation in space on aluminum alloy AA7075

Anna Bouzekova-Penkova

Space Research and Technology Institute - Bulgarian Academy of Sciences, Sofia, Bulgaria
email: a_bouzekova@space.bas.bg

Abstract: Electromagnetic radiation in space presents a significant challenge to the durability of aluminum alloys used in spacecraft construction. This study analyzes the effects of ionizing radiation (gamma rays, cosmic rays, solar particles), ultraviolet and solar radiation, electromagnetic pulses (EMP), and extreme temperature fluctuations on a novel composite material based on AA7075 (B95) aluminum alloy. The results demonstrate that prolonged exposure of the material in outer space (28 months) leads to structural changes and alterations in mechanical properties. To ensure the reliability of the results, the space-exposed samples were compared with reference samples stored under terrestrial conditions.

Keywords: ALUMINUM ALLOYS, AA7075, ELECTROMAGNETIC RADIATION, SPACE

1. Introduction

Aluminum alloys are among the most widely used materials in the space industry due to their combination of high physical-mechanical properties and specific characteristics such as strength, hardness, and more. The vast variety of aluminum alloys, each with its own unique combination of material properties and chemical composition, along with the need for lightweight, stress-resistant, fatigue-resistant, and deformation-resistant materials, makes them a primary choice for constructing spacecraft structures, hulls and supporting elements, rocket nose cones, launch vehicle fuel tanks, fastening elements, and more. These alloys allow for a reduction in the mass of structures and components without compromising their reliability and operational lifespan. Additionally, they are heat-resistant, making them ideal for use under high loads and extreme temperatures—a critical requirement for spacecraft. The versatility of aluminum enables it to be formed into necessary shapes, sheets, plates, extrusions, and castings, along with heat treatments, each tailored for specific aerospace applications [1-5].

For example, the International Space Station (ISS) extensively uses aluminum in its trusses, station modules, solar panels, and other components. The frames and panels of satellites are predominantly made of aluminum alloys. They are also an integral part of the construction of antennas and communication systems for satellites and the ISS [6].

Aluminum alloy AA7075 is one of the most widely used high-strength alloys in space missions. It belongs to the Al-Zn-Mg-Cu system and is characterized by exceptional strength, good fatigue resistance, and relatively low weight, making it an ideal material for manufacturing critical space components where reliability and performance are of vital importance.

Satellite and probe housings require lightweight yet robust load-bearing structures capable of withstanding the mechanical stresses of launch, resisting thermal expansion and contraction in space, and supporting various payloads. Rocket stages are also subjected to extreme mechanical loads. Solar panel frames and antennas demand high stability and low weight.

Thanks to its high tensile strength (~500–570 MPa), AA7075 is also used to produce fastening elements such as bolts and nuts. Modern aluminum alloys like 7075-T6 and 7050-T7451 have been developed to provide even higher tensile strength and improved fatigue resistance, which are crucial for components exposed to repeated stress and harsh environments [7-9].

Space exploration and the study of the Solar System represent the most demanding environment for materials used in space missions. They must withstand extreme vibrations and mechanical stresses, vacuum conditions, severe temperature fluctuations, and electromagnetic radiation.
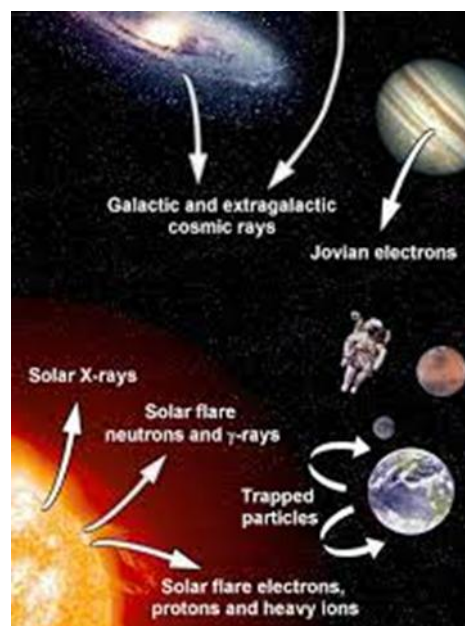

Fig. 1 *Sources of radiation in the Solar System [10].*

Electromagnetic radiation in space is intense and originates from various sources – both natural (stars(sun), galaxies, black holes) and artificial (satellites, spacecraft). It is a form of energy that propagates as waves across different spectral ranges from low-energy radio waves to high-energy gamma rays or particles (photons) in the vacuum of space. Solar radiation and Galactic Cosmic Rays include: ultraviolet, X-ray, and infrared radiation, ionizing radiation (gamma rays, cosmic rays, solar particles), and electromagnetic fields from the solar wind [11-12]. All these forms of electromagnetic radiation affect the mechanical and physicochemical properties of aluminum alloys, particularly under long-term exposure.

Due to the exceptional importance of issues related to the development of new materials for space applications and the characterization of their structures and physico-mechanical properties, a new material was created in the "Space Materials Science" section at the Institute of Space Research and Technology - Bulgarian Academy of Sciences (BAS). Based on an extensive literature review, the aluminum alloy AA7075 (7075 by USA standartds and B95 by Russian clasification) was selected with the potential to upgrade its basic properties. A method was chosen to achieve this enhancement through the addition of ultra-dispersed nanodiamond powder and tungsten alloying, along with the application of an appropriate heat treatment process.

The newly developed composite material was exposed to space mounted on the exterior of the Russian module Zvezda of the International Space Station (ISS) between 2013-2015. This marked Bulgaria's first technological experiment in open space, where the SRTI-BAS participated with a device called the "DP-PM" block, forming part of the international space project "Obstanovka (1-step)" [13].
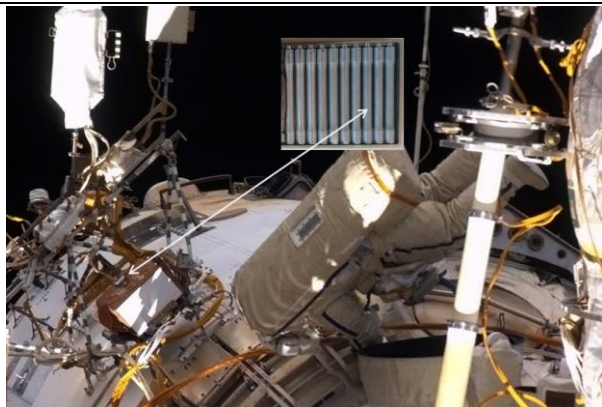
Fig. 2 *DP-PM block with Samples of aluminum alloy 7075 (B95) with quantitative addition of ultradisperse diamond powder and tungsten mounted on a plasma-wave complex (PWC) on the ISS, Zvezda module*

The objective of the experiment was to study the material's resistance to long-term radiation and thermal exposure, its reliability in extreme environments, and the changes that occurred in its physicochemical, particularly mechanical properties. To ensure the validity of the results, the space exposed samples were compared with reference samples stored under Earth conditions.

2. Effect of electromagnetic radiation in space on aluminum composite AA7075

Effects of Ionizing Radiation Exposure (Cosmic Rays and Solar Particle Radiation)

Structural Changes:

High-energy particles induced alterations in the material's microstructure:

- Transformation in the crystal lattice. Increasing the size of Al and $MgZn_2$ crystallites on the surface of the samples;

- Transformation in the distribution of precipitates. Decomposition and formation of new unstable phases [14];

- Vacancy generation and interstitial atom clustering.

These microstructural transformations consequently degraded mechanical performance.

Mechanical Properties:

- Reduced tensile strength;

- Increased material embrittlement.

Effects of Ultraviolet (UV) and Solar Radiation

Ultraviolet (UV) and solar radiation in space exert surface effects on AA7075, primarily through photochemical degradation and alterations in corrosion properties.

- High-energy UV radiation induced surface oxidation of the samples, leading to the formation of a thicker and more brittle aluminum oxide (Al_2O_3) layer;

- UV exposure caused microcracks on the surface of some specimens;

- In combination with the space vacuum, UV photons broke chemical bonds in surface oxides [14].

Thermal Effects (Heating/Cooling) from Solar Radiation

The extreme temperature fluctuations caused by solar radiation in space significantly impact the structural integrity of materials. The tested material underwent cyclic thermal stress from alternating heating (up to +150°C in sunlight) and cooling (-150°C in shadow) every two hours. This led to additional thermal aging of the material on the surface and had an impact on the microstructure and mechanical properties of the material.

- Due to the different thermal expansion coefficient of the different phases, deformation of the crystal lattice on the surface of the studied samples was found. Loss of dimensional stability.

Electromagnetic fields (solar storms)

- High-energy particles from solar storms induce variable magnetic fields, which generate eddy currents, leading to localized heating of the material. Strong magnetic fields can cause minor deformation of the crystal lattice, but in combination with thermal cycles from solar radiation, they have resulted in thermal stress in the material's structure.

- Electrostatic discharges (ESD), accumulated from the solar wind in combination with radiation, have caused microcracks on the surface of some samples.

The combined effects of ionizing radiation, vacuum, thermal cycling, and electromagnetic fields have altered the structure of the AA7075 (B95) alloy-based composite reinforced with nanodiamond and tungsten exposed to open space. Consequently, this has led to changes in the composite's mechanical properties.

Alteration in the composite's mechanical properties

- The introduced radiation defects in the crystal lattice outweigh the effects of thermal stress and make the material (space-exposed samples) harder and more elastic than the reference samples [15-16].
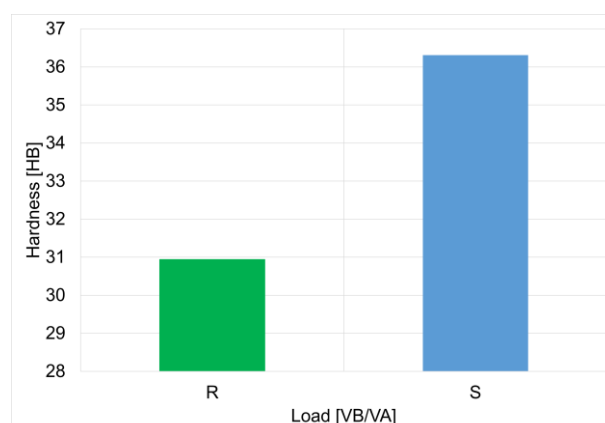

Fig. 3 *Average results of Leeb hardness measurements for "reference" (R) and "space" samples (S)*

Figure 3 presents averaged results from Leeb hardness measurements for reference (R) and space exposed (S) samples. The experimental studies on penetration resistance were conducted using a universal digital hardness tester in accordance with the Leeb/Al-150A standard. This approach was necessary because the investigated space samples have a diameter of d = 5 mm and a length of 70 mm, making them unsuitable for testing on standard hardness testers.

Both the space exposed and reference samples were shaped as cylindrical samples to facilitate their use in subsequent experiments. The dimensions and weight of the samples were designed in compliance with the strict specific requirements for space experiment implementation [13].

Following the conducted Leeb hardness (HL) tests, it was determined that the absorbed radiation dose (~425 kGy [17-19]) and temperature fluctuations (-150°C in shadow to +150°C) induce modifications in the crystal lattice, particularly in the specimen's surface layer. A specific elemental redistribution is observed - migration of elements leading to the formation of new intermetallic phases that alter the base material's properties, consequently resulting in increased hardness.

Figure 4 displays tensile testing data comparing three reference (R) and three space exposed (S) samples. Testing was performed on a Tira Test 2300 universal testing machine featuring automated test diagram recording capabilities.

A comprehensive pre test inspection was conducted for each samples to identify surface defects including cracks and swelling. Geometrical parameters including 90° cross-section (S_0), initial gauge length (L_0), and diameter (d) were precisely measured for all cylindrical specimens prior to testing.
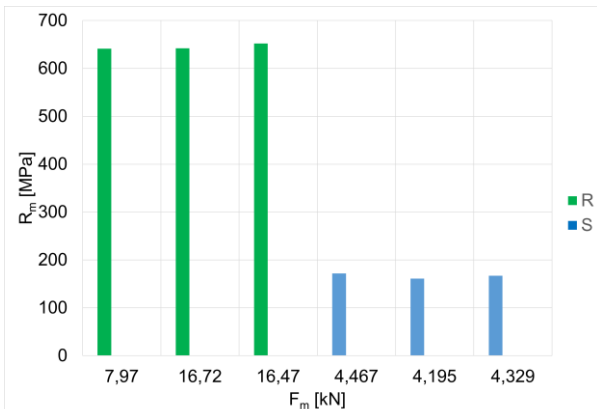

Fig. 4 Tensile test results for three reference (R) and three space exposed (S) samples
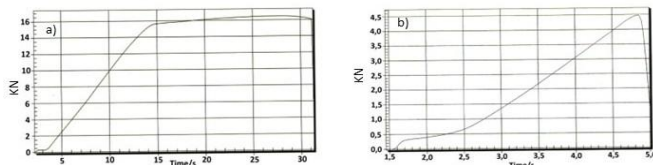

Fig. 5 Tensile diagrams: a) reference sample and b) space sample

Following tensile testing of cylindrical specimens made from AA7075-based composite (UDDP+W), it was established that:

- A substantial strength degradation in space exposed samples relative to reference samples

- Mean tensile strength values:

Reference samples: R_m = 645 MPa

Space exposed samples: R_m = 167 MPa (74% reduction)

- Space exposed samples exhibit low fracture resistance (Fig. 5b). The material is brittle with low plasticity. No yield strength $Rp_{0,2}$ is observed.

- The reference samples exhibit a clearly defined yield plateau $Rp_{0,2}$, characteristic of ductile materials.

4. Conclusions

Electromagnetic radiation in space poses a significant challenge to the durability of the newly developed AA7075 aluminum composite. The material shows sensitivity to ionizing radiation, particularly during prolonged space exposure (28 months).

The observed changes in material properties result from:

- The intensity of the radiation environment

- The accumulated radiation dose during exposure (~425 kGy)

- The thermal energy from temperature fluctuations during exposure

These factors led to improvements in certain mechanical properties (hardness and elasticity) in the space exposed samples. However, the accumulated radiation dose simultaneously caused degradation in other mechanical characteristics.

Space exposed samples under cosmic environmental effects exhibited:

- Reduced strength parameters

- Defects in the crystalline structure

5. References

1. J. Davis, Aluminum and aluminum alloys, ASM Speciality Handbook, ASM International, Materials Park, OH, USA (1994)
2. J. Hatch, Aluminum: Properties and Physical Metallurgy, ASM international: Metals Park, OH, USA (1984)
3. C. Kammer, Aluminum and Aluminum Alloys, In: Springer Handbook of Materials Data, Springer Nature Switzerland AG, 157-193 (2018)
4. C-H Ng, S. Yahaya, A. Majid, Reviews on aluminum alloy series and its applications, Acad. J. Sci. Res., 5(12) (2017) https://doi.org/10.15413/ajsr.2017.0724
5. S-S Li, X. Yue, Q.-Y. Li, He–Li Peng, B-X Dong, T-S Liu, H-Y Yang, J. Fan, S-L Shu, F. Qiu, Q-Ch. Jiang, Development and applications of aluminum alloys for aerospace industry, J. Mater. Res. Technol., 27, 944-983 (2023) https://doi.org/10.1016/j.jmrt.2023.09.274
6. E. Kimiya, Aluminum in Space: Pushing the Limits of Aerospace Technology
7. L. Mondolfo, Aluminum Alloys: Structure and Properties; Butterworths: London, UK (1976)
8. I. Fridlyander, Generating aerospace and nuclear energy technologies from aluminum alloys, M.: Nauka, 286 (2006) ISBN 5-02-035750-2 (in Russian) https://elib.biblioatom.ru/text/fridlyander_vospominaniya_2006/p2/
9. V. Antipov, O. Senatorova, E. Tkachenko, High-strength aluminum alloys, J., Non-ferrous metals, 9 (2013) (in Russian)
10. C. Hellweg, C. Baumstark-Khan, Getting ready for the manned mission to Mars: the astronauts' risk from space radiation, Naturwissenschaften, 94(7), 517-526 (2007) DOI: 10.1007/s00114-006-0204-0
11. Nasa Science, Chapter 6: Electromagnetics (2024) https://science.nasa.gov/learn/basics-of-space-flight/chapter6-1/
12. G. Badhwar, F. Cucinotta, P. O´Neill, Depth-dose relationships for cosmic rays at various solar mimima, Radiat. Res., 134(1), 9-15 (1993)
13. A. Bouzekova-Penkova, S. Klimov, V. Grushin, O. Lapshinova, D. Novikov, D. Teodosiev, Space Experiment "Obstanovka (1 - step)", block DP - PM of the Russian segment of the International Space Station (ISS), Aerospace Research in Bulgaria, 35, 156-164, (2023) DOI: https://doi.org/10.3897/arb.v35.e15
14. A. Bouzekova-Penkova, P. Tzvetkov, Investigation of outer space influence on structural properties of strengthened 7075 aluminum alloy. Experiments onboard the international space station (ISS), C. R. Acad. Bulg. Sci., 72(7), 939-946 (2019) DOI: 10.7546/CRABS.2019.07.12
15. A. Bouzekova-Penkova, K. Grigorov, M. Datcheva, C. Cunha, Influence of the outer space on Nanohardness properties of Al-based alloy, C. R. Acad. Bulg. Sci., 69(10), 1351-1354 (2016)
16. A. Bouzekova-Penkova, M. Datcheva, R. Iankov, Mechanical properties of the enhanced with nanodiamond and tungsten strengthened aluminium alloy being exposed in the Outer space, International Journal "NDT Days", II (4), 396-401 (2019)
17. Ts. Dachev, G. Horneck, D.-P. H¨ader, M. Lebert, Expose-R cosmic radiation time profile, Intern. J. Astrobiol., 14(1), 17-25 (2015)
18. J. Semkova, R. Koleva, Overview on the radiation quantities observed by Liulin-5 instrument in a human phantom on International Space Station during the minimum of 23rd solar cycle, C. R. Acad. Bulg. Sci., 63(10), 1533-1542 (2010)
19. https://cosmicrays.oulu.fi/

The properties of carbon plastics modified with polyphenylmethylsiloxane

Oleksii Derkach; Dmytro Makarenko; Yevhen Muranov; Olha Holovchenko; Valerii Sukhachov

Faculty of Engineering and Technology – Dnipro State Agrarian and Economic University, Ukraine

e-mail: addsau@gmail.com

Abstract: *The article presents a technology of carbon plastics producing based on polyamide-6 with the incorporation of PMS-400 grade lubricant into the material structure. A brief review of the results of carbon plastic applications in engineering is provided. The research methodology and initial parameters are outlined. The experiments were carried out using a single-screw extruder EKG-45, modernized to produce the carbon plastics. As the object of the study, a laboratory-produced carbon plastic CPA-6-20 was used. This material is a carbon plastic based on polyamide-6 reinforced with 20 wt.% carbon fiber. Experimental results established that the optimal screw rotation speed of the EKG-45 extruder is 90 min⁻¹. Under this processing mode, the compressive yield stress increased by 4%, while the impact toughness rose by 4.5%. At this stage of the research, mechanical strength properties were considered, as the most critical for applications in heavily loaded components of moving joints. The investigations carried out at the Dnipro State Agrarian and Economic University.*

KEYWORDS*: POLYAMIDE, CARBON FIBER COMPOSITES,* POLYPHENYLMETHYLSILOXANE.

1. Problem Statement

The development of modern mechanical engineering and autonomous robotic systems [1] is impossible without the use of polymer composites (PCs), particularly structural plastics. Such materials are widely employed by foreign manufacturers of machinery and equipment. Over the past three years, in the context of the war in Ukraine, domestic producers of agricultural machinery have demonstrated a significant demand for the development of their own polymer composites. The use of these materials in the design of moving machine components not only increases reliability and service life but also enhances maintainability under field and production conditions. Until 2023, the majority of PCs used in Ukrainian industry were imported raw materials. Ensuring the supply of domestically manufactured machine-building components made of PCs is therefore a pressing task today. Aliphatic polyamide-6 has become widely used as a material for friction components in machines and mechanisms of various purposes. However, its mechanical properties impose certain limitations on its range of applications. One approach to improving the performance of polyamide-6 is the incorporation of fillers such as fibrous materials, powders, and others into its structure. The authors propose a technology for reinforcing polyamide-6 with carbon fibers using the EKG-45 extruder. The design of extruder was modernized to enable the production of carbon plastics incorporating polyphenylmethylsiloxane lubricant (PMS-400) into its structure. The introduction of PMS-400 is expected to facilitate relaxation of components manufactured from carbon plastics (CPs) and to form a lubricating film in friction zones, thereby enhancing the strength, wear resistance, and durability of machine friction parts. However, the influence of processing parameters on the key mechanical properties—such as impact toughness, compressive and tensile strength limits, as well as other characteristics—remains unclear.

2. Analysis of Recent Research and Publications

The development and investigation of new polymer composites (PCs) in Ukraine has also been conducted over the past several decades. For example, parts for grain harvesters were designed and implemented in production [2], which increased the reliability of the harvesters and the durability of the developed components. The development of new designs of parallelogram mechanisms for seeding machines, in which carbon plastic components were applied, made it possible to abandon traditional maintenance systems [3]. This resulted in a 9…11% increase in the productivity of seeding units by eliminating downtime during technical servicing. In [4], comprehensive studies were carried out to substantiate the structure (composition) of carbon plastics for use in various mechanisms under different loading conditions (pressure, rotation frequency, etc.). The application of heat-resistant polymers in machinery for the chemical industry and in agricultural equipment was also investigated [6]. However, the above-mentioned studies were conducted on materials and finished composites of foreign origin. In recent years, the primary task has been to obtain carbon plastics and modified carbon plastics of domestic Ukrainian production. To achieve this, it is necessary to substantiate a technology for producing carbon plastics with the incorporation of PMS-400.

3. Objectives

Therefore, the aim of this study is to investigate the influence of the operating modes of the modernized extruder on selected properties of carbon plastics based on PA-6 with the incorporation of PMS-400 into their structure.

Raw Materials and Technological Parameters of Carbon Plastic Processing

The technological parameters settings of the extrusion line operation typically have a significant impact on the quality of the final product. Therefore, when working with new materials, it is necessary to optimize the processing parameters. One of the variable parameters of the extruder's operating mode was the screw rotation speed, which was set within the range of 70…90 min⁻¹.

The following components were selected as the raw materials for the polymer composite material (PCM):

- granulated polyamide-6 with a melt flow index of 5.8 g/10 min (at 235 °C, load 0.325 kg);

- chopped carbon fiber, 3 mm in length (Productcode 210137–X, manufacturer: R&GFaserverbundwerkstoffe GmbH);

- PMS-400 oil (according to GOST 13032–77, kinematic viscosity at 20 °C: 385–415 cSt).

The main stages and technological parameters for obtaining CP:

- polyamide-6 and carbon fiber were dried before using following the known methods [2];

- before using PMS, it was pre-mixed with PA-6 granules in a hot state before loading into the extruder hopper;

- number of heating zones – six; temperature by extruder heating zones (starting from the loading opening): zone 1 – 230 °C, zone 2 – 240 °C, zone 3 – 245 °C, zone 4 – 250 °C, zone 5 – 250 °C, zone 6 – 255 °C;

- the extruder's productivity was set using feeders, which were calibrated before the research.

Research methods. The strength properties were tested on an FP-100/1 testing machine in accordance with DSTU EN ISO 604:2019 and GOST 11262-80.

Tensile test modes:
- load scale – 4 kN;
- traverse speed – 1.795 mm/min;
- chart paper speed – 60 mm/min.

Compression test modes:
 - load scale – 40 kN;
 - traverse speed – 0.208 mm/min;
 - chart paper speed – 60 mm/min.

The test results were simultaneously displayed on a personal computer screen.

Impact toughness was tested in accordance with ISO 179:1993 (without notching) using a KM-0.4 pendulum impact tester.

Results

The results of studies of the yield strength and impact toughness of PCM CPA-6-20, depending on the rotation speed of the main extruder screw, are shown in Fig. 1.
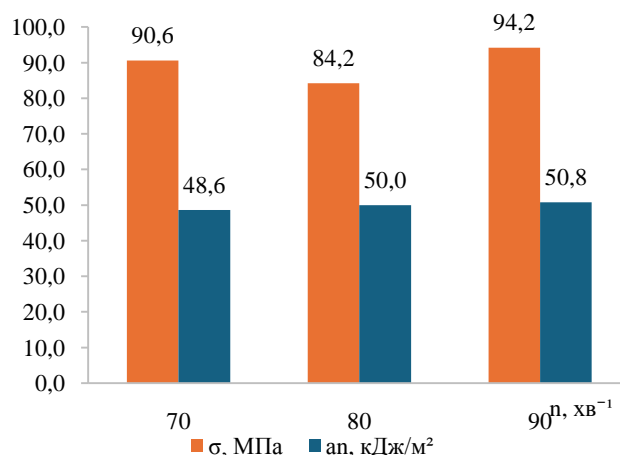

Fig. 1 – *The impact of the screw rotation frequency of the extruder on yield stress under compression and impact toughness of PCM CPA-6-20*

It has been established that increasing the screw rotation frequency of the extruder, without changing the operating modes of the component feeders, leads to a 4.5% increase in impact toughness. It should be noted that the material's yield stress decreases by 7% when the screw rotation frequency is increased from 70 min^{-1} to 80 min^{-1}. A further increase in frequency to 90 min^{-1} results in a 4% increase in yield stress compared to the initial screw rotation frequency of 70 min^{-1}.

The results of the study on the effect of screw rotation frequency on the tensile strength properties of the CPA-6-20 material are shown in Figure 2.
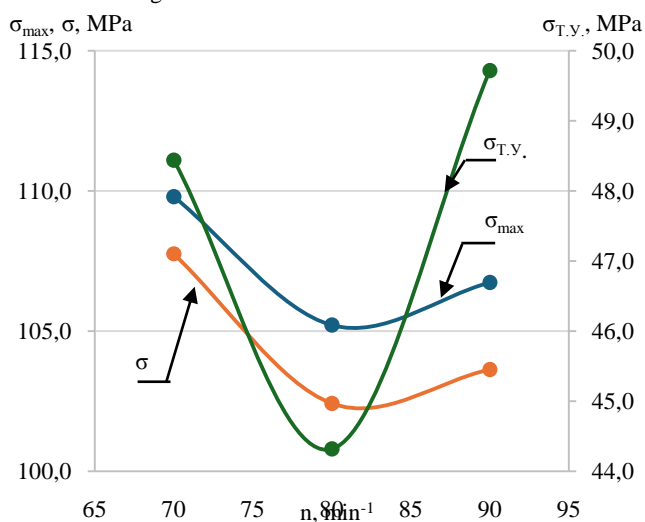

Fig. 2– *The effect of the screw rotation frequency of the extruder on tensile strength (σmax), fracture strength (σ), and conditional yield strength ($\sigma_{CYS.}$) for PCM CPA-6-20*

Thus, the optimal screw rotation frequency for processing CPA-6-20 can be recommended as 90 min^{-1} for the chosen extruder. This mode allows for a slight increase in compressive yield stress (by 4%) and impact toughness (by 4.5%), with a minor decrease in tensile strength values.

In works [3, 4], it has been proven that introducing small amounts of lubricants into the composition of the CP enhances certain properties. The results presented above confirm that the screw rotation frequency of the main extruder, without altering the component feeder settings, also impacts the physical and mechanical properties of materials.

The results of the study on the effect of screw rotation frequency and the introduction of the PMS-400 lubricant into the PCM composition on yield stress and impact toughness are shown in Figure 3.
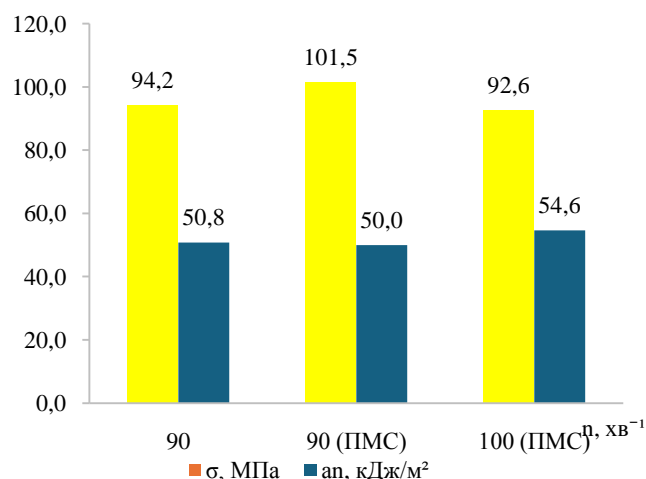

Fig. 3 – *The effect of the screw rotation frequency of the extruder and the introduction of PMS-400 lubricant into the PCM composition on the yield stress and impact toughness of the resulting material.*

The obtained results show that the introduction of PMS-400 lubricant at 0.5 mass % into the PCM composition, without changing the technological operating modes of the extruder, leads to a 7.7% increase in the yield stress of CPA-6-20 PCM. This increase occurs due to material relaxation, accompanied by an increase in plasticity. The change in impact toughness is within the margin of error of the study, so it is considered unchanged. It should be noted that increasing the screw rotation frequency to 100 min^{-1}, along with the introduction of PMS-400 lubricant into the PCM composition, results in a 9.2% increase in impact toughness. At the same time, the yield stress of the studied PCM decreases by 8.7% when the screw rotation frequency is increased from 90 min^{-1} to 100 min^{-1}.

The results of the study on the effect of introducing lubricant into the PCM structure and changing the screw rotation frequency of the extruder on the tensile strength characteristics of the obtained materials are shown in Figure 4.
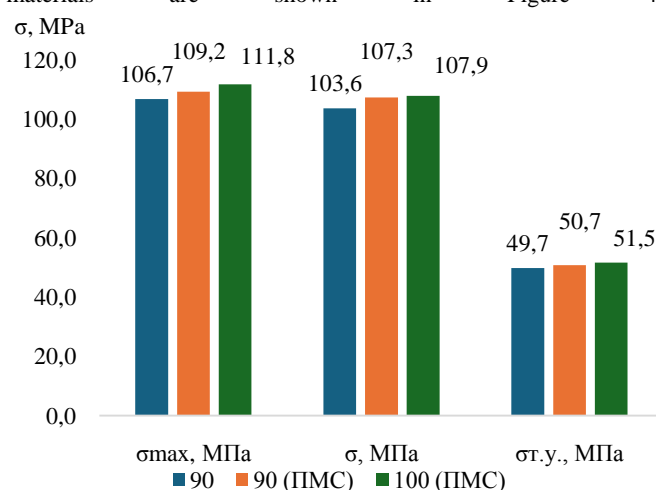

Fig. 4 – *The effect of introducing PMS-400 lubricant and changing the screw rotation frequency of the extruder on the tensile strength characteristics of the CPA-6-20 material.*

The results presented (Figure 4) indicate that the introduction of PMS-400 lubricant into the structure of the CPA-6-20 material at 0.5 mass % leads to an increase in all tensile strength characteristics. Increasing the screw rotation frequency of the extruder from 90 min^{-1} to 100 min^{-1} causes a slight increase in the studied characteristics.

4. Conclusions

On the basis of the analysis of the problem and conducted research work, the following conclusions can be drawn:

1. The introduction of carbon fiber-reinforced polyamide 6-based composites with 20% carbon fiber content and PMS-400 lubricant into the structure ensures the stabilization and improvement of the material's strength properties.

2. The optimal screw rotation frequency for the EKG-45 extruder is 90 min^{-1}. At this setting, the compressive yield stress increased by 4%, and impact toughness rose by 4.5%. The slight decrease in tensile strength is not critical, as the parts will be subjected to compression rather than stretching.

5. References

1. Derkach O.; Makarenko D.; Melnychenko V.; Holovchenko O. Harmonization of maintenance systems for agrorobots and aggregated equipment / INTERNATIONAL SCIENTIFIC JOURNAL "MECHANIZATION IN AGRICULTURE & CONSERVING OF THE RESOURCES". p. 9-12. WEB ISSN 2603-3712; PRINT ISSN 2603-3704.

2. Деркач, О.Д. Обгрунтування параметрів обертових елементів робочих органів зернозбиральних комбайнів: Дис. канд. техн. наук: 05.05.11. – Тернопіль, 2006. – 182с.

3. Підвищення довговічності паралелограмного механізму посівних комплексів зміною конструкції рухомих з'єднань [Текст] : автореф. дис. ... канд. техн. наук : 05.05.11 / Макаренко Дмитро Олександрович ; Центральноукр. нац. техн. ун-т. - Кропивницький, 2018. - 20 с.

4. О.Д. Деркач, Д.О. Макаренко, Є.С. Муранов, В.В. Сукачов, О.Ю. Береза. Обгрунтування складу полімерно-композитного матеріалу конструкційного призначення для трибоспряжень сільськогосподарської техніки. Центральноукраїнський науковий вісник. Технічні науки. 2025. Вип. 11(42), ч. 2, 260-267.

5. Kabat O. S., Kobets A. S., Derkach O. D., Makarenko D. O. and Hnatko O. M. Practice of using parts made of the heat-resistant polymer composites in the chemical industry and agricultural engineering / ARPN Journal of Engineering and Applied Sciences. Vol.25, № 1, January 2024

Global Best Practices and Recommendations for Assessing and Improving Cybersecurity by Applying Intrusion Detection / Prevention System Selection Metrics

Veselina Gagamova[1,*], Ivo Tasev [2], Violeta Vasileva[3])
G. S. Rakovski National Defence College Sofia, Bulgaria[1]
ITWorks, Sofia, Bulgaria[2]
Future Innovation Labs[3]

v.gagamova@rndc.bg, ivo.tasev@itworks.bg, violetta.ziv@gmail.com

Abstract: This article proposes an approach to improving the use of IDS/IPS systems in computer networks of forces and means of state and local administration bodies in the event of incidents, disasters, accidents and catastrophes. To this end, good practices for selecting an appropriate type of IDPS to increase the level of cybersecurity in the organization are studied. It is proposed to use the "type" metric to develop a comparative analysis of the correspondence between the types of IDPS and their ability to protect against ransomware, using the classification of tactics and techniques in accordance with the MITRE ATT&CK framework.
Keywords: METRICS, CYBERSECURITY ASSESSMENT, IDPS, MITRE FRAMEWORK

1. Introduction

In the context of rapidly evolving cyber threats and the increasing sophistication of attack vectors [5, 6, 7], organizations across the globe face the urgent challenge of maintaining resilient and adaptive cybersecurity systems. Traditional security mechanisms are no longer sufficient to ensure the integrity, confidentiality, and availability of information assets. Consequently, Intrusion Detection Systems (IDS) and Intrusion Prevention Systems (IPS) have emerged as critical components within modern cybersecurity architectures. Their efficiency, however, largely depends on the methodology applied for their evaluation, selection, and integration into complex network environments.

The development of global best practices for IDS/IPS assessment provides a systematic framework for identifying relevant performance, security, and operational metrics. These include detection accuracy, false positive and false negative rates, scalability, latency, interoperability, and cost-effectiveness. Furthermore, recommendations by leading international organizations, such as ISO/IEC, NIST, and ENISA, [3, 4, 7] highlight the importance of adopting standardized selection criteria to achieve balanced trade-offs between technical performance and organizational requirements.

This paper explores global best practices and recommendations for assessing and improving cybersecurity through IDS/IPS selection metrics. The objective is to provide a structured overview of methodologies, criteria, and evaluation models that support decision-makers in selecting optimal solutions tailored to specific risk landscapes. By synthesizing international standards, case studies, and comparative analyses [1], the study aims to contribute to the enhancement of both theoretical understanding and practical implementation of IDS/IPS or IDPS technologies in diverse organizational contexts.

2. Standards and Good Practices for Planning, Creating and Implementing Intrusion Prevention and Detection Systems

There are numerous studies and publications on the planning, creation and implementation of intrusion prevention and detection systems, but for the purpose of the study, two main ones are considered, which were also used as sources.

In the international information security community, numerous studies, researches, and documents describing good practices have been conducted. For the purpose of this re, a publication by the National Institute of Standards and Technology (NIST) – SP 800-94 [4], as well as the international standard ISO/IEC 27039 "– Information technology – Security techniques – Selection, deployment and operations of intrusion detection systems (IDPS)" [2] were taken into account. The two documents have a similar purpose and largely overlap in content. The purpose of the documents is to assist organizations in selecting, configuring, and installing intrusion detection and prevention systems.

Special Publication SP 800-94 of the US National Institute of Standards and Technology (NIST)

The National Institute of Standards and Technology (NIST) has developed the special publication in fulfillment of its statutory responsibilities under the Federal Information Security Management Act of 2002 (FISMA), Public Law 107-347. This publication is intended to help organizations understand intrusion detection system (IDS) and intrusion prevention system (IPS) technologies, and to help organizations design, implement, configure, secure, monitor, and maintain intrusion detection and prevention systems (IDPS). It provides practical, real-world guidance for each of the four classes of IDPS: network-based, wireless, network behavior analysis software, and host-based. The publication also provides an overview of additional technologies that can detect intrusions, such as security information and event management software. It focuses on enterprise IDPS, but much of the information in the publication is also applicable to stand-alone and small-scale IDPS deployments.

International Standard ISO/IEC 27039 – "Information technology — Security techniques — Selection, deployment and operations of intrusion detection and prevention systems (IDPS)" This standard provides guidance to assist organizations in preparing to implement intrusion detection and prevention systems (IDPS). Specifically, it addresses the selection, deployment, and operations of IDPS. It also provides background information from which this guidance is derived.

MITRE ATT&CK® [9] is a globally accessible knowledge base of tactics and techniques used maliciously, based on real-world observations. The ATT&CK knowledge base isused as a foundation for developing specific threat models and methodologies in the private sector, government, and cybersecurity product and services community.

A study of the correspondence between IDPS types and their ability to impact a ransomware attack according to the classification of tactics and techniques in the MITRE ATT&CK framework [3] is proposed and presented in [1].

The types of IPDS (Network, Wireless, Behavioral, Host) and their security functionalities can be successfully used as a metric option when selecting the appropriate IPDS for the organization's infrastructure.

3. The Possibilities for Improving Cybersecurity Through the Use of IDS/IPS/IDPS in Computer Networks

The existing variety of IDPS solutions, as well as the analysis of modern threats, lead to the conclusion that improving the use of

IDPS in computer networks is a complex task. It requires a systematic approach to the analysis, design, construction and maintenance of the protection system and the prevention of intrusion. This task can be accomplished using the Deming approach, which includes the phases of planning, implementation, verification and action [8].

3.1. Planning

3.1.1. Risk Analysis

Before selecting an appropriate IDPS system, an organization should conduct an information security risk assessment aimed at identifying the attacks and intrusions (threats) to which the organization's specific information systems may be vulnerable, taking into account factors such as the nature of the information used by the system and how it needs to be protected, the types of communication systems used, and other operational factors. By considering potential threats in the context of their specific information security objectives, an organization can identify controls that provide cost-effective risk mitigation. Once an IDPS is installed and operational, an ongoing risk management process should be implemented. This includes periodically reviewing the effectiveness of the controls in light of changes in the system's operations and threat environment.

Based on the security risk assessment, the organization must first determine, in order of priority, which assets need to be protected and then adapt the IDPS to this environment. To achieve this goal, it is necessary to collect, categorize and analyze the following information:

• Network diagrams and maps indicating the number and location of hosts, network entry points, and connections to external networks;
• Description of the organization's network management system;
• Operating systems for each host;
• Number and types of intermediate network devices such as routers and switches;
• Number and types of servers and dial-up connections;
• Description of any network servers, including types, configurations, application software, and versions running on each;
• Connections to external networks, including nominal bandwidth and supported protocols;

3.1.2. Analysis of Current Security Measures

After documenting the technical characteristics of the system environment, security protection the currently installed technologies should be identified. At a minimum, the following information is required:

• Demilitarized Zone (DMZ)
• Number, types, and location of firewalls and filtering routers;
• Identification of servers for authentication;
• Encryption of data and connections;
• Endpoint Detection and Response (EDR). cybersecurity solutions /Antivirus suites;
• Products for access control;
• Specialized security hardware such as cryptographic hardware;
• Virtual Private Networks (VPNs);
• Any other security technologies installed.

3.1.3. Designing an IDPS Installation Procedure and Creating an IDPS Security Policy

Once the risk analysis has been performed and the current security measures have been identified, an IDPS security policy should be defined. It should answer the following key questions:

• What information assets need to be monitored?
• What is the policy for emergency open and emergency close conditions?

• What type of IDPS is needed?
• Where can the IDPS be placed?
• What types of attacks need to be detected?
• What type of information needs to be recorded?
• What type of response or warning can be provided when an attack is detected?

3.1.4. Set Metrics to Monitor

Metrics are a management tool that allows you to set goals and track them. Metrics when using IDPS should be set to fulfill at least the following objectives:

• Measure the right indicators
• Report to the right people
• Be in the right format
• Be planned, created and reported at the right time

3.2. Implementation

Based on the criteria provided in the previous point, a successful IDPS implementation can only be achieved through:
• A thorough requirements analysis that includes the security needs of the IDPS, based on a risk assessment.
• A careful selection of an IDPS implementation strategy;
• Identification of a solution that is compatible with the organization's network infrastructure, policies, and resources;
• Specialized training for the maintenance and operation of the IDPS;
• Documentation of training and rehearsal procedures for operating and responding to IDPS alerts.
• Due to the advantages and limitations of the different types of IDPS, it is necessary to consider hybrid use of the systems.

3.3. Check

It is necessary to review the metrics already set at a pre-planned period of time. For this purpose, it is advisable to form a permanent working group and a formal validation process.

3.4. Action

In case of deviation from the expected values of the metrics, it is necessary to carry out a partial or complete analysis of the points of the planning and execution process. The necessary corrections must be made and a new measurement must be carried out.

4. Metrics for Measuring the Effectiveness of Intrusion Detection and Prevention Systems .

Measuring the effectiveness of Intrusion Detection and Prevention Systems (IDPS) is crucial for ensuring reliable protection of information systems [10]. The metrics used to evaluate the performance of these systems can be divided into several main categories:

1. **Detection Rate**: This metric measures the ability of an IDPS to identify malicious activities or threats. It is calculated as the ratio of correctly detected incidents to the total number of actual incidents. A high detection rate indicates that the system successfully recognizes and alerts about potential threats.

2. **False Positive Rate**: This is the percentage of legitimate actions that are incorrectly classified as malicious. A low false positive rate is important as it reduces unnecessary workload on administrators and minimizes the risk of disrupting normal system operations.

3. **Response Time**: This metric measures the time taken by the IDPS to respond to a detected incident. Fast response times are critical for minimizing damage and limiting the spread of an attack.

4. **Coverage**: Coverage refers to how well the IDPS can protect various parts of the network or system. It includes both physical components and types of threats that the system can detect and prevent.

5. **Throughput**: This metric measures the amount of traffic that the IDPS can process without significant delay. High throughput is important for maintaining network and system performance.

6. **Configuration Complexity**: This metric evaluates the complexity of setting up and managing the IDPS. Simpler and more intuitive interfaces allow for faster and accurate configuration, leading to more effective protection.

7. **Integration with Other Systems**: The ability of the IDPS to integrate with other security and monitoring systems is important for overall organizational protection. Good integration facilitates information sharing and coordinated actions.

8. **Cost of Implementation and Maintenance**: This includes both initial costs for purchasing and installing the IDPS, as well as ongoing costs for maintenance, updates, and staff training. Minimal costs while maximizing efficiency are desirable.

Using a combination of these metrics provides a comprehensive view of the effectiveness of IDPS and helps organizations make informed decisions regarding their implementation and optimization.

There are many IDS/IPS systems, but they are not sufficient as a separate product to guarantee a very high level of security for the computer networks of the forces and means of the state and local administration bodies in the event of incidents, disasters, accidents and catastrophes. A lot of money is invested in developing new attacks or masking already known ones. Weak international cooperation on cybercrime issues leads to a very low level of detection and punishment. Information assets, both of individuals and entire organizations, will increasingly be the subject of attacks.

Good practices and recommendations for assessing and improving cybersecurity would be to combine IDS/IPS with other systems supporting information security such as:
• File integrity checkers
• Firewalls
• Honeypots
• Network management tools
• Security Information and Event Management (SIEM)
• End Point Detection and Response (EDR) solutions
• Vulnerability assessment tools

5. Conclusion

In conclusion, it can be summarized that In conclusion, it can be summarized that the process of improving the use of IPS/IDS in an organization by state and local administration bodies in the event of incidents, disasters, accidents and catastrophes requires in-depth work and commitment of managers and all responsible persons. There is no technical solution, software or hardware, that can guarantee absolute security. The process of planning the implementation of the solution is extremely important and it must be economically justified.. It is necessary to take into account many factors.

Metrics for measuring the effectiveness of intrusion detection and prevention systems when using IDPS should be prepared in advance. The process of checking and updating IDS/IPS should be constant, using the metrics for selecting a suitable IPDS system depending on its type.

6. References

1. Veselina Aleksandrova, Ivo Tasev, Violeta Vasileva, Challenges In Choosing The Type of Intrusion Detection and Prevention System to Increase the Level of Cybersecurity in the Organization, 12th International Conference on Application of Information and Communication Technology and Statistics in Economy and Education (ICAICTSEE – 2022), December 02-03rd, 2022, Publishing Complex – UNWE, Sofia, Bulgaria. Volume: 50, ISSN 2367-7635 (PRINT), ISSN 2367-7643 (ONLINE), Issued for publication: June 27th, 2024 pp. 27-33, https://icaictsee.unwe.bg/past-conferences/ICAICTSEE-2022.pdf
2. Information technology — Security techniques — Selection, deployment and operations of intrusion detection systems (IDPS) - ISO/IEE 27039 2015.02.15
3. Information technology – Security techniques – Information security management systems – Requirements ISO/IEE 270001:2015
4. National Institute of Standards and Technology - Guide to Intrusion Detection and Prevention Systems (IDPS) – Special Publication 800-94
5. ENISA – ENISA THREAT LANDSCAPE 2021
6. ENISA – ENISA THREAT LANDSCAPE 2022
7. ENISA – ENISA THREAT LANDSCAPE FOR RANSOMWARE ATTACKS 2022
8. Cybersecurity & Infrastructure Security Agency CISA – "Plan, Do, Check, Act" Nov 01 2013
9. https://attack.mitre.org/
10. Kumar, Gulshan. (2015). Evaluation Metrics for Intrusion Detection Systems-A Study. International Journal of Computer Science and Mobile Applications. 11.

Challenges in implementing management systems in small and medium-sized enterprises

Deyan Gradinarov

Institute of Metal Science, equipment, and technologies with Center for Hydro- and Aerodynamics "Acad. A. Balevski"

Bulgarian Academy of Sciences

Abstract: This article examines the main difficulties faced by small and medium-sized enterprises (SMEs) in implementing management systems according to ISO standards. The focus is on the real barriers – resource, organizational, cultural and market – and on practical approaches to overcome them. Examples from practice are presented, as well as recommendations for more effective adaptation of the systems to the SME context.

KEYWORDS: SMALL AND MEDIUM-SIZED ENTERPRISES, MANAGEMENT SYSTEMS, ISO STANDARDS, CHALLENGES, IMPLEMENTATION

1. Introduction

Management systems according to ISO standards (such as ISO 9001[1], ISO 14001[2], ISO 45001[3], etc.) are a well-established tool for improving the quality, efficiency and compliance of organizations with the requirements of customers, regulators and the market. The implementation of such systems is particularly important for SMEs seeking sustainable development and better positioning. Despite the potential benefits, SMEs often face a number of barriers in implementing and maintaining such systems.

2. Resource limitations

One of the most serious problems facing SMEs is the lack of sufficient resources – human, financial and technological[4]. Unlike large corporations that have quality or sustainability departments, most SMEs do not have specialized staff and often assign responsibilities for implementing systems to employees with other core functions. This leads to overload, insufficient expertise and delays in the process.

Financial constraints are also significant. The costs of external consultants, staff training, documentation development and certification fees are often beyond the means of SMEs. This necessitates the search for alternative approaches, such as participation in externally funded projects (e.g. under European programs), the use of ready-made templates and the promotion of internal resources through training.

3. Limited management and organizational capacity

Many SMEs are characterized by an informal and flexible organizational structure, which, although it brings advantages in decision-making[4], is often an obstacle to the implementation of structured management systems. In the absence of clearly assigned responsibilities and established procedures, the implementation of ISO standards can be perceived as a formal and unnecessary complication.

Furthermore, the lack of experience and strategic understanding of the long-term benefits of certification often leads to weak commitment from management. Without active support and leadership from management, management systems remain on paper and are not integrated into daily practice[4]. In this regard, it is essential to conduct training and consultations to direct management's attention to the real added value of the systems approach.

4. Cultural and behavioral barriers

Cultural attitudes in SMEs can also be an obstacle. In many cases, management systems are not perceived by staff as useful, but rather as an administrative burden. This is especially true when communication is one-way – from management to employees – and when participation and feedback are lacking. Implementing standards requires a change in mindset, a sense of discipline and systematicity, which are often seen as conflicting with the entrepreneurial spirit of SMEs.

Overcoming these barriers involves cultivating an organizational culture in which quality, safety and sustainability are seen as values and not just formal requirements. This can be achieved by involving employees in the system development process, encouraging initiative and recognition of good practices.

5. External factors and market pressures

SMEs often do not see a direct need for certification, especially if they operate primarily in the local market or in sectors with lower regulatory requirements. This reduces the motivation to invest in management systems. However, with the introduction of stricter environmental and social requirements, as well as the globalization of markets, even small companies feel the pressure to demonstrate compliance with standards.

Another external factor is the lack of sufficiently targeted government support and consulting services specialized for SMEs. Many of the available resources and programs are poorly promoted or inaccessible to the smallest companies. In this context, there is a need for a targeted policy to support SMEs in implementing standards through training, financing and exchange of good practices.

6. Practical examples

A small furniture manufacturing company[4] with about 25 employees implemented ISO 9001 to improve its order and complaint management. Initially, the process encountered strong resistance, including from management, who viewed the standard as unnecessary bureaucracy. After implementing an electronic order tracking system and conducting internal training, the company reported a 20% reduction in complaints within one year.

Another example is a micro-enterprise in the field of IT[4] support with less than 10 employees, which implements an integrated system according to ISO 9001 and ISO/IEC 27001. By using cloud-based tools for document and process management, the company manages to achieve certification at minimal cost and position itself as a reliable supplier for international clients. The approach is based on adapting the requirements to the real capacity of the team, while ensuring efficiency and compliance.

Conclusion:

Implementing management systems in SMEs is a process full of challenges, but also opportunities. Successful implementation depends on the ability of organizations to adapt the requirements of the standards to their context, to motivate staff and to ensure management commitment. Support from external experts and government programs can also play a key role. With the right approach, management systems become not only a means of compliance, but also a tool for sustainable growth, trust and competitive advantage.

References:

1. ISO 9001:2015 - Quality management systems. Requirements.
2. ISO 14001:2015 – Environmental management systems – Requirements with guidance for us.
3. ISO 45001:2018 – Occupational health and safety management systems – Requirements with guidance for use.
4. Lectures course for internal auditors ISO 9001:2015 – Quality management systems, ISO 14001:2015 – Environmental management systems and ISO 45001:2018 – Occupational health and safety management systems by TUV Nord Bulgaria – Lecturer – Deyan Gradinarov

Comparative analysis of integrated management systems according to ISO 9001, ISO 14001 and ISO 45001 standards

Deyan Gradinarov

Institute of Metal Science, equipment, and technologies with Center for Hydro- and Aerodynamics "Acad. A. Balevski"

Bulgarian Academy of Sciences

Abstract: The article reviews the main similarities and differences between the three most widely used standards – ISO 9001 (quality), ISO 14001 (environment) and ISO 45001 (occupational health and safety), as well as the benefits of their integration within a single management system. Practical examples, challenges and recommendations for effective implementation in a real organizational environment are presented.

KEYWORDS: INTEGRATED MANAGEMENT SYSTEMS, ISO 9001, ISO 14001, ISO 45001, STANDARDS, MANAGEMENT, CERTIFICATION

Introduction:

In modern organizational practice, more and more organizations are aiming for integrated implementation of management systems. ISO standards, which concern quality, environment and occupational safety, allow the creation of a unified management framework. The purpose of this article is to present a comparative analysis of these three standards, to identify their common characteristics and specificities, and to justify the benefits and challenges of their integration.

1. Similarities and structure of the standards

The ISO 9001, ISO 14001 and ISO 45001 standards share a common structure, known as Annex SL[1,2,3]. This structural alignment includes key sections such as organizational context, leadership, planning, maintenance, activities, performance measurement and improvement. The common approach allows for the creation of a single management framework that is easier to implement, maintain and improve. Each of the systems follows a risk-oriented process approach and strives for continuous improvement, which contributes to achieving high efficiency and sustainability.

In practice, this means that organizations that have already implemented one of the management systems can significantly ease the implementation of the other two. For example, elements of internal audit or document management can be developed to comply with all three standards simultaneously. This not only facilitates coordination between departments, but also increases the awareness and commitment of staff who operate in a clearer and more unified process management.

2. Key differences in content and focus

Despite structural similarities, each system has a unique focus. ISO 9001 focuses on customer satisfaction and control over processes related to the quality of products and services. ISO 14001 requires management of environmental aspects, pollution reduction and compliance with environmental laws and regulations. ISO 45001, in turn, emphasizes the creation of safe and healthy working conditions, requiring systematic risk assessment and active employee participation.

The differences in the content of these standards mean that integration must take into account both the compatibility and the specificities of each approach. For example, risk analysis must take into account risks related to employees' health and safety [3,4] as well as risks related to the environment[2,5] and risks related to the quality of products produced and services offered[1,6]. This requires a unified approach to management, in which strategic planning and operational implementation are interconnected.

3. Benefits of integrated implementation

Integrating the three systems offers organizations the opportunity for more efficient resource management, better internal coordination and increased competitiveness[7]. Instead of managing separate systems with overlapping processes, integration allows the development of unified procedures that meet the requirements of all three standards simultaneously.

One example of this is non-conformance management – instead of maintaining three separate registers and processes, a well-built integrated system can collect, analyze and handle all deviations in a single framework, thus improving traceability and the ability to analyze the root cause of the non-conformance. The same applies to internal audits, management reviews and resource and document management. In addition to easing administrative work, this leads to a reduced risk of errors, faster incident response, greater transparency and a systematic approach to decision-making.

The financial benefits are also not to be underestimated. By combining training, sharing resources, and conducting certification audits simultaneously, organizations can significantly reduce the costs associated with maintaining separate systems. In addition, improved quality, environmental, and safety performance leads to greater trust from customers, regulators, and the public.

4. Practical challenges in integration

The integration of management systems, although logical from an efficiency point of view, is associated with a number of practical challenges. First of all, there is the issue of the different level of development of each of the systems. Very often, organizations have a well-established and mature quality management system, but the environmental and occupational safety elements are less developed. This requires efforts to standardize processes, which sometimes leads to internal changes in the activities of organizations.

Another significant problem is related to the competence of the personnel. Integrated systems require a multidisciplinary approach, which implies knowledge of the requirements of the three standards. This necessitates conducting targeted training and building cross-functional teams to support the implementation. In the absence of such an approach, there is a risk of formal implementation, in which the system exists only at the documentary level.

Also, active support from management is a critical factor. Without clear commitment and leadership from senior management, the integration process can lose momentum and be perceived as a bureaucratic requirement. This often leads to resistance from employees, especially if the integration changes established practices or obligations.

Last but not least, cultural aspects play a significant role. Organizations need to build an internal culture that embraces quality, safety and environmental care as shared values. This requires systematic communication efforts, good example setting from leaders and active feedback from employees.

5. Practical examples

A packaging company[7] with around 150 employees implemented ISO 9001 in 2017, then added ISO 14001 and ISO 45001 in 2020 in response to key customer requirements. After initial difficulties related to employee resistance and unclear responsibilities, the company organized internal working groups, including representatives from all departments. Through monthly meetings and consistent training, a unified documentation and a common management platform were created. The result was a 35% reduction in non-conformities and better results in external audits.

Another example is a software company[7] with 70 employees that implemented all three management systems simultaneously as part

of a strategy to position itself for international customers. By using a digital process management platform and actively involving senior management, the organization was able to build a sustainable integrated system. Within a year of certification, the company reported increased employee satisfaction and significantly improved internal communication between departments.

Conclusion:

Integrated management systems offer significant advantages for organizations seeking consistency and efficiency in management. Comparative analysis shows a high degree of compatibility between the three standards, making integration both possible and advisable. Despite the challenges, with the right approach, organizations can build a system that not only meets requirements, but also creates value through risk reduction, culture improvement, and sustainable development.

References:

1. ISO 9001:2015 - Quality management systems. Requirements.
2. ISO 14001:2015 – Environmental management systems – Requirements with guidance for us.
3. ISO 45001:2018 – Occupational health and safety management systems – Requirements with guidance for use.
4. Lectures course for lead auditors ISO 45001:2018 – Occupational health and safety management systems by TUV Nord Bulgaria
5. Lectures course for lead auditors ISO 14001:2015 – Environmental management systems by TUV Nord Bulgaria
6. Lectures course for lead auditors ISO 9001:2015 – Quality management systems by TUV Nord Bulgaria
7. Lectures course for internal auditors ISO 9001:2015 – Quality management systems, ISO 14001:2015 – Environmental management systems and ISO 45001:2018 – Occupational health and safety management systems by TUV Nord Bulgaria – Lecturer – Deyan Gradinarov

Wine microfiltration (MF) and water ultrafiltration (UF) flat sheet industrial membrane unit

George Bibileishvili[1*], Mzia Kezherashvili[2], Manana Mamulashvili[3]
Engineering Institute of Membrane Technologies of Georgian Technical University[1,2,3]
75bibileishvili@gmail.com, kezherashvilimzia@gmail.com, mananamamula59@gmail.com

Abstract: *They are designed for microfiltration membrane installations for wine (turbidity of the filter FTU 0.12-0.32) of the flat-parallel type with a filtration area of 10 m², pore size of the membrane 0.1μm, 0.45μm, with a capacity of 250 l/h and for ultrafiltration membrane installations for water (turbidity of the filter FTU 0.02-0.05) with a capacity of 500 l/h. The wine microfiltration membrane installation ensures 100% removal of microorganisms and yeast, which results in ecologically clean, crystal clear, sterile, stable, high-quality wine. Installation of ultrafiltration membrane water purification completely removes suspended particles, colloids, bacteria, microorganisms, viruses, proteins, large organic compounds, microbiological residues and partially chemical components, including hardness salts, from water. Sterile drinking water (bottled water) is produced. Microfiltration and ultrafiltration membrane installations can be used by companies for the production of wine and drinking water, such as "family wineries" and "chateau"-type enterprises. Micro- and ultrafiltration membranes and equipment have a low cost, which significantly reduces the costs of wine and drinking water production.*

Keywords*: MEMBRANES, MICROFILTRATION, ULTRAFILTRATION, WINE, WATER, UNIT*

1. Introduction

To solve the main problems associated with the shortage of clean drinking water, maintaining ecological balance and stable economic growth, rational and sustainable management of water resources is necessary. In this area, the use of membrane technologies is important for cleaning liquids and improving their quality [1–5].

The aim of the work is to develop membrane separation processes and technologies for processing wine, aqueous solutions and products based on them [6-8]. The main objective of the research is to develop polymer membranes with improved physical and chemical characteristics and a new design of the membrane apparatus, as well as to optimize hydrodynamic indicators, allowing to increase their productivity and extend their service life.

2. Results and discussion

Micro- and ultrafiltration membranes with pore sizes of 0.1μm, 0.2μm, 0.45μm and 0.8μm were manufactured, and tangential sterile filtration membrane devices for wine microfiltration and natural water ultrafiltration were created by developing appropriate modules and filtration technologies.

The membranes were made of polyethersulfone and aromatic polyamide by the liquid-phase phase inversion method [9,10]. Polymer compositions were created in which organic and inorganic substances of a given composition and molecular weight were used as additives. The properties of the membranes obtained are given in Table 1.

Table 1: *Properties of the membranes (20⁰C)*

Membranes	Water uptake %	Viscosity (Cp)	Water permeability L/m²h	Mean Pore size (μm)
PMIA 0.1	54	1427	242	0,1
PMIA 0.2	68	1434	468	0,2
PMIA 0.45	72	1425	597	0,45
PMIA 0.8	76	1421	785	0,8

The structure and morphology of the obtained membranes were studied using scanning probe microscopy (SPM, Certus Standard V, Nano Can Technologies).
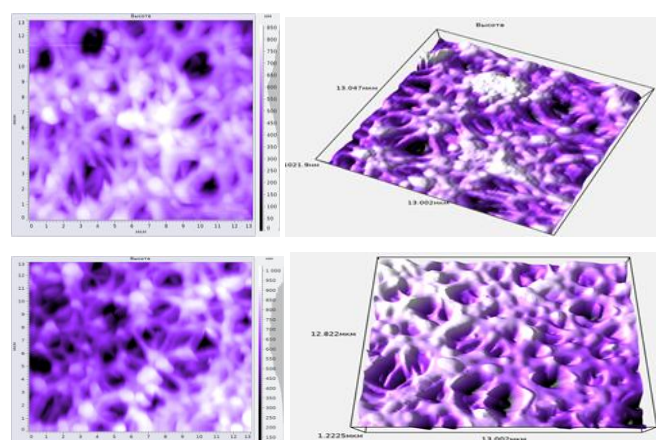

Fig.1 *Two and three-dimensional surface images of PMIA Membranes*

Depending on production requirements, polymer membranes with a width of 0.5-1 m are manufactured.

Fig.2 *110 cm wide membrane production device*

By changing the design of the pressure cell of the membrane block, regulating the height, pressure, speed, laminar and turbulent circulation flow, the hydrodynamic parameters were optimized, which led to a decrease in the degree of concentration polarization and optimization of the membrane separation process.
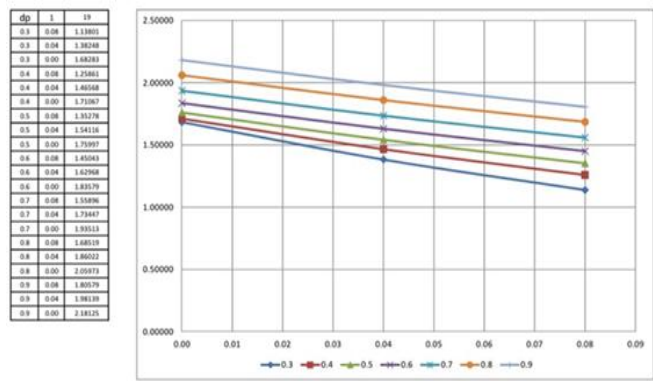
Table 2. Dependence of pressure, cell length and concentration on polarization; Fig.3 Graph of dependence of pressure on concentration on polarization

Molds for casting plastic parts were made and the corresponding parts were cast from polyethylene using an injection molding machine.

Fig. 4 Filter-drainage and turbulator, casting mold and molded plastic parts

Based on theoretical and experimental work, high-performance membrane filtration units for wine and water have been developed. Unlike standard cartridge-type modules, where membrane replacement implies complete disposal of the membrane module contents, our innovative membrane module design concept ensures replacement of only worn-out flat membranes with new ones, while the plastic parts of the module are reused.

Fig. 5 Universal membrane filter device for wine and water
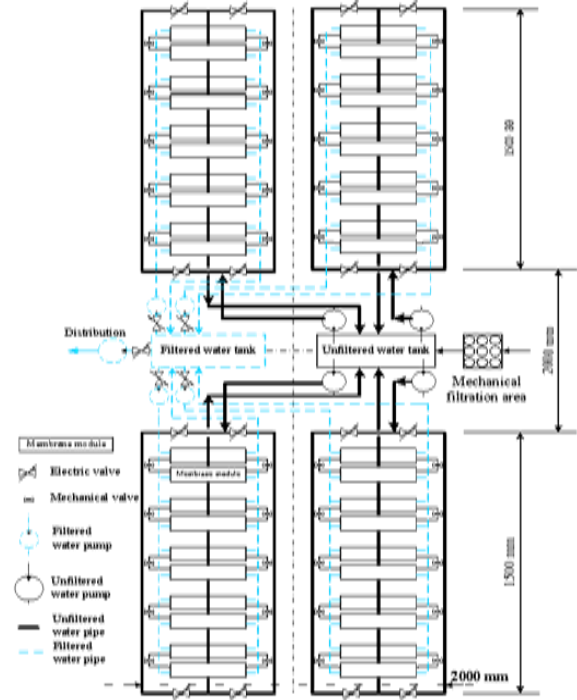
Fig. 6 The principle scheme of the ultrafiltration membrane unit for natural water and wine

3. Conclusion

The wine microfiltration device with a membrane with a pore size of 0.45 μm removes small fibrous particles, yeast (Brettanomyces, Saccharomyces, etc.), bacteria - lactobacilli, acetobacter, colloidal particles and protein molecules, tartaric acid salts - tartrate crystals, ensuring the production of microbiologically stable wine with a turbidity of FTU 0.32, which is especially important for sterile bottling of wine in order to stop fermentation processes in it.
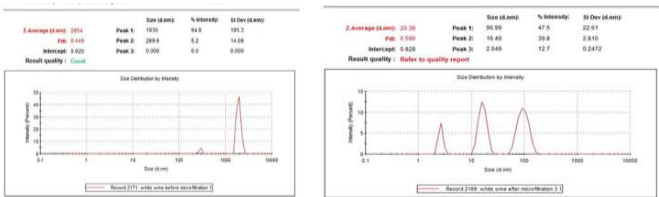

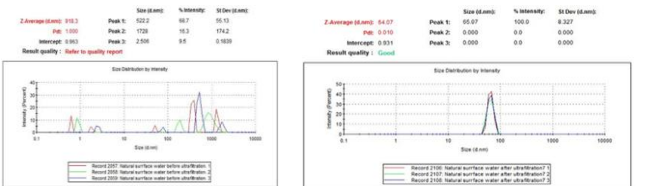*Fig. 7 Particle sizes in white wine "Rkatsiteli" before and after microfiltration*

Fig.8 Particle size in natural surface water before and after ultrafiltration

Purification-sterilization, disinfection of natural water involves the removal of microorganisms, bacteria (0.5-10 μm in size), rickettsia (0.4-1 μm in size), viruses (100-400 nm in size) and fungi (3-50 μm in size), suspended particles (0.5-50 μm in size) from natural water. Purification-disinfection of natural water contaminated with the above impurities ensures a reduction in the turbidity index in Formazan units from 50 to 0.02 FTU.

4. References

1. M. Issaul, S. Jellali, A. A. Zorpas, P. Dutournie, Sustainable Chemistry and Pharmacy, Volume 25, p.10590, (2022).

2. S. A. Ani, T. N. Mustafa, N. Hilal, J. Water Proc. Eng., 35, p.101241, (2020).

3. E.S. Award, T.M. Sabirova, N.A. Tretyakova, Q.F. Alsalhy A. Figoli,. Chem. Eng., 5 (3), p.34, (2021).

4. K. Elsaid, E.T.Sayed, M.A.Abdelkareem, M.S. Mahmoud, M.Ramadan, J. Environ. Chem. Eng. 8 (2020).

5. W. Sun, J. Liu, H. Chu, and B. Dong, Membranes (Basel), 3, (3), 226–241, (2013).

6. C. Zhou, Z. Hou, X. Lu et al., Industrial & Engineering Chemistry Research, vol. 49, no. 20, pp. 9988–9997, (2010).

7. T. Yu, J. Zhou, F. LIu, B. M. Xu, B. Y. Pan, Membranes, 12, 519 (2022).

8. G. V. Bibileishvili, M.G. Kezherashvili, M.A. Manulashvili, Oxidation Communications, Vol. 47, (3), (2024).

9.G. Bibileishvili, M. Kezherashvili, N. Gogesashvili, L. Kuparadze, European Journal of Scientific Research (EJSR), 161 (1), 5 (2022).

10. G. Bibileishvili, M. Kezherashvili, N. Gogesashvili, L. Kuparadze, Oxidation Communications, 45 (2), 300 (2022).

Comparative analysis of the braking behaviour of a single track vehicle with different types of front suspensions

Simona Hesapchieva[1,*], George Yanachkov[2]
Burgas State University "Prof..DR. Asen Zlatarov"[1]
Technical University of Sofia,Bulgaria [2]
simona_hesapchieva@abv.bg

Abstract:. *Modal simulations comparing the behaviour of different types of motorcycle suspension in specific conditions are found in the literature. However, there is a lack of sufficient field experiments that can be used both to calibrate the models and to realistically assess the advantages and disadvantages of alternative designs. The aim of this publication is to evaluate the behavior of the authors' alternative front suspension of a motorcycle in braking mode. To achieve this goal, a series of road tests were conducted on the same motorcycle equipped with a different type of front suspension. Both experiments were conducted with the same equipment using the same methodology. The results were processed in the Matlab environment. The obtained results can be used both to evaluate the designed suspension and to validate simulation models and optimize the suspension according to the same methodology. The results were processed in the Matlab environment. The obtained results can be used to validate simulation models and optimize the suspension*

Keywords: MOTORCYCLE FRONT SUSPENSION, TELESCOPIC FORK, MULTILINK SUSPENSION, MOTORCYCLE BRAKING, ROAD EXPERIMENT

1. Introduction

Modal comparison of the behaviour of different types of alternative suspension is presented in [1]. Kinematic and dynamic simulations of different types of alternative suspensions - with a central hub and with a double wishbone suspension - were carried out. In order to validate the systems performance, various simulations of situations close to real driving conditions have been carried out. The significant superiority of the alternative systems over the model equipped with a conventional telescopic fork is noted. Authors in [2] develop a modal study of the dynamic behaviour of the alternative front suspensions – Girder fork and Hossack's suspension, which is a prototype of the modern Duolever suspension, was compared with the conventional telescopic suspension. In order to evaluate the influence of the suspension parameters, experiments were made with three of its configurations - a parallelogram, where the levers are parallel and the angle between them is equal to zero, a configuration where the suspension is designed so that the trajectory of the front wheel to be similar to that using a telescopic fork and a configuration where the trail is kept constant throughout the suspension range. In [3, 4] the development of motorcycle suspension over the years is described, and the advantages and disadvantages of the fork as a front suspension system vs alternative constructions are explained. In studies such as [5-9] and many others, various models of alternative front suspension are presented. Each of the considered designs has advantages and disadvantages. The choice of a kinematic scheme is inevitably associated with a number of compromises - in terms of the mass of the unsprung masses, complexity of the construction, stability and controllability. From the review of theoretical and experimental studies related to the impact of different front suspension structures in the scientific space, the following conclusions can be drawn:

1. Despite alternative front suspension systems, the telescopic fork still remains the most common type of motorcycle front suspension, despite its disadvantages. It also means that these series of research and innovations have not fundamentally solved all the problems of the front suspension.

2. When using a link suspension, the trajectory of the wheel during deformation in the suspension is curvilinear.

3. When using a link suspension, with deformation in the suspension, the main geometric characteristics change significantly less, compared to the telescopic fork. In this way, greater stability is achieved.

4. Using a link suspension achieves a greater anti-dive effect when braking.

5. There is a lack of sufficient road experiments with alternative front suspensions studying their impact in different driving modes to validate the mathematical models.

The purpose of this study is to make a comparative analysis of the results obtained from road experiments with a motorcycle equipped with different front suspension systems while braking. In the first case, the test machine was equipped with the standard serial suspension, which is a simple telescopic fork. In the second case, it is equipped with a MULTILINK suspension designed and manufactured by the authors.

2. Alternative front MULTILINK suspension

MULTILINK suspension (Fig.1) is a type of independent suspension with three or more longitudinal links. It is common used in the automotive industry, mostly for luxury and sports cars. A 3D model was developed in a SolidWorks environment to physically investigate how the suspension would perform in 3D space and to check the geometric constraints. In developing this process, the tubular structure that represents the suspension upright is first modeled. The bike's handling was developed similar to some existing designs, using Hossack's suspension kinematics as a prototype. By turning the handlebars of the motorcycle, a moment is transmitted to the upper arm, from which the steering scissor is formed through the triples. Holes are drilled at both ends to allow it to be mounted to the lower triple. The test bike originally had a tubular steel frame. At one end, the suspension levers are hinged to the designed tubular structure. At their other end, they need to be hinged to the frame of the motorcycle. For this purpose, a model of a suspension element was developed to be welded to the frame. 4 p-shaped plates are modeled, in which the four levers are mounted, located at the specified vertical and horizontal distance. In order to increase the movement of the links, conical bushings are located on both sides of the hinge. Ohlins TTX22M Universal was selected for the elastic and damping element of the suspension. This is an adjustable shock absorber with twin tube technology. This technology (TTX) is based on the principle of creating a damping force by increasing oil pressure on one side of the piston and having gas pressure on the other side. A common problem with monotube shock absorbers is a reduction in pressure on one side of the piston, leading to cavitation. This problem is solved by keeping the oil and gas pressure constant. In order to make the results between the standard and the design suspension comparable, the spring was chosen with approximately the same spring rate as the conventional. To allow for comparison of results, the spring rate was chosen to be approximately the same as that of the original suspension.
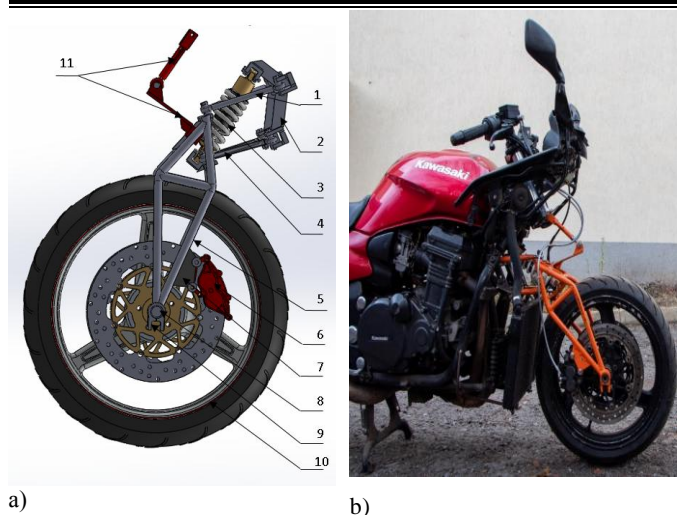
Fig.1. *Assembled suspension type MULTILINK a – prototype, b – real type of suspension.*
1- upper levers of the suspension, 2 - attachment to the frame of the motorcycle, 3- elastic and damping element, 4- lower levers of the suspension, 5- upright, 6 - brake callipers, 7 - attachment of the brake callipers, 8- axis, 9 – hub, 10-wheel, 11 – handling arms.

According to the kinematic scheme, the place of the shock absorber is also determined. One of the main requirements for the suspension was its minimum cost. With the exception of the elastic and damping element, one of the main goals was minimal costs for the suspension materials, technological processes and treatments for its manufacture. Maximum recycled materials available in the department were used. When creating the MULTILINK suspension, maximum preservation of the main geometric dimensions of the motorcycle - trail, castor angle, wheelbase of the motorcycle was ensured. When producing the suspension, the mass of the unsprung masses was invariably increased. This also leads to a redistribution of the weight of the motorcycle along the axes and a change in the horizontal coordinates of the mass center.

3. Methodic of the measurement

A series of road tests were conducted on a horizontal section with dry asphalt concrete pavement in a controlled and safe environment. During the experiment, the displacements in the front and rear suspension, the longitudinal and vertical accelerations were measured. The angle of the trim, the redistribution of the normal load on the front and rear running wheels and the change in the geometric parameters of the motorcycle were determined using a numerical method. The purpose of the study is to determine the deformation in the suspension during braking. In this way, the tendency of the suspension to "dive" can be assessed.

To achieve the aim of the research, it is necessary to perform the following tasks:
1. Smooth start of the motorcycle, acceleration to the selected speed, from which braking begins, and braking of the motorcycle using only the front brake;
2. Determine the displacement in the front and rear suspension. It is necessary to use displacement sensors;
3. Determine the horizontal acceleration of the motorcycle's mass center using an accelerometer';
4. Use a data acquisition;
5. Processing of results and analysis.

The measurements are carried out on Kawasaki GPZ 1100 motorcycle,year of manufacture 1997 (ZX 1100 D), with a maximum power of 108 kW which is not factory-equipped with ABS system.The wheels are equipped with new Continental ContiMotion tires 120/60 R17 at the front and 170/60 R17 at the rear. The internal air pressure in the tires before the start of the experiment (cold tires) is 2.2 bar. The road experiments are carried out on the same section of the roadway in both directions. The measurement equipment used was the same in both experiments.

The only necessary change was the change in the location of the sensor that detects the deformation in the front suspension. When using a telescopic fork, it is located parallel to the fork tubes. In the second experiment, it was mounted parallel to the upright using clamps and brackets near the wheel axis. Since the designed suspension is new and under investigation, for safety reasons the experiment was conducted using only the front brake. Also, the initial speed from which the braking begins has been reduced. This does not affect the results, because as is known from the theory of the car, the maximum braking delay is not a function of the speed of movement, but depends on the realized braking force and the coefficient of traction. The average duration of each trial is about 20 s. In some of them, the braked wheel locks. Details of the methodology and measuring equipment, as well as the results of experiments with telescopic suspension are presented in [10-11]. Fig. 2 shows the location of the sensors during the motorcycle test. Since the suspension design is new and under investigation, for safety reasons the experiment was conducted using only the front brake. Also, the initial speed at which braking begins was reduced, compared to the telescopic fork. This did not affect the results because, as is known from automobile theory, the maximum braking delay is not a function of the speed of travel, but depends on the realized braking force and the coefficient of adhesion. In order to experimentally determine the deformations of the front and rear suspension, as well as the differential, a series of experiments were conducted using the front brake from an initial speed of about 5.71 m/s (20 km/h) to full stop.

Fig.2. *Kawasaki motorcycle equipped measuring equipment, 1-front suspension sensor, 2- accelerometer, 3 rear suspension displacement sensor*

4. Impressions of the driver when riding the motorcycle with MULTILINK suspension.

The described features of the behavior of the MULTILINK suspension are entirely subjective impressions of the motorcycle rider, both during the experiment and during free riding without restrictions and equipment:

1. Difficult turning of the steering wheel, at higher speeds the negative effect disappears.

2. Weaker stabilizing effect (self-stabilization of the front wheel). Need to adjust the angle of rotation of the wheel.

3. Perceptibly less dive when braking.

4. Better braking.

5. Fast stabilization and recovery after front tire lockup when braking. The effect has been observed several times.

As a result of the test drive, the conducted experiments and the processing of the results, the following conclusions can be drawn:

With the MULTILINK suspension, the dive of the motorcycle is 50% less.

The trail, normal trail, and wheelbase are kept nearly constant throughout the suspension's compression/rebound range of operation.

5. Results obtained from the road experiment with telescopic front suspension and MULTILINK suspension

In order to make a real evaluation of the designed MULTILINK suspension and to determine its advantages and disadvantages in braking mode compared to the telescopic suspension, a comparison of the obtained results of the road experiments was made.

Fig.3 compares the pitch angle at which the sprung masses of the motorcycle rotate when braking with only the front brake using different kinematics of the front suspension. ϑ_1 presents the results obtained for a motorcycle with a MULTILINK front suspension, and ϑ_2 – for a telescopic fork suspension. In both experiments, the initial speed from which the braking process begins is different. With a telescopic fork suspension, the braking process is longer, but the realized braking force, respectively braking delay, is the same. The nature of the change in the studied quantity is the same. The pitch angle when using a MULTILINK front suspension is half as small. This is due to the resistance against "diving", set as a goal when designing the suspension.
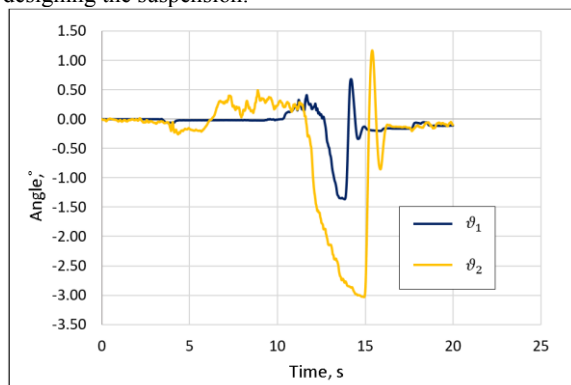

Fig.3 Comparison between the pitch angle of a MULTILINK and a telescopic suspension motorcycle while braking using front brake only

Fig. 4 compares the results obtained by the sensor measuring the displacement in the front suspension when braking with the two types of suspension. F_1 represents the displacement in the MULTILINK front suspension, and with F_2 respectively in the telescopic one. When accelerating to the selected speed from which to start the braking process, extention is noticed in both cases. When the maximum braking delay is achieved, the maximum displacement in the suspension is obtained. When using a MULTILINK suspension, the maximum compression in the suspension is reduced by nearly 50%. This is due to the twice smaller pitch angle. When braking with a telescopic fork, a significant damping vibration occurs at the end of the braking process. With the MULTILINK, this process is absent due to the greater resistance in the shock absorber.
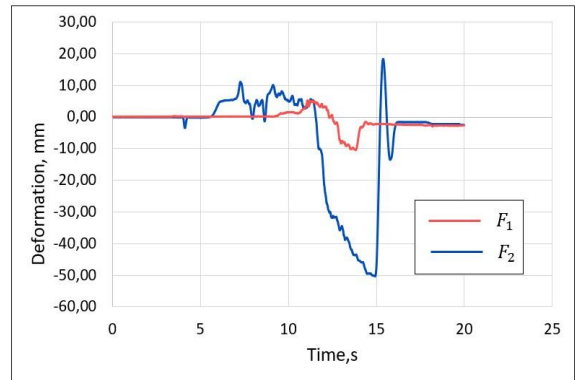

Fig.4 Comparison of Front Suspension Deformation when braking with MULTILINK and Telescopic Suspension Motorcycle

Fig. 5 compares the results obtained from the road tests with the two types of suspension. R_1 shows the displacement in the rear suspension of a motorcycle with the designed multi-link suspension, and R_2 presents the rear suspension when using the standard telescopic. The deformation measured in both experiments has the same nature. When stopping the motorcycle, as a result of the load transfer, the rear wheel is unloaded and the suspension is extended accordingly. When using a MULTILINK suspension, the deformation is slightly less compared to a telescopic suspension.
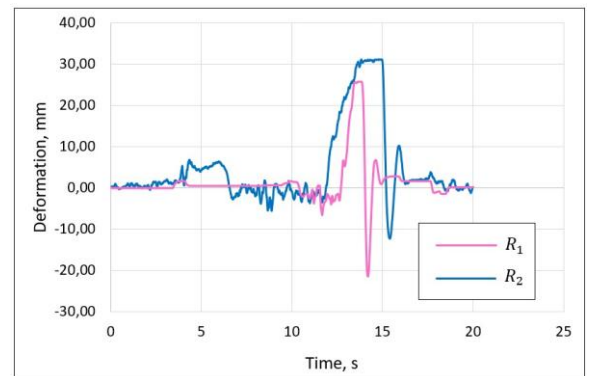

Fig.5 Comparison of deformation in the rear suspension when braking a motorcycle with MULTILINK suspension and with Telescopic suspension

Fig. 6. presents the results obtained for the horizontal acceleration of the motorcycle during the road experiments with both types of suspension. $\ddot{X}_1$ represents the acceleration during test with the MULTILINK front suspension, and $\ddot{X}_2$ – with the standard telescopic fork suspension. The variation in the studied quantities was the same nature. When using the designed suspension, the speed to which the motorcycle accelerates is lower and, accordingly, the braking period is shorter. However, the applied braking force and, accordingly, the resulting braking delays in both cases are almost the same. In the braking process, in addition to the normal load, the front suspension is subjected to two additional forces: the front braking force and the weight transfer generated by the total braking force. In both experiments, the applied braking force is the same.
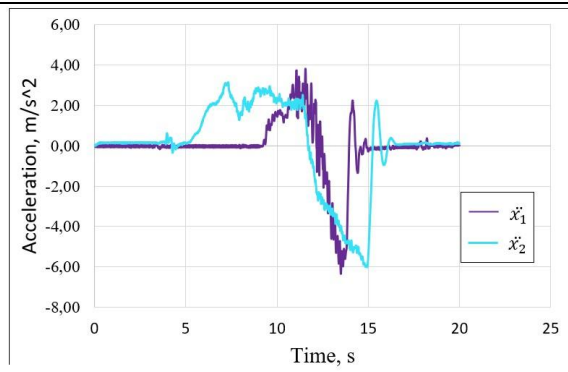
Fig.6. *Comparison in horizontal acceleration of a motorcycle with MULTILINK front suspension and with telescopic fork front suspension*

As a result of the test drive, the experiments carried out and the processing of the results, the following advantages and disadvantages can be deduced:

Advantages of MULTILINK suspension

1. Separation of suspension and steering functions.

2. Possibility of predetermining the trajectory of the center of the contact spot depending on the turning angle by changing the location and length of the levers.

3. When braking, the pitch of a motorcycle with MULTILINK suspension is about 50% less than with a standard telescopic fork suspension.

4. Deformation in the front suspension while braking is significantly less with the MULTILINK suspension than with the telescopic fork.

5. The trail maintains its dimentions throughout the suspension travel.

6. Better braking. Less energy from the brakes is not wasted on compressing the suspension and is used for clean braking.

7. Quick stabilization and recovery after front tire lockup when braking. (More experimental data are needed, but in a tightly controlled environment).

Disadvantages of MULRILINK suspension

1. Complication of the construction, the presence of many elements, more complex production and requirements for the accuracy of individual details.

2. Increase in unsprung masses, which can be compensated by the use of lighter materials.

3. Less suspension travel.

5. More difficult to assemble, the links are located where the coolant and oil radiators are usually located.

6.   *Conclusions*

Road experiments were conducted with a motorcycle with different types of front suspension while braking with front brake. The variation in the front and rear suspension are measured and the longitudinal acceleration of the mass centre. The variation in the pitch angle were determined numerically. Since the safety of traffic and the security of the driver and the equipment used are of primary importance, the repeatability of the experiments is limited. In order to make a more complete assessment of a real prototype of an untested and alternative design, it is necessary to conduct additional tests in a strictly controlled environment under different modes - under different methods of braking, maneuvering, acceleration. However, the obtained experimental data give a real insight into the behaviour of the multilink suspension, the advantages it achieves over the conventional suspension and the problems that are yet to be solved.

The results obtained can be used in dynamic models studying the behaviour of the suspension, and for studying the behaviour of the motorcycle during braking.

The results obtained can be used to compare the influence of different types of front suspension on the geometric parameters of the motorcycle during suspension deformation, and from there to create out-of-plane dynamic models for studying the stability of motion.

Based on the results obtained, suspension optimization can be made.

References

[1]   B. Mavroudakis and P. Eberhard, Analysis of alternative front suspension systems for motorcycles, *Vehicle System Dynamics*, vol.**44**, no. sup1, pp. 679–689 (2006).

[2]   M. Ramírez, C., T. Rodríguez, M. & S. Evangelou, Dynamic analysis of double wishbone front suspension systems on sport motorcycles. *Nonlinear Dyn* **91**, 2347–2368 (2018).

[3]   M.Gadola, D Chindamoa., F. Vitale and E. Bonera The Design of A Motorcycle Featuring Fully Independent Adjustability for Front Suspension and Steering Geometry, *IOP Conference Series: Materials Science and Engineering* **538**, (2019)

[4]   T. Foale Motorcycle Handling and shassis Design: The Art and Science, (2006)

[5]   T. Foale, *Steer for the Future*. Tony Foale. [Online] 2002.

[6]   Liu, Changdong, *A Multibody Dynamics Model of a Motorcycle with a Multi-link Front Suspension* (2017).Electronic Theses and Dissertations.

[7]   C. Davis, *Hub Centre Steering*, Bachelor of Science University of Cincinnat.

[8]   J. Tobolar Design of a Multi-link Suspension for Motorcycles with a Sidecar. In: Klomp M., Bruzelius F., Nielsen J., Hillemyr A. (eds) *Advances in Dynamics of Vehicles on Roads and Tracks. IAVSD* (2019)

[9]   J Lange *Development of front suspension for an electric two-wheeled amphibious vehicle*, Thesis, KTH, Maskinkonstruktion (Inst.), 2015

[10]   S. Hesapchieva, D, Hlebarski, G. Yanachkov Experimental Determination of the Impact of Load Transfer on the Basic Geometrical Parameters of the Motorcycle during Braking, *AIP Conf. Proc. 13 October 2022*; 2557 **(1)** (2022)

[11]   S. Hesapchieva, D. Hlebarski, G. Yanachkov, E. Dimitrov and Z. Georgiev, "Experimental study ofmotorcycle trim while braking" *Proceedings of International Scientific Conference on Aeronautics,Automotive and Railway Engineering and Technologies BulTrans-2020*, pp. 106–113 (2020)

DESIGNING AND MODELING OF FIXTURES
FOR MANUFACTURING GRAPPLE BUCKETS

Asst. Prof. Nikolay Stankov, PhD
University of Ruse, Bulgaria
nstankov@uni-ruse.bg

Abstract: *The paper presents the process of automated designing and parametric modeling of fixtures for manufacturing grapple buckets using the CAD system. The presented grapple buckets are designed for bulk materials and they are part of the grapple construction. Grapples are installed on cranes, excavators and other specialized machines. A methodology has been developed that covers all stages of design – from the creation of 3D models of the parts, sub-assemblies and assemblies, to the generation of design documentation through template files. The presented approach allows the development of parametric models with multiple configurations, which cover different variants of the products. Using the presented methodology leads to a reduction in the volume of generated documentation and optimizes the design process. Data management within a PDM system ensures centralized storage, actuality and accessibility of information.*

Keywords: *GRAPPLE BUCKETS, GRAPPLES, CRANES, EXCAVATORS, FIXTURES, METHODOLOGY, DEVELOPMENT, 3D MODELS, AUTOMATED DESIGNING, PARAMETRIC MODELING, CAD SYSTEM, TEMPLATE FILES, DESIGN DOCUMENTATION, PDM SYSTEM, ERP SYSTEM*

1. Introduction.

The paper introduces the process of developing a fixture for manufacturing grapple buckets with a CAD system. The parts, sub-assemblies and assembly of the fixture are parametrically designed.

Grapple buckets are designed for bulk materials and they are part of the grapple construction. The grapples are used for loading and unloading of various materials. They are mounted on cranes, mobile cranes, scrap gondolas, light trucks, excavators and other specialized machines [1, 2].

Grapples are the structure consisting of grapple buckets (left and right), a central body, a rotator and a carrier. Through the buckets, the grapple grabs materials. The left and right buckets are attached on the central body. The rotator rotates the grapple during operation. The carrier attaches the grapple to the corresponding machine.

The fixture for manufacturing the grapple buckets was designed and developed with the SolidWorks CAD system [3]. Using the CAD systems significantly facilitates the process of developing the product. The design is performed in three-dimensional space. 3D models of the parts, sub-assemblies and assemblies are developed. The process of creating the design documentation is automated by using template files.

2. Literature review.

2.1. Parametric modeling of products with a CAD system.

Creating 3D models is an important step in the product development process. 3D models can be used to create new design documentation. In 3D models of parts and assemblies, the additional information is set by attributes (users and systems ones). The information from the attributes can be used for documentation management with PDM system, as well as by other departments in a company with an ERP system [3, 4, 5, 6].

Based on the 3D models, the technology for parts manufacturing is also developed – adding or removing holes, determining allowances for mechanical processing, pre-processing of certain surfaces, and others [7]. This requires the development of new design and technological documentation to be used in production. The 3D models are used to create the cutting files for the parts, which are made of sheet metal.

Very often the product is divided into sub-assemblies which are pre-manufactured and then a fixture is used to assemble them into the final product [8].

The next steps are developing the necessary fixtures for assembling, welding, machining and product control [9, 10]. The fixtures are developed with a CAD system using parametric modeling through configurations [11, 12].

This means that the design of products and the fixtures needed for their manufacture is a long process that is implemented in multiple stages. Each stage is characterized by its own specific features [13, 14, 15, 16, 17, 18].

Parametric modeling is used when the designed products have many versions and varieties. A single 3D model is created, where different versions of the product are presented with configurations. This leads to a small amount of design documentation for each specific product. The accumulated big amount of documentation can cause many problems, for example – how to manage, organize, classify and archive the documentation; who has the right to change and update it; the documents should always be with the latest version; which other departments of the company have access to this documentation and the specialized information they are interested in [5, 6].

Parametric modeling reduces the time of the design process and increases its efficiency. Design automation is achieved, which means that designers do not have to redesign the product when there is a change in the dimensions of the model. The dimensions of the model, geometric constructions in the model (*Features*), constraints between parts in an assembly *(Mates)*, etc. can be modelled parametrically.

2.2. 3D bucket models.

Different models of grapple buckets vary in purpose, dimensions and construction. Fig. 1 shows the 3D model of a grapple bucket, for which a fixture is designed and developed [1, 2]. The fixture is used to assemble the bucket's parts and sub-assemblies.
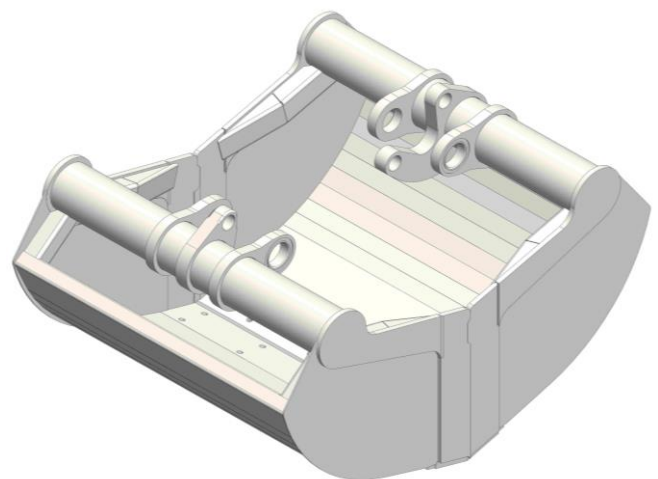

Fig. 1. Grapple bucket 1000 mm.

The grapple buckets of this model come in three types, which differ in length – 640 mm (623016201), 800 mm (623016204) and 1000 mm (623016207).

A set of grapple buckets (left and right) is manufactured for each grapple. Each of them consists of pre-assembled sub-assemblies and parts.
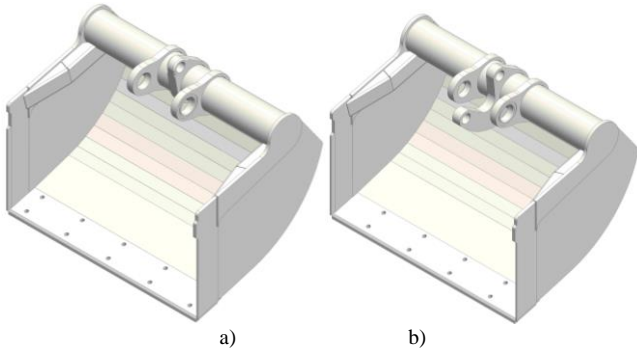
a)   b)

Fig. 2. Components of the grapple bucket 1000 mm.
a) Left bucket, b) Right bucket

Fig. 3 shows the 3D models of the sub-assemblies from which the grapple buckets are made.
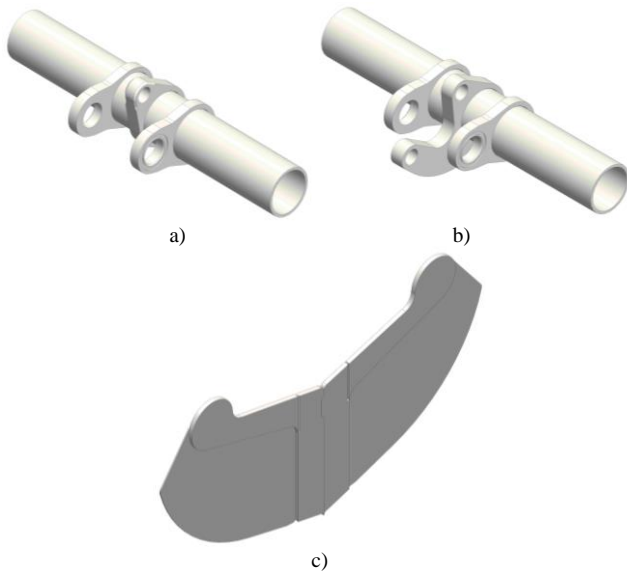

a)   b)

c)

Fig. 3. Sub-assemblies of the grapple bucket 1000 mm.
a) Left tube, b) Right tube, c) Bucket side

Each of the parts from the sub-assemblies is developed by using different 3D modeling commands – *Extruded Boss/Base*, *Revolved Boss/Base*, *Extruded Cut*, *Revolved Cut*, etc. Parts that are made from sheet metal are designed using the module *Sheet Metal* and in this way their unfolding is obtained. The parts are assembled into individual sub-assemblies, which are assembled into the assembly of the bucket [8, 9].

The development of 3D models is consistent with the manufacturing technology of the buckets, as well as with the possibility of using the models from the PDM and ERP systems.

2.3. Technology and fixtures for manufacturing grapple buckets.

According to the requirements in the drawings, the functional surfaces of some of the parts are mechanically processed. After that they are assembled into certain sub-assemblies, which are part of the construction of the left and right grapple buckets. The sub-assemblies are assembled with all other parts of the grapple buckets.

Since the grapple buckets differ only in length, the fixtures for their manufacturing will be of the same type, but with different length. This will significantly reduce the time for developing and constructing the necessary technological equipment, as well as the costs associated with its production.

Additional mechanical processing is applied to parts Blade I and Blade II i.e., chamfers of a certain size are made. To establish them on the machining center, the fixtures shown in Fig. 4 are used [7].
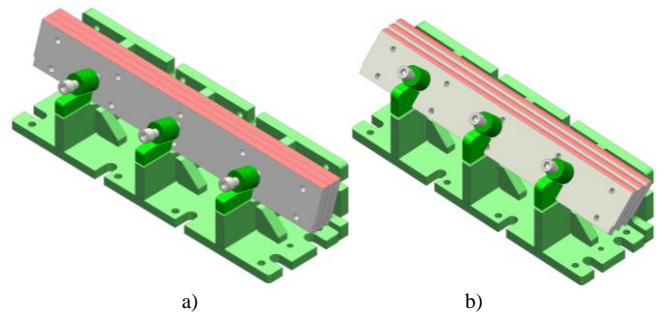

a)   b)

Fig. 4. Fixtures for machining chamfers of Blade I and Blade II parts.
a) Fixture I, for milling a chamfer with an angle of 15°,
b) Fixture II, for milling a chamfer with an angle of 45°

The fixtures are designed for manufacturing Blade I and Blade II parts from the left and right buckets 640 mm, 800 mm and 1000 mm, a total of six models. The fixtures are parametrically modeled through configurations.

Fixtures are used to manufacture the sub-assemblies shown in Fig. 3. A specialized fixture is used to produce the left and right tubes, shown in Fig. 5 [8].
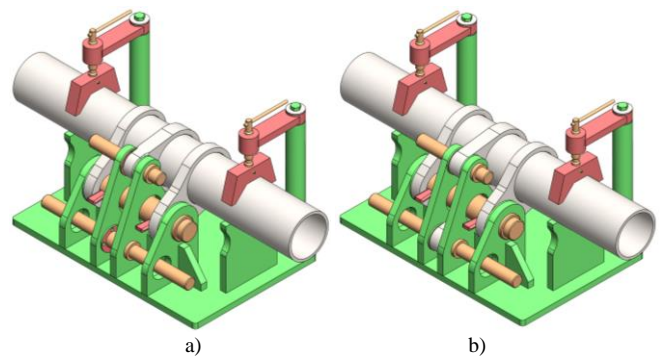

a)   b)

Fig. 5. Fixture for assembling left and right tubes for grapple buckets.
a) Left tube, bucket 1000 mm, b) Right tube, bucket 1000 mm

The fixture is designed for manufacturing left and right tubes for 640 mm, 800 mm and 1000 mm buckets, a total of six models. The fixture is also parametrically modeled through configurations.

The parts of the grapple buckets, as well as the parts of the sub-assemblies, are manufactured according to the drawings and according to the technology developed for each of them. Most of the parts are made of sheet metal. For example, the side and central ears of the tubes are cut from sheet metal of the appropriate thickness, after which all their holes are machined on a machining center. A specialized quick-change fixture is used to set the ears on the machine (Fig. 6). Specialized CAM software is used to create the control program [3].
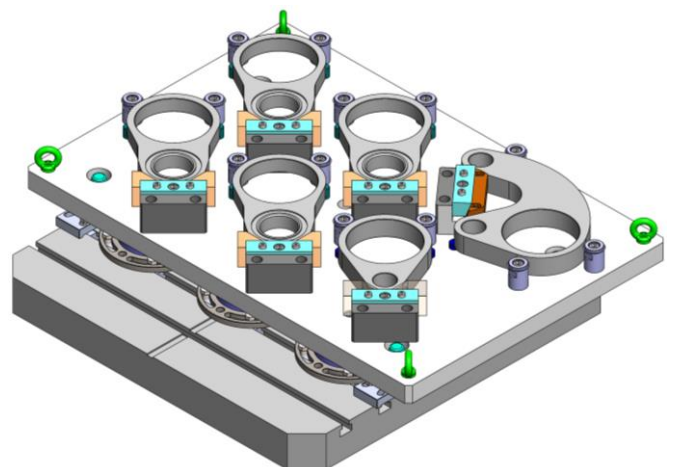

Fig. 6. Fixture for mechanical processing
of the side and central ears of the tubes.

The bucket sides are manufactured from sheet metal parts and are also assembled using a fixture (Fig. 7). After the parts are tack welded, the bucket sides are welded using a welding robot.
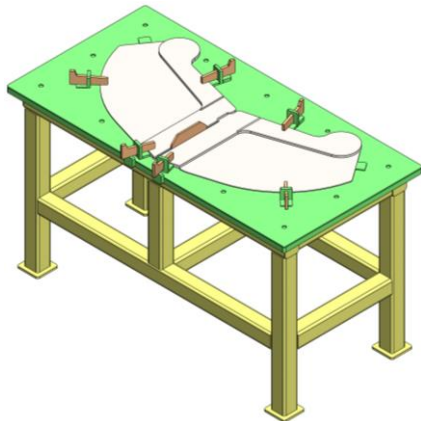

Fig. 7. Fixture for assembling the bucket sides of the grapple buckets.

After the parts and sub-assemblies for the left and right grapple buckets are manufactured, they are assembled using the fixture shown in Fig. 8 [9].
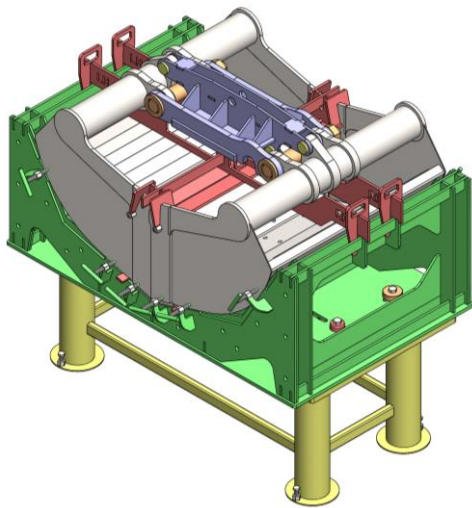

Fig. 8. Fixture for assembling a 1000 mm grapple bucket.

According to the developed technology for assembling grapple buckets, the left and right buckets are manufactured as a set with a specialized fixture. During operation, the fixture is installed on a specially designed table. The table is designed to install all fixtures for manufacturing different models of grapple buckets.

A single 3D model of the fixture for assembling the 640 mm length grapple bucket (623016201) has been developed first. After that, through configurations, the fixture is modeled for grapple buckets with a length of 800 mm (623016204) and 1000 mm (623016207).

3. Parametric modeling of the fixture for assembling grapple buckets.
3.1. Modeling methodology.

The paper presents an approach to improve the efficiency of the fixtures design process by using parametric modeling. The CAD system SolidWorks was used for this purpose [3].

The SolidWorks CAD system enables parametric modeling through *parametric tables* or through *configurations*.

The paper discusses the parametric modeling approach using configurations. During modeling, configurations are created in 3D models of parts, sub-assemblies and assemblies.

A design methodology has been used in the development and modeling of the fixtures with the SolidWorks CAD system. This makes the modeling process easier and reduces the time required for designing. Fig. 9 shows a summarized algorithm of the methodology for designing the fixture for assembling the grapple buckets.
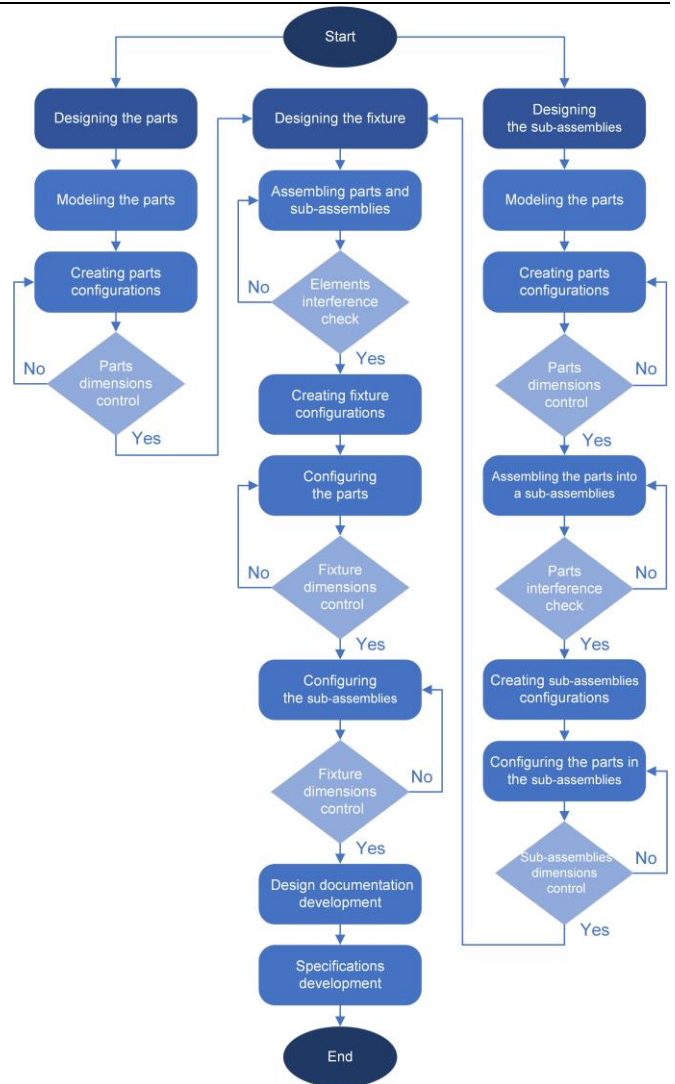

Fig. 9. Algorithm for designing the grapple buckets assembly fixture.

3.2. Parametric modeling of the fixture.

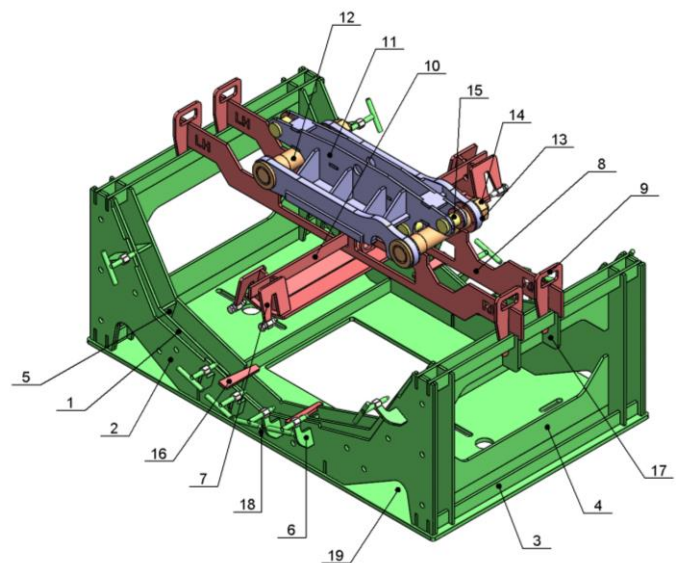The following figures show the components of the fixture [9, 10, 11].

Fig. 10. Components of the fixture.
1 – Base plate I, 2 – Base plate II, 3 – Plate I,
4 – Rib I, 5 – Rib II, 6 – Fixator I, 7 – Fixator II,
8 – Base plate III, 9 – Fixing plate, 10 – Centering plate,
11 – Attachment, 12 – Pin I, 13 – Washer, 14 – Nut M48x3,
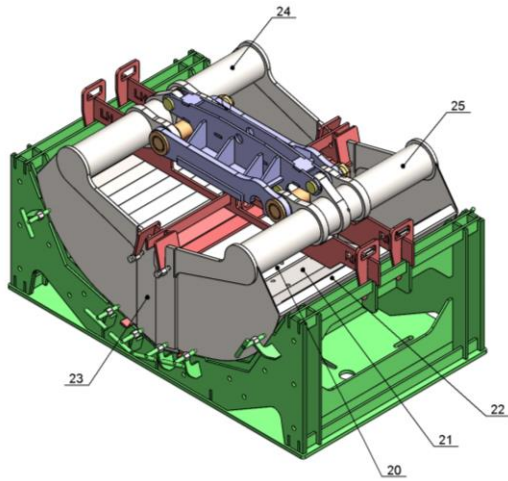15 – Pin II, 16 – Wedge, 17 – Plate II, 18 – Plate III, 19 – Base

Fig. 11. The fixture with established parts and sub-assemblies
of the grapple bucket.
20 – Blade I, 21 – Blade II, 22 – Bottom,
23 – Bucket side, 24 – Left tube, 25 – Right tube

Parts with positions 3, 4, 10 and 19 are parametrically modeled and they have different length configurations.

The sub-assembly with position 7 and the assembly of the grapple bucket consisting of left bucket and right bucket are also parametrically modeled and have configurations with different lengths [11].

To model parametrically the 3D model of the fixture, configurations are created in the *Configuration Manager* (Fig. 12). Each configuration represents a different length of the fixture. For the corresponding bucket lengths, the fixture has the following configurations – 640 mm (PZ 623016201 - 00 00 00), 800 mm (PZ 623016204 - 00 00 00) and 1000 mm (PZ 623016207 - 00 00 00).
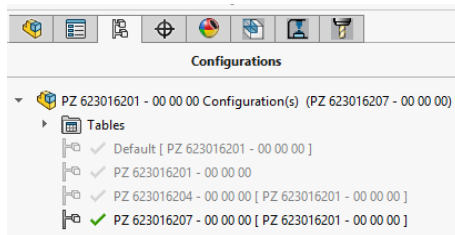

Fig. 12. Configurations in the 3D model of the fixture.

The next step is to configure the parts and sub-assemblies in the assembly of the fixture.

Parts with positions 3 (Plate I), 4 (Rib I), 10 (Centering plate) and 19 (Base) contain configurations with different lengths. For each configuration of the fixture, the corresponding configuration of the parts is set.

Fig. 13 shows the fixture configurations and the specified configurations of the Plate I part. For the corresponding fixture lengths, the Plate I part has the following configurations – 640 mm (PZ 623016201 - 00 00 03), 800 mm (PZ 623016204 - 00 00 01) and 1000 mm (PZ 623016207 - 00 00 01).

Fig. 13. Configuring the Plate I part.

The configurations of the Plate I part have different drawing numbers. The parts differ only in length, so one drawing of the part with a parametric table including each of the variants must be created.

The sub-assemblies in the assembly of the fixture should be configured. These are an assembly with position 7 (Fixator II) and the grapple bucket assembly. They also have different length configurations.

Fig. 14 shows the fixture configurations and the specified configurations of the Fixator II sub-assembly. For the respective fixture lengths, the Fixator II sub-assembly has the following configurations – 640 mm (PZ 623016201 - 02 00 00), 800 mm (PZ 623016204 - 01 00 00) and 1000 mm (PZ 623016207 - 01 00 00).

Fig. 14. Configuring the Fixator II sub-assembly.

The configurations of the Fixator II sub-assembly have different drawing numbers. The sub-assemblies differ only in length, so one assembly drawing of the sub-assembly with a parameter table including each of the variants must be created.

Fig. 15 shows the fixture configurations and the specified configurations of the assembly of the grapple bucket. For the respective fixture lengths, the grapple bucket has the following configurations – 640 mm (623016201), 800 mm (623016204) and 1000 mm (623016207).

Fig. 15. Configuring the grapple bucket.

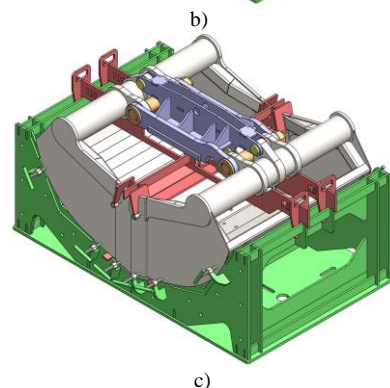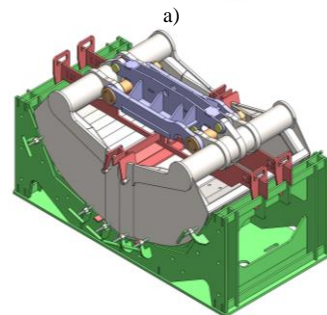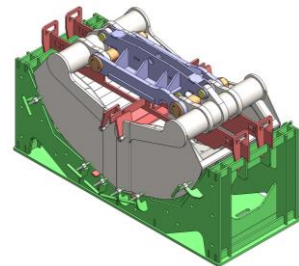Fig. 16 shows the different lengths of the fixture, parametrically modeled with configurations.

a)

b)

c)

Fig. 16. Parametric models of the fixture.
a) 640 mm, b) 800 mm, c) 1000 mm

3.3. Design documentation of the fixture.

Complete design documentation has been made for the developed fixture. The process of its creation is automated by using document *Template files* in the SolidWorks CAD system.

Template files for the *Part* and *Assembly* documents are used to create the 3D models of the parts and assemblies. In the template of each 3D model of the part or assembly, from the *File Properties* menu, in the *Summary Information* window, in the *Custom* section the required attributes (users and systems ones) are selected. The attributes for each configuration are filled in the *Configuration Specific* window [5, 6, 11, 12].

After the attributes of the 3D models have been filled in, the design documentation of the product (drawings and specifications) is developed. For considered example of the fixture, drawings of all parts and sub-assemblies are developed. A drawing of the fixture is also being developed.

To develop the drawings, template files for *Drawing* documents are used, which represent the standard drawing formats – A4, A3, A2, A1 and A0. Information from the attributes is automatically visualized in the drawing tables, in the assembly drawing specifications and in individual product specifications [5, 6, 11, 12].

The following figures show examples of completed templates for the Plate I part (PZ 623016207 - 00 00 01) and the fixture for assembling 1000 mm grapple bucket (PZ 623016207 - 00 00 00).

The following attributes are used in the template of each part – Description (Name of the part), PartNo (Drawing number), AssemblyNo (Assembly from which the part is), Weight (Weight of the part – command "SW-Mass@Part1.SLDPRT"), Material (Material designation – command "SW-Material@Part1.SLDPRT"), Assortment (Type and dimensions of the workpiece), TYPE (Manufacturing operations), DrawnBy (Developed the document), CheckedBy (Checked the document), ApprovedBy (Approved the document), Revision (Document revision).
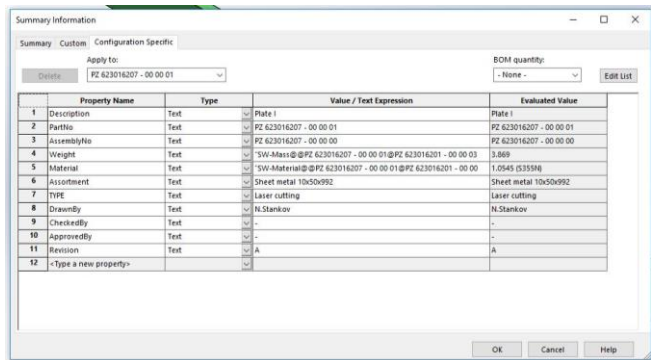

Fig. 17. Template of a Plate I part.

Fig. 18 shows the drawing of a Plate I part, with an automatically filled table, based on the attributes specified in the 3D model of the part.
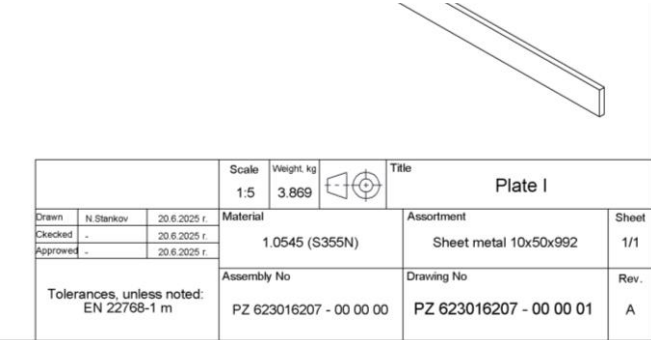
Fig. 18. Drawing of the Plate I part.

The following attributes are used in the template of each assembly – Description (Name of the assembly), PartNo (Drawing number), AssemblyNo (Assembly unit from which the current assembly is), Weight (Weight of the assembly – command "SW-Mass@Assem1.SLDPRT"), TYPE (Manufacturing operations),

DrawnBy (Developed the document), CheckedBy (Checked the document), ApprovedBy (Approved the document), Revision (Document revision).
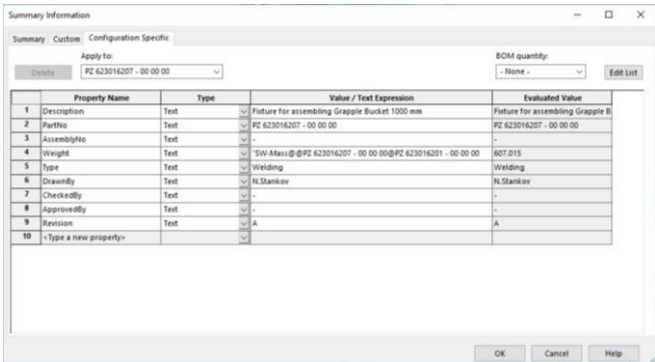
Fig. 19. Template of the fixture for assembling a 1000 mm grapple bucket.

Fig. 20 shows the drawing of the fixture, with an automatically filled table and specification, based on the attributes set in the 3D model of the assembly.
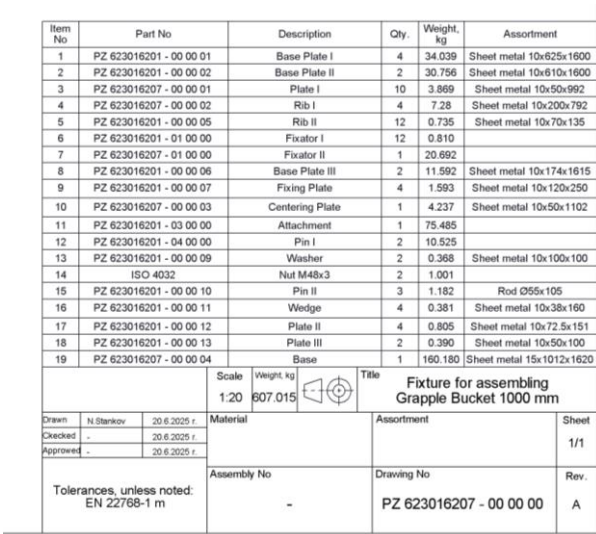
Fig. 20. Drawing of the fixture for assembling a 1000 mm grapple bucket.

After the 3D models of the parts, sub-assemblies, assemblies and all drawings of the fixture have been developed, the next step is their management by the specialized systems – PDM and ERP. The design documentation is managed by the PDM system Solid-Works Enterprise PDM [3]. The various departments of the company have access to this information and operate with it through the ERP system Microsoft Dynamics NAV ERP [4].

Fig. 21 shows an example card of a fixture (PZ 623016207 – 00 00 00) for assembling a 1000 mm grapple bucket (623016207) in the ERP system.
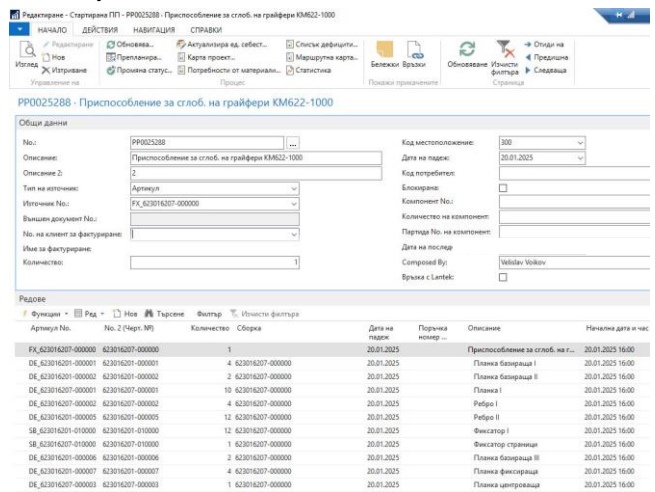
Fig. 21. Card of the fixture for assembling a 1000 mm grapple bucket.

4. Methods for modeling the fixture.

A certain product can be designed by applying two main methods – *traditional modeling* or *parametric modeling*. Both approaches are applied in practice. The method to be used is also chosen depending on the products being developed.

The paper discusses the approach to parametric modeling through configurations. The fixture for assembling the grapple buckets is modeled. The modeling of 3D models of parts and assemblies as well as the creation of drawings and product specifications, are presented.

The parametric modeling approach through configurations has been chosen because of the advantages it has. The reason for using this approach becomes clear after comparing the two modeling methods.

4.1. Traditional modeling of the fixture.

In the traditional modeling approach, a 3D model of the fixture is created for each size of bucket that is assembled. The 3D model of the fixture is an assembly composed of parts and sub-assemblies. All parts are modeled in advance. Parts that are structurally the same but differ in length, for different fixtures models must be modeled as separate parts. There are 5 such parts in the fixture. These parts are Plate I, Rib I, Centering plate, Base and part Main plate from Fixator II sub-assembly. Some of the parts are the same for all fixtures and they are modeled once. After modeling the parts, they are assembled into the 3D models of the fixtures. Table 1 shows the fixtures and their components.

Table 1. Fixtures, designed using the traditional modeling approach.

Fixture size, mm	640	800	1000
Number of unique parts, that do not require changes	32		
Number of parts that require changes	5	5	5
Total number of parts	154	154	154
3D model of the fixture (Assembly)	Yes	Yes	Yes

This approach has many disadvantages:

- a large number of parts that must be modeled in advance;

- a large number of assemblies to model;

- possible modeling errors due to the large variety of 3D models of parts and assemblies;

- creation of a big amount of design documentation – drawings of parts, drawings of assemblies, specifications;

- redesigning the product when the size is different.

All these leads to a decreased efficiency of engineering work during design and an increased possibility of errors.

4.2. Parametric modeling of the fixture.

In parametric modeling through configurations, a single 3D model of the fixture is modeled and it includes all its variations (Table 2). The 3D model of the fixture is composed of parts and sub-assemblies. All parts are modeled in advance. Parts that differ only in length are modeled parametrically through configurations. The parts are assembled into sub-assemblies, which are modeled parametrically. The sub-assemblies are assembled into the assembly of the fixture, which is also modeled parametrically.

Table 2. Fixture, designed using the parametric modeling approach.

Fixture size, mm	640	800	1000
Number of unique parts, that do not require changes	32		
Number of parts that require changes	5		
Total number of parts	154		
3D model of the fixture (Assembly)	Yes		

Parametric modeling through configurations achieves high design efficiency, which is an advantage of the method. This is especially important when designing and modeling with CAD systems.

According to the data presented in the Table. 1 and Table. 2, the following conclusions can be made:

- in traditional modeling, the total number of parts and fixtures that need to be modeled is bigger – **47** parts and **3** fixtures, compared to **37** parts and **1** fixture in parametric modeling;

- parametric modeling significantly increases the efficiency of engineering work - the volume of design documentation created is reduced and the time required for modeling products is reduced;

- as a result of the smaller amount of design documentation, the number of errors in product modeling is significantly reduced;

- reducing design time is especially important in modern working conditions, where engineering departments consist of only a few people;

- parametric modeling is an approach that should be used for products with many variants and variations, as is the case with the considered fixture for manufacturing grapple buckets.

5. Conclusion.

1. An approach for parametric modeling of technological equipment to produce specialized products using a CAD system is presented. The implementation of parametric modeling through the SolidWorks CAD system allows significant automation in the design of fixtures. The use of configurations facilitates the creation of various product variants, reducing the time and volume of manually created documentation. Parametric modeling facilitates the process of developing products that have many variants and varieties.

2. The use of attributes (user and systems ones) in the 3D models of parts and assemblies enables the automated creation of design documentation (drawings of parts, drawings of assemblies and specifications).

3. The proposed approach of modeling through configurations improves the efficiency of engineering work, by reducing the design time, the volume of the designing documentation and errors during product design.

4. The presented integration between the 3D models and PDM system allows effective management of a large volume of design documentation. The files can also be used by other company departments through ERP system.

5. The presented approach is applicable to other similar products, and this emphasizes its universal nature. In this way, similar problems related to the development and management of documents can be solved.

6. References.

1. https://www.kinshofer.com/en/. 2025.

2. https://sl-industries.com/bg/. 2025.

3. https://www.solidworks.com/. SolidWorks, 3D Design Software. SolidWorks CAM, CAM Software. SolidWorks Enterprise PDM, PDM Software. 2025.

4. https://www.dynamicssquare.co.uk/products/microsoft-dynamics-nav/. ERP Software, Microsoft Dynamics NAV ERP. 2025.

5. Stankov N., Al. Ivanov. **Design documentation management with SolidWorks Enterprise PDM.** Collection of scientific works, vol. 54, series 2, "Mechanics and Mechanical Engineering Technologies", p. 158-165, Ruse, Bulgaria, 2015, ISSN 1311-3321. *https://conf.uni-ruse.bg/bg/docs/cp15/2/2-26.pdf*

6. Truhcheva D., N. Stankov, Al. Ivanov. **Management and organization of design documentation with SolidWorks and SolidWorks Enterprise PDM.** Collection of reports of a student scientific session – SSS'15, p. 20-30, Ruse, Bulgaria, 2015, ISSN 1311-3321. *https://conf.uni-ruse.bg/bg/docs/sns/2015/MTF.pdf*

7. Stankov N. **Technology and fixtures for machining of parts for grapple buckets.** XIX International Scientific Congress – Summer Session, "Machines. Technologies. Materials", Section

"Technologies", vol. 4, p. 308-312, Varna, Bulgaria, 2022, ISSN 2535-0021 (Print), ISSN 2535-003X (Online). *https://mtmcongress.com/winter/sbornik/4-2022.pdf*

8. Stankov N. **Technology and fixture for assembling of the left and right tubes for grapple buckets.** XX Jubilee International Scientific Congress – Winter Session, "Machines. Technologies. Materials", Section "Technologies", vol. 2, p. 101-105, Borovets, Bulgaria, 2023, ISSN 2535-0021 (Print), ISSN 2535-003X (Online). *https://mtmcongress.com/winter/sbornik/2-2023.pdf*

9. Stankov N. **Technology and fixture for assembling grapple buckets.** XX Jubilee International Scientific Congress – Summer Session, "Machines. Technologies. Materials", Section "Technologies", vol. 3, p. 209-213, Varna, Bulgaria, 2023, ISSN 2535-0021 (Print), ISSN 2535-003X (Online). *https://mtmcongress.com/winter/sbornik/3-2023.pdf*

10. Stankov N. **Technology and fixture for control of grapple buckets**. XXI International Scientific Congress – Summer Session, "Machines. Technologies. Materials", Section "Machines", vol. 2, p. 186-190, Varna, Bulgaria, 2024, ISSN 2535-0021 (Print), ISSN 2535-003X (Online). *https://mtmcongress.com/winter/sbornik/2-2024.pdf*

11. Stankov N. **Designing and modeling of grapple buckets.** International Scientific Journal "Machines. Technologies. Materials", Section "Machines", vol. 19, Issue 2, p. 42-48, 2025, ISSN 1313-0226 (Print), ISSN 1314-507X (Web). *https://stumejournals.com/journals/mtm/2025/2/42*

12. Stankov N., Al. Ivanov. **Automated design and parametric modeling of excavator buckets.** Journal "Applied Sciences", 2025, vol. 15, Issue 6, 3389, Section "Mechanical Engineering", Special Issue "Computer-Aided Design in Mechanical Engineering", ISSN 2076-3417. *https://doi.org/10.3390/app15063389*

13. Miedema, S.A. **Sensitivity Analysis of the Production of Clamshells**. WEDA J. Dredg. Eng. 2008, 9 (1).

14. Xu, C.; Xiao, H.; Zou, S.; Zeng, R. **Research on Monitoring Force of Steel Wire Rope of Grab Dredger Base on Wireless Sensing.** Procedia Engineering 2017, 174, 385–391.

15. M. Javad Mohajeri, W. de Kluijver, Rudy L.J. Helmons et al. **A validated co-simulation of grab and moist iron ore cargo: Replicating the cohesive and stress-history dependent behaviour of bulk solids.** Advanced Powder Technology 32 (2021) 1157–1169.

16. D. Schott, J. Mohajeri, J. Jovanova et al. **Design framework for DEM-supported prototyping of grabs including full-scale validation.** Journal of Terramechanics 96 (2021) 29–43.

17. Xu, C.; Li, Z.; Zhu, Z.; Li, Z. **Unit Integration Method Solution and Experimental Research on Mechanism Characteristics for Flat Digging of Grab Dredgers.** Appl. Sci. 2022, 12, 6968. *https://doi.org/10.3390/app12146968*

18. Ding, J., Ding, H., Yang, W. **Dynamic Modeling of a Novel Multi-Loop Multi-Body Mechanism of Face-Shovel Excavator.** Chin. J. Mech. Eng. 38, 38 (2025). *https://doi.org/10.1186/s10033-024-01166-7*

Development of an Internal Combustion Engine for Shell Eco-marathon Competition Vehicle

BSc Aleksander Jänes*, MSc Vello Vainola, BSc Janis Piiritalo
TTK University of Applied Sciences, Estonia
*masin@tktk.ee

Abstract: *In this article, the authors describe the development process of a custom internal combustion engine (ICE) for a vehicle competing in the Shell Eco-marathon. The engine will be designed to replace the Honda GX35 previously used in the vehicle. The new engine has to comply with competition regulations and improve the overall fuel efficiency of the vehicle. An engine test stand was developed for measuring the power and brake-specific fuel consumption (BSFC) of small IC engines which allowed tests to be carried out on the GX35 to collect data for the design. Based on the data obtained from the tests and the information gathered from educational materials, a suitable IC engine will be later developed.*

Keywords: *INTERNAL COMBUSTION ENGINE, SHELL ECO-MARATHON, BSFC, FUEL EFFICIENCY, HONDA GX35, ENGINE DESIGN*

1. Introduction

The aim of the project is to design a custom internal combustion engine for a vehicle participating in the Shell Eco-marathon. The engine must comply with the regulations of the competition and improve the energy efficiency of the vehicle. The custom engine is a further development of the currently used Honda GX35 and will be more in line with the basic principles and purpose of the vehicle. This article will focus specifically on gathering the information needed for the design.

The research described in this article is being carried out as part of a student project at the TTK University of Applied Sciences. The project team is working on the development of an ICE eco-vehicle for the Shell Eco-marathon competition series. The goal of the competition is to build a vehicle that is as energy efficient as possible. Competitors are given one litre of fuel to cover as much distance as possible. The series takes place on famous circuits around the world and is divided into three major regions: America, Europe-Africa and Asia and the Middle East.

The vehicles participating in the Shell Eco-marathon are divided into two main classes, UrbanConcept and Prototype (Fig 1). The vehicle being built by the TTK team is in the Prototype class. In this class, the aim is to maximise fuel efficiency by any means necessary and everything else, including driver comfort, is secondary. The vehicles are usually three-wheeled, light and have an elongated aerodynamic shape. The current official world record for the Prototype class is 3,771 kilometres per litre of gasoline. [1]

Fig. 1 *Prototype class competition vehicle.*

Until now, the vehicle of the TTK team has been powered by a Honda GX35 engine. It is a 35.8 cm³ four-stroke, air-cooled gasoline engine, mainly intended for use on trimmers, brushcutters, cultivators, water pumps and various construction and industrial equipment. Thanks to its simple design, compactness and a suitable displacement, the engine is widely used by teams in the Eco-marathon series. [2]

Before starting development on the new engine, the project team made significant modifications to the GX35 (Fig 2). Amongst other things, a new exhaust system was manufactured, a fuel injection system with a programmable electronic control unit (ECU) MaxxECU MINI was added, along with the corresponding sensors and components, and an electric starter was attached to the engine.
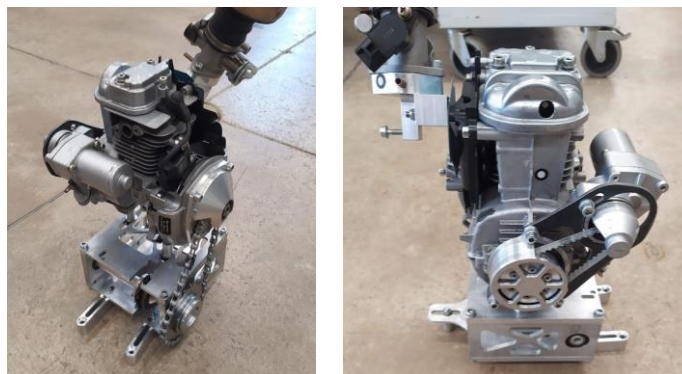

Fig. 2 *Honda GX35, the previous engine of the vehicle.*

When designing a new engine, it is essential to ensure that it complies with all Shell Eco-marathon competition regulations and requirements. The following are the competition rules for engines and transmission systems [3]:

1) There are no restrictions on the type and design of internal combustion engines, but they must run on the fuel provided by the Organizers and must not consume engine oil (two-stroke engines are not permitted).

Teams using internal combustion engines can choose between three fuels:

a) Shell FuelSave unleaded gasoline with an octane rating of 95,
b) Shell FuelSave diesel,
c) Ethanol E100 (denatured);

2) Carburettor engines are prohibited (fuel injection systems are mandatory);

3) The engine must have an electric starter; manual starting of the engine is prohibited. The starter must not contribute to the forward propulsion of the vehicle in any way;

4) All vehicles with internal combustion engines must have a clutch system;

5) If a centrifugal/automatic clutch is used, the engine speed generated by the starter must be lower than the speed at which the clutch engages;

6) The intake manifold must not contain or allow the accumulation of fuel or crankcase gases. Crankcase gases must not be directed into the intake system and must be collected in a container for environmental protection purposes. The use of air filters in the intake system is prohibited;

7) The vacuum generated in the intake system must not be used for external devices/components;

8) The environmental impact of all vehicles (exhaust smoke, odor, and noise levels) must be within reasonable limits.

In addition to the competition rules, one of the most important design requirements is the compactness of the engine, which would allow the vehicle to use a single-stage transmission.

2. IC Engine Test Methodology Development

Before design work could begin, it was first necessary to collect relevant and usable data. For this purpose, a test methodology was developed for testing and comparing small IC engines.

The main parameter to be compared in the context of this project is the brake specific fuel consumption (BSFC) of the engines. BSFC is a parameter that indicates the efficiency of an internal combustion engine in producing power from the fuel burned. The unit of BSFC is kilograms per joule (kg/J), the lower the value, the more efficient the engine. BSFC is expressed by the formula [4]:

$$BSFC = \dot{m} / P , \quad (1)$$

where $\dot{m}$ – fuel mass flow rate, kg/s;
P – effective (brake) engine power, W.

Usually however, units of grams per second (g/s) and kilowatts (kW) are used in this context, which gives BSFC a unit of grams per kilowatt-hour (g/kWh). [4]

The engine output power is derived from the engine speed and the corresponding torque and can be calculated using the following formula [5]:

$$P = 2 * \pi * M * n , \quad (2)$$

where n – engine speed, r/min;
M – effective (brake) engine torque, Nm.

Therefore, to test and compare engines, it is necessary to measure the mechanical power and, at the same time, the amount of fuel consumed by the engine. This makes it possible to map the brake specific fuel consumption of the engine, which is the main basis for comparisons.

In order to measure the torque and mechanical power of the engine at different speeds, a suitable dynamometer had to be created. For this purpose, several methods based on different principles, such as electrical and hydraulic, were tested during development.

The finalized dynamometer is based on the Lucas-Nülle CO3636-6X electric motor test system. The test stand consists of a digital controller, a 4.2 kW servo motor, and ActiveServo software. The servo motor, which acts as a brake for the IC engine, can be controlled manually or via software. It is possible to program the speed or torque of the servo, either statically or dynamically, according to the user's specifications. [6]

Fig 3. Left - L-N CO3636-6X [6], right - finalized engine test-stand.

In addition to measuring engine power and torque, it is also necessary to know the corresponding fuel consumption. It was decided that the engine's electronic control unit was to be used to measure this.

The MaxxECU MINI programmable ECU used in the vehicle provides essentially unlimited access to all possible information related to the sensors and actuators used in the vehicle. Amongst other values, it is possible to know the duration of the time that the fuel injector has stayed open, i.e. the time during which fuel exits the fuel system and enters the engine combustion chamber. Knowing the size of the injector (the amount of fuel flowing out of the injector per minute) expressed in cm^3/min, it is possible to calculate the theoretical amount of fuel injected.

However, it should be noted that the actual size of the injector may differ to some extent from the nominal size. There is also a

delay in fuel injectors called injector dead time which depends on several factors such as battery voltage and fuel system pressure.

In order to determine the fuel consumption during engine operation using the control unit, thorough tests were carried out to calibrate the vehicle's fuel system and to measure the actual size of the injector and the injector dead time. The tests consisted of mapping the characteristics of the injector at different input voltages. Using pulse width modulation, the injector was switched to operate at different pulse widths for a fixed time, after which the mass of the collected fuel was weighed.

To find the injector dead time, the pulse width and the corresponding mass of one injection were plotted on a coordinate system, where the pulse width is the y-value and the fuel mass per injection is the corresponding x-value. If a line is drawn, which is the approximation function of the points, then the shift value (marked red in the graph) of this function is the injector dead time (Fig. 4).
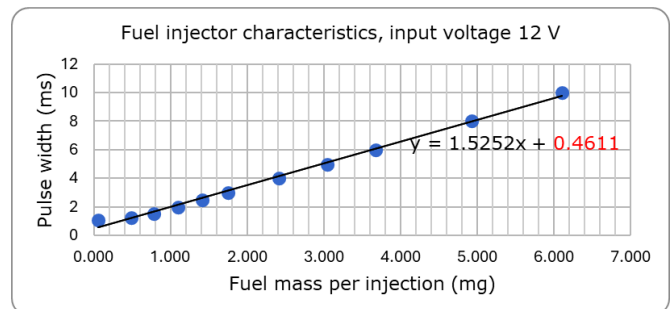

Fig 4. Fuel injector test result at 12V.

The data obtained from the fuel system calibration was entered into the control unit and the fuel consumption calculation was programmed in the software. As a result, the ECU log records the mass of fuel consumed during engine operation (Fig. 5)
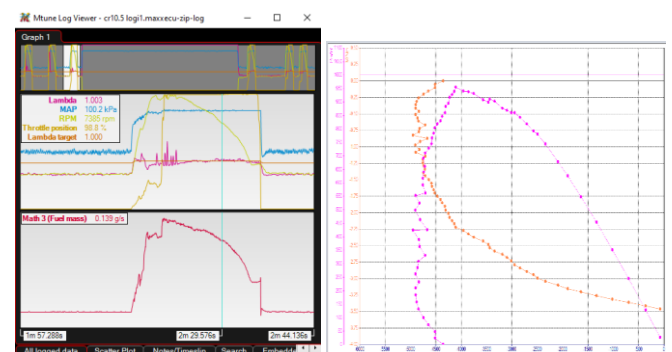
Fig 5. Left - ECU log with fuel data, right – dyno test data.

By combining the fuel consumption with data obtained from the dynamometer, it is possible to test engines and map their power and torque curves together with BSFC (Fig. 9).

3. Engine Testing - Data Collection

After developing the test methodology, tests were conducted on the vehicle's GX35 engine to get an overview of the current situation, identify the engine's bottlenecks, and find possible areas for development. Various modifications were made to the engine with the aim of improving its performance and efficiency. The data obtained from the tests and the conclusions drawn from them will be used as input for the design of the new engine.

Honda has published both the torque and power curves for the GX35. The corresponding values have been measured in accordance with the SAE J1349 standard. The engine's maximum power is 1 kW at a speed of 7000 rpm. The maximum torque is 1.6 Nm at 5500 rpm. Less data is provided on fuel efficiency, only the consumption at maximum power is given, 0.71 L/h at 7000 rpm [2].

Chalmers Vera Team, a team participating in the Shell Eco-marathon, commissioned a study on the fuel efficiency of the Honda GX35 from Semcon. The study mapped the BSFC of the engine at different speeds. The results of these tests showed that the GX35 achieves its best fuel efficiency at a speed of approximately 4200 rpm, with a BSFC of approximately 380 g/kWh (Fig 6). [7]
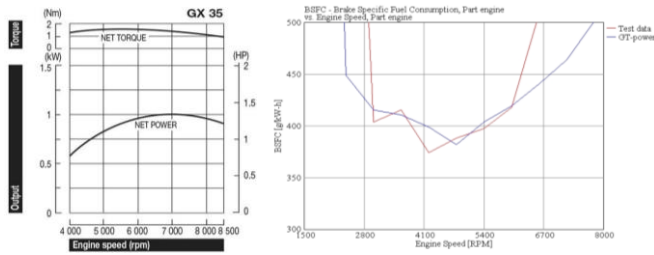

Fig 6. GX35 test data from online sources.[2][7]

Since the TTK team now had the necessary capabilities, new tests were carried out on an unused GX35 engine, which was first run in according to the manufacturer's recommendations. Testing took place over a period of three weeks. A total of about 50 different engine configurations were tested.
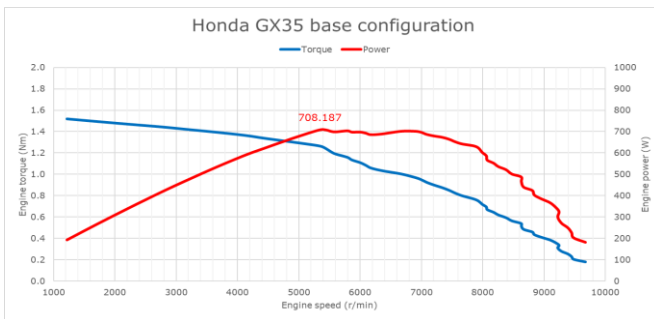First, the standard configuration of the GX35 was tested (Fig. 7).

Fig 7. GX35 base configuration test data from the new test stand.

While analysing the results, it was concluded that the engine power curve matched Honda's graph, but the absolute value of the output parameters differed slightly from the manufacturer's data. The maximum power of the engine was measured at 708.19 W. The lower result is probably explained by the losses occurring in the transmission between the engine and the servo motor.
Using the base configuration with a carburettor, the team was unable to obtain real-time data on fuel consumption, which is why BSFC is not shown in the graph. By adding an injection system to the base configuration, it was also possible to map the fuel consumption, which was measured to be 478.83 g/kWh at approximately 4000 rpm.

After testing the stock configuration, several different modifications were made to the GX35 with the aim of improving engine performance and increasing fuel efficiency.

Fig 8. Modifications made to the engine. Top left – custom exhaust vs stock GX35. Top right – GX35 stock con rod vs custom. Bottom left – stock camshaft vs machined. Bottom right – GX35 cut open for examination.

Due to the design of the GX35, the physical modifications that could be made to the engine were limited, but there were still some aspects that could be improved.

The most significant modifications were increasing the engine compression ratio, manufacturing a new exhaust system, and remachining the profile of the camshaft (Fig. 8).
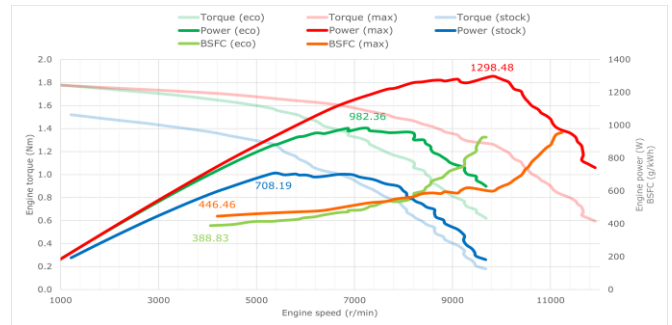

Fig 9. Comprehensive data from the tests.

The most economical configuration of the tests yielded a minimum brake specific fuel consumption of 388.83 g/kWh and a power output of 982.36 W. Compared to the base configuration, this represented a 19% improvement in both power and efficiency (Fig. 9). In this test, the compression ratio of the engine was increased from 8:1 to 10.5:1 and a new exhaust system was used.

In the most powerful configuration, the maximum power of the engine was measured at 1298.5 W, which is an 83.4% increase compared to the first test (708 W), an almost a twofold increase in engine performance (Fig. 9). Although this configuration is not reasonable for an eco-vehicle due to high fuel consumption and impractical engine speed, the test showed that the various components of the engine have a significant safety factor and could also be used in a somewhat larger engine.

4. Design of the New Engine - Engine Parameters

Based on the data obtained from tests and the information gathered from educational materials, automotive handbooks and reports made by competing teams, a suitable internal combustion engine will be designed. The engine will be made up of both custom manufactured parts and components reused from the Honda GX35.

The engine will be of the same type as the GX35 used until now. Thus, the new engine will also be a four-stroke, single-cylinder, air-cooled, overhead cam gasoline engine. It is not reasonable to change the engine type (fuel, operating cycle), as the development has focused entirely on such gasoline engines. Several components used in the new engine are selected from the GX35, as the manufacture of some of them is not possible with the university's equipment or is unreasonably complicated. In addition, the design of certain subassemblies is a much more time-consuming process that requires more thorough analysis than the available time allows.

Before the physical design of the engine can begin, the design parameters that affect the performance characteristics of the engine must be determined. This is based on the objectives of the competition, vehicle-related restrictions, previously conducted tests, and data collected from various sources. The most important parameters are the cylinder bore, piston stroke, compression ratio, and connecting rod length.

First, the cylinder bore and piston diameter for the engine were selected. This was determined by the technological limitations of the project team. Namely, it is difficult to manufacture custom piston rings in the laboratory conditions. It was decided that it would be reasonable to use the existing GX35 pistons and piston rings. The cylinder bore of the new engine is therefore 39 mm.

The main factor in selecting the piston stroke length was the bore/stroke ratio, which is one of the important parameters used to characterize piston engines. The Chalmers Vera Team report concluded that teams participating in the Eco-marathon series use varying stroke ratios in their engines. However, it was noted that short-stroke engines are rarely used and, in most cases, a long-stroke ratio or a square engine is preferred, with the ratio varying between 0.5 and 1. [8]

Because of the characteristics of the vehicle, it is important that the power curve of the new engine is shifted towards the lower revs. Therefore, it was decided that the stroke had to be lengthened. At the same time, it had to be considered that an increase in the piston stroke would also increase the engine's displacement. However, increasing the engine's size and performance is not infinitely beneficial, because above a certain point, it becomes excessive and less efficient for the vehicle. As a compromise, a piston stroke of 39 mm was chosen for the new engine, in which case the stroke ratio is 1 and the engine is square.

Another crucial parameter in terms of engine efficiency is the compression ratio. Tests showed that increasing the compression ratio of the GX35 from the original 8:1 to 10.5:1 significantly improved engine performance and fuel efficiency. The compression ratio of gasoline engines used in the competition is usually quite high, reaching up to 14:1. However, as the compression ratio increases, the increase in efficiency is not infinite. Additionally, very high compression ratios can cause negative effects, such as detonation, in which case the air-fuel mixture ignites uncontrollably before the spark plug fires. To avoid this, a more conservative compression ratio of 12:1 was initially selected for the engine. Since the new engine will be designed to be more easily modified than the GX35, the compression ratio can be increased or decreased later as needed, for example by changing the thickness of the cylinder head gasket.

A computational model of the kinematics and dynamics of the crankshaft mechanism was created to select the length of the connecting rod and the subsequent rod to stroke ratio. The model was used to compare the effect of different con rod lengths on piston acceleration and piston side force at a fixed engine power.

Using the model, it was noted that extending the connecting rod by even a relatively small amount noticeably reduces the piston thrust force on the cylinder wall. Therefore, it was decided to select the largest possible rod to stroke ratio for the engine, i.e., the connecting rod length was determined by the design limitations of the vehicle chassis. It was found that the maximum connecting rod length that leaves sufficient space under the upper cover of the vehicle is 150 mm. With a piston stroke of 39 mm, the rod to stroke ratio is 3.85.

The following table (Table 1) summarises the selected design parameters of the new engine. For comparison, the corresponding dimensions of the Honda GX35 are shown alongside.

Table 1: Main parameters of the GX35 and the new engine.

Parameter	Honda GX35	Custom Engine
Cylinder bore (mm)	39	39
Stroke (mm)	30	39
Displacement (cm^3)	35,84	46,59
Bore to stroke ratio	1,3	1
Compression ratio	8:1	12:1
Combustion chamber volume (cm^3)	5,12	4,24
Connecting rod length (mm)	51	150
Rod to stroke ratio	1,7	3,85

5. Results and Discussion

The aim of the research was to gather data for the design of a custom internal combustion engine for a vehicle participating in the Shell Eco-marathon. The engine must comply with the rules of the competition, increase the energy efficiency of the vehicle and

eliminate the shortcomings caused by the unsuitability of the previously used Honda GX35 engine.

The research was divided into three main parts.

First, a test methodology was developed for testing and comparing small internal combustion engines, using brake specific fuel consumption as the comparable parameter. For this purpose, a suitable test stand was created, which can be used to measure the output parameters of IC engines. While measuring engine power, it was also necessary to determine the amount of fuel consumed. This was done using the engine's electronic control unit together with the data obtained while calibrating the fuel system.

Tests were then carried out on the vehicle's old engine, the Honda GX35, to map the current status of the project and collect data needed for the design. During the tests, several different modifications were made to the GX35 with the aim of increasing its fuel efficiency. The most economical configuration of the modified engine ultimately showed a nearly 19% reduction in BSFC and the most powerful configuration showed an approximately 85% increase in power.

Based on the data obtained from the tests and the information collected from educational materials, the main design parameters of the new engine were chosen. Although the new engine will reuse some components from the GX35, it will significantly differ from that engine. The chosen parameters are the basis for the physical design which will be described in a future article.

The research and development discussed in this article can be considered successful. The engine test methodology development along with the tests carried out on the GX35 are of crucial significance to both the design of the engine and the future development of the project as well as educational work related to the subject.

References

1. Shell Eco-marathon, „Everything You Need to Know About Shell Eco-marathon", [Accessed: 28 05 2025] [Online]. Available: https://www.shellecomarathon.com/stories/everything-you-need-to-know-about-shell-eco-marathon.html

2. Honda Engines, „GX35", [Accessed: 28 05 2025] [Online]. Available: https://engine.honda.ca/en/mini_4_stroke/gx35

3. Shell, „Shell Eco-marathon 2024 Official Rules, Chapter I", [Accessed: 28 05 2025] [Online]. Available: https://www.shellecomarathon.com/about/global-rules.html

4. X-Engineer, „Brake Specific Fuel Consumption (BSFC)", [Accessed: 28 05 2025] [Online]. Available: https://x-engineer.org/brake-specific-fuel-consumption-bsfc/

5. K.-H. Dietsche, K. Reif, „Bosch Automotive Handbook, 11th Edition", Karlsruhe: Robert Bosch GmbH, 2022, pg 709–710.

6. Lucas-Nülle, „Dynamic servo machine test system for 0.3kW machines incl. software ActiveServo", [Accessed 28 05 2025] [Online]. Available: https://www.lucas-nuelle.us/2776/pid/22637/apg/11298/Dynamic-servo-machine-test-system-for-03kW-machines-incl-software-ActiveServo.htm

7. D. Willermark, F. Dunert, „GT-power Simulation Report", Semcon, 2009. [Accessed 28 05 2025] [Online]. Available: https://www.chalmersverateam.se/Rapporter/GTPowerGX35.pdf

8. A. Johansson, A. Thulin, „Design of a Fuel Efficient Internal Combustion Engine", Chalmers University of Technology, Sweden, 2010. [Accessed 30 05 2025] [Online]. Available: https://www.chalmersverateam.se/Rapporter/Mk1%20Engine%20Design.pdf

Effect of vortex generator shape and attack angle on thermal-hydraulic performance of a finned-tube heat exchanger

Josip Batista[1*], Paolo Blecich[1], Mateo Kirincic[1], Fran Torbarina[2]
University of Rijeka, Faculty of Engineering, Vukovarska 58, Rijeka. Croatia[1]
University of Rijeka, Faculty of Maritime Studies, Studentska 2, Rijeka, Croatia[2]
josip.batista@riteh.uniri.hr

Abstract: *The objective of this study is to numerically investigate the fluid flow and heat transfer performance of a finned-tube heat exchanger (FTHEX). The analysis focuses on the implementation of three vortex generator (VG) configurations: rectangular winglet (RW), delta-winglet upstream (DWU), and delta-winglet downstream (DWD) — mounted on the fin surface in a "common-flow-up" orientation. Attack angles of 15°, 30°, and 45° are considered for each VG type to evaluate their impact on the heat exchanger's heat transfer potential and friction losses. The air-side Reynolds number, based on the outside tube diameter, was varied within the range $684 \leq Re \leq 1532$. The results indicate that among the tested configurations, the RWP setup with an attack angle of 45° achieves the highest enhancement in the air-side Nusselt number, with improvements ranging from 20% to 45% compared to the reference configuration, but at the expense of a higher pressure drop. For attack angles $\alpha_{vg} = 15°$ and $\alpha_{vg} = 30°$, the highest overall performance (TPF factor) is achieved with the rectangular winglet configuration across the entire Reynolds number range. At an attack angle of $\alpha_{vg} = 45°$, the heat exchanger with downstream delta winglets shows higher TPF values compared to the other configurations, except at Re = 1278.*
Keywords*: HEAT EXCHANGERS, HEAT TRANSFER ENHANCEMENT, VORTEX GENERATORS, NUMERICAL ANALYSIS.*

1. Introduction

Finned-tube heat exchangers (FTHEXs) are widely used across various industries, including aerospace, chemical processing, refrigeration, and electronics cooling. A key challenge in their design is achieving optimal thermal performance while operating within constraints such as limited space, minimal flow resistance, and reduced material usage. In most cases, the primary source of thermal resistance in these devices is on the gas side [1]. To enhance heat transfer efficiency, researchers have proposed a number of innovative techniques.

Longitudinal vortex generators (VGs), as a passive heat transfer enhancement technique, have been extensively studied for improving the performance of heat exchangers. These small flow-disturbing devices create longitudinal vortices that promote fluid mixing, disrupt the boundary layer, and delay flow separation. As a result, the convective heat transfer on the gas side is increased, making them an effective and energy-efficient solution for compact and high-performance heat exchanger designs [2]. The conventional shapes of vortex generators are usually in form of delta wings, rectangular wings, delta winglets, rectangular winglets, and trapezoidal winglets. Rectangular and delta winglets are preferred VG shapes, representing the most widely investigated configurations in experimental and numerical studies.

The application of VGs to improve the thermal performance of heat exchangers dates back to the mid-1970s when Edwards and Alker [3] conducted one of the first experimental investigations on the effects of delta winglets and block-shaped inserts on the average Nusselt number (*Nu*) in rectangular air ducts. In the initial phase, VGs were mainly installed on flat heating plates or channel walls. The first studies on their integration into FTHEXs were carried out by Fiebig et al. [4,5], who demonstrated through experimental and numerical analyses that longitudinal vortices induced by delta winglet pairs can significantly reduce thermal resistance and increase heat transfer rates.

He et al. [6] numerically identified the optimal punching arrangement for delta winglets in inline-tube FTHEXs, while Hwang et al. [7] examined the flow and heat transfer characteristics of delta winglets placed upstream of the tubes. Their results confirmed that enhanced fluid mixing and boundary-layer disruption contribute to improved thermal performance, with minimal pressure drop penalties, particularly at higher Reynolds numbers. Wu and Tao [8] further analyzed the influence of attack angle on thermo-hydraulic performance, finding that larger angles of attack generally improved heat transfer. Salviano et al. [9] employed a genetic algorithm to optimize winglet position and inclination, showing that reduced frontal area could lower pressure losses without sacrificing thermal enhancement. Modi and Rathod

[10] demonstrated that perforated rectangular winglets can both improve thermal performance and reduce pressure loss. Modifications to straight rectangular winglets, such as curved [11,12] or wavy [13] designs, have been shown to further increase efficiency. Comparative studies highlight that performance differences between delta and rectangular winglets often depend on operating conditions. Li et al. [14] reported that rectangular winglets provided slightly better overall thermo-hydraulic efficiency, while Hu et al. [15] observed that rectangular winglets were advantageous at low inlet velocities and delta winglets at high velocities, with differences in *Nu* and *j/f* generally within 5%.

In this paper, the comparative thermal-hydraulic performance of FTHEX with three VG shapes (rectangular, delta-winglet upstream and delta-winglet downstream) was systematically evaluated. All configurations have identical dimensions and are arranged in a 'common flow up' layout. Three angles of attack (15°, 30°, and 45°) were investigated in order to improve air-side heat transfer performance and overall FTHEX performance.

2. Mathematical model, numerical solving and validation

The study examines fluid flow and heat transfer process occurring in a crossflow air-water FTHEX. Aluminum fins are vertically attached to copper tubes to enhance air-side heat transfer, forming channels through which the air is heated. In this investigation, pairs of VGs are symmetrically positioned on the fin surface near the circular tubes and arranged in a "common-flow-up" configuration, as illustrated in Fig. 1. Three types of VGs are considered: rectangular winglet (RW), delta-winglet downstream (DWD) and delta-winglet upstream (DWU), having identical height and length but differing in the orientation of the hypotenuse of their
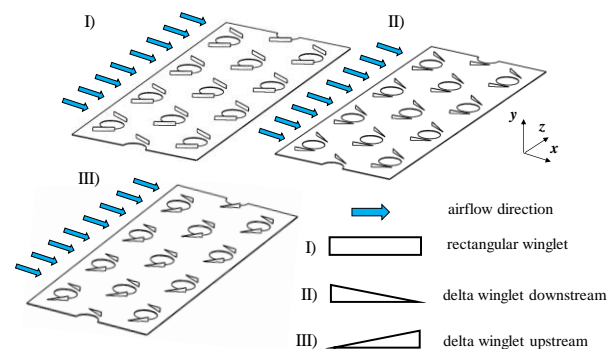

Fig. 1 Three-dimensional view of a fin segment with rectangular and delta winglet VGs.

The main dimensions of FTHEX, are as follows: longitudinal tube pitch $X_L = 30$ mm, transverse tube pitch $X_T = 60$ mm, fin pitch $F_p = 2.81$ mm, fin length $L_x = 90$ mm, fin thickness $\delta_f = 0.2$ mm, inside tube diameter $d_i = 14.8$ mm, outside tube diameter $d_o = 15.9$ mm. Winglet height equals $0.65\ F_p$ ($H_{vg} = 1.827$ mm) and chord length of each winglet is $0.9\ d_o$ ($L_{vg} = 14.31$ mm). The central distances between the tube and the winglet in the airflow direction and in the spanwise direction are $\Delta x = 0$ mm and $\Delta y = 13$ mm, respectively.

Computational domain consists of three subdomains: air, water and solid (fin, tubes and vortex generators). A schematic view of the computational domain has been shown in Fig. 2. The 3D numerical model was developed under the assumptions that air and water are incompressible Newtonian fluids with constant thermal-physical properties, and that viscous dissipation is negligible. Perfect thermal contact between fins and tubes was considered, while heat transfer and fluid flow are in steady state with turbulence modeled in both air and water flows.
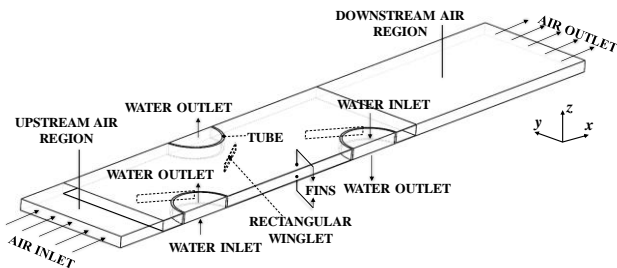

Fig. 2 *The computational domain.*

Based on the stated assumptions, the governing conservation equations for the air and water subdomains include the continuity equation to satisfy mass conservation and the Reynolds-averaged Navier–Stokes momentum equations for the x, y, and z directions. Energy transfer is described by the steady-state energy equation, with Reynolds stresses determined using the Boussinesq approximation. Turbulence closure is achieved via the SST k-ω model, which combines k-ω accuracy near walls with k-ε robustness in the free stream, solving transport equations for turbulent kinetic energy k and specific dissipation rate ω. In solid domains, steady-state heat conduction governs thermal behavior.

Suitable boundary conditions are defined at the outer boundaries of the calculation domain and at the interfaces between subdomains, appropriate boundary conditions are specified. The uniform velocity and temperature profiles are assigned to the air inlet and fully developed velocity and temperature distributions are prescribed at the water inlets. At both the air and water outlets, the flow is assumed to be fully developed, with no variation of field variables along the streamwise direction. Symmetry boundary conditions are applied to the front, back, top, and bottom planes of the domain. Heat transfer at fluid–solid interfaces is modelled by near-wall boundary layer treatment, while the no-slip condition ensures that fluid velocity at solid surfaces is zero due to viscous effects.

The governing equations and boundary conditions are solved by Fluent 18.2. The computational region is discretized with a hexahedral mesh using multi-block grid approach. To achieve good accuracy with shorter computation time, all simulations were performed with the grid size of approximately 1.6 million control volumes. The SIMPLE algorithm is applied to ensure the pressure-velocity coupling. The second order upwind scheme is used in the discretization. The least squares cell-based gradient method was used to evaluate the values of a scalar at the cell faces, secondary diffusion terms and velocity derivatives. The iteration process stops when the convergence criteria are achieved. The convergence criteria were: 10^{-5} for continuity, momentum, turbulence kinetic energy and turbulent frequency equations and 10^{-9} for energy

equation. A comparison between experimental and numerical results for the baseline air-water FTHEX with plain fins is presented in Fig. 3. The results comprise values of air-side Nusselt numbers Nu and air-side pressure drops Δp for different inlet air velocities $u_{air,in}$: 0.46 m/s, 0.65 m/s, 0.86 m/s and 1.04 m/s. The comparison between numerical predictions and experimental data shows good agreement of the analyzed variables. The agreement between experimental and numerical results demonstrates that the chosen computational domain and mathematical model, incorporating fully developed water inlet flow, together with the applied numerical procedure, can reliably simulate the flow and heat transfer behavior within the examined FTHEX.
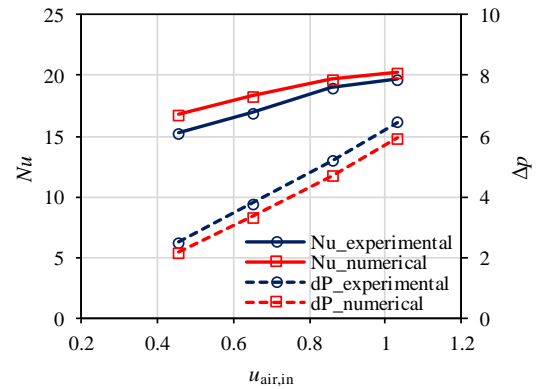

Fig. 3 *Experimental validation.*

3. Results and discussion

The vortex generator's angle of attack relative to the airflow streamlines (α_{vg}) is one of the parameters that most strongly influences the amount of heat exchanged in the recirculation zone and the process of forming secondary flows, i.e., vortices that further enhance convective heat transfer between the air and the fin. A comparison of results was made for three angles of attack: 15°, 30°, and 45°. Numerical simulations were carried out under the following conditions: $T_{air,in} = 295$ K, $T_{water,in} = 313$ K, 0.46 m/s $\leq u_{air,in} \leq 1.04$ m/s, $u_{water,in} = 0.76$ m/s. For the given inlet air velocities, the Reynolds number (Re), based on the tube's outer diameter, ranges between 684 and 1532.

From the comparison of air-side Nu for three different vortex generator configurations and three angles of attack (Fig. 4), it can be observed that the Nu is highest for the FTHEX with rectangular winglet vortex generators (RW) for the given ranges of air-side Reynolds numbers, at all analyzed angles of attack.
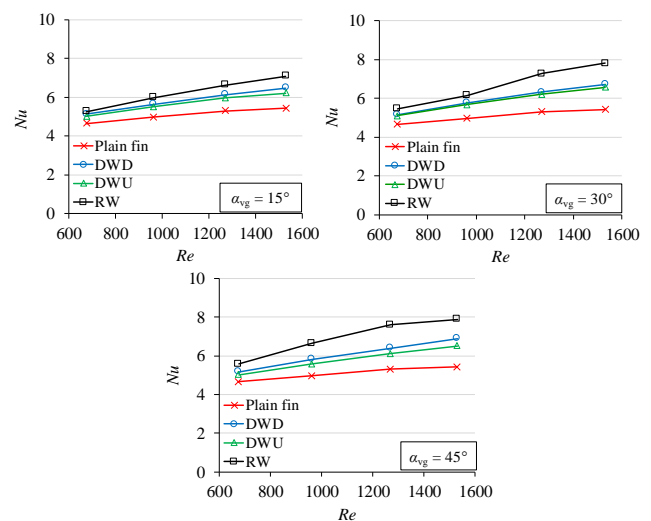

Fig. 4 *The effect of winglet shape and attack angle on Nusselt number.*

Compared to the reference heat exchanger with plain fins, the Nu in the heat exchanger with RW increases between 13.1% and 30.4% for an angle of attack of $\alpha_{vg} = 15°$, between 17.5% and

43.7% for $\alpha_{vg} = 30°$, and between 19.7% and 45.2% for $\alpha_{vg} = 45°$. At higher *Re*, and thus higher inlet air velocities, convective heat transfer between the air and solid surfaces becomes more intense, resulting in higher *Nu*. The *Nu* is slightly higher in the heat exchanger with downstream delta winglets (DWD) compared to the upstream delta winglet configuration (DWU). The maximum relative increase in *Nu* for the DWD configuration is 27% at an attack angle of $\alpha_{vg} = 45°$, while for the DWU configuration it is 21% at an angle of attack of $\alpha_{vg} = 30°$, compared to the reference plain fin case.

Heat transfer enhancement is often associated with additional flow resistance, which results in a higher pressure drop. Fig. 5 shows the dependence of air-side pressure drops on Reynolds numbers for the considered FTHEX configurations and analyzed angles of attack. The smallest pressure drop is observed for the reference case with plain fins. The largest pressure drop occurs in the configuration with the rectangular winglets, due to their larger surface area compared to the other two shapes. As the vortex generator's angle of attack increases, a sharper rise in pressure drop is noticeable, caused by higher form drag that obstructs the airflow streamlines and induces more intense vortex formation. From the perspective of pressure drop, a comparison of the three analyzed VG shapes shows that the lowest values are obtained in the heat exchanger with the upstream delta winglets.
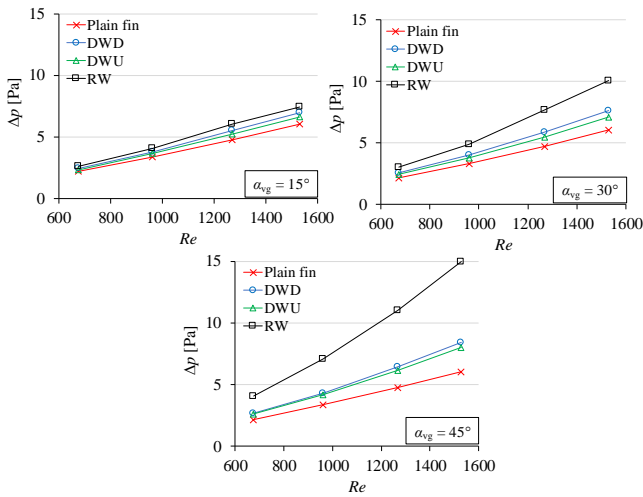

Fig. 5 *The effect of winglet shape and attack angle on air-side pressure drop.*

Fig. 6 shows velocity vector distributions in the central *xy*-plane between the fins ($z = 1.405$ mm), at Re = 1532. The recirculation zone behind the tube is largest for the case of the FTHEX with plain fins. This zone is a consequence of the form drag of the tube, where, due to an unfavorable pressure distribution along its surface, reverse airflow occurs in the region behind the boundary layer separation point. Heat transfer is poorest within this zone. This issue can be mitigated by installing vortex generators, which form a nozzle-like passage that directs the airflow streamlines behind the tube. The VGs with a rectangular shape contribute most to the reduction of poor heat transfer zones, which also decrease with increasing angle of attack for all three winglet configurations. The analysis of the velocity vector field in the central plane shows low velocity zones behind the VGs, particularly at $\alpha_{vg} = 45°$, which indicates the presence of intense secondary flow structures.
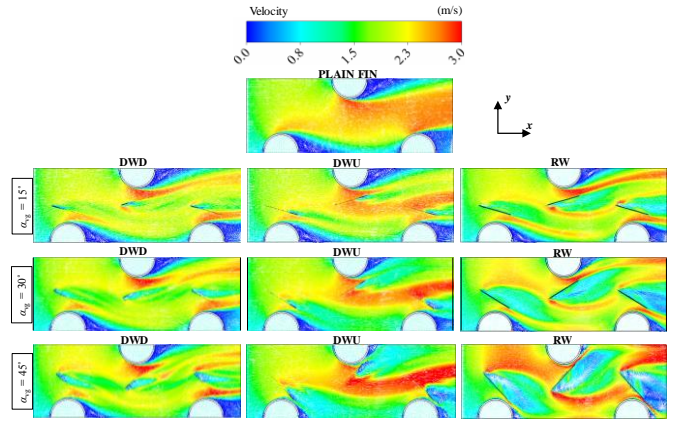

Fig. 6 *Comparison of velocity vector distributions at xy mid-plane obtained numerically at Re = 1532.*

Yun and Lee [16] defined the volume goodness factor $Nu/f^{1/3}$ as a measure for evaluating the flow and heat transfer performance on the gas side of FTHEX. Here, *f* refers to the Fanning friction factor, a dimensionless parameter that characterizes the pressure drop due to friction in the flow passages of the heat exchanger. A higher volume goodness factor indicates better heat transfer for the same fan power required to compensate for the air-side pressure drop, and allows for the design of a more compact heat exchanger while maintaining the same thermal-hydraulic characteristics. The comparison of the volume goodness factors of heat exchangers with vortex generators and the reference heat exchanger with plain fins is presented using the factor $TPF = Nu/Nu_{ref} \times (f_{ref}/f)^{1/3}$. The dependence of the *TPF* factor on the air-side *Re* for the VG attack angles of 15°, 30°, and 45° is shown in Fig. 7. The *TPF* factor increases with increasing *Re*, except for the case of the heat exchanger with RW at $\alpha_{vg} = 45°$, where a slight decrease is observed at Re = 1532. From Figs. 4 and 5 (at $\alpha_{vg} = 45°$), it can be concluded that both the Nusselt number and the air-side pressure drop are higher at Re = 1532 compared to Re = 1278, but the *TPF* decreases due to the lower value of their ratio. Furthermore, after Re = 1278, a sharper increase in air-side pressure drop is observed compared to the *Nu*, which increases only slightly. For $\alpha_{vg} = 15°$ and $\alpha_{vg} = 30°$, the heat exchanger with RW configuration achieves the highest *TPF* values over the entire range of *Re*. At $\alpha_{vg} = 45°$, the heat exchanger with downstream delta winglets attains higher *TPF* compared to the other configurations, except at Re = 1278.
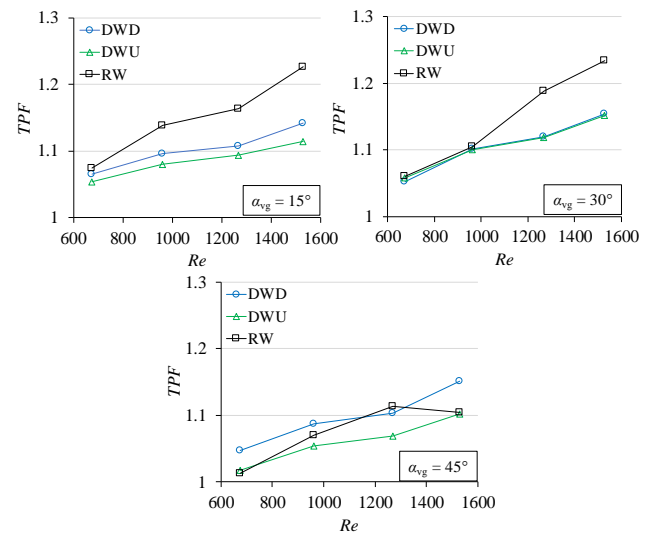

Fig. 7 *The effect of winglet shape and attack angle on overall thermal-hydraulic performance.*

4. Conclusion

A numerical investigation was performed to assess the effect of vortex generator (VG) shape and attack angle on the thermal–hydraulic performance of a finned-tube heat exchanger (FTHEX). Three VG configurations: rectangular winglet (RW), upstream delta winglet (DWU), and downstream delta winglet (DWD) were analyzed at attack angles of 15°, 30°, and 45° for air-side Reynolds numbers between 684 and 1532. Results showed that the RW configuration produced the highest air-side Nusselt numbers for all attack angles, with enhancements of 13.1–45.2% compared to the reference case with plain fins. However, this improvement was accompanied by higher pressure drops, which increased with attack angle due to greater form drag and more intense vortex formation. Velocity vector analysis confirmed that all VG types reduced recirculation zones behind the tubes, with the RW shape providing the largest reduction. Comparison of *TPF* values showed that heat exchanger with RW VGs provided the best overall performance at 15° and 30°. At 45°, the DWD configuration reached higher *TPF* values than the other VG types, except at *Re* = 1278, owing to a more favorable trade-off between heat transfer and flow resistance. Therefore, a separate analysis should be conducted for each FTHEX design to ensure the most suitable choice of vortex generator type and geometry, balancing thermal enhancement with acceptable flow resistance.

5. References

1. R. K. Shah, D. P. Sekulic, Fundamentals of heat exchanger design, John Wiley & Sons, Hoboken, New Jersey, 2003.
2. A. M. Jacobi, R. K. Shah, "Heat Transfer Surface Enhancement through the Use of Longitudinal Vortices: A Review of Recent Progress," Experimental Thermal and Fluid Science, 11(3), 295–309 (1995).
3. F. J. Edwards, C. J. R. Alker, "The Improvement of Forced Convection Surface Heat Transfer Using Surface Protrusions in the Form of (A) Cubes and (B) Vortex Generators", Proc. Fifth International Heat Transfer Conference 2, 244-248 (1974).
4. M. Fiebig, N. K. Mitra, Y. Dong, "Simultaneous heat transfer enhancement and flow loss reduction of fin-tubes", Proc. Ninth International Heat Transfer Conference 4, 51-56 (1990).
5. G. Biswas, N. K. Mitra, M. Fiebig, "Heat transfer enhancement in fin-tube heat exchangers by winglet type vortex generators", International Journal of Heat and Mass Transfer 37(2), 283-291 (1994).
6. Y. L. He, H. Han, W. Q. Tao, Y. W. Zhang, "Numerical study of heat-transfer enhancement by punched winglet-type vortex generator arrays in fin-and-tube heat exchangers", International Journal of Heat and Mass Transfer 55(21-22), 5449-5458 (2012).
7. S. W. Hwang, D. H. Kim, J. K. Min, J. H. Jeong, "CFD analysis of fin tube heat exchanger with a pair of delta winglet vortex generators", Journal of Mechanical Science and Technology 26(9), 2949-2958 (2012).
8. J. M. Wu, W. Q. Tao, "Investigation on laminar convection heat transfer in fin-and-tube heat exchanger in aligned arrangement with longitudinal vortex generator from the viewpoint of field synergy principle", Applied Thermal Engineering 27(14-15), 2609-2617 (2007).
9. L. O. Salviano, D. J. Dezan, J. I. Yanagihara, "Optimization of winglet-type vortex generator positions and angles in plate-fin compact heat exchanger: Response Surface Methodology and Direct Optimization", International Journal of Heat and Mass Transfer 82, 373-387 (2015).
10. A. J. Modi, M. K. Rathod, "Experimental investigation of heat transfer enhancement and pressure drop of fin-and-circular tube heat exchangers with modified rectangular winglet vortex generator", International Journal of Heat and Mass Transfer 180, 122742 (2022).
11. H. Naik, S. Harikrishnan, S. Tiwari, "Numerical investigations on heat transfer characteristics of curved rectangular winglet placed in a channel", International Journal of Thermal Sciences 129, 489-503 (2018).
12. J. Xie, H. M. Lee, "Thermo-Hydraulic Performance of a Fin-and-Tube Heat Exchanger with Differently Configured Curved-Rectangular Vortex Generators", Heat Transfer Engineering 43(1), 63-82 (2020).
13. J. Wu, P. Liu, M. Yu, Z. Liu, W. Liu, "Thermo-hydraulic performance and exergy analysis of a fin-and-tube heat exchanger with sinusoidal wavy winglet type vortex generators", International Journal of Thermal Sciences 172, 107274 (2022).
14. L. Li, X. Du, Y. Zhang, L. Yang, Y. Yang, "Numerical simulation on flow and heat transfer of fin-and-tube heat exchanger with longitudinal vortex generators", International Journal of Thermal Sciences 92, 85-96 (2015).
15. W. Hu, L. Wang, Y. Guan, W. Hu, "The effect of shape of winglet vortex generator on the thermal-hydrodynamic performance of a circular tube bank fin heat exchanger", Heat and Mass Transfer 53, 2961-2973 (2017).
16. J. Y. Yun, K. S. Lee, "Influence of design parameters on the heat transfer and flow friction characteristics of the heat transfer with slit fins", International Journal of Heat and Mass Transfer 43(14), 2529-2539 (2000).

Air-Side Pressure Drop and Heat Transfer Analysis in Slotted Fin and Tube Heat Exchanger

Fran Torbarina[1*], Mateo Kirinčić[2], Josip Batista[2], Paolo Blecich[2]

University of Rijeka, Faculty of Maritime Studies, Studentska 2, Rijeka. Croatia[1]

University of Rijeka, Faculty of Engineering, Vukovarska 58, Rijeka, Croatia[2]

fran.torbarina@pfri.uniri.hr

Abstract: *Compact air-cooled fin-and-tube heat exchangers are widely used in various fields, including the automotive and computer industries, as well as in heating, air conditioning, refrigeration, and process applications. Due to the thermal characteristics of air, the majority of heat transfer resistance occurs on the air side of the heat exchanger. As a result, research in this area primarily concentrates on enhancing the air-side performance. Numerous studies in the literature explore different fin and tube configurations aimed at optimizing the design of these heat exchangers however, pressure drop is sometimes neglected. In this study, a numerical analysis was conducted to investigate air-side pressure drop and heat transfer in various configurations of slotted fin-and-tube heat exchangers whereby heat exchangers with different ellipticity ratios were considered. The numerical model of the three-dimensional, laminar, steady-state problem of air-side flow and heat exchange was done using the finite volume method. The convection-diffusion equations were discretized using the Power Law scheme, and the SIMPLE algorithm was employed to couple pressure and velocity. Simulations were carried out in ANSYS Fluent 18.2. The validation of the proposed model was tested by comparing the numerical results with experimental measurements available in the literature whereby no discrepancies greater than 5% were observed. Four different inlet air velocities ranging from 1 to 4 m/s, corresponding to Reynolds numbers between 558 and 2233 were considered. Both the inlet air temperature and the tube surface temperatures were kept constant at 293 K and 373 K, respectively. The results emphasize potential benefits of using elliptic instead of round tubes in slotted fin and tube heat exchangers to achieve lower air-side pressure drop without penalty of lower heat transfer.*

Keywords*: HEAT EXCHANGER, FIN AND TUBE, ELIPTICITY RATIO, NUMERICAL ANALYSIS.*

1. Introduction

Fin-and-tube heat exchangers are fundamental components in HVAC, automotive, and process- industry applications, yet their performance is often limited by the low heat transfer coefficient of air, which makes air- side thermal resistance dominant [1]. To overcome this, extended surfaces are added around tubes to increase the wetted area and enhance convective heat transfer. Beyond conventional straight fins, several enhanced geometries have been explored, such as wavy, louvered, corrugated, dimpled and slotted fins, as well as fins fitted with vortex generators, which serve to disrupt boundary layers and promote mixing [2].

Vortex generator fins, which induce longitudinal vortices, have shown particular promise. Curved delta- winglet generators placed near tubes result in significant heat transfer enhancement in laminar flow, while larger winglets are better suited for higher Reynolds numbers [3]. Punched hole longitudinal vortex generators can boost average convective coefficients by up to 28%, with minimal pressure drop increase [4]. Optimization studies using genetic algorithms and response surface methods reveal that tube pitch ratios and fin pitch strongly affect performance, with winglet dimensions exerting secondary influence [5]. Multi- objective optimizations further demonstrate that winglet roll angles can significantly reduce pressure drop without compromising vortex strength [6].

Simpler fin enhancements also result in substantial improvements. Numerical analyses of wavy and corrugated fins paired with elliptical tubes report Nusselt- number increases up to 20% and friction factor reduces by nearly 19% relative to plain designs [7]. Dimpled fins can raise heat transfer by about 30%, but with a higher pressure drop cost [8].

Slotted fins constitute another effective strategy. Numerical studies identify "front sparse, rear dense" slot arrangements that enhance convective performance by up to 86% compared to plain fins [9, 10]. Experimental investigations confirm that slot geometry must be tailored to flow conditions: X- type, arc- type and butterfly- type layouts each optimize the Nusselt- number- friction- factor trade- off under specific mass- flow rates [11].

In this paper, a numerical study on how the tube ellipticity ratio affects air-side heat transfer and pressure drop in slotted fin and tube heat exchangers has been performed. The thermal performance has been assessed by comparing Nusselt numbers for a slotted fin and round tube heat exchanger and multiple slotted fin and elliptical tube heat exchangers. This analysis offers guidelines for selecting the favorable tube ellipticity ratio for the described slotted fin and tube heat exchangers in order to enhance their thermal performance.

2. Physical problem, mathematical model and numerical solving

The numerical study examined air-side flow and heat transfer within a slotted fin and tube heat exchangers. Both round and elliptical tubes are considered. The purpose behind considering slotted fin and elliptical tube heat exchangers lies within the ability of the slots and elliptical tubes to potentially improve heat transfer while not increasing the air-side pressure drop. Figure 1 shows the baseline physical model of a slotted fin-and-tube heat exchanger. Air flows around the tubes, passes through the channels formed between the fins and tubes, and also moves through the slotted passages. The tubes are arranged in a staggered configuration. The fin pitch was set to 3 mm, with a fin thickness of 0.3 mm and a slot height of 1.5 mm.

Four different tube ellipticity ratios were considered: 7.5/7.5, (round tube), 8/7.1, 9/6.54 and 9.5/6.4 mm. The lengths of the ellipse's semi-axes were chosen such that the equivalent diameter of the tube in the finned heat exchanger matched the diameter of the tube in the reference heat exchanger with round tubes. Both the water and tubes subdomains were excluded from the model, based on the assumption that their temperatures remain nearly constant over the selected domain; accordingly, a constant temperature boundary condition was applied to the outer wall of the tubes.
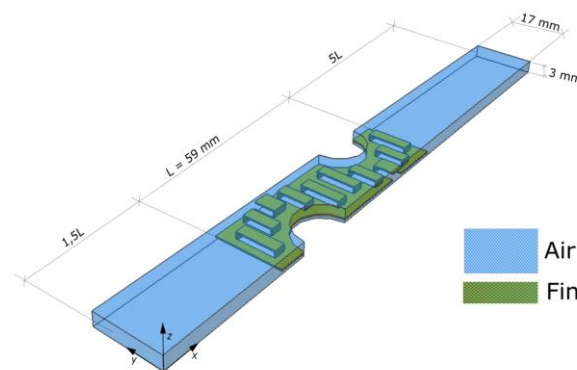

Fig. 1 *Isometric view of a slotted fin and tube unit with selected domain and denoted subdomains.*

The domain was selected in such a way so as to minimize the computational cost since symmetry and geometric repetition allow modeling only a half of each tube and a single fin. The computational domain is divided into air and slotted fin subdomains (also showed in Fig. 1).

A three- dimensional, steady- state conjugate heat- transfer and airflow model was developed for the slotted fin- and- tube heat exchanger. The airflow is treated as incompressible, laminar, and governed by constant fluid properties, while heat transfer resistance through the tube walls is neglected owing to the high thermal capacity of the tube fluid.The computational domain is split into air and slotted- fin subdomains; the air inlet zone extends 1.5 times the fin length and the outlet zone 5 times the fin length to ensure proper application of inlet and outlet boundary conditions (Fig. 1).

For the air subdomain, continuity and momentum equations were applied. Continuity equation is the mass conservation equation, while three momentum equations are the Navier-Stokes equations. Finally, the energy equation is applied to both subdomains. For the air subdomain, it is a convection-diffusion equation for temperature, while for the slotted fin subdomain, it is a diffusion equation for temperature, describing pure conduction.

Inlet and outlet conditions are imposed on the air: the inlet specifies temperature (273 K for all cases) and velocity (ranging 1-4 m/s), while the outlet assumes fully developed flow (no downstream gradients). The domain top and bottom surfaces are set to periodic boundary condition and the walls representing tube outside surfaces enforce a constant temperature of 373 K and no-slip boundary condition (zero fluid velocity). At all air–slotted fin interfaces, conductive heat transfer and no-slip conditions apply. All remaining outer faces of the air subdomain and fin walls are set to symmetry boundary conditions, reflecting identical flow and temperature profiles across these boundaries.

The governing equations were discretized using the finite volume method and solved in ANSYS Fluent [12]. Pressure-velocity coupling employed the SIMPLE algorithm, while convective fluxes were handled with the Power Law scheme. Convergence thresholds were set at 10^{-4} for continuity, 10^{-5} for momentum, and 10^{-7} for energy. Mesh independency study compared Nusselt numbers from grids of 2447928, 3,597,508 and 4421165 cells, showing under 1% difference between the two finer meshes. Balancing accuracy and run time, the 3597508- cell mesh was selected for all simulations.

3. Experimental validation and numerical analysis results

Validation of the model and numerical procedure was performed by comparing Nusselt numbers and friction factors obtained using the numerical results to those published in a study by Li et al. [11] which were obtained using the results of the experimental measurements. The comparisons are showed in Fig. 2. From Fig. 2, it can be observed that values of both Nusselt numbers and friction factors obtained numerically are in good agreement with those available from the literature, thus indicating that the proposed mathematical model and numerical procedure can be used to accurately simulate air-side heat transfer and flow in slotted fin and tube heat exchangers.

The effect of different tube ellipticity ratio on selected air flow and heat transfer characteristics in slotted fin and tube heat exchangers was examined by comparing four different configurations with ellipticity ratio values of 7.5/7.5, (round tube), 8/7.1, 9/6.54 and 9.5/6.4 mm. All simulations used air inlet temperature 293K, while considered air inlet velocities were 1, 2, 3 nad 4 m/s.

Performance metrics included graphical representations of the air temperature contour distributions and velocity vectors, Nusselt number and pressure drop across the heat exchanger unit.
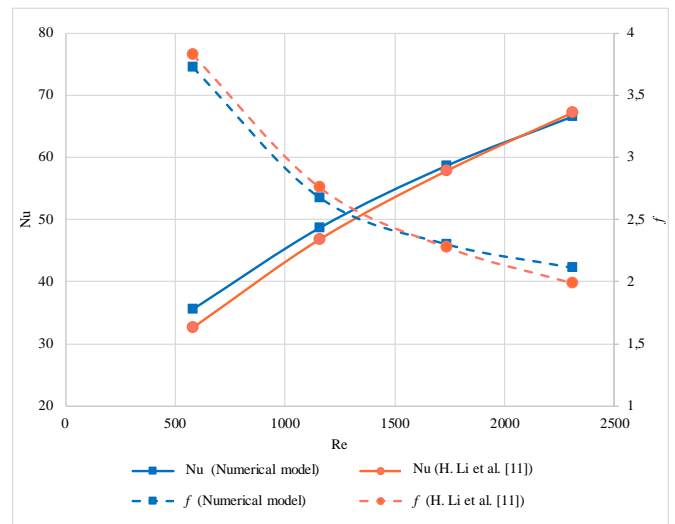

Fig. 2 Experimental validation.

Contours of the temperature distributions in the *xy*-plane located at the slots mid-height cross-section are given in Fig. 2.
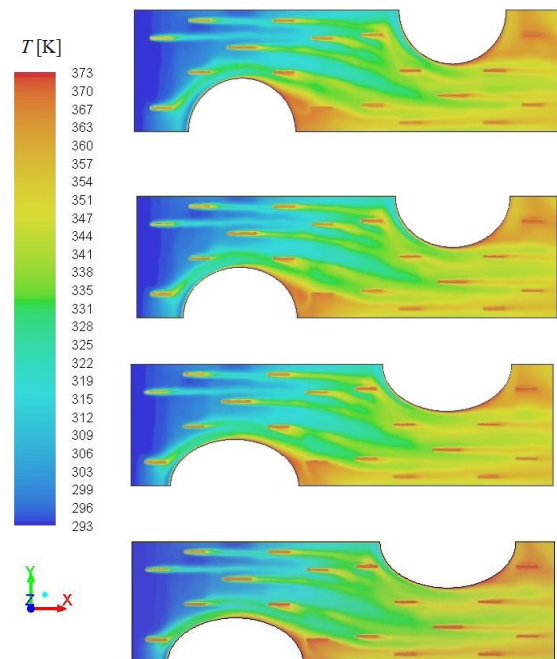
Fig. 3 Temperature contours at the slots mid-height cross-section for different tube geometries.

A certain similarity can be observed in the presented countours of temperature distributions, which suggests that there is no significant difference in the transferred heat fluxes and outlet air temperatures among the analyzed fin and tube heat exchangers with different tube cross-sectional geometries. Figure 4 shows the velocity vectors in the slots mid-height cross-section for all considered cases of different tube cross-sectional geometries of the finned heat exchanger.

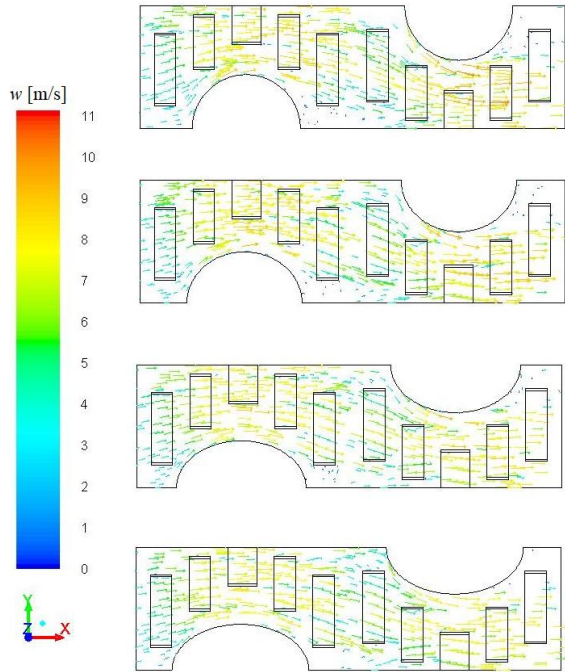**Fig. 4** *Velocity vectors at the slots mid-height cross-section for different tube geometries.*

The results presented in Fig. 4 suggest that slightly higher flow velocities occur in cases of tubes with lower ellipticity ratios, that is, the highest flow velocity is achieved in the base-line heat exchanger with round tubes. This can be explained with the fact that the narrowest cross-sectional area is the smallest in the case of round tubes and the largest in the case of tubes with the highest ellipticity ratio.

Dependences of the Nusselt number on the Reynolds number for three different combinations of semi-axis dimensions of elliptical cross-section tubes, as well as for the reference heat exchanger with round tubes are showed in Fig. 5.
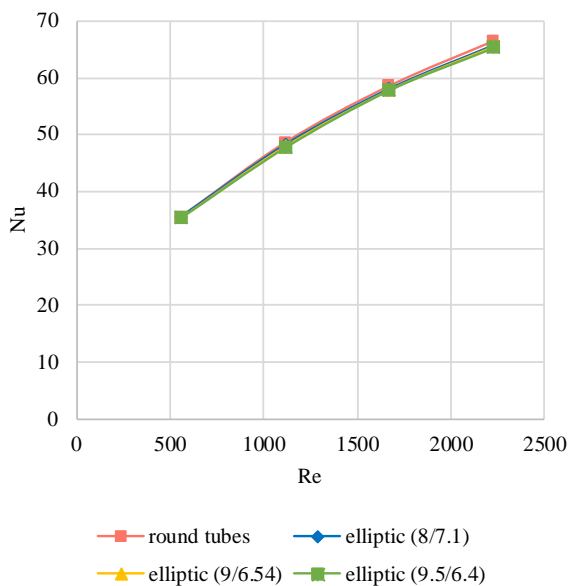

Fig. 5 *Comparison of Nusselt numbers for different Reynolds numbers and the tube ellipticity ratio.*

As can be seen from Fig. 5, the shape of the tube has a negligible effect on the Nusselt number, which corresponds to the results presented in Fig. 3. The interpolation curves showing the dependence of the Nusselt number on the ellipticity ratio of the tube cross-section in the heat exchanger in Fig. 5 almost overlap.

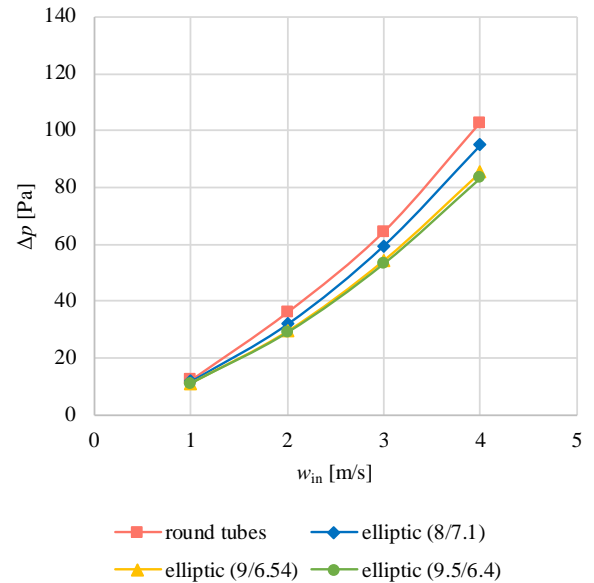Fig. 6 shows the air pressure drop due to flow through the heat exchanger.

Fig. 6 *Comparison of pressure drops across the heat exchanger unit for different inlet velocities and the tube ellipticity ratio.*

It can be observed that at lower air velocities, the difference in pressure drops is negligible, while the greatest difference occurs at the highest inlet air velocity, specifically between the heat exchanger with tubes of circular cross-section and the one with tubes of elliptical cross-section with the highest aspect ratio (the ratio between the two semi-axes of the ellipse).

Although numerical simulations have shown that, from a thermodynamic perspective, the shape of the tube's cross-section has no significant impact under the observed operating conditions, from the standpoint of pressure drop, tubes with an elliptical cross-section and a higher aspect ratio will cause a smaller air pressure drop due to the airflow through the heat exchanger.

Heat exchangers with elliptical tube cross-sections achieve a slightly lower heat transfer rate, but they cause up to 20% lower pressure drops at higher air velocities compared to heat exchangers with circular tube cross-sections.

4. Conclusion

In this study, the impact of tube ellipticity on air-side thermal and hydraulic performance in slotted fin-and-tube heat exchangers were systematically evaluated via steady-state, 3D CFD simulations. Selected thermal and flow criteria were compared for four fin and slotted tube heat exchangers with different ellipticity ratios, from perfectly round tubes (7.5/7.5 mm) to highly elliptical (9.5/6.4 mm) tubes. The comparison has been made at Reynolds numbers 500 to 2300 corresponding to inlet velocities of 1 to 4 m/s. Validation against experimental data confirmed that the numerical approach accurately predicts both Nusselt numbers and friction factors. Results show that, across all flow rates, tube shape exerts a negligible influence on convective heat transfer: Nusselt- versus- Reynolds curves for round and elliptical tubes collapse onto nearly identical trends. In contrast, tube ellipticity significantly affects pressure drop; at high velocities, elliptical tubes with larger aspect ratios reduce the air- side pressure drop by up to 20% compared to round tubes, due to their increased flow passage area. These findings indicate that replacing circular tubes with

appropriately sized ellipses can achieve the same thermal performance while lowering pressure drops and ultimately contribute to reducing energy consumption and increasing energy efficiency of such devices. Finally, it can be concluded that influencing tube ellipticity is a straightforward means to improve hydraulic efficiency without compromising heat transfer rates.

5. *References*

1. A. M. Jacobi, R. K. Shah, "Heat Transfer Surface Enhancement through the Use of Longitudinal Vortices: A Review of Recent Progress," Experimental Thermal and Fluid Science, 11(3), 295–309 (1995).
2. A. Sadeghianjahromi, C. C. Wang, "Heat Transfer Enhancement in Fin- and- Tube Heat Exchangers—a Review on Different Mechanisms," Renewable and Sustainable Energy Reviews, 137, 110470 (2021).
3. K. Song, Z. Zhang, H. Wang, et al., "Effect of Geometric Size of Curved Delta Winglet Vortex Generators and Tube Pitch on Heat Transfer Characteristics of Fin–Tube Heat Exchanger," Experimental Thermal and Fluid Science, 82, 8–18 (2017).
4. J. M. Wu, C. C. Lee, S. H. Tung, "Experimental Study on the Performance of a Novel Fin–Tube Air Heat Exchanger with Punched Longitudinal Vortex Generator," Energy Conversion and Management, 57, 42–48 (2012).
5. X. Wu, L. Zhang, H. Liu, "Optimization of Fin–Tube Heat Exchanger with Longitudinal Vortex Generators Using Response Surface Approximation and Genetic Algorithm," Heat and Mass Transfer, 52, 1871–1879 (2016).
6. L. O. Salviano, D. J. Dezan, J. I. Yanagihara, "Optimization of Winglet- Type Vortex Generator Positions and Angles in Plate- Fin Compact Heat Exchanger: Response Surface Methodology and Direct Optimization," International Journal of Heat and Mass Transfer, 82, 373–387 (2015).
7. A. Gholami, M. A. Wahid, H. A. Mohammed, "Thermal–Hydraulic Performance of Fin- and- Oval Tube Compact Heat Exchangers with Innovative Design of Corrugated Fin Patterns," International Journal of Heat and Mass Transfer, 106, 573–592 (2017).
8. J. F. Fan, L. Liu, Z. Zuo, "Three- Dimensional Numerical Study of Fluid and Heat Transfer Characteristics of Dimpled Fin Surfaces," Numerical Heat Transfer, Part A: Applications, 62, 271–294 (2012).
9. W. Q. Tao, X. G. Hu, X. L. Liu, "Optimum Design of Two- Row Slotted Fin Surface with X- Shape Strip Arrangement Positioned by Front Coarse and Rear Dense Principle," Numerical Heat Transfer, Part A: Applications, 50, 731–749 (2006).
10. Y. P. Cheng, S. L. Lee, Y. S. Wang, "Numerical Design of Efficient Slotted Fin Surface Based on the Field Synergy Principle," Numerical Heat Transfer, Part A: Applications, 45, 517–538 (2004).
11. H. Li, T. Zhu, Z. Chen, et al., "PIV and Thermal- Vision Experimental and Numerical Investigation on the Air- Side Performance of Slotted Fin Surfaces," International Journal of Heat and Mass Transfer, 82, 568–580 (2015)
12. H.K. Versteeg, W. Malalasekera, An Introduction to Computational Fluid Dynamics: The Finite Volume Method (Longman Scientific and Technical, Essex, England, 1995).

Reducing the number of pores in the tungsten-cobalt carbide tips of the road milling cutter in order to increase its wear resistance

Gadji H. Ramazanov[1], Mikhail G. Shalygin[1]
[1]Bryansk State Technical University, Russia
tts-dm@ya.ru

Annotation: *Studies of the tip of a road milling cutter made of tungsten-cobalt alloy have been carried out. It is established that one of the factors influencing the wear resistance of the tip is the porosity of the sintered hard alloy. Laser treatment of the surface of the cutter tip was performed. It has been found that under certain laser radiation conditions, the number of pores in the cutter decreases.*
KEYWORDS: WEAR, CHISEL, ROAD MILLING CUTTER, POROSITY, WEAR RESISTANCE.

Introduction

When repairing the roadway, the top layer of the asphalt surface is removed with a special technique – a road milling cutter. The milling cutter contains a drum on which the cutters are located, the number of which depends on the diameter of the drum. The cutters are positioned in such a way as to make an even cut when removing the asphalt surface. During the milling process, the drum with cutters is rotated at high speed and the asphalt layer is cut to a predetermined depth [1, 2]. In this regard, the purpose of this article is to increase the development of a technology to increase the wear resistance of a road milling cutter with a tip made of tungsten-cobalt hard alloy.

Methods and materials

The object of the study was a carbide cutter of a road milling cutter with a tungsten-cabolt carbide tip. Some of the sample tips were subjected to laser treatment of varying intensity: wavelength – 25-75 nm, power density -20-30 Watts, spot area of the laser beam (contact) - 0.05 mm2; radiation frequency – 30 Hertz.

Wear tests were carried out on a designed installation that simulates the operation of a road milling cutter drum (Fig. 1a). The installation is equipped with a drum containing 3 cutters, positioned so that in the installation the cutters move relative to the counterbody being cut in the same way as in real conditions. That is, the cutters, making rotational movements on the drum, cut into the abrasive material (counterbody) at an angle to the normal. This arrangement of the incisors allows for an even cut, as it happens in real conditions. The tests were carried out before the incisors were sunk into the asphalt surface to a depth of 450 mm. A drum with cutters was brought to the asphalt surface using a lever system (Fig. 1b). The asphalt-concrete mixture was manufactured in accordance with GOST R 58406.2-20 (Fig. 1b). The porosity of the asphalt-concrete mixture was in the range of 1.0-2.5%. In order to speed up testing, gravel grains with an average grain size of 40 mm were used as the mineral grains of the mixture.

The wear of the cutters is controlled by the weight method, by measuring the weight of the cutters before and after the testing process. The cutter of the road milling cutter supplied by the manufacturer has a weight of 321.6 g (Wirtgen HT3/HT11). Porosity according to GOST 9391-80 was determined using a Leica DM750 microscope at a magnification of 100x.

Results and discussion

Of the 6 samples, 5 were subjected to various laser treatments. Considering the design of the test facility, each sample consisted of 3 cutters. To determine the number of pores, the concept of porosity and the research methodology according to GOST 9391-80 were used. When studying the images of micrographs with an increase of x100, it was found that the porosity decreased (Fig. 2). The range of porosity values of the samples is shown in Table 1.

b)

b)

Fig. 1. *Installation for testing the wear of road milling cutters:*
a) – general view;
b) – the cutter on the drum;
c) – samples of asphalt pavement

It should be noted that comparing porosity according to GOST 9391-80 is a difficult task for samples with similar visualization of pores on the slot. The surface of the carbide cutter tip of a road milling cutter made of tungsten-cobalt alloy was subjected to low-intensity laser treatment in order to selectively excite molecules and reduce the number of pores. The ability to focus laser radiation allows you to inject energy into a specific area of the volume. The monochromacy of laser radiation makes it

possible to selectively excite molecules of the same type. The laser radiation modes are selected as follows (Table No. 2),

The wear of the cutters is controlled by the weight method, by measuring the weight of the cutters before and after the testing process. The cutter of the road milling cutter supplied by the manufacturer has a weight of 321.6 g (Wirtgen HT3/HT11). Porosity according to GOST 9391-80 was determined using a Leica DM750 microscope at a magnification of 100x.

Results and discussion

Of the 6 samples, 5 were subjected to various laser treatments. Considering the design of the test facility, each sample consisted of 3 cutters. To determine the number of pores, the concept of porosity and the research methodology according to GOST 9391-80 were used. When studying the images of micrographs with an increase of x100, it was found that the porosity decreased (Fig. 2). The range of porosity values of the samples is shown in Table 1.

It should be noted that comparing porosity according to GOST 9391-80 is a difficult task for samples with similar visualization of pores on the slot. The surface of the carbide cutter tip of a road milling cutter made of tungsten-cobalt alloy was subjected to low-intensity laser treatment in order to selectively excite molecules and reduce the number of pores. The ability to focus laser radiation allows you to inject energy into a specific area of the volume. The monochromacy of laser radiation makes it possible to selectively excite molecules of the same type. The laser radiation modes are selected as follows (Table No. 2), in which the activation of molecules in the matrix occurs in the area of the largest accumulation of pores, in particular in this case near the cobalt bond. As a result, the metal base is fused at a certain depth from the surface, and as a result, the pores are closed (Fig. 3). In this regard, the conductivity of the surface of the tips of the carbide cutter on AFM Femtoscan was investigated. In the absence of conductivity (dark spots in Fig. 3) it was assumed that there was a time in this place.
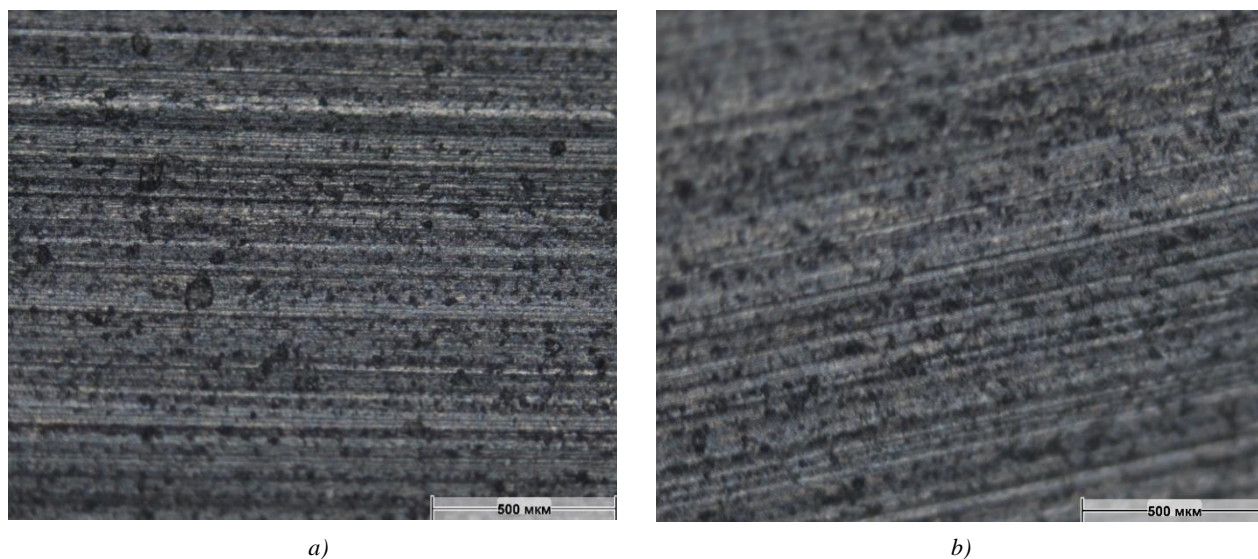

a)   *b)*

Fig. 2. *The surface of the tip of the cutter x100:*
a) basic; b) laser-treated

Table 1 – Range of porosity values of the samples

	Scale according to GOST 9391-80 (RU)				
	A	B	C	D	E
Basic samples	0,2-0,8	0,4	0,4-0,8	0,1-0,8	3
Laser-treated samples	0,08	0,02-0,2	0-0,1	0-0,1	2-3

Table 2 – Laser treatment modes and porosity of samples

Sample, No	wavelength, nm	power, Watts	contact spot area, mm^2	frequency of radiation, Hertz	porosity (by conductivity)
1	untreated cutter, initial condition				A 0,4
2	50	20	0,05	30	A 0,2
3	50	25	0,05	30	A 0,04
4	50	30	0,05	30	A 0,2
5	25	25	0,05	30	A 0,4
6	75	25	0,05	30	A 0,4

When compared, areas with low conductivity that are darker are clearly visible. At the same time, in Fig. 3a, crystallites are clearly visible, which are not visible in Fig. 3b. The difference in conductivity of the sites is due to the different conductivity of different carbides and the binder element. The completely black areas have zero conductivity and are most likely pores between the crystallites obtained by sintering a hard alloy.

So, sample No. 1, which was not treated with a laser, had a porosity of A 0.4. Next, the laser power was changed, with the remaining unchanged parameters, at which: at a power of 20 Watts (sample No. 2), the porosity decreased to A0.2; at a power of 25 Watts (sample No. 3) – A0.04; at a power of 30 Watts (sample No. 4) – A0.2. It was found that at a power value of 25 Watts (sample No. 3), the lowest porosity is achieved. Further, at this power value, the wavelength varied: at a wavelength of 25 nm. (Sample No. 5) the porosity was A0.4, at a wavelength of 75 nm. (sample No. 6) – A0,4. Since the change in wavelength did not lead to a change in porosity compared to sample No. 1, which was not subjected to laser treatment, rational laser treatment modes were established to reduce the porosity of the carbide cutter of the road milling cutter made of tungsten-cobalt alloy. Thus, samples No. 1 and No. 3 were tested for wear (Table 2). The test results are summarized in one table. 3. The table shows that for the production of an asphalt layer 450 mm deep, cutters No. 1 were worn out by an average of 18.2 grams, cutters No. 3 – 9.2 grams.
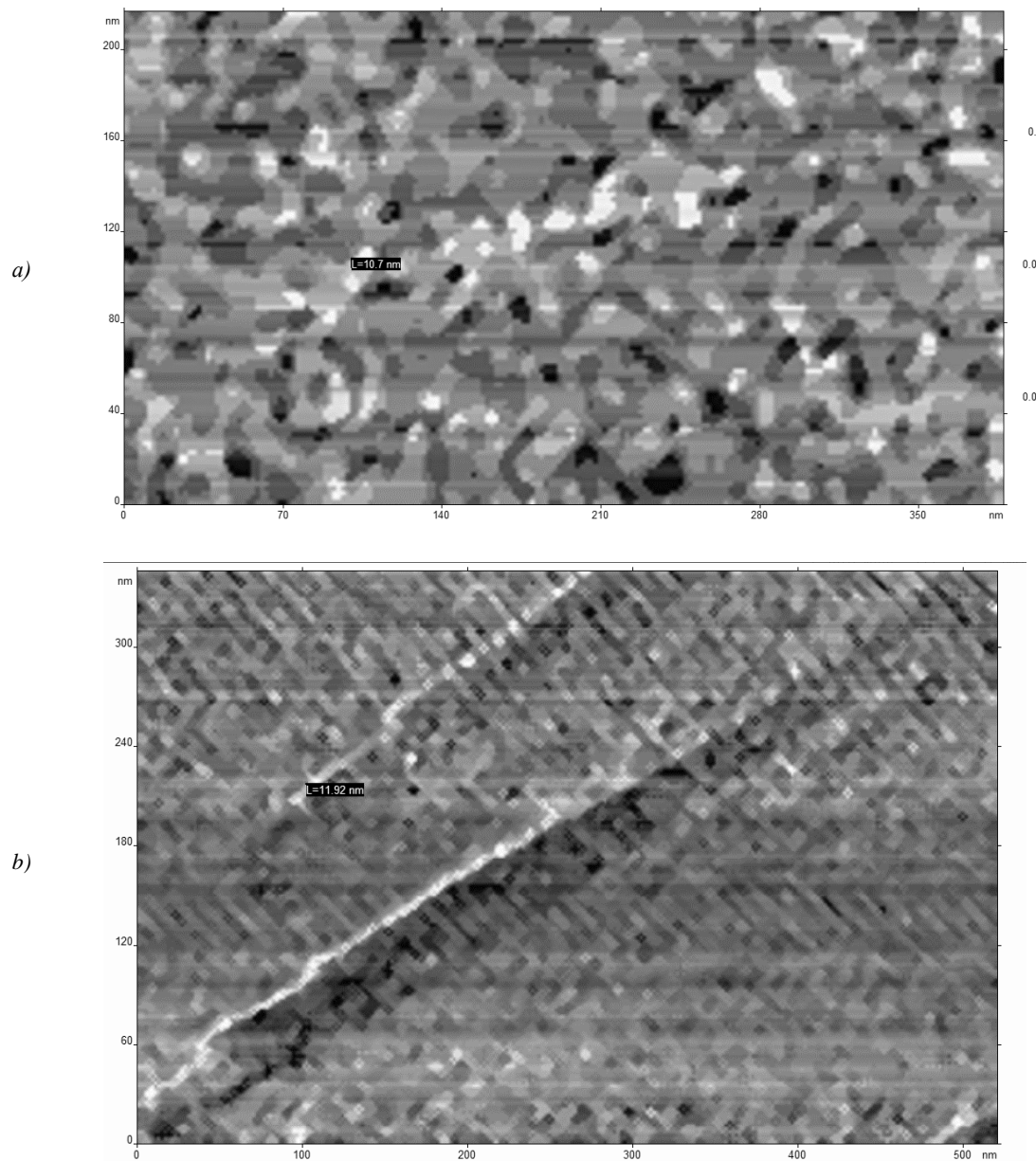
a)

b)

Fig. 3. *Study of the conductivity of the site:*
a) – sample No. 1 (Table. 2); b) – sample No. 3 (Table 2)
Table 3 – Test results for the wear of the cutters of the road milling cutter

Sample, No	Asphalt production by depth, mm	Weight after wear tests, mg			
		cutter 1	cutter 2	cutter 3	average for 3 incisors
1		303,3	303,6	303,3	303,4
2		306,6	306,6	306,7	306,63
3	450	312,5	312,4	312,3	312,4
4		306,7	306,6	306,7	306,66
5		303,3	303,5	303,4	303,4
6		303,6	303,5	303,4	303,5

According to the average values, the lowest mass loss is observed in sample No. 3. Samples No. 1 and No. 5 have the greatest mass loss, on average, therefore, the selected laser treatment mode for sample No. 5 does not lead to a decrease in cutter wear.

The main parameters of the tool's operation during the destruction of asphalt concrete are: P is the depth of loosening, V is the speed of relative movement of the cutter, t is the processing time, S is the area of asphalt concrete removed. A characteristic feature of the asphalt concrete destruction process is the frequency of operation of the milling cutters, the variable area of the layer to be removed with one cutter, as well as the variable number of cutters simultaneously in operation, which causes a variable value of forces, moments and power required for processing. Therefore, the dependences for loosening and removing asphalt pavements were derived for one cutter based on the average values of forces, moments and power. The total length of the path of one cutter traveled in asphalt concrete is determined from the expression:

$$L_{cut} = Lnt,$$

where L is the length of the cutter path traveled in one revolution of the milling cutter drum from point a to point b

$$L = R\alpha_{cut},$$

where α_{cut} is the angle formed between the extreme points a and b, where contact with asphalt concrete occurs; n is the rotation frequency of the milling cutter drum; t is the processing time of the asphalt concrete layer.

Then, turning to the area S of the produced coating, the total length of the cutter path is determined:

$$L_{cut} = \frac{S}{6}arcos\left(1 - \frac{P}{R}\right),$$

where P is the depth of the cutter; R is the radius of the milling cutter drum.

The pressure of the wear medium during the interaction of the working body of the road milling cutter with the abrasive material is expressed by the feed rate (S) during loosening. Which in turn is reflected in the volume of asphalt concrete removed.:

$$S_{max} = Ssin\gamma,$$

where S is the feed; γ is the contact angle.

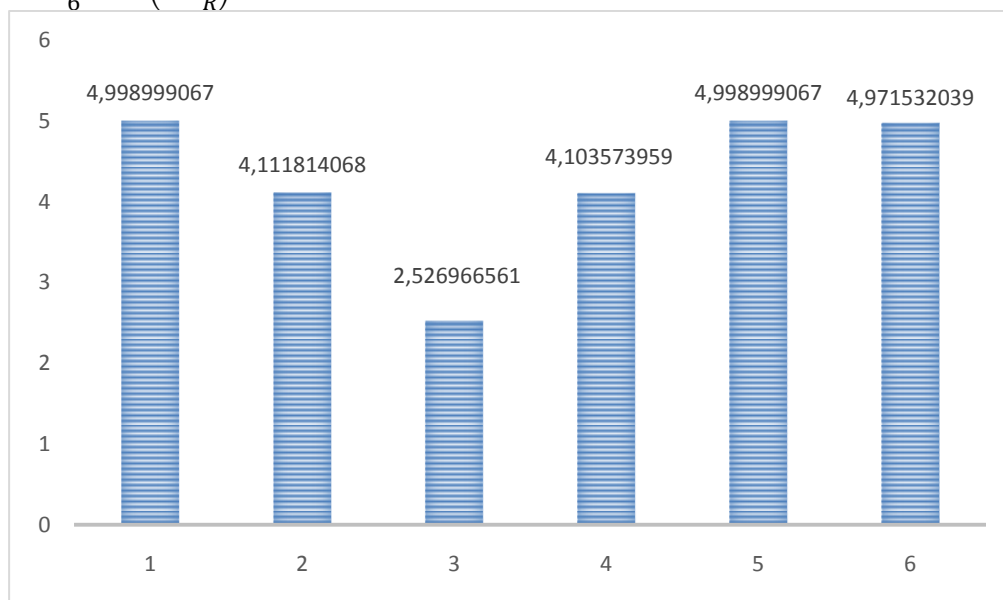The calculated values of the wear intensity are shown in Fig. 4.

Fig. 4. Wear intensity $x10^{-4}$ samples according to Table 3

Conclusion

When studying the material structure of the carbide cutter of a road milling cutter, the surface porosity was determined. The number of black spots on the laser-treated sample is significantly lower. Thus, laser treatment of a hard alloy reduces the number of pores. Wear tests have shown that the laser-treated samples have lower porosity due to the production of a 450 mm deep asphalt layer. They were worn out by an average of 9.2 grams, incisors, without additional processing – 18.2 grams.

References

1. Ramazanov G.H. Tool wear of a road milling cutter and models of cutting efficiency. Science-intensive technologies in mechanical engineering. No. 1. 2023. pp. 42-48.
2. Ramazanov G.H. The problem of wear resistance of a road milling cutter. Construction and road machinery. No. 3. 2023. pp. 24-26.

Green waste composter with energy cogeneration – energy storage and utilization

Rosen Ivanov
University of Mining and Geology, Bulgaria
r.ivanov@mgu.bg

Abstract: Microbial fuel cells (MFCs) have significant potential for sustainable energy production and waste management, but despite this, they are still not widely commercialized due to several main reasons, such as relatively low power generation, technical challenges, scalability, and others. In the present study, we tested the possibilities for storage and utilization of energy from our developed green waste composter with cogeneration of energy. The composter consists of 24 stacked solid phase microbial fuel cells. The generated energy was increased through a voltage boost converter and used for charging batteries, power banks, and low-energy consumption devices. The composter demonstrated stable operation, and the obtained results regarding the storage and utilization of the energy generated by it are promising for its commercialization.

Keywords: GREEN WASTE, GREEN ENERGY, WASTE MANAGEMENT, BIO-ELECTROCHEMICAL SYSTEMS

1. Introduction

Over the past century, the use of fossil fuels and non-renewable energy sources has contributed to humanity's economic growth. The connection between economic and industrial development and energy is undeniable. The adverse consequences of using fossil fuels, as well as their limited and non-renewable nature, are driving the world to seek new renewable energy sources. One of the main challenges over the past century has been generating clean and sustainable energy. On the other hand, pollution caused by the use of fossil fuels and the increase in greenhouse gases pose irreversible consequences for the world. [1] For these reasons, researchers have been searching for new renewable energy sources with potential for industrial application over the last few decades. Wind energy, solar energy, water energy, geothermal energy, and biomass are some of the renewable energies that have been discovered, optimized, and increasingly applied in recent years. [2]

Biomass is abundant on our planet and in recent years has emerged as one of the most important and researched energy sources. It is rich in organic and inorganic materials that can decompose and release energy. One way to generate clean energy from biomass is through Microbial Fuel Cells (MFCs). An MFC is a device that directly converts the chemical energy released during the breakdown of organic materials by microorganisms into electricity. Various organic materials can be used as substrates in MFCs, including simple materials such as glucose and acetate or more complex compounds such as starch, organic sludge from treatment plants and various industries, plant waste, and others. Microbial fuel cells (MFCs) are versatile technology, primarily used for wastewater treatment, bioelectricity generation, and environmental monitoring. Microbial fuel cells are typically operated with a liquid organic phase because the ion transfer process is efficient in a liquid medium. However, some researchers have investigated the potential of operating microbial fuel cells with a solid organic phase. [3]

Solid-phase microbial fuel cells (SMFCs) are one of the innovations in MFC technologies that can be applied to solid waste. They have been found to accelerate the anaerobic digestion process of waste, directly generate electricity, and produce mature compost from organic compounds. Solid-phase microbial fuel cells are cost-effective because they require inexpensive materials for their construction and operation. Furthermore, their ability to generate electricity makes them a direct alternative source of renewable energy, which has attracted considerable attention from researchers. [4] Also, solid-phase microbial fuel cells are an alternative method to overcome the problem of solid waste treatment, as it uses them as a substrate to provide an environmentally friendly and sustainable source of electricity. Therefore, solid-phase microbial fuel cells are considered capable of addressing multi-sectoral problems, as they can be integrated with other waste treatment methods, such as aerobic composting or anaerobic digestion. [5]

Solid-phase Microbial Fuel Cells (SMFCs) can be considered a renewable energy source for powering low-energy devices.

However, recent research on SMFCs shows that they can generate only a small amount of energy at the mW level. Therefore, these systems cannot be used directly to power devices that require higher power. [6] Researchers have focused on improving the efficiency of these cells by creating larger electrodes, enhancing electrode materials, and using different substrates to increase the generated energy. By optimally storing the generated electricity, it can be used to power systems that require more energy. [7]

SMFCs have successfully been used to power environmental sensors, communication systems, and magnetometers. [8] Additionally, the use of SMFCs as a continuous energy source for electrical devices has been demonstrated. [9] Although SMFCs are a rapidly developing technology, some issues need to be addressed before most practical applications can be commercialized. [10] The primary limitation of SMFCs is their low output power, which usually ranges from several to tens of mW, making them unsuitable for directly powering devices that require watt-level power. The limited power production in SMFCs results from multiple factors, such as substrate and water characteristics, cathodic activation losses, and high ohmic resistance due to the long distance between the anode and cathode. [11] To date, various attempts have been made to overcome these obstacles and thus improve the output power. These strategies mainly involve modifying the electrodes, regulating the electrolyte, optimizing the SMFC design, and optimizing the energy harvesting mode. [12]

For high-power applications, the cell voltage can be increased using a boost converter, supercapacitor, or a combination of both. [13] In some studies, the cell voltage was increased up to 3-4 V by combining two supercapacitors and one boost converter. [14] In other studies, the cell voltage was raised from 0.5 V to 5-6 V using a supercapacitor and two boost converters. [15] The boost converter can regulate the operation of the cell by increasing its voltage and helping to provide maximum power to the load. In this article, we present an energy harvesting system consisting of a supercapacitor and a non-isolated DC boost converter for a stack of microbial fuel cells. Four different modules of microbial fuel cells were realized by connecting individual cells in series-parallel configurations. The charging and discharging behavior of the supercapacitors and the output voltage of the power management system were investigated for each cell module. Experimental validation of the proposed scheme shows that one PMS is capable of producing an output voltage of 9 V/12 V. [16]

The aim of this study is to investigate the possibilities for storage and utilization of energy generated from stacked solid-phase microbial fuel cells (SMFCs). Stacked SMFCs represent a scaled-up green waste composter with cogeneration of energy, constructed in previous developments by the team. [17] In this study, various options for increasing the output voltage, storing the energy in different batteries, and utilizing it for different purposes will be tested.

2. Materials and methods

Construction of SMFC biosensor

The composter is a plastic container with a volume of 360 cm^3. The composter consists of 24 PVC pipes arranged vertically. Each PVC pipe has a diameter of 110 mm and a height of 900 mm. The bottom of the pipes is closed with PVC plugs. At the bottom of the pipes are located stainless steel AISI 304 electrodes with an area of 414.48 cm^2 acting as an anode. At the top of the pipes is a second stainless steel AISI 304 electrode with an area of 414.48 cm^2 acting as a cathode. Copper wires were used as conductors in the electrical circuit. Each of the 24 tubes represents a solid-phase microbial fuel cell (SMFC). Then the plant biomass was placed in the tubes and filled with water. The plant biomass consists mowed grass with a length of 10 - 15 centimeters. In plant biomass, ancestral species are *Cynodon dactylon*, *Capsella* and *Taraxacum*. The approximate volume of plant biomass in each tube is 7.5 dm^3. The physicochemical characteristics of water was pH 7.12, Eh 352 mV and EC 73 µS cm^{-1} measured by Vernier LabQuest Mini. On Figure 1 is shown a scheme of single segment (PVC pipe) of the composter.
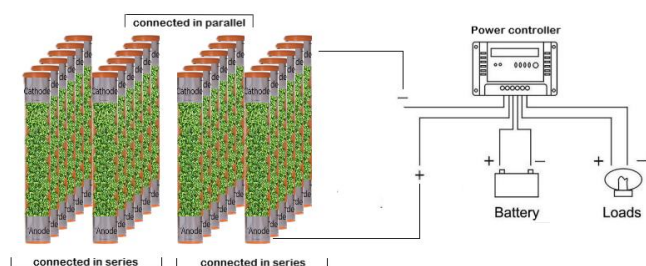

Fig. 1 *The schematic diagram of single segment (SMFC) of the composter*

The individual segments (SMFCs) (fig. 2) were stacked in the plastic container and after the segments reached a base voltage, the electrical parameters of the composter were measured. The electrical parameters were measured with the segments connected in series and in parallel. Then the segments were connected in series 12x12 and both pairs connected in parallel, and the electrical parameters were measured again.

Fig. 2 *Photo of single segment of the composter*

Electrochemical analysis

To determine the operation and effectiveness of the composter polarization and power curves were obtained by varying external resistances sequentially from 10, 8, 6, 4, 2, 1.5, 1.3, 1, 0.7, 0.5, 0.3 to 0.1 KΩ using MCP lab electronics BXR-04 ResistorBox. The voltage dynamic were measured and recorded in real time with Vernier LabQuest Mini and Logger Lite software.

3. Results and discussion

Initial studies [17] have shown that after filling all segments of the composter with plant biomass, an increase in the open circuit voltage of the individual segments is observed. Figure 3 presents the averaged voltage data of the individual segments.
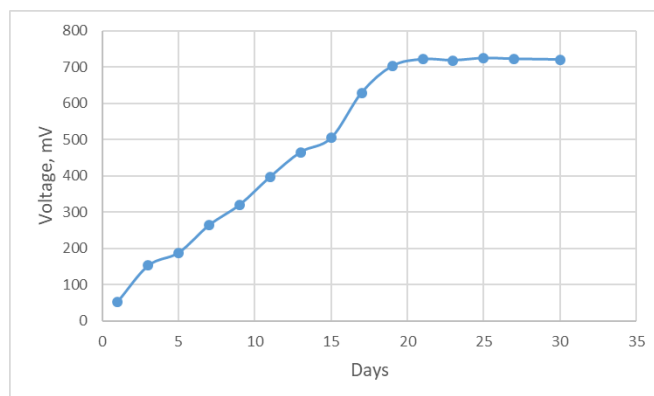

Fig. 3 *Average open circuit voltage of individual segments of the composter*

The graph shows that after filling the segments with plant biomass, a slow, smooth increase in the open circuit voltage begins. The voltage increases until the 19th day after filling with plant biomass, after which the segments begin to maintain an average base voltage of 725 mV.

From the research conducted, it was found that the composter has the best electrical parameters when connecting the 12x12 segments in series and connecting the two pairs in parallel. The results for this type of connection are shown in Figure 4.
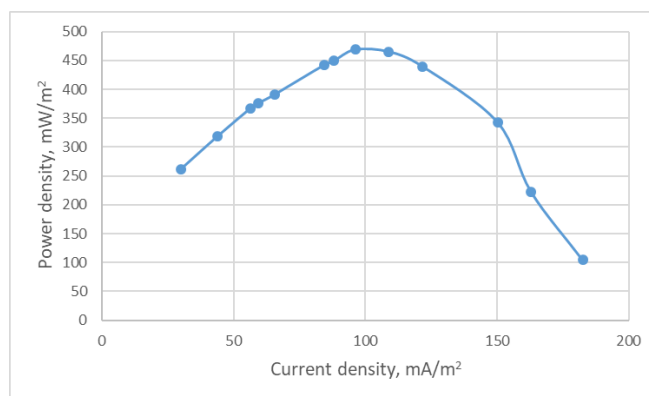

Fig. 4 *Power density dynamics when connecting 12x12 segments (SMFCs) in series and connecting two pairs in parallel*

With this connection, the composter achieved the best electrical parameters of the tested variants. A maximum power density of 474.6 mW/m^2 was recorded at a current density of 97.4 mA/m^2 and an applied resistance of 1.1 kΩ.

Based on the obtained electrical parameters of the composter, a solution for storing and utilizing the generated energy has been proposed, using an energy management system.

The Power Management System (PMS) increases the voltage from a low level to a high level and controls the composter's operating point. The PMS includes a supercapacitor (5.5V, 1 F), a switch, and a DC-DC boost converter. The block diagram of harvesting energy from the composter using the PMS is shown in Fig. 5.
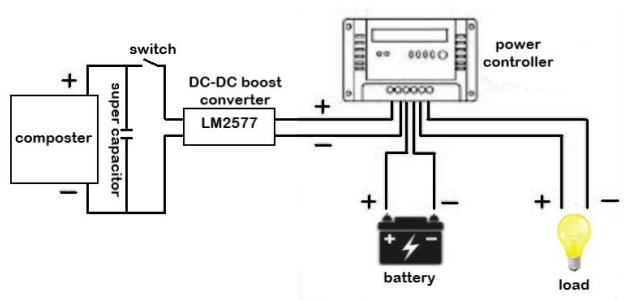

Fig. 5 *The schematic diagram of harvesting energy from the composter using the PMS*

The output voltage of the composter varies between 8.5 and 9 volts. The switch is used to connect and disconnect the supercapacitor from the boost converter. Initially, the switch is open to charge the supercapacitor from the composter. When the switch is closed, the charged supercapacitor provides power to the boost converter. The boost converter is built with the LM2577 integrated circuit (Fig. 6a). The schematic of the DC converter is shown in Fig. 6b. The boost DC/DC converter features smooth regulation of the output voltage. The converter has the following specifications: input voltage: 3-34V; output voltage: adjustable (4-35V); output current: 2.5A (max); input current: 3A (max); power: 50W.

a)
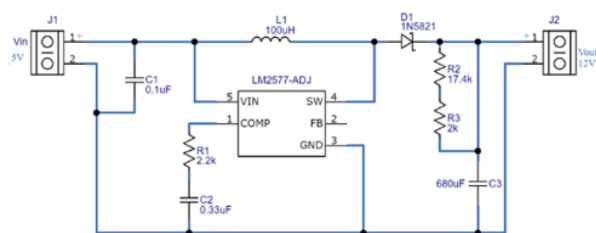
b)

Fig. 6 *DC-DC boost converter a) photo of the converter; b)block diagram of the converter*

Using the potentiometer, the output voltage of the boost converter is fixed at 12.6V. This boost converter has a current mode configuration, which leads to stable operation with a wide range of output voltages. After fixing the output voltage at 12.6V, through the power controller, the converter is connected to a lithium-ion battery pack 18650, 12V, 20A. The battery is constantly charged by the composter, and when needed, after charging, it can be disconnected from the controller and used as intended with compatible devices. The power controller allows the battery to be used during charging by connecting a load to it. Additionally, the

power controller has two built-in USB ports, providing an output voltage of 5 volts and a current of 2 amperes for charging mobile devices, power banks, and others.

4. Conclusion

In previous studies conducted by our team, a composter with cogeneration of energy was developed. The composter consists of stacked solid-phase microbial fuel cells filled with grass. In the current study, an initial method for managing, storing, and utilizing the energy generated by the composter has been proposed. The method is based on using a super capacitor connected to the composter, from which the energy passes through a boost converter. The output voltage of the converter is regulated at 12.6 volts, which charges an accumulator battery. Energy management is carried out through a power controller, which charges the battery and can simultaneously provide energy to various consumers. The voltage of the composter (which normally ranges between 8.5 and 9V) has been successfully increased to 12V using the proposed PMS. The obtained results show that the proposed method can effectively manage the energy generated by the composter. However, to achieve a commercial product, it is necessary to investigate other options for energy management, as well as the factors influencing the operation of the composter and the generated energy.

5. References

1. A. T. Hoang, S. Nizetic, K. H. Ng, A. M. Papadopoulos, A. T. Le, S. Kumar, H. Hadiyanto, V. V. Pham, Microbial fuel cells for bioelectricity production from waste as sustainable prospect of future energy sector, Chemosphere 287 (2022) 132285

2. N. Islam, B. Gogoi, R. Saikia, B. Yousaf, M. Narayan, H. Sarma, Encouraging circular economy and sustainable environmental practices by addressing waste management and biomass energy production, Regional Sustainability (2024) 5(4) 100174

3. S. Wang, A. Adekunle, B. Tartakovsky, V. Raghavan, Synthesizing developments in the usage of solid organic matter in microbial fuel cells: A review, Chemical Engineering Journal Advances 8 (2021) 100140

4. T. Ewing, P. T. Ha, J. T. Babauta, N. T. Tang, D. Heo, H. Beyenal, Scale-up of sediment microbial fuel cells, Journal of Power Sources, 272 (2014) 311e319

5. M. A. Budihardjo, Syafrudin, A. J. Effendi, S. Hidayat, C. Purnawan, A. I. D. Lantasi, F. I. Muhammad, B. S. Ramadan, Waste valorization using solid-phase microbial fuel cells (SMFCs): Recent trends and status, Journal of Environmental Management 277 (2021) 111417

6. H. Wang, Y. Ye, J. Zhang, H. Ning, Y. Xiang, X. Song, W. Zhao, F. Guo, Power performance improvement in sediment microbial fuel cells: Recent advances and future challenges, International Journal of Hydrogen Energy, 48 (2023) 24426-24446

7. R. Alipanahi, M. Rahimnejad, G. Najafpour, Improvement of sediment microbial fuel cell performances by design and application of power management systems, International Journal of Hydrogen Energy, 44 (2019) 16965-16975

8. Y. Hubenova, I. Bardarov, E. Hubenova, E. Slavcheva, Sediment microbial fuel cells capable of powering outdoor environmental monitoring sensors, Sensing and Bio-Sensing Research 46 (2024) 100695

9. J. Dziegielowsky, B. Metcalfe, M. Di Lorenzo, Towards effective energy harvesting from stacks of soil microbial fuel cells, Journal of Power Sources 515 (2021) 230591

10. J. Prasad, R. K. Triphati, Effect of sediment microbial fuel cell stacks on 9 V/ 12 V DC power supply, International Journal of Hydrogen Energy, 46 (2021) 14628-14638

11. J. Prasad, R. K. Tripathi, Review on improving microbial fuel cell power management systems for consumer applications, Energy Reports 8 (2022) 10418–10433

12. J. Prasad, R. K. Tripathi, Voltage control of sediment microbial fuel cell to power the AC load, Journal of Power Sources, 450 (2020) 227721

13. A. Mukherjee, V. Patel, M. T. Shah, D. A. Jadhav, N. S. Munshi, A. D. Chendake, D. Pant, Effective power management system in stacked microbial fuel cells for onsite applications, Journal of Power Sources 517 (2022) 230684

14. C. Donovan, A. Dewan, H. Peng, D. Heo, H. Beyenal, Power management system for a 2.5W remote sensor powered by a sediment microbial fuel cell, Journal of Power Sources, 196 (2011) 1171–1177

15. S. Li, Z. Zhao, B. Li, T. Wei, H. Jiang, Z. Yan, Supercapacitors accumulating energy harvesting from stacked sediment microbial fuel cells and boosting input power for power management systems, International Journal of Hydrogen Energy, 47 (2022) 10689-10700

16. J. Prasad, R. K. Tripathi, Scale-up and control the voltage of sediment microbial fuel cell for charging a cell phone, Biosensors and Bioelectronics 172 (2021) 112767

17. Rosen Ivanov, Design and study of the operation of a green waste composter with energy cogeneration, International Scientific Journal "Industry 4.0", Vol. 10 (2025), Issue 4, 132-135

Simulation of roll leveler housing in heavy plate leveling

Viachaslau Tamila[1], Vladimir Klubovich[2], Viktar Liaukovich[3], Anton Vetoshkin[4]
Belarusian National Technical University [1,2], The Physical-Technical Institute of the NAS of Belarus [3,4], Belarus
levkovich@phti.by

Abstract: *Roll leveling is a technological process of metal forming, used to minimize the flatness of sheet plates and reduce the level of residual stresses. The report presents the design of a 13-roll leveler for straightening sheet plates of complex configuration. The straightening precision is directly affected by the stiffness of the leveler housing. To determine the characteristics and patterns of deformation, the equivalent finite element model of the leveler housing are established and then the features of stress and strain about the leveler housing are studied.*

KEYWORDS: *LEVELLING PROCESS, LEVELLING FORCE, HOUSING*

1. Introduction

Sheet blanks are widely used in industrial production. For their cutting, laser and plasma cutting is often used. After that, sheet blanks often have insufficient geometric accuracy (flatness). To improve the geometric accuracy of sheet blanks various methods can be used, including roll levelling.

Roll levelling is a technological process of metal forming, used to minimize the flatness of sheet blanks and reduce the level of residual stresses. When levelling, the workpiece is subjected to cyclic alternating bending with decreasing amplitude. In this case, the penetration depth of deformation should be at least 0,7 of the thickness of the workpiece [1].

The existing experience of the world's leading manufacturers of process equipment (ARKU, KOHLER, etc.) shows the feasibility of using multi-roll levelers both for straightening piece sheet parts and for integrating levelers into existing and planned automated lines for the production of piece sheet blanks of a wide range for machine-building, petrochemical, aerospace and other branches of industrial production.

Multi-roll levelers are used for cold straightening of steel sheet blanks and blanks of non-ferrous alloys up to 50 mm thick and up to 5000 mm wide. Hot straightening of steel sheet blanks is carried out at temperatures of 500-700 °C, mainly immediately after leaving the working stand of the rolling mill. Hot straightening cannot provide a sufficiently even surface of the blanks, since they undergo buckling during the cooling process. Sheets with a thickness of over 40 - 50 mm are usually straightened in a cold state under presses.

At present, there is a demand for versatile and productive equipment for levelling sheet blanks with complex contours. These requirements are met by multi-roll levelers.

Roll leveler mainly composed of 6 parts (Fig. 1):

- Upper and lower roll frames. They include upper and lower leveling rolls, which are used for cyclic alternating bending of sheet blanks. The roll frames also contain back up rolls which are designed to prevent excessive bending of the leveling rolls under operating loads.

- Upper and lower frames.

- Mechanisms for adjusting the inlet and outlet inter-roll gap. Used for the initial setting of the roll leveler for straightening blanks of a certain thickness.

- Drive unit. The leveling rolls are driven by a drive unit. It consists of electric motors and reducers.

- Compensation mechanisms. Serve to compensate for the elastic deformation of the elements of the roll leveler under the working load.

- Mechanical means for moving blanks.

The roll leveler is designed for straightening blanks with a thickness of 6 to 50 mm with a maximum width of up to 2000 mm.

It is equipped with 13 leveling rolls with a diameter of 200 mm and 15 back up rolls. The distance between rolls is 205 mm (Fig. 2). In the roll leveler, a roll arrangement is used, in which the upper frame of rolls is located at an angle to the lower one, which ensures cyclic bending with decreasing amplitude of the billet. The levelling speed is in the range from 3 to 12 m/min.
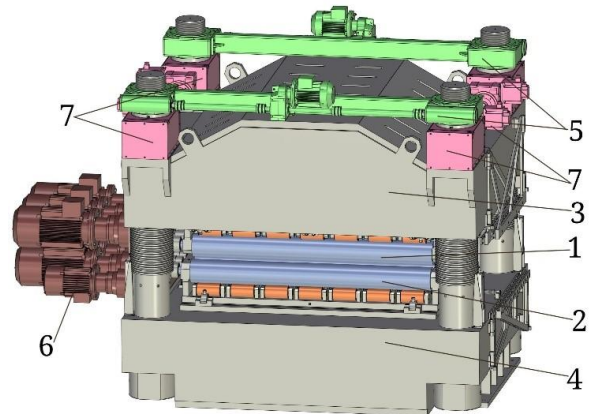

Fig. 1. *Components of the roll leveler*
1 – upper roll frame; 2 – lower roll frame; 3 – upper frame; 4 – lower frame; 5 – mechanisms for adjusting inlet and outlet inter-roll gap; 6 – drive unit; 7 – compensation mechanisms
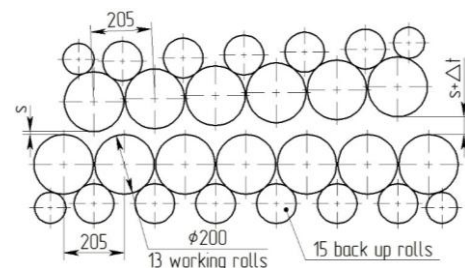

Fig. 2. *Roll arrangement*
s – inlet inter-roll gap; s+Δt – outlet inter-roll gap

Force on the most loaded leveling roll reaches 5 MN, the total force during leveling is 30 MN. The total power of the drive unit is 115 kW.

2. FEA simulation of leveler housing

2.1. Establishment of leveler housing FEM model

The housing includes the lower frame, the upper frame and the columns with nuts that connects them together. Upper and lower frames have a cellular structure. They are shown in Fig. 3 and 4 along with their FE models. The FE model of the housing is shown in Fig. 5. In this model columns and nuts have tie constraints, nuts and frames have contacts with the friction coefficient of 0,3.
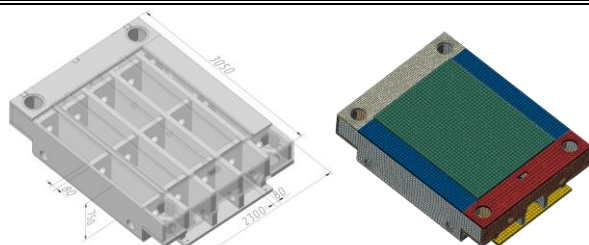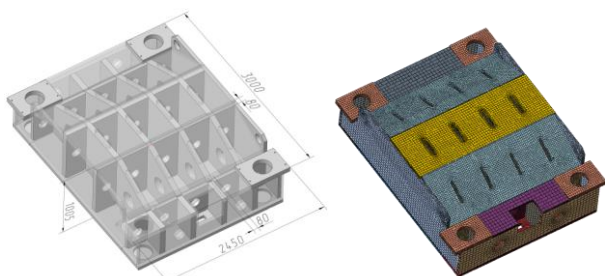
Fig. 3 *View of the lower frame.*

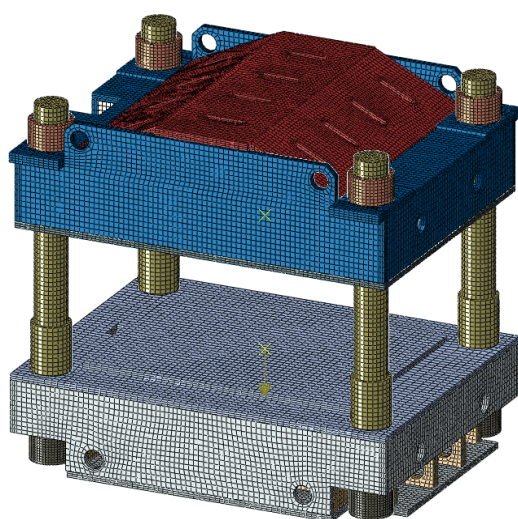**Fig. 4** *View of the upper frame.*

Fig. 5 *View of the leveler housing.*

In the meshing 8 node elements is chosen, housing has 184000 elements and 251000 nodes. The working force (30 MN) is applied to the upper and lower frames at the places of their contact with the roll frames. The working force is applied uniformly. In order to avoid movement of the entire housing, the lower surface of the housing is fixed.

Lower frame and upper frame material is steel 09G2S, column material is steel 45, nuts material is forged steel 35. Table 1 lists mechanical properties of the specified materials.

Table 1: *Mechanical properties of steels*

	09G2S	35 (forging)	45
Young's modulus E [GPa]	210		
Poisson's ratio ν	0,3		
Density ρ [kg/m³]	7850		
Yield strength σ_t [MPa]	280	490	355
Tensile strength [MPa]	445	655	600
Relative elongation δ [%]	21	12	16

2.2. *Deformation and stress of the leveler housing*

After loading, the deformation in leveling force direction is shown in Fig. 6 (sections passing through the center point of the housing are shown). Although the total displacement of the upper frame reaches 3,51 mm, this is due to the elongation of the columns. The deviation from the flatness of the platforms for installing the roll frames does not exceed 0,05 mm. When the roll leveler is in operation, the elongation of the columns will be eliminated by the compensation mechanisms. This model shows the minimum required working range of the compensation mechanism. At a working load of 30 MN, the stiffness of the structure will be 8.55×10^6 N/mm. In practical use, the deformation can be estimated by multiplying this stiffness indicator by the working force of the leveler, since the entire structure is an elastomer.
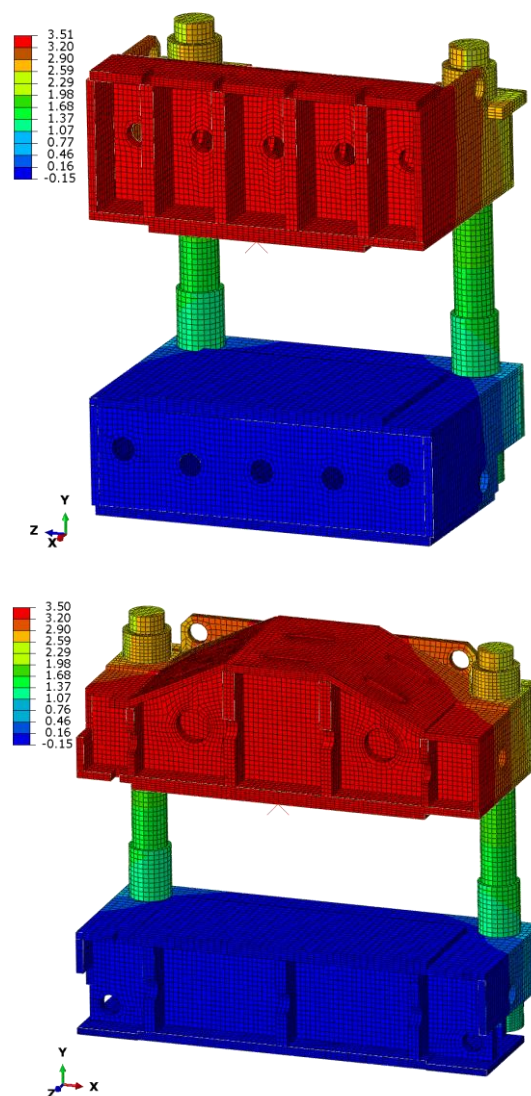

Fig. 6 *Displacement of the leveler housing.*

After loading, the stress distribution is shown in Fig. 7. The stresses in the places where the roll frames are installed do not exceed 190 MPa. The highest stresses occur in the places where the nuts contact the support surfaces of the upper and lower frames and reach 230-280 MPa.
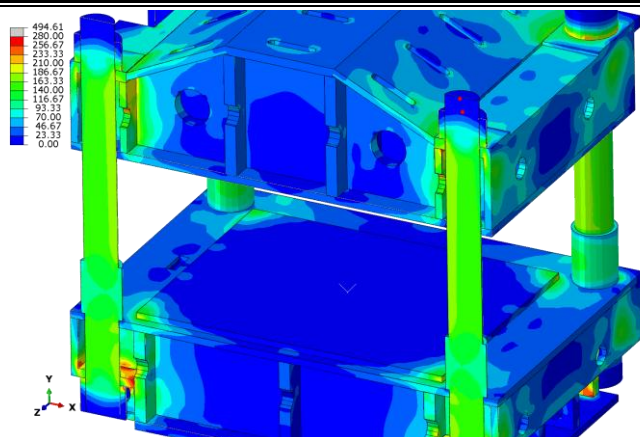
Fig. 7 *Equivalent Von Mises stress of the housing.*

3. Conclusion

The article studied the stresses and deformations of the roll leveler housing based on the developed finite element model. The results show that with the accepted housing configuration, the overall stiffness reaches 8.55×10^6 N/mm. Maximum stresses occur at the points of contact of the nuts with the upper and lower frames and do not exceed the yield strength of the materials. The total deformation reached 3,51 mm due to the elastic elongation of the columns. During straightening, the elongation of the columns will be eliminated by compensation mechanisms to maintain the inter-roll gap within acceptable limits.

4. References

1. A.A. Korolev *Konstrukciya i raschet mashin i mekhanizmov prokatnyh stanov [Design and calculation of machines and mechanisms of rolling mills]* (Moscow, Metallurgiya Publ., 1985) [in Russian]

Power Sources for Unmanned Aerial Vehicles: A Review

Assoc. Prof. Gencheva P.[1,*], Col. Assoc. Prof. Hutov I.[1*], Col. Assoc. Prof. Genov B.[1*]
Defence Institute "Professor Tsvetan Lazarov", Sofia, Bulgaria[1]
p.gencheva@di.mod.bg

Abstract: *Unmanned Aerial Vehicles (UAVs) are increasingly being deployed across a broad range of applications, including surveillance, logistics, environmental monitoring, and military operations. However, their operational effectiveness remains fundamentally constrained by current energy storage technologies, primarily lithium-ion batteries. These conventional power sources suffer from low specific energy, limited endurance, prolonged charging times, and safety concerns under extreme operating conditions.*
This paper presents a comprehensive review of alternative energy solutions for UAV platforms, focusing on hydrogen fuel cells, solar photovoltaic systems, tethered power configurations, wireless power transfer (WPT) technologies, and hybrid propulsion architectures. Each technology is assessed in terms of energy density, system complexity, operational endurance, and suitability for specific mission profiles.

Keywords: UNMANNED AERIAL VEHICLES (UAVS), ALTERNATIVE ENERGY, HYBRID PROPULSION.

1. Introduction

Unmanned aerial vehicles (UAVs) have become an essential element in the modern world, covering a wide range of civil and defense applications, surveillance and reconnaissance (ISR), environmental monitoring, logistics, and military missions. Their application is due to their adaptability, flexibility, and ability to operate in hazardous or inaccessible environments without putting human life at risk. However, their effectiveness in performing a specific mission is threatened by the shortcomings of existing energy storage systems, especially lithium-ion batteries, whose disadvantages include low specific energy, limited operational life, and long recharge cycles.

Given the increased interest in the application of unmanned aerial vehicles, there is also a growing scientific and engineering interest in the development and integration of alternative and hybrid energy solutions that can meet the ever-increasing energy needs of modern UAV platforms [1]. Alternative technological solutions include the implementation of hydrogen fuel cells, solar photovoltaic systems, wireless power transfer (WPT) technologies, and hybrid propulsion architectures. Each of these technological solutions also defines different advantages and disadvantages in terms of energy density, system complexity, weight, system integration, and system synchronization.

2. Prerequisites and means for solving

This review paper summarizes modern battery-based power systems for use in the design of unmanned aerial vehicles (UAVs) to increase operational efficiency, extend endurance, operational reliability, and adaptability in performing missions in a wide range of logistical and tactical conditions.

Given the growing industrial process and the ever-wider deployment of unmanned aerial vehicles (UAVs), this paper examines existing technical solutions for energy provision for long-term and reliable logistical and combat support.

The lack of battery power during operation is considered one of the key technical challenges in modern UAV applications [26]. On the one hand, the mission duration of a typical small drone that can be used for operational surveillance is limited by the capacity of its energy storage system. On the other hand, from the perspective of drone applications such as inspection and monitoring of power lines or gas pipelines, the time during which a UAV can be autonomous should be as long as possible. In addition, performing a mission in high-risk areas is not feasible or even impossible due to dangerous environments or inaccessibility of the destination, while a UAV provides a viable alternative to perform this task. Therefore, there is an open discussion on how to extend the mission duration of unmanned aerial vehicles (UAVs) and make drones more durable.

There are two options for increasing the flight time. The first is to increase the battery capacity, which is a very limited option under current battery material technologies. Specifically, the battery may

be too large for the drone to fly, or the battery material may be too expensive for implementation to be feasible.

The second option is to periodically charge the battery from an external power source. This can be either a wired or a wireless approach. While wired technology is associated with some complexities, such as insufficient mobility of the drone during charging, wireless options provide sufficiently greater freedom of movement. Also, they can be applied on demand, in other words, the drone does not need to return to its charging base. A review of the existing literature on the topic of UAV charging reveals that, in addition to the conventional type of charging via cable, there are numerous wireless options for extending the duration of the UAV mission. Wind gusts [2], installation of solar photovoltaic panels [3], [4], laser radiation [5], wireless charging [6, 7, 8] and the use of fuel cells [9] are just some of them. Also, some researchers propose and recommend charging UAVs via a transmission line [10], [11]. Some of the solutions are patented in [12] and [13].

3. Solution of the examined

This paper reviews battery types for unmanned aerial vehicles (UAVs).

One of the main issues with batteries is their aging. The approach proposed by Amorosi et al. [14] addresses the effects of battery aging by integrating the energy management model of unmanned aerial vehicles (UAVs), including capacity degradation due to charge and discharge cycles. The authors report the development of an original mathematical formulation – EMUC (Energy Management for UAV-based Cellular Networks) – that optimizes the energy levels of both UAVs and ground base stations in solar-powered mobile networks. The extended model, EMUC-AGE, builds on this by incorporating constraints that reflect battery aging and degradation, including the number of charge/discharge cycles, remaining capacity, and a threshold for maximum allowable cycles.

The authors' proposed [14] algorithms, D-EMUC and GAUP-LS, allow for the processing of large-scale scenarios, demonstrating performance close to the original model, with significantly improved computational times. Furthermore, the trade-off analysis between maximizing the charge of the UAVs and ground stations reveals real impacts on mission range, energy autonomy, and operational duration. As a basis for future research, the authors emphasize the need for more detailed modeling of communication parameters, traffic constraints, alternative energy sources (e.g., wind or geothermal energy), and the integration of advanced optimization techniques (e.g., Branch & Bound) and realistic battery aging models [14].

3.13.1. Lithium-Ion Capacitors as a Hybrid Energy Storage Solution for UAV Systems

In the design of power systems for unmanned aerial vehicles (UAVs), a major engineering challenge lies in balancing two critical parameters: power density, which defines the rate of energy

delivery at a given time, and energy density, which determines the total amount of energy that can be stored and used over time. These two parameters typically exhibit a trade-off, making it difficult to optimize both simultaneously within a single storage technology.

According to the Ragone plot [17], supercapacitors demonstrate very high power densities, typically ranging between 80 and 75,000 W/kg, allowing them to deliver rapid bursts of energy. However, they suffer from very low energy densities—around 0.09 to 0.10 Wh/kg—which severely limits their capability to support sustained operations, especially in aerial platforms that require longer mission durations.

In contrast, lithium-ion batteries, which are commonly used in UAV systems, offer significantly higher energy densities—ranging from 200 to 3,000 Wh/kg—enabling prolonged operation times. Nevertheless, their relatively low power densities (typically 1.5 to 20 W/kg) limit their responsiveness, particularly in scenarios requiring rapid energy discharge such as takeoff, evasive maneuvers, or high-thrust phases.

To address this inherent limitation, lithium-ion capacitors (LICs) have emerged as a promising hybrid energy storage technology. LICs combine the high energy density of batteries with the high power density and fast charge–discharge capabilities of supercapacitors. They typically achieve power densities between 1,000 and 55,000 W/kg and energy densities in the range of 18 to 350 Wh/kg [15], effectively bridging the performance gap between the two conventional technologies.

Structurally, LICs consist of insertion-type anodes, commonly made from materials such as graphite, and capacitive-type cathodes, often based on activated carbon. These electrodes operate in nonaqueous electrolytes, which provide a wider electrochemical stability window and enhanced thermal resistance, both critical for airborne applications. The insertion-type anodes allow for reversible lithium-ion intercalation, significantly enhancing charge storage capacity, cycle life, and operational safety.

In the context of UAV operations, the hybrid nature of LICs supports both high-power demands during dynamic flight phases and sufficient energy capacity for cruising or hovering. Their integration enables enhanced syst,extended mi, and great, whileba,degradation under cyclic loads.

3.2. Battery

In the context of energy sources for unmanned aerial vehicles (UAVs), the selection of an appropriate battery type is critical to ensuring optimal flight duration, payload performance, and operational reliability. Table 1 presents a comparative analysis of different battery types commonly employed in UAVs, based on key parameters such as energy and power density, cycle life, charge/discharge efficiency, self-discharge rate, cost, and Technology Readiness Level (TRL). The data are adapted and extended from the comprehensive review by Townsend et al. (2020) and have been updated to reflect their relevance for modern UAV platforms.

Table 1. Battery Chemistry Benchmarking: Voltage, Energy, Power, Cycle Life, and Cost Indicators [16]

Parameter	Pb-acid	NiMH	NiCd	Alkaline	Zn-O2
Nominal cell voltage (V)	2.1	1.2	1.2	1.3–1.5	1.45–1.65
Energy density (Wh/kg)	30–40	60–120	40–60	85–190	442
Power density (W/kg)	180	250–1000	150	50	100
Cycle life	<350	180–2000	2000	NA, non-rechargeable	100
Charge/Discharge efficiency (%)	50–95	66–92	70–90	45–85	60–70
Self-discharge rate (%)	3–20	13.9–70.6	10	<0.30	0.17
Typical Rating	12 V	12 V	12 V	1.5 V	1.4 V
Capacity	2 Ah	2 Ah	1.8 Ah	2.2 Ah	300 mAh
Costs (US$/Wh)	0.6975	0.8546	2.6778	1.6727	0.3095
TRL	9	9	9	9	9

This table presents a comparative overview of the key electrochemical and operational parameters of five commercially available battery chemistries relevant to UAV applications. The metrics include nominal cell voltage, energy and power density, cycle life, efficiency, self-discharge rate, typical ratings, capacity, specific cost (US$/Wh), and Technology Readiness Level (TRL). The data allows for precise evaluation of the strengths and limitations of each battery type in the context of performance-critical aerial platforms.

Pb-acid batteries, though widely used and mature (TRL 9), exhibit relatively low energy (30–40 Wh/kg) and power densities (180 W/kg), limiting their use in weight-sensitive UAV platforms. However, they offer moderate charging efficiency (50–95%) and are cost-effective (0.6975 USD/Wh), making them attractive for ground-based or heavy-duty support systems.

Nickel-metal hydride (NiMH) batteries offer a better balance between energy density (60–120 Wh/kg) and power density (250–1000 W/kg). Their broad cycle life range (180–2000 cycles) and moderate self-discharge rate (13.9–70.6%) make them suitable for UAVs requiring frequent charging and medium endurance. However, higher costs (0.8546 USD/Wh) compared to Pb-acid may restrict large-scale deployments.

Nickel-cadmium (NiCd) batteries provide robust cycle life (up to 2000 cycles) and stable power output (150 W/kg), but are disadvantaged by moderate energy density (40–60 Wh/kg) and environmental toxicity due to cadmium. Their self-discharge rate is relatively low (10%), and their cost remains manageable (2.6778 USD/Wh), though higher than NiMH.

Primary alkaline batteries, with energy densities between 85–190 Wh/kg and voltages ranging from 1.3–1.5 V per cell, are non-rechargeable and thus unsuitable for long-term UAV missions. However, their very low self-discharge (<0.3%) and high availability make them viable for one-time or low-consumption systems. Their cost (1.6727 USD/Wh) and lack of rechargeability remain key drawbacks.

Zinc–oxygen ($Zn–O_2$) batteries stand out for their exceptionally high energy density (442 Wh/kg) and extremely low self-discharge (0.17%). These features make them ideal for extended missions where weight and energy capacity are paramount. However, their relatively short cycle life (100 cycles), moderate efficiency (60–70%), and specialized use cases may limit.

Table 2. Performance Comparison of Advanced Lithium-Based Battery Chemistries: Li-ion, Li-Po, Li-air, and Li-SOCl$_2$ [16].

Parameter	Li-ion	Li-Po	Li-air	Li-SOCl2
Nominal cell voltage (V)	3.6–3.85	2.7–3	2.91	3.5
Energy density (Wh/kg)	100–265	100–265	11140	500–700
Power density (W/kg)	250–340	245–430	11400	18
Cycle life	400–1200	500	700	NA
Charge/Discharge efficiency (%)	80–90	90	93	6–94
Self-discharge rate (%)	0.35–2.5	0.3	1–2	0.08
Typical Rating	3.6 V	3.7 V	N/A	3.6 V
Capacity	2 Ah	2 Ah	2.2Ah	2.2 Ah
Costs (US$/Wh)	0.9361	2.3095	N/A	0.5492
TRL	9	9	6	9

The comparative evaluation of lithium-based battery chemistries—Li-ion, Li-Po, Li-air, and Li-SOCl$_2$ —reveals significant differences in energy performance, technological maturity, and suitability for various applications. Among these, Li-air batteries exhibit the highest theoretical energy density (11,140 Wh/kg) and power density (11,400 W/kg), far surpassing conventional Li-ion and Li-Po batteries, which both range between 100–265 Wh/kg and 250–430 W/kg, respectively. This positions Li-air as a promising candidate for applications demanding ultra-lightweight and high-

endurance energy storage, such as military unmanned aerial vehicles (UAVs), aerospace missions, and deep-space probes. However, the practical deployment of Li-air technology remains constrained by unresolved challenges, including electrolyte stability, lithium dendrite formation, and limited rechargeability, as reflected in its relatively low Technology Rea

In contrast, Li-ion batteries offer a proven and mature solution (TRL 9), with a well-established balance between energy density, cycle life, cost, and efficiency. Their cycle life of 400–1200 cycles and moderate cost of approximately \$0.94/Wh make them the de facto standard for both civil and defense applications, ranging from portable electronics to hybrid electric vehicles. Li-Po batteries, while comparable to Li-ion in terms of energy density and performance, offer advantages in weight and form factor flexibility. These characteristics are particularly advantageous in compact or mobile defense systems, although their cost is significantly higher (~\$2.31/Wh) and their cycle life is slightly lower (~500 cycles), limiting their long-term value in some contexts.

Li-$SOCl_2$ batteries present a different profile altogether. With a high energy density of 500–700 Wh/kg and extremely low self-discharge rates (as low as 0.08%), these batteries are best suited for low-power, long-duration, non-rechargeable applications such as remote surveillance systems, unattended ground sensors, and military devices that require decades-long shelf life. Their very low power density (18 W/kg) and non-rechargeable nature exclude them from high-drain or dynamic applications, but their reliability and stability under harsh environmental conditions make

Regarding efficiency, Li-air leads with a discharge efficiency of 93%, followed closely by Li-Po at 90% and Li-ion at 80–90%. Li-$SOCl_2$ presents variable efficiency (6–94%), likely dependent on load profile and discharge conditions. In terms of self-discharge, Li-$SOCl_2$'s performance is superior, making it ideal for standby or emergency power. Li-Po exhibits the lowest self-discharge among rechargeables (0.3%), while Li-ion can vary up to 2.5% depending on chemistry and temperature.

In summary, the selection of a lithium-based battery chemistry must be aligned with specific mission requirements. Li-ion remains the most balanced and commercially viable solution. Li-Po offers form factor flexibility at a premium cost. Li-air represents the most forward-looking technology, with transformative potential for lightweight, high-capacity energy storage, albeit still in experimental stages. Li-$SOCl_2$ is highly specialized for low-drain, long-duration applications where rechargeability is not required. Each chemistry presents distinct advantages and limitations, and ongoing advancements in materials science, safety engineering, and manufacturing will continue to shape their respective roles in future defense, aerospace, and industrial systems.

4. Conclusion

The comprehensive evaluation of both advanced lithium-based and conventional battery chemistries—specifically Li-ion, Li-Po, Li-air, Li-$SOCl_2$, Pb-acid, NiMH, NiCd, Alkaline, and Zn–O_2 — reveals pronounced differences in terms of voltage, energy density, power output, cycle life, self-discharge behavior, efficiency, cost, and technology readiness levels (TRL). These factors are critically important when selecting power sources for unmanned aerial vehicles (UAVs), especially within the context of military applications, where high performance, reliability, and mi

Among the lithium-based systems, Li-ion and Li-Po batteries exhibit a well-established balance of energy density (100–265 Wh/kg), power density (up to 430 W/kg), and moderate-to-high cycle life (400–1200 cycles), making them ideal for rechargeable applications in tactical UAVs. Their high TRL (9) and acceptable cost-per-energy metrics position them as current industry standards. In contrast, Li-air batteries show exceptionally high theoretical energy and power densities (up to 11,400 Wh/kg and W/kg, respectively), but remain at an early stage of development (TRL 6), with unresolved challenges in rechargeability, stability, and scalability. Li-$SOCl_2$ batteries, being primary cells with high energy density (up to 700 Wh/kg) and extremely low s

Conventional chemistries like Pb-acid and NiCd, although mature and widely available, offer limited energy density and unfavorable weight profiles, making them suboptimal for modern UAV systems where energy-to-mass ratio is critical. However, their robustness and cost-effectiveness may justify their use in auxiliary or ground-support applications. NiMH batteries provide a better energy-to-weight trade-off and longer cycle life (up to 2000 cycles), though at a higher cost. Alkaline batteries, while readily available and inexpensive, are non-rechargeable and thus unsuitable for long-term deployment in UAVs, though they may be leveraged for disposable or low-power payload systems. Zn–O_2 batteries emerge as a promising alternative due to their outstanding energy density (442 Wh/kg) and minimal self-discharge, yet their limited cycle life and niche operational suitability currently restrict broader use.

In conclusion, the optimal battery chemistry for UAV deployment must be selected based on the specific mission profile—balancing rechargeability, power and energy demands, endurance, operational temperature range, and economic feasibility. Rechargeable lithium-based systems dominate current military UAV platforms due to their mature performance profiles. However, emerging chemistries such as Li-air and Zn–O_2 show great potential for future UAV architectures, provided their technological limitations can be overcome through continue

Overall, ongoing advancements in battery technology, combined with mission-specific optimization, will play a pivotal role in enhancing the operational capabilities, endurance, and reliability of UAVs in military applications, ultimately contributing to more effective and sustainable defense systems.

Recognition

5. References

1. M. Lu, M. Bagheri, A. P. James and T. Phung, "Wireless Charging Techniques for UAVs: A Review, Reconceptualization, and Extension," in IEEE Access, vol. 6, pp. 29865-29884, 2018, doi: 10.1109/ACCESS.2018.2841376

2. P. L. Richardson, "Upwind dynamic soaring of albatrosses and UAVs," *Prog. Oceanogr.*, vol. 130, pp. 146–156, Jan. 2015.

3. S. Jashnani, T. R. Nada, M. Ishfaq, A. Khamker, and P. Shaholia, "Sizing and preliminary hardware testing of solar powered UAV," *Egyptian J. Remote Sens. Space Sci.*, vol. 16, no. 2, pp. 189–198, Dec. 2013.

4. S. Morton, R. D'Sa, and N. Papanikolopoulos, "Solar powered UAV: Design and experiments," in *Proc. IEEE/RSJ Int. Conf. Intell. Robots Syst. (IROS)*, Sep./Oct. 2015, pp. 2460–2466.

5. M. C. Achtelik, J. Stumpf, D. Gurdan, and K.-M. Doth, "Design of a flexible high performance quadcopter platform breaking the MAV endurance record with laser power beaming," in *Proc. IEEE/RSJ Int. Conf. Intell. Robots Syst.*, Sep. 2011, pp. 5166–5172.

6. A. B. Junaid, Y. Lee, and Y. Kim, "Design and implementation of autonomous wireless charging station for rotary-wing UAVs," *Aerosp. Sci. Technol.*, vol. 54, pp. 253–266, Jul. 2016.

7. S. Dunbar, "Wireless far-field charging of a micro-UAV," in *Proc. IEEE Wireless Power Transf. Conf. (WPTC)*, May 2015, pp. 1–4.

8. M. Simic, C. Bil, and V. Vojisavljevic, "Investigation in wireless power transmission for UAV charging," *Procedia Comput. Sci.*, vol. 60, no. 1, pp. 1846–1855, 2015.

9. M. Gadalla and S. Zafar, "Analysis of a hydrogen fuel cell-PV power system for small UAV," *Int. J. Hydrogen Energy*, vol. 41, no. 15, pp. 6422–6432, Apr. 2016.

10. J. Moore and R. Tedrake, "Powerline perching with a fixed-wing UAV," in *Proc. AIAA Infotech@Aerospace Conf.*, Apr. 2009, pp. 1–16.

11. J. Moore and R. Tedrake, "Magnetic localization for perching UAVs on powerlines," in *Proc. IEEE/RSJ Int. Conf. Intell. Robots Syst.*, Sep. 2011, pp. 2700–2707.

12. E. J. Silberg and J. H. Milgram, "Battery charging arrangement for unmanned aerial vehicle utilizing the electromagnetic field associated with utility power lines to generate power to inductively charge energy supplies," U.S. Patent 7 714 536 B1, May 11, 2010.

13. P. T. Marshall, "Power line sentry charging," U.S. Patent 7 398 946 B1, Jul. 15, 2008.

14. L. Amorosi, L. Chiaraviglio and J. Galán-Jiménez, "Optimal Energy Management of UAV-Based Cellular Networks Powered by Solar Panels and Batteries: Formulation and Solutions," in IEEE Access, vol. 7, pp. 53698-53717, 2019, doi: 10.1109/ACCESS.2019.2913448.

15. V. Aravindan, J. Gnanaraj, Y. Lee, and S. Madhavi, "Insertion-type electrodes for nonaqueous Li-ion capacitors," Chemical Reviews, vol. 114, no. 23, pp. 11619–11635, Jul. 2014.

16. Ashleigh Townsend, Immanuel N. Jiya, Christiaan Martinson, Dmitri Bessarabov, Rupert Gouws, A comprehensive review of energy sources for unmanned aerial vehicles, their shortfalls and opportunities for improvements, Heliyon, Volume 6, Issue 11, 2020, e05285, ISSN 2405-8440, https://doi.org/10.1016/j.heliyon.2020.e05285.

[17] D.V. Ragone, "Review of Battery Energy Storage Technology," *Proceedings of the IEEE*, vol. 67, no. 4, pp. 497–511, Apr. 1979.

Ударник - силомер за махален чук на Шарпи

Маг. Инж. Теодор Атанасов

Институт по металознание, съоръжения и технологии с Център по хидро- и аеродинамика „Академик Ангел Балевски"
Българска академия на науките

Резюме: Разработен е специален елемент (ударник – силомер) използван при изпитване на ударно огъване по метода на чук на Шарпи. Ударника е изработен и монтирани на видоизменено махало на стандартен (300 J) махален чук на Шарпи. Последният е изпитан с помощта на стандартни тестови образци с V-надрез. Изследвана е възможността за запис на диаграма сила – време при разрушаване на тестовия образец, която ще даде възможност за подробен анализ на поведението на материала.
КЛЮЧОВИ ДУМИ: УДАРНИК - СИЛОМЕР, ЧУК НА ШАРПИ, УДАРНО ОГЪВАНЕ, ТЕНЗОСЪПРОТИВЛЕНИЕ

Impactor - forcemeter for pendulum hammer of Sharpie

Master engineer Teodor Atanasov

Institute of Metallurgy, Equipment and Technologies with Center for Hydro- and Aerodynamics "Academician Angel Balevski"
Bulgarian Academy of Sciences

Abstract: A special element (impactor - force gauge) used in impact bending testing using the Charpy hammer method has been developed. The impactor is fabricated and mounted on a modified pendulum of a standard (300 J) Charpy pendulum hammer. The latter was tested using standard V-notch test specimens. The possibility of recording a force-time diagram upon failure of the test specimen has been investigated, which will allow for a detailed analysis of the material's behavior.
KEYWORDS: IMPACTOR - FORCE METER, CHARPY HAMMER, IMPACT BENDING, TENSILE STRENGTH

1. Въведение:

За определяне на механичните характеристики на материалите чрез динамични тестове по метода – Махален чук на Шарпи 300J, основно се отчита работата K за разрушаване на тестовият образец чрез разликата на първичната кинетична енергия, генерирана при ускорението на махалото от ъгъл α и остатъчната кинетична енергия след разрушаване на тестовият образец, която отклонява махалото на ъгъл β по формулата:

$$K = G*l \ (cos\beta - cos\alpha), \quad [J] \qquad [3]$$

Където:
K – работа за деформация и разрушаване на тестовия образец,
G – масата на махалото, [kg]
l - дължина на рамото на махалото, [m]
α – ъгъл на първоначално отклонение, [rad]
β – ъгъл на отклонение след разрушаване на тестовия образец, [rad]

Съвременните технологии позволяват залепване на тензосъпротивления по ударника на махалото или опорите, чрез които може да се отчете и запише силата по време на различните фази на деформация и разрушаване на пробното тяло, диаграма сила – време, чрез която може да се направи по – подробен анализ на механичните свойства на материала, от който е изработено пробното тяло. На диаграмата сила – време

ясно си проличава поведението на материала при нарастване на силата на натоварване върху него, като: еластична деформация, зона на провлачане, пластична деформация, критична точка на уякчаване, точка на окончателно разрушаване. Тензосъпротивлението представлява елемент, който си променя съпротивлението при промяна на геометричните размери. Монтиран върху ударника на махалото той отчита повърхностната деформация при натоварване в следствие от съприкосновението му с тестовия образец. При подходящо свързване на тензосъпротивления (единичен полумост или пълен мост) и захранване се получава електрически сигнал, който чрез поредица от спомагателни измервателни и усилващи апарати бива записан. Записите могат да бъдат обработвани математически, визуализирани в графичен вид, анализирани и др. В настоящата работа ще бъде описан процеса по изработване, монтиране и възпроизвеждане на диаграма сила – време.
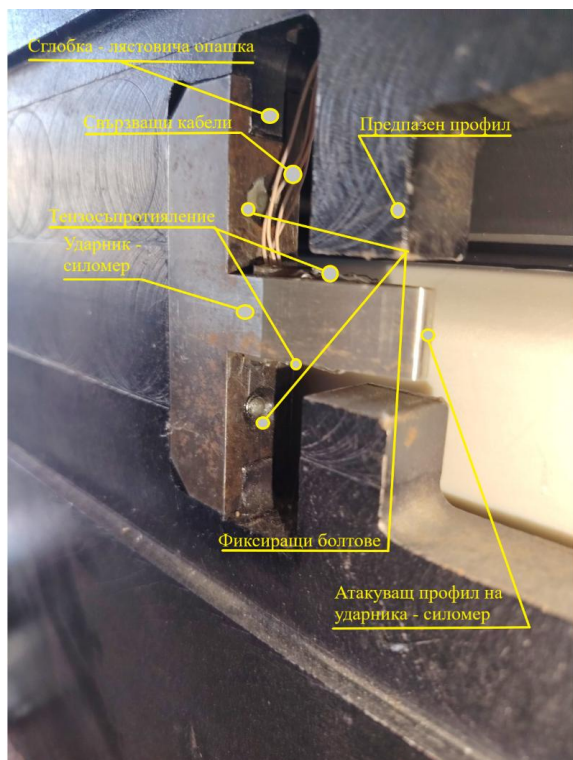
2. Конструктивна разработка:

За изпитване на ударно огъване по метода на Чук на Шарпи е конструирана специална съставна пита-ударник, показана на (фиг.1) , състояща се от:
-ударник със специална геометрия и профил на върха отговаряща на стандарта [1][2].
-пита с необходима форма и тегло

*Фиг. 1 Сглобено махало за махален чук на Шарпи*

Фиг. 2 Ударник - силомер

Ударникът е изработен от висококачествена стомана със специална геометрия позволяваща прикрепване към питата чрез високояки специални притягащи болтове. На него има залепени тензо датчици свързани в пълна мостова снема [3], които служат за измерване на силата при удара. Контактните повърхности между ударника и питата са шлайфани за максимален акустичен контакт. За прецизно фиксиране и осигуряване против разместване на ударника спрямо питата е изработено съединение тип „лястовича опашка"

На повърхностите не подложени на директно механично въздействие, прецизно са залепени фолиеви 350Ω тензодатчици тип XY произведени от HBM.

Използваните тензорезистори са показани на фиг. 3

Във вътрешният край на силомера е изработен малък отвор за оптимално извеждане на кабелите. Допълнително през питата също е изработен подходящ отвор за извеждане и механична защита на кабелите от силомера. С двата специално изработени издатъка върху питата се осъществява допълнителна защита на електрическите елементи от външни механични въздействия.
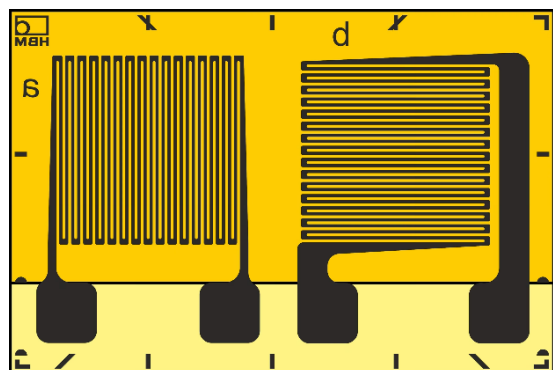
Фиг. 3 - Тензорезистор тип XY - HBM

На фигура 4 е показана блок схема на свързване на измервателната и записваща апаратура.
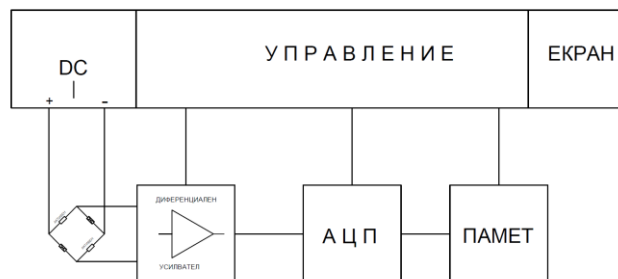
Фиг. 4 – Блок схема на свързване на тензорезистори

Апаратурата се състои от:

- Постоянно токов източник захранващ моста тензорезистори
- Широколентов усилвател с диференциален вход
- Аналогоцифров преобразувател с подходяща честотна лента за преобазуване
- Цифрова памет за запис на преобразувания по време на удара сигнал
- Блок за управление и захранване на всички останали елементи
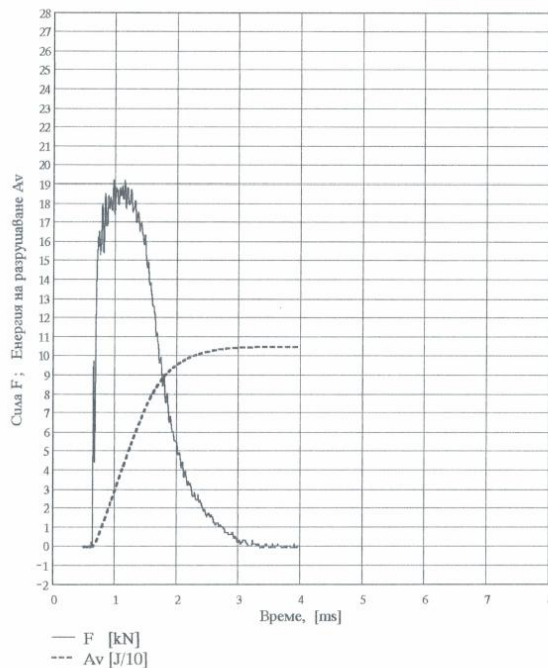- Екран за визуализация на диаграма сила – време и получените резултати

3. Експериментална част:

Посоченото устройство е калибрирано и изпитано в реални условия и показва съвпадение на получените резултати. На Фигура 5 е показана реално записана диаграма сила – време с описаната апаратура.

Фиг. 5 Запис на графика сила – време

От диаграмата ясно се вижда, че E_α – енергията за разрушаване, отчетена по скалата на чука, сравнена с A_V – енергията за разрушаване отчетена от ударника – силомер, формира изчисленото отклонение $\varepsilon_\% = 1,14\%$. Съотношението между двата параметъра е изчислено по формулата:

$$\varepsilon_\% = \frac{A_V * 100}{E_\alpha} - 100, \qquad [\%] \qquad [3]$$

Където:

$\varepsilon_\%$ - Изчислено отклонение, $\qquad [\%]$

E_α – Енергия за разрушаване изчислена по скала на установката, $\qquad [J]$

A_V – Енергия за разрушаване изчислена по диаграмата сила – време, $\qquad [J]$

4. Заключение:

o   Разработен е специален ударник – силомер за динамично триточково огъване по метода махален чук на Шарпи.
o   Ударника - силомер е калибриран статично [1].
o   Ударника - силомер е монтиран на чука на Шарпи.
o   Чука на Шарпи е калибриран съгласно стандартите [1], [2].
o   Проведени са експерименти с стандартни пробни тела с V – надрез.
o   Записана е диаграма сила – време за стандартен образец.
o   Изчислена е енергията на разрушаване по диаграмата.
o   Получените резултати съвпадат с данните получени на стандартната скала на чука на Шарпи.

5. Литература:

[1]   Annual Book of ASTM Standards – section three –Volume 03.01; Jul 2006

[2]   EN 10 045-1 Metallic materials — Charpy impact test —Part 1: Test method; March 1990

[3]   Воденичаров Ст. Колев Ст. „Динамични изпитания на стомани, предназначени за реакторостроенето" – Научна сесия по ПТМ – Варна, ноември 87